Nano-orifice based Dielectrophoretic Manipulation and Characterization of Nanoparticles and Biological Cells

by

Kai Zhao

A thesis

presented to the University of Waterloo
in fulfillment of the
thesis requirement for the degree of
Doctoral of Philosophy
in
Mechanical and Mechatronics Engineering

Waterloo, Ontario, Canada, 2019

EXAMINING COMMITTEE MEMBERSHIP

The following served on the Examining Committee for this thesis. The decision of the Examining Committee is by majority vote.

External Examiner

NAME	Xinyu Liu
Title	Associate Professor

Supervisor(s)

NAME	Dongqing Li
Title	Professor

Internal Member

NAME	Carolyn Ren
Title	Professor

Internal Member

NAME	Zhongchao Tan
Title	Professor

Internal-external Member

NAME	Bernard P. Duncker
Title	Professor

AUTHOR'S DECLARATION

I hereby declare that I am the sole author of this thesis. This is a true copy of the thesis, including any required final revisions, as accepted by my examiners.

I understand that my thesis may be made electronically available to the public.

ABSTRACT

Dielectrophoresis (DEP) is the motion of a dielectric particle in an aqueous solution due to the polarization effects in a non-uniform electric field. Due to its property of label-free, scalable, and capable of generating both negative and positive forces to manipulate bio-particles, DEP shows crucial applications in various biological and clinical analysis such as trapping, sorting, separation and characterization of micro and nanoparticles, cells, viruses, bacteria, and DNA. However, to date, the traditional DEP techniques involve the issues of complex fabrication of arrays of the embedded microelectrodes, particles clogging, low sensitivity and resolution, as well as the Joule heating effect with high electric fields applied.

This thesis investigates and develops a novel dielectrophoretic platform for the asymmetric-orifices based manipulation and separation of nanoparticles and micron droplets, as well as characterization and identification of droplets and biological cells by the pressure-driven flow in the polydimethylsiloxane (PDMS) microchannels. At the beginning of this thesis, a nano-orifice based dielectrophoretic microfluidic chip is developed. In such a chip, the non-uniform electric field is generated by applying the electric field via a pair of asymmetric orifices, a small orifice on one side of the channel walls and a large orifice on the opposite side of the channel walls. In order to obtain a strong gradient of the non-uniform electric fields, i.e., a large width ratio between the small orifice and the large orifice, a small microchannel or a nanochannel fabricated by the solvent-induced cracking method is used to form the small orifice. The electric field and the flow field inside the channel are simulated and studied.

Then two fundamental research projects are conducted on the nano-orifice based direct current (DC) DEP microfluidic chips to investigate the separation of the nanoparticles and Janus particles in microchannels. In the first research project, the size-dependent separation of micro and nanoparticles and the separation of similar size nanoparticles by type are studied. The Clausius-Mossotti factors of the particles as a function of the electrical conductivity of the suspending medium are discussed, and the effects of the applied electric field, the flow rate as well as the width and length of the small orifice are investigated. The experimental results of the particle trajectory show good agreements with the numerical simulation results. Distinguishing of nanoparticles as small as 51 nm and 140 nm, as well as 140 nm polystyrene (PS) and 150 nm magnetic nanoparticles with high separation resolution, have been achieved. In the second research project, the dielectrophoretic manipulation and separation of the Janus particles are numerically investigated. Effects of the strength of the electric fields, as well as the coating coverage, thickness, and electrical conductivity of the Janus particles on their DEP behaviors and trajectories under DC electric field are systematically studied. The effect of the coating thickness of the Janus particles on their

dielectrophoretic behaviors is negligible when using the DC-DEP method and the Janus particles with gold coating coverage over 50% will experience positive DEP effects.

Afterward, the manipulation and separation of the oil and ionic liquid (IL)-in-water emulsion droplets are investigated under DC electric field in the asymmetric orifice based microfluidic chips. The effects of the type and content of the oil droplets and the ionic concentration and types of the electrolyte solutions on the trajectories of the emulsion droplets are analyzed. By using the pressure-driven flow and a stream of sheath flow, the mixed emulsion droplets move closely to the vicinity of the nano-orifice and experience the stronger DEP effects. As the magnitude of DEP forces exerting on the droplets is determined by the size of the droplet, the separation of smaller silicone oil droplets with a small size difference of only 3.5 μm is demonstrated. By selecting the surrounding solution with a specific electrical conductivity, the separation of the emulsion droplets of similar size but different contents is achieved by opposite DEP effects, i.e., p-DEP and n-DEP, respectively, providing a platform to manipulate different kinds of emulsion droplets carrying different biomolecules or bioparticles.

Lastly, by using the alternating current (AC) DEP microfluidic chips, the tunable characterization and identification of droplets and biological cells are investigated. To generate DEP forces, two electrode-pads are embedded in a set of asymmetric orifices on the opposite sidewalls to produce the non-uniform electric fields. In the vicinity of a small orifice, the cells experience the strongest non-uniform gradient. The effects of the strength and frequency of the applied AC electric field, as well as the ionic concentrations, i.e., different electrical conductivities on their DEP behaviors, are investigated, respectively. By adjusting the frequency and strength of the AC electric field, the separation of live and dead yeast cells, as well as the cells with the targeted diameter and dielectric property, are achieved. To evaluate the critical frequency of the specific droplets and cells and manipulate the targeted cells, a microfluidic system is developed to measure the lateral distance between the cells center and the centerline of the main channel as a function of the AC frequency. The trends of measured lateral migrations of yeast cells are similar to the corresponding Clausius−Mossotti (CM) factors. This system provides a method to characterize the crossover frequency of the specific cells and manipulate the targeted cells.

This thesis provides the microfluidic research platform with a comprehensive working procedure for the asymmetric orifice based DEP microfluidic applications. The fundamental studies in this thesis expand our understanding of the dielectrophoretic behaviors of the nanoparticles, micron droplets, Janus particles, and the biological cells and overcome the shortcomings of the conventional DEP methods, and the microfluidic systems developed on the asymmetric orifice based dielectrophoretic chips open a new avenue to nanoparticles separation as well as biological cells characterization.

ACKNOWLEDGEMENTS

It has been almost four years since my graduate study journey at the University of Waterloo in 2015. I have been working hard to reach my goal, and finally, I am about to achieve it. During this journey, I have met a lot of great people who helped and supported me to improve myself and develop my academic strength.

First and foremost, I would like to thank my supervisor, Dr. Dongqing Li for his patient encouragement and incredible support. Under his guidance, I had a great Ph.D. study in this interesting research area. His foresight and confidence in academic research always inspire me, and his positive and motivating attitude has always helped me to feel the pleasure of this graduate degree. I also would like to thank Dr. Xinyu Liu from the University of Toronto, Dr. Carolyn Ren, Dr. Zhongchao Tan, and Dr. Bernard P. Duncker from the University of Waterloo for their valuable times that spent for academic discussions with me, for being a member of my PhD committee and for their thoughtful comments on the preparation of my thesis.

Hereby, I would like to thank Dr. Bernard P. Duncker and Ms. Larasati from the Department of Biology for their collaboration, Dr. Ruifeng Yang from the Department of Electrical and Computer Engineering and Mr. Ming Xiao from the Department of Mechanical Engineering for their technical support, and Dr. Gordon Stubley from the Department of Mechanical Engineering for providing me with the excellent teaching skills and supervising strengths. My special thanks go to my former lab member Dr. Ran Peng for his assistance and hard-core contribution in this work.

During my four years at the University of Waterloo, my friends Dr. Yun Yang, Dr. Junjie Wang, Dr. Song Ding, Dr. Jingmei Wang, Dr. Heng Zhang, Mr. Changliang Xu, Mr. Chaojie Ou, Mr. Jie Wang, Mr. Weiqiang Liu always backed me and helped me in Waterloo. I would like to thank all of them for their friendship and support. My colleagues at the Microfluidic and Lab-on-a-Chip Lab also helped me a lot and it was really enjoyable to work with them.

Additionally, I am grateful to my funding sources from the Natural Sciences and Engineering Research Council (NSERC) of Canada, and the China Scholarship Council (CSC).

Finally, I would like to thank the most special people in my life for her existence; my wife Hang Ren. You are the one who makes my life meaningful.

TABLE OF CONTENTS

LIST OF FIGURES

LIST OF TABLES

LIST OF ABBREVIATIONS

µTAS	Micro total analysis systems	**LOC**	Lab-on-a-chip
DEP	Dielectrophoresis	**DEP force**	Dielectrophoretic force
AC-DEP	Alternating current dielectrophoresis	**DC-DEP**	Direct current dielectrophoresis
EOF	Electroosmotic flow	**EP**	Electrophoresis
AFM	Atomic Force Microscopy	**IL**	Ionic liquid

CHAPTER 1 Introduction

1.1 Background and Motivation

The rapid development of micro total analysis systems (μTAS) and lab-on-a-chip (LOC) devices has attracted growing interest in recent decades [1–3]. LOC systems bring miniaturization, parallelization, and integration to the analyses and applications in chemical, biological and clinical fields [4–6]. One of the crucial applications is the continuous and accurate manipulation of particles and droplets [7–15], such as bacteria [16–18], protein [19–21], DNA [22], virus [23–25] and cells [26–28]. Among the various technologies that have been developed and utilized to manipulate particles in microfluidic systems, such as mechanical, optical, magnetic, thermal, chemical, acoustic and electrical methods [29–38], dielectrophoresis (DEP) may be the most popular method because it is label-free, scalable, and capable of generating both negative and positive forces.

DEP means the induced movement of a polarizable particle in the non-uniform electric fields. For the particles whose polarizabilities are higher than that of the suspending solution, they experience the positive DEP (p-DEP) forces and move toward the area of the strongest electric fields. Otherwise, the particles undergoing the negative DEP (n-DEP) effects are pushed away and move toward the weak electric field region if they have lower polarizability than that of the surrounding medium. Both the p-DEP and n-DEP effects have been widely employed for the manipulation and sorting of the particles and biological cells. The non-uniformity of the electric fields can be produced by applying the alternating current (AC) electric field to arrays of electrodes with patterned structures, which are inserted in the microfluidic channel [7,11]. The non-uniform electric field can also be induced by employing direct current (DC) electric fields via the external microelectrodes through the electrically insulated microchannel with various constricted structures (e.g., hurdles or obstacles) [39–41].

Generally, the DC-DEP methods can be used not only for particle manipulation by size but also for separating particles by their electrical properties, and the insulator-based DC-DEP approach requires simple fabrication, avoids the electrochemical reaction on the electrodes, and provides a chemically inert platform. However, high voltages are typically required for DC-DEP to induce sufficiently strong DEP forces. The high voltages applied through the whole microchannel (end to end) may induce Joule heating inside the microchannel. This effect may limit their applications to manipulate biological particles and decrease the performance of the microfluidic chips [42]. The viability of cells can be affected by varying temperature inside the microchannel, and a 4 °C temperature increase above the cell physiological temperature can lead to cell death [27]. Furthermore, due to the limitation of the microfabrication techniques, the smallest space formed by the insulator hurdles/obstacles in the microchannel is relatively large, typically tens of microns. Consequently, the resulting gradient of the non-uniform electric field is not sufficiently high. This is a key

reason that the existing DC-DEP methods cannot be used for the separation of particles with a size difference smaller than a few microns and particles smaller than 500 nm [16,17,43–45].

As the magnitude of the DEP forces is proportional to the diameter of the particles and droplets [46], the manipulation and sorting of the particles and droplets by size are straightforward. Generally, different kinds of particles or droplets have different but unique dielectric signatures. Such a distinct dielectric characteristic is widely used to sort and characterize the targets by means of AC-DEP. To induce the inhomogeneous electric field, that is, the DEP effects, microelectrodes of various structures and dimensions, as well as ionic liquid electrodes [47] and liquid metal electrodes [48,49] with different configurations and shapes in the desired pattern, are usually integrated into the microfluidic systems [50]. Traditionally, electrode-based AC-DEP microfluidic devices can generate a strong non-uniform electrical field by applying a low electrical voltage and avoid electrokinetic flow over the whole microchannel. However, these current AC-DEP methods involve issues of complicated fabrication of microelectrodes in microchannels with patterned structures and electrochemical reactions on the surface of electrodes. Furthermore, because of the challenge of producing a high gradient of the non-uniform electric field, these methods always involve high electrical potentials, which require expensive amplifier instruments [51,52]. Moreover, in the AC-DEP methods, by modifying the frequency of the applied ac electric fields, various particles, soft droplets, or bioparticles will show different DEP behaviors. The key parameter of the transition between p-DEP and n-DEP effects is named as the crossover frequency, where the DEP forces are zero. This important AC-DEP characteristic is reflected by the Clausius−Mossotti (CM) curve for each kind of particle. As the crossover frequency depends on the electrical properties of the particles and surrounding solution, this unique information can be utilized to optimize the characterization and separation schemes [53–55]. Nevertheless, it is difficult to calculate the CM factor of the particles, cells, or biomolecules and to find the corresponding crossover frequency, owing to the heterogeneous structures in biological cells, complex compositions, and charging distributions [56]. As a consequence, it is highly desired to develop a dielectrophoretic microfluidic chip to achieve the high-throughput separation of particles with high sensitivity and resolution and to provide a platform to characterize the critical frequency of biological cells.

1.2 Research objectives

The major objective of this thesis is to solve the above-mentioned challenges in conventional dielectrophoresis (DEP) chips and to provide a novel microfluidic platform to theoretically and experimentally investigate the dielectrophoretic motion and behaviors of the particles, droplets and biological cells in suspension. To achieve a high manipulation sensitivity and separation resolution, the asymmetric-orifices based polydimethylsiloxane (PDMS) microchannel is developed. As an important extension of this major topic, on-chip identification of the droplets and biological cells using the lateral

migration measurement technique will be explored and demonstrated. Overall, the asymmetric-orifices based microfluidic devices will be developed for the separation and characterization of the particles and biological cells using dielectrophoresis and pressure-driven flow.

1.3 Thesis outline

This complete thesis comprises the following 7 chapters and the structure of this thesis is shown in Figure 1-1.

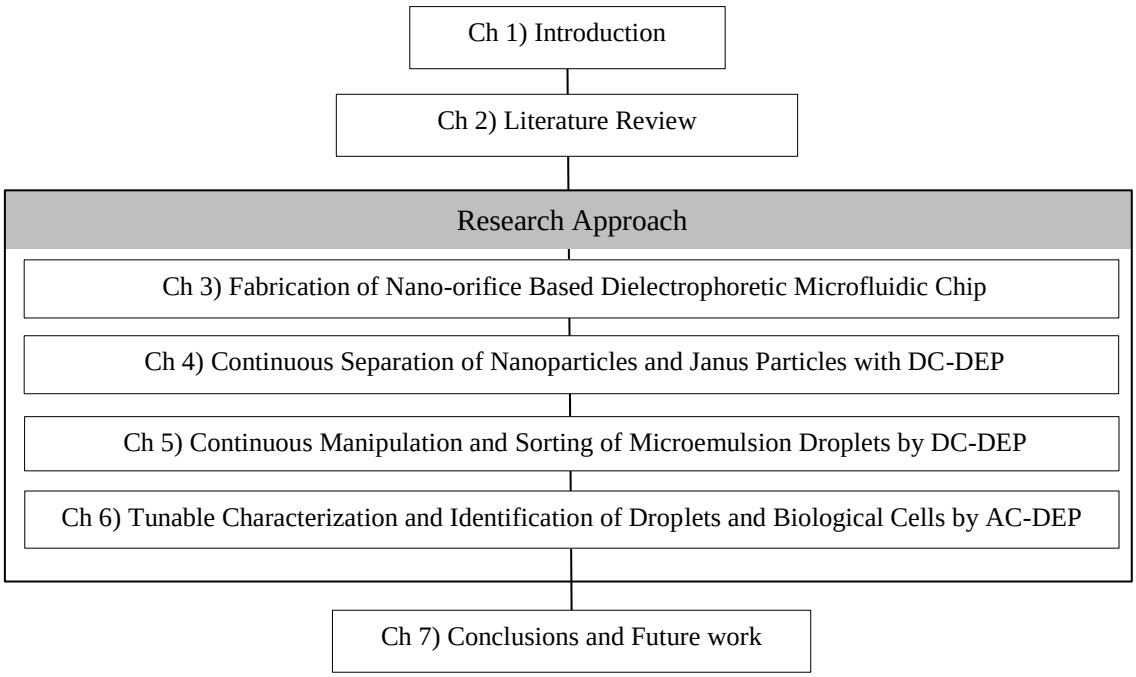

Figure 1-1 Outline of the thesis.

CHAPTER 1 gives a brief introduction to the background, motivations, and a statement of the problems of this thesis. A general review of the rapid development of microfluidic technologies and the latest applications of the lab-on-a-chip (LOC) devices are presented. The manipulation of particles using dielectrophoretic methods is specifically discussed.

CHAPTER 2 reviews general electrokinetic phenomena, such as the classical theories of the electric double layer (EDL), electrophoresis (EP), electroosmosis flow (EOF), and dielectrophoresis (DEP), which are related to a variety of particle manipulation in microfluidic chips. These various applications with dielectrophoresis will be focused on with special attention.

CHAPTER 3 demonstrates the fabrication of asymmetric-orifices based dielectrophoretic microfluidic chips. This chapter starts with the generation of the non-uniform electric field, i.e., dielectrophoretic forces, by applying the electric field via a pair of asymmetric orifices, a small orifice on one side of the channel

walls and a large orifice on the opposite side of the channel walls. In order to induce a strong gradient of non-uniform electric fields, i.e., a large width ratio between the small orifice and the large orifice, a small microchannel or a nanochannel is used to form the small orifice on one side of the microchannel walls. In this part, the creation of the small micro-cracks or nanocracks on polystyrene surface and the fabrication of positive small microchannel or nanochannel molds are presented. The microfluidic chip was made by bonding a top PDMS layer having the microchannel structure with a bottom polydimethylsiloxane (PDMS) layer having a single small microchannel or nanochannel. Then, the effects of the structures of the asymmetric orifices and the strength of the electric fields on the gradient of the non-uniform electric field are numerically analyzed and summarized.

CHAPTER 4 presents the experimental study of direct current (DC) DEP size-dependent separation of micro and nanoparticles and separation of similar size nanoparticles by type, as well as theoretical analysis of the behaviors of the Janus particles under DC electric fields. The motion of particles is controlled by pressure-driven flow, and a local DC electric field is employed to induce a non-uniform electric field via a pair of asymmetric orifices on opposite channel walls. The particle mixture experiences the DEP effect when passing through the vicinity of the small orifice where the strongest electric field gradient exists and the mixed particles deviate from the streamline into two different streams and moved into two individual outlet channels. The effects of the strength of the electric field, flow rate and structure of the small orifice upon the separation resolution of the nanoparticles, and the effects of the applied electric fields, as well as the coating coverage, thickness, and electrical conductivity of the Janus particles on their DEP behaviors and trajectories are systematically studied. The PDMS microfluidic chip is able to separate nanoparticles as small as 51 nm and 140 nm, and 140 nm polystyrene (PS) and 150 nm magnetic nanoparticles with a size difference of 10 nm.

As an extension of the asymmetric-orifices based DC-DEP method, CHAPTER 5 demonstrates the practical applications of the manipulation and separation of the silicone oil and ionic liquid (IL)-in-water emulsion droplets. Effects of the type of the oil droplets, the oil droplet content, and ionic concentration and types of electrolyte solutions on the trajectories of the emulsion droplets are studied. The experimental results are compared with those of the numerical simulations conducted by COMSOL software, which show good agreement with each other. By choosing the suspension with a specific electrical conductivity, the separation of the emulsion droplets of similar size but different contents is presented by experiencing the oppositely positive and negative DEP behaviors, respectively. Moreover, distinguishing silicone oil droplets with a small size difference of only 3.5 μm is also demonstrated.

CHAPTER 6 describes a microfluidic system for the tunable manipulation and characterization of droplets and biological cells combining alternating current (AC) DEP and pressure-driven flow. The

dielectrophoretic manipulation is achieved by embedding two electrode-pads in a pair of asymmetric orifices located on the opposite walls in the microchannel to induce non-uniform AC electric fields. As liquid flow is driven by the hydraulic pressure in the channel, biological cells are exposed to the non-uniform electric field only when they move through the vicinity of the dielectrophoretic region and hence the adverse effects caused by the electric field, such as Joule heating, are significantly reduced. Effects of the strength and frequency of the applied AC electric field and ionic concentrations of the suspension on their DEP behaviors are investigated. Mixtures of viable and non-viable yeast cells and cells with specific size and dielectric property were successful separated. By measuring the lateral distance between the cells center and the centerline of the main channel as a function of the AC frequency in the microfluidic chip, the critical frequency of the specific droplets and cells were evaluated. The trends of measured lateral migrations of yeast cells are similar to that of the corresponding Clausius−Mossotti (CM) factors, providing a platform to characterize the crossover frequency of the specific cells and to manipulate the targeted cells.

Finally, CHAPTER 77 summarizes the major conclusions and contributions of this thesis. Some potential directions for future studies are outlined and discussed.

CHAPTER 2 Literature Review

This chapter provides an overview of general electrokinetic phenomena, including the classical theories of the electric double layer (EDL), electrophoresis (EP), electroosmosis flow (EOF), and dielectrophoresis (DEP), which are related to a variety of particle manipulation in microfluidic chips. Various applications with dielectrophoretic technologies under direct current (DC) and alternating current (AC) electric fields are discussed. This chapter builds up a fundamental background of this thesis.

2.1 Electrokinetics

Electrokinetics refers to the motions of electrically charged or polarizable fluids and suspended particles by electrostatic forces in the presence of an applied electric field. With the significant improvement of micro and nanofabrication techniques, the electric field can be scaled down to the micro and nanoscale which enables electrokinetics to be one of the most favorite methods to transport and manipulate particles in the microfluidic channel [57]. Generally, electrokinetics include electroosmotic flow, electrophoresis of particles and the dielectrophoresis phenomenon, etc.

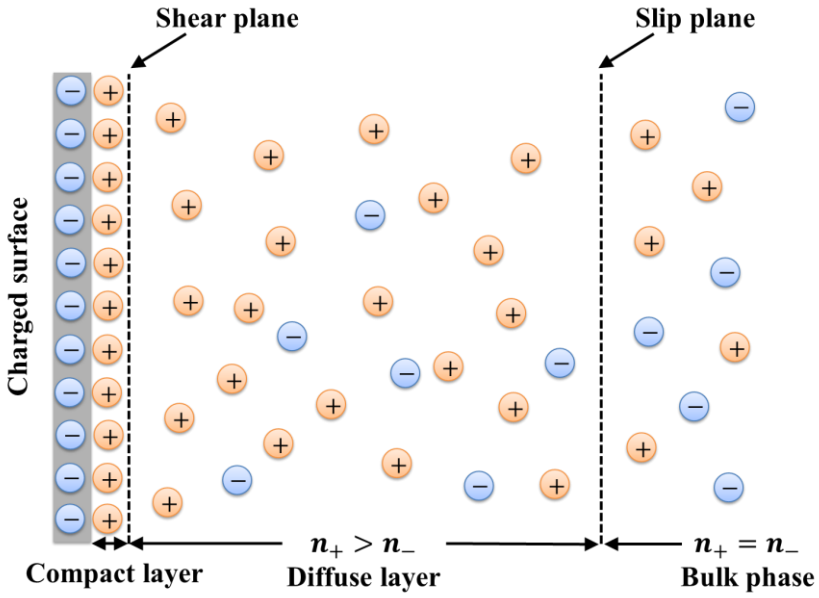

Figure 2-1 Schematic illustration of the electric double layer (EDL).

2.1.1 Electric double layer theory

In microchannels, the electrokinetic phenomenon originates from the charge separation at the interface of two different phases and is dominated by the electric double layer theory. For most surfaces, they will acquire electric charges when contacting an aqueous solution. The charging mechanisms involved in the

formation of the surface charge are commonly ionization, ion adsorption, and ion dissolution [58]. Then, the charged surface attracts the counter-ion toward the surface and repels the co-ions away from the surface, which results in a net charge in the region near the surface. The charged surface and a layer of liquid containing the corresponding balancing charges lead to the electric double layer (EDL), i.e., a compact layer and a diffuse layer (shown in Figure 2-1) [1].

2.1.2 Electroosmotic flow

Electroosmotic flow describes fluid motion caused by interactions between electric double layers and the applied electric field. For a solid surface, the surface will be charged and the electric double layer will be generated when contacting the electrolyte. Since there are more counter-ions than the co-ions, hence no charge neutrality within the EDL, the Coulomb force acting on the net charge in the diffuse layer will lead to the movement of the ions in the EDL when an external electric field is applied. The migration of the mobile ions, in return, drives the liquid to flow along the channel by viscosity, resulting in the plug-like electroosmotic flow which is illustrated in Figure 2-2. Therefore, EOF is usually utilized as a popular method for particle transport in microchannels. In most cases, as the thickness of the EDL is extremely small compared with the microchannel size, the EDL is normally negligible. The EOF velocity in the microchannel is expressed by the Helmholtz-Smoluchowski (H-S) equation

$$\boldsymbol{V_{EOF}} = -\frac{\varepsilon_0 \varepsilon_r \zeta}{\mu} \boldsymbol{E} \qquad (2\text{-}1)$$

where ζ is the zeta potential of the microchannel wall, μ is the viscosity of the suspending solution, and $\boldsymbol{E}$ is the externally applied electric field.

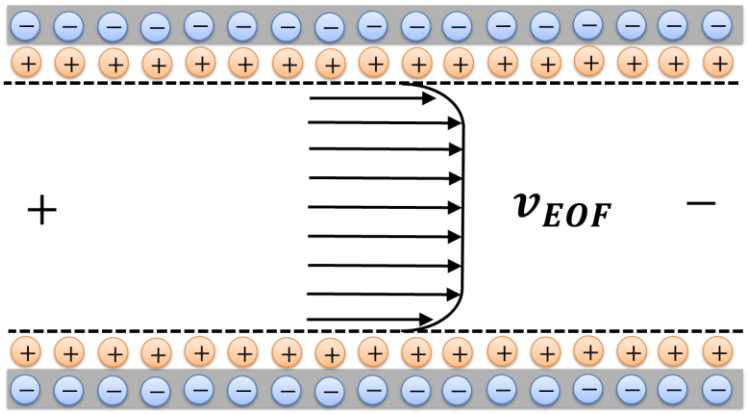

Figure 2-2 Schematic illustration of the electroosmotic flow (EOF).

The electrokinetic movements of the particles, droplets and biological cells occur in the microchannel under the externally applied electric fields in the microfluidic devices. Besides the EOF method,

hydrodynamic flow technique is another important method for particle transportation in the microchannel networks. Generally, the motion of the particles driven by EOF is combined with other electrokinetic phenomena which will not be discussed in this review. Then, the dielectrophoresis method and its various applications will be demonstrated and the basic principle of this specific physical phenomenon will be expressed in each section.

2.1.3 Electrophoresis of particles

For charged particles which are suspended in liquids under an external applied electric field, the Coulomb force, generated by the interaction between the net charges on the particle and the applied electric field, leads to the migration of the particles towards the direction of the opposite electric polarity as illustrated in Figure 2-3. The movement of the charged particles is known as electrophoresis (EP). Together with several familiar phenomena (i.e., streaming potential, colloid vibration potential, and sedimentation potential, etc.) [59], electroosmotic flow and electrophoresis constitute the majority of the electrokinetic phenomena.

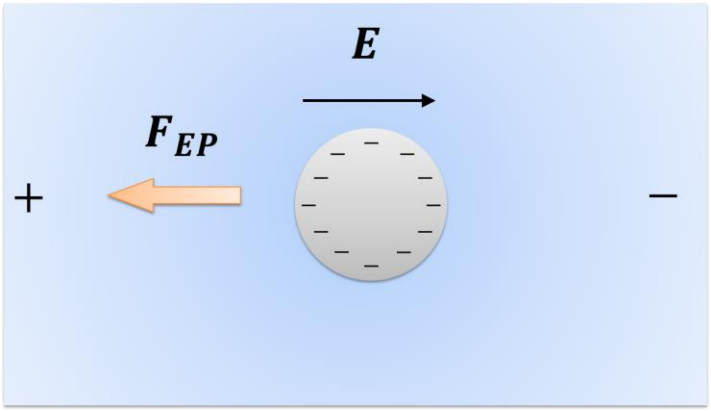

Figure 2-3 Schematic illustration of the electrophoretic motion of a spherical particle in the microchannel.

The electrophoretic force exerting on the charged particles with a net charge q under the externally applied electric field $\boldsymbol{E}$ is expressed as

$$\boldsymbol{F_{EP}} = q\boldsymbol{E} \qquad (2\text{-}2)$$

For a thick diffuse layer, the electrophoretic velocity of the spherical particle (treated as a point charge) can be given by the *Hückel equation* [58]

$$\boldsymbol{V_{EP}} = \frac{2}{3}\frac{\varepsilon_0 \varepsilon_r \zeta_p}{\mu}\boldsymbol{E} \qquad (2\text{-}3)$$

where ζ_p is the zeta potential of the particle. Considering a thin diffuse layer, the particles are large and the ionic strengths are high. Then, the electrophoretic velocity of the particle can be expressed as *Helmholtz-Smoluchowski equation* [58]

$$\boldsymbol{V_{EP}} = \frac{\varepsilon_0 \varepsilon_r \zeta_p}{\mu} \boldsymbol{E} \qquad (2\text{-}4)$$

2.2 Dielectrophoresis

Dielectrophoresis (DEP) is the motion of an electrically polarizable particle in a non-uniform electric field due to the interaction between the dipole induced in the particle and the spatial gradient of the electric field. When an electric field is applied, the electric charge within the particle and the suspending electrolyte will move and redistribute at the particle-electrolyte interface, depending on their polarizability. If the polarizability of the dielectric particle is higher than that of the electrolyte, more charges will accumulate at the particle side. While, if the suspending medium has higher polarizability than that of the particle, more charges will accumulate at the medium side. This non-uniform distribution of the electric charges results in a slight asymmetry in the charge density on the particle, leading to an induced dipole across the particle. From classical electrostatics, the effective dipole moment of a homogenous dielectric sphere in an electric field is given by [46,60]

$$\boldsymbol{p} = 4\pi\varepsilon_m \, a^3 Re(f_{CM}) \, \boldsymbol{E} \qquad (2\text{-}5)$$

where ε_m represents the absolute permittivity of the suspending medium, a is the radius of the particle, and Re indicates the real part. f_{CM} is called the Clausius-Mossotti (CM) factor which is a function of the frequency of the electric field and, depending on the dielectric properties of the particle and the suspending medium.

The CM factor describes the relative polarizability of the particles and the surrounding medium and is given by

$$f_{CM} = \left(\frac{\varepsilon_p^* - \varepsilon_m^*}{\varepsilon_p^* + 2\varepsilon_m^*}\right) \qquad (2\text{-}6)$$

where ε_p^* and ε_m^* are the complex permittivity of the particle and the suspending medium, respectively.

Since both the dielectric and conductive properties of the particles and the suspending medium are exhibited in the presence of the electric fields, the complex permittivity is presented and defined as

$$\varepsilon^* = \varepsilon - (j\sigma/\omega) \qquad (2\text{-}7)$$

where ε and σ are the permittivity and electric conductivity of the particle and solution, respectively, $\omega = 2\pi f$ represents the angular frequency of the applied electric field, and $j = \sqrt{-1}$.

As shown in Figure 2-4, when the particle is placed in a non-uniform electric field, different forces are generated at each side of the particle. Then the difference in force at both sides of the particle induces a net force, i.e., dielectrophoresis (DEP) force. The direction of the DEP force is determined by the polarizability of the particle and the suspending medium. The general expression for the DEP force exerting on a homogeneous spherical particle is expressed as [46,60]

$$\boldsymbol{F}_{DEP} = (\boldsymbol{p} \cdot \nabla)\boldsymbol{E} = 2\pi\varepsilon_m \, a^3 \, Re(f_{CM})(\nabla|\boldsymbol{E}|^2) \qquad (2\text{-}8)$$

where $\nabla|E|^2$ is the gradient of the square of the electric field.

It can be inferred from Equation (2-8) that the DEP phenomena have the following features [61]:

(1) DEP force is present only when the non-uniform electric field exists;

(2) DEP phenomenon is non-linear since it is dependent on the gradient of the electric field;

(3) DEP force is independent of the polarity of the electric field;

(4) The magnitude of DEP force is proportional to the particle size, which enables DEP manipulation and separation of particles by size;

(5) The magnitude of DEP force is proportional to the electrical properties of the particle and the suspending medium, i.e., the permittivity and conductivity of the particle and the medium, as well as the frequency of the electric field, which enables DEP manipulation and separation of particles by their different electrical properties;

(6) DEP behaviors, i.e., positive DEP (p-DEP) and negative DEP (n-DEP), are determined by the sign of the Clausius-Mossotti factor, f_{CM}, ranging from -0.5 to 1.0. If the particles are less polarizable than the suspending medium (i.e., $f_{CM} < 0$), the particles will experience n-DEP force and be repelled from the high electric field towards the weak region (illustrated as Figure 2-4(a)). While if the particle is more polarizable than the solution (i.e., $f_{CM} > 0$), the particles will be attracted by the p-DEP force towards high electric field gradients (shown in Figure 2-4(b)).

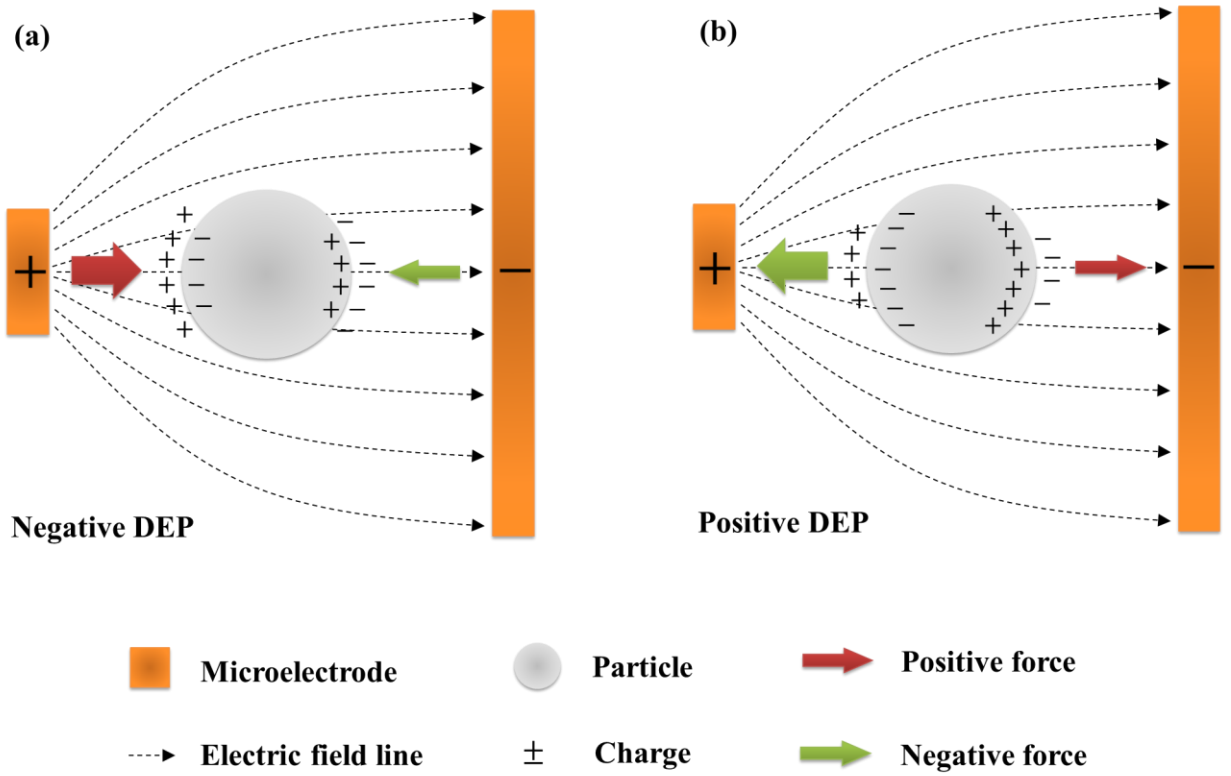

Figure 2-4 Schematic illustration of the dielectrophoretic motion of spherical particles. (a) The particle is less polarizable than the suspending medium and repelled by the negative DEP away from the high electric field. (b) The particle is more polarizable than the suspending medium and attracted by the positive DEP towards the high electric field.

To date, DEP has become one of the most popular methods for the manipulation of particles, due to its label-free property, low consumption of samples, ability to offer a selective and sensitive analysis of particles, and fast speed [62–66]. In order to achieve DEP effect, a non-uniform electric field is required which can be generated by a variety of methods, such as insulator-based direct current dielectrophoresis (DC-DEP), micro-electrodes embedded alternating current dielectrophoresis (AC-DEP), as well as traveling-waving DEP. In this section, various popular techniques for the dielectrophoretic manipulation of micro and nanoparticles are reviewed and presented.

2.2.1 Alternating current-dielectrophoresis

Alternating current-dielectrophoresis (AC-DEP) is the motion of a particle by induced polarization in a non-uniform electric field and the applied electric field is an alternating current (AC) signal. As implied by Equation (2-8), the magnitude of the DEP force is a function of the frequency of the applied electric field, it will vary with the frequency of the electric field. As different kinds of particles or bio-particles have

a distinct dielectric property, a distinct response is presented ranging from positive DEP to negative DEP in the frequency spectrum, which enables the separation and identification of different particles. For the AC-DEP chips, the non-uniformity of the electric field is commonly generated by an array of microelectrodes embedded within the microchannel. These microelectrodes are fabricated by basic manufacturing techniques, such as lithography [67], electroplating [68], photolithography [69–74], e-beam evaporation [75], etching [76,77], and C-MEMS [78,79].

Configurations of the microelectrode structures

2D planar electrodes. 2D planar microelectrodes are fabricated by photolithography techniques and followed by film deposition and etching or lift-off. These microelectrodes are commonly patterned on the bottom surface of the microchannel. The microelectrode patterns are transferred from a software designed (e.g., AutoCAD) mask to a photoresist by the standard photolithography method. Then a film of various metal materials (e.g., gold and silver) is deposited on the substrate by evaporation or sputtering methods. After the etching or lift-off process, an array of microelectrodes with defined structures remains on the substrate. In comparison with the lift-off technique, a relatively smaller structure with high aspect ratios can be obtained by using the etching method [80].

An array of interdigitated electrodes is fabricated to generate the non-uniform electric field. The gradient of the electric field is induced above the surfaces of the electrodes, where the particles are attracted or repelled. By adjusting the ratio between the length of the electrodes and the width of the microchannel, a large trapping area can be obtained inside the microchannel. In this way, these microfluidic devices are widely used for the concentration and trapping of particles [81–87]. Interdigitated electrodes based microfluidic platforms have also been applied for the manipulation and separation of particles [88–93]. In addition, Crews et al. [80] demonstrated a method to model the gradient of the electric field as a function of the dimensions of the electrodes (i.e., width and gaps), as well as the height and the applied electric field.

The design of the polynomial electrodes includes two pairs of electrodes (show in Figure 2-5) and generates the maximum non-uniform electric field along the pads of the electrodes and a minimum electric field at the center. These devices are used to achieve particle patterning, concentration and characterization [94–97]. However, for the triangular polynomial electrode structures, the strongest electric field gradient is induced at the tips of the electrodes and a low electric field along the pads. These devices are used for the trapping [98,99] and separation [100,101] of particles.

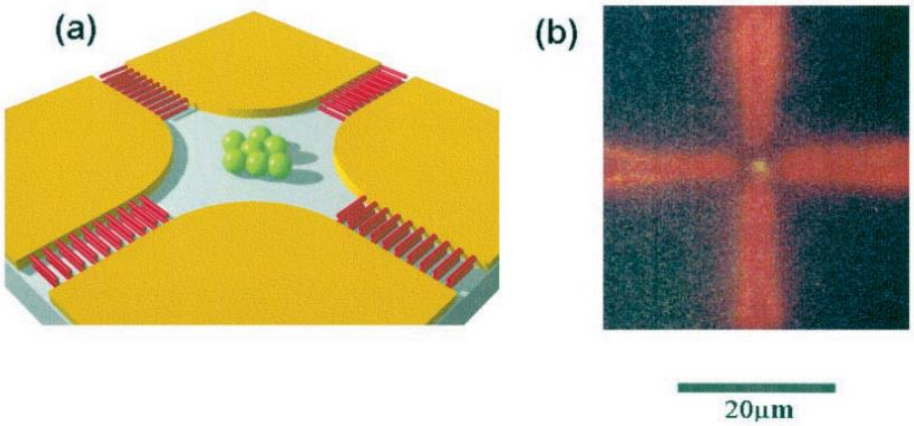

Figure 2-5 Schematic diagram (a) and experimental photograph (b) of the separation of TMV (red) and HSV (green/yellow) in polynomial electrodes [93].

Arrays of castellated electrodes are designed to generate stronger non-uniformity of the electric field at the tips of the castellations and a weaker electric field between the tips. In order to adjust the gradient of the electric field near the castellations, various shapes of the castellations are introduced (i.e., triangular and square). By using the castellated electrodes, the manipulation of particles [92,94,102–104], as well as the fabrication of microdevices such as a nanowire sensor [105,106], is achieved. Moreover, other designs such as arrays of slanted [107–110] or curved [111] electrodes placed at an angle to the flow direction, and circular [13] and ring-shaped [112,113] electrodes are also used for continuous sorting and separation of particles.

3D electrodes. 3D microelectrodes are fabricated by patterning planar microelectrodes on two sides of microchannel surfaces (i.e., top and bottom), as well as by manufacturing extruded microelectrodes from the channel bottom and vertical microelectrodes on the microchannel sidewalls. In comparison with 2D microelectrode structures, which suffers from the adhesion of the particles on the electrode or channel wall surfaces and a confined DEP effective area over the electrode surface [61], hence a low efficiency, 3D electrode-based microsystems offer an increased DEP effective region, leading to an efficiency increase of the microfluidic devices, and the adhesion of the particles is avoided.

Microfluidic devices comprising 3D top-bottom patterned microelectrodes are manufactured by the standard microfabrication methods. The fabrication process always involves: deposition of microelectrodes on both top and bottom surface of the microchannel by magnetron or reactive sputtering process, and patterned with the lift-off technique; formation of the microchannel using epoxy-based SU-8 photosensitive resist using standard photolithography techniques; and precise electrodes face-to-face alignment and bonding under the microscope with UV curable adhesives or epoxy-based adhesives, which avoids the contamination of the microchannel [76,114–117].

For the fabrication of extruded microelectrodes, various electrode materials such as metal, carbon, and silicone [118–120], and techniques have been used. The extruded metal electrodes are manufactured by evaporating and patterning thin-film electrodes on the substrate to define the interconnections. Then a SU-8 photoresist is deposited and patterned to form the designed mold, followed by electroplating the electrodes into the mold. After stripping the SU-8 mold, the microfluidic device is completed by depositing and patterning another SU-8 layer to form the flow chamber [121] as illustrated in Figure 2-6.

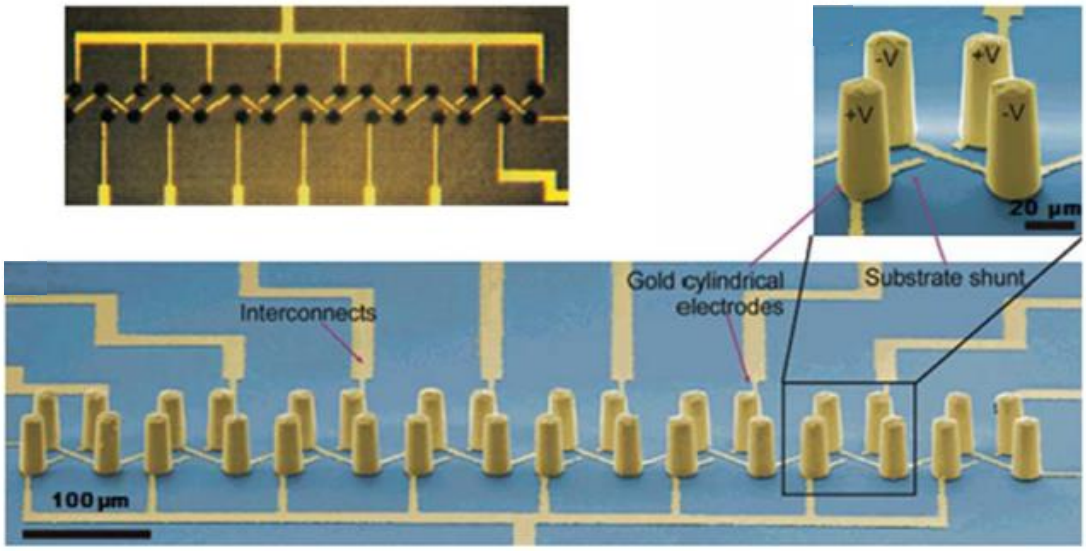

Figure 2-6 Schematic illustration of the extruded electrodes [121].

In the case of sidewall-patterned electrodes, microelectrodes are patterned on the sidewalls of the main microchannel. In order to fabricate 3D vertical microelectrodes, the electroplating technique combined with standard photolithography method has been utilized. The commonly used microelectrodes are gold electrodes [122], micro copper electrodes [70], and alloy microspheres [123]. Nowadays, liquid electrodes [124,125] and conductive polydimethylsiloxane (PDMS) such as AgPDMS [77,126] have attracted growing interest and been widely used to generate the gradient of the electric fields. In this way, the effective electric field gradient region is extended and the DEP effect is improved.

Applications of AC-DEP

Separation. The manipulation and separation of particles or bio-particles is one of the most important applications in chemical and biological fields and has attracted most of the interest in this area. Applying AC electric fields with high frequencies between 1 MHz to 2 MHz, Asokan et al [97] demonstrated the manipulation and orientation of action in a pair of quadrupole microelectrodes. Using similar triangular electrodes [100,101], the separation of human breast cancer cells from HCT-116 colorectal cancer cells, and the isolation of colorectal cancer cells from mixed samples with HEK 293 and E. coli cells were achieved.

Moreover, the separation of particles in AC-DEP microfluidic devices with an array of castellated microelectrodes was investigated [71,92,100,104,127–130]. Different kinds of particles or cells experience different DEP behaviors, i.e., p-DEP and n-DEP effects, by choosing specified driving frequencies. In this way, the particles experiencing p-DEP forces are attracted at the tips of the castellated electrode arrays where the high gradient of electric field exists, while the particles undergoing n-DEP are repelled away towards the low electric field region between the microelectrode tips. Following this concept, Tai et al [131] used a similar structure to achieve the separation of viable and non-viable human lung cancer cells. By integrating the serpentine-shape micropump and pneumatic microvalves, different cells are automatically transported and separated into different channels by DEP forces with a high resolution.

In the microdevices with interdigitated microelectrodes, Li et al [91] investigated the separation of live Listeria innocua cells (collecting on the edges of the microelectrodes) and heat-treated dead cells (collecting on the top centers of the electrodes) by p-DEP and n-DEP, respectively. The separation efficiency is up to 90% by applying AC electric fields with a low voltage of 1V and a frequency of 50 kHz. Besides, a similar microelectrode structure was employed for the separation of polystyrene beads and human blood erythrocytes [92], live and dead yeast cells [89], HT-29 cancer cells and red blood cells [90], and C. Muris and G. lamblia at a frequency of 10 MHZ and a 3 $V_{peak\ to\ peak}$ voltage [88]. By using the dielectrophoretic field-flow fractionation (DEP-FFF) method, circulating tumor cells (CTCs) were isolated from blood [132,133].

By placing the microelectrode arrays at an angle to the direction of the main flow, Polystyrene particles were continuously separated based on different sizes, i.e., larger particles experience stronger DEP forces and have greater trajectory shifts, while the particles with smaller size undergo weaker DEP effects and achieve smaller shifts, into different streams and moved into different channels [108,111,134,135]. Using similar structures, Kim et al [136] demonstrated multitarget cells sorting with high purity using a microfluidic device with two pairs of microelectrodes positioned at two different glancing angles to the flow direction [136]. In this way, the electrical surface conductance-based separation of polystyrene beads and frequency-dependent separation of viable and non-viable yeast cells [109], and separation of red and white blood cells in a suspending medium with high electrical conductivity [110] were achieved. In addition, Krishnan et al [13,137] and Sonnenberg [138,139] developed a circular microelectrode device which can detect and isolate DNA and nanoparticles into high electric field regions.

Another AC-DEP particle separation technique is presented by using 3D microelectrode structures. Durr and Kentsch et al [116,117] and Chen et al [76,114] reported the manipulation and separation of microparticles (i.e., 4.8 μm and 9 μm) by particle size-dependent DEP force in a microfluidic device with arrays of paired microelectrodes placed face to face on the top and bottom sides of the channel. In order to improve the throughput and sorting sensitivity of the 3D microelectrode devices, arrays of asymmetric microelectrodes

were fabricated and patterned [140]. Due to the changing widths of the microelectrodes, the magnitudes of the electric field continuously vary along the transverse direction of the microchannel, which results in an increased separation sensitivity and achieves the separation of mouse P19 embryonic carcinoma and red blood cells. Furthermore, by manufacturing the microelectrode arrays with defined geometry by silicon, the required gradient of the electric field for DEP effect as well as the gradient of liquid velocity was generated which lead to the successful separation of live and dead yeast cells [141,142].

The manipulation and separation of microbeads and cells [68,143] were demonstrated by patterning pairs of vertical interdigitated microelectrodes on the sidewalls of the microchannel to generate non-uniformity of the electric fields in a microfluidic device. As the height of the microchannel can be adjusted without losing the strength of the electric fields, this dual frequency DEP device achieves high sorting throughput. By integrating the sidewall microelectrode with the electrical insulator hurdles, continuous separation of polystyrene particles with a minimum 5 μm difference in diameter and yeast cells based on size [70] and separation of latex particles and white blood cells and particles due to different electrical properties [73] were achieved. In addition, by using liquid electrodes, i.e., arrays of microelectrode chambers patterned on single [144,145] or both [146–148] sidewalls of the microchannel, the particles and cells were continuously separated. However, due to weak adhesion between the metal electrodes and the PDMS microchannel, it is challenging to integrate them. In order to avoid this issue, Lewpiriyawong et al [126,149,150] and Jia et al [77] demonstrated the conducting PDMS composites, i.e., AgPDMS, to perform as the vertical microelectrodes and induce the non-uniform electric field (shown in Figure 2-7). In this way, the DEP forces behave in three dimensions which enhances the DEP effect regions and enables the high-efficiency separation of particles by size, and separation of live yeast cells and bacterial cells from latex particles with similar size.

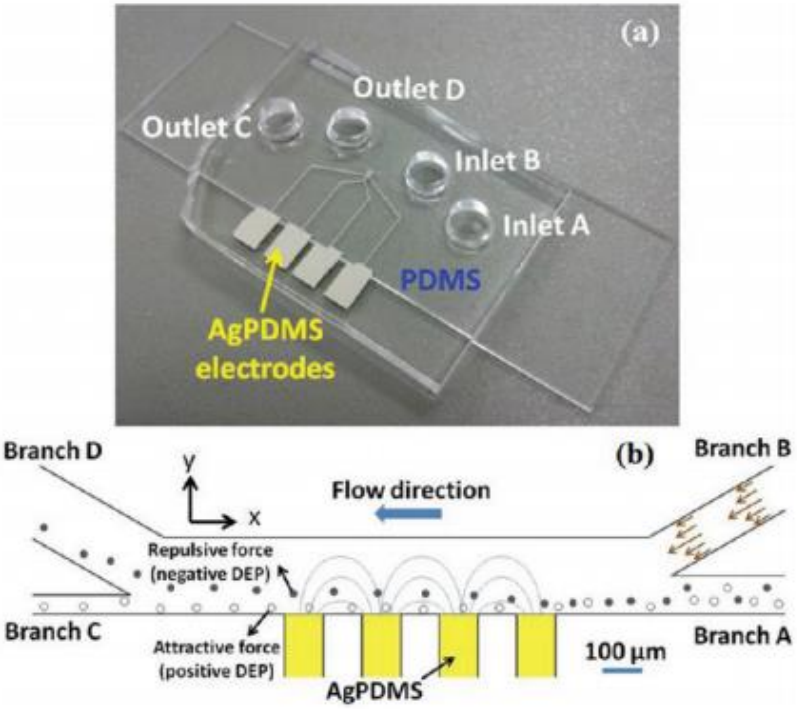

Figure 2-7 (a) The microfluidic device with AgPDMS microelectrodes. (b) The schematic illustration of the separation of particles with similar sizes by positive and negative DEP forces, respectively [150].

Focusing and trapping. Flow cytometry is a powerful method which can measure and analyze the various physicochemical characteristics of particles and cells. By integrating with optical fluorescent probes, this device enables the detection of the fluorescence property of each different individual particle which can be used for the determination of the morphological features and functional properties of the particles such as size, morphology, geometry, as well as surface markers. In such a microfluidic device, the particles are continuously focused as a narrow stream by the DEP forces and flowing with the driving liquid into the center of the device. In this way, the particles are detected one by one at high flow rates. In comparison with the various conventional focusing systems, the AC-DEP focusing methods offer the advantages of low sample consumption, fabrication flexibility in combination with other manipulation and analysis techniques, as well as high throughput [151]. Morgan and Homes et al [152,153] demonstrated focusing and analyzing fluorescent particles at a high rate up to 250 particles per second by placing two pairs of microelectrodes on both the top and bottom of the microdevice which is shown in Figure 2-8. By applying high-frequency AC electric field, the particles were repelled by the negative DEP forces and focused as a tight stream in the microchannel center. In addition, an elliptic-like microelectrode array [154] and a face-to-face liquid electrode [124,155] were designed and fabricated to direct the cells from different directions towards the microchannel center.

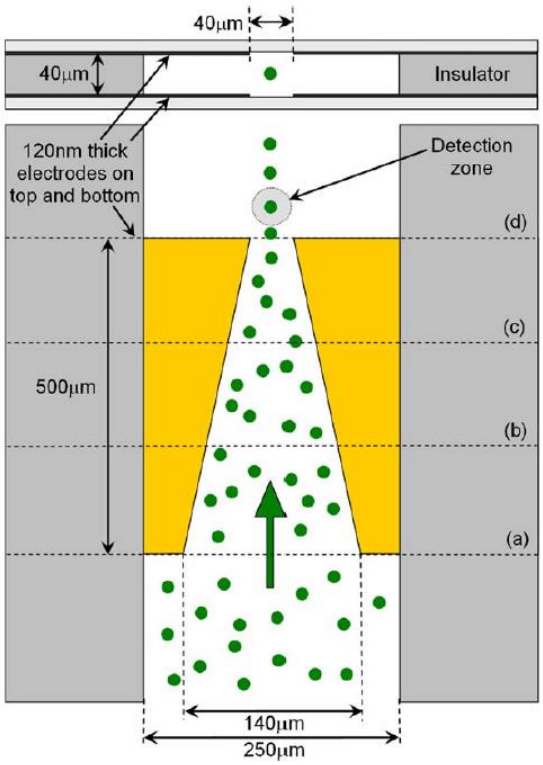

Figure 2-8 Schematic illustration of the AC-DEP flow-focusing microfluidic chip from a top view [152,153].

AC-DEP also offers a method for the trapping or concentration of the interesting particles in the desired position for further manipulation and analysis. Du et al [95] presented the trapping and concentration of DNA molecules by AC-DEP in combination with the nonlinear electroosmotic flow (EOF) under high-frequency AC electric fields in a microchannel with pairs of asymmetric quadrupole electrodes. Using the similar microelectrode structures, the mammalian virus HSV-1 was concentrated by both positive and negative dielectrophoretic forces with different frequencies applied [96]. Moreover, a strong gradient of the electric field was generated by applying the electric voltages to sharp triangular microelectrodes which enable the trapping of single R-phycoerythrin protein molecules [99] and individual bacterial spores [98]. In addition, by using arrays of castellated microelectrodes, the trapping of cells and beads [156] and concentration of murine embryonic stem cells by positive DEP effects in high electric field regions [102] were achieved.

By using arrays of interdigitated electrodes integrated into the microfluidic chips, the trapping of individual human spermatozoa by negative DEP forces under high-frequency electric fields [157], the capture of ribosomal RNA [82] and trapping of DNA molecules [87], as well as capturing E.coli cells by positive DEP and quantitative evaluation of particle concentration [83,86] was achieved. Using similar microelectrode structures, the bacteria cells [81] and the polystyrene particles [84] were concentrated with high efficiency and throughput. Furthermore, Lagally et al [85] designed an integrated microfluidic device including the microelectrode arrays, a series of PDMS microvalves, and an optical molecular beacon which enables the

concentration of bacterial cells and optical detection of E. coli MC1061 cells via the sequence specific hybridization of an rRNA-directed optical molecular beacon. In order to trap and position individual polystyrene microspheres [158–160] and living cells [161–163], microdevices with integrated quadrupole and microwell electrodes, and circuit microchips with a grid of microelectrodes were designed and utilized. Additionally, Hsiung et al [164] and Thomas et al [112,113] developed microfluidic chips with arrays of ring electrodes for the patterning of human hepatocellular carcinoma cells and trapping of single Hela cells and human osteoblast-like cells.

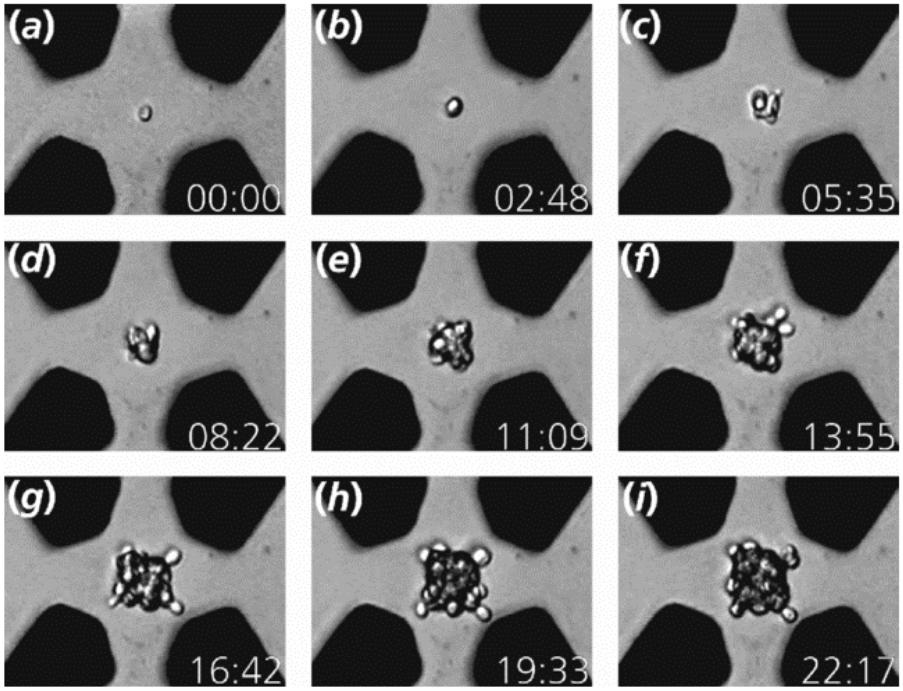

Figure 2-9 Example of yeast proliferation in an n-DEP field cage. The black cases represent microelectrodes. Image (a)-(i) shows the trapping of a single yeast cell and a cell agglomerate after several divisions [165].

Integrated AC-DEP microfluidic platforms with 3D microelectrode arrays patterned on the top and bottom sides of the microchannel were developed for the concentration of polystyrene microparticles with different sizes and yeast cells [115,166], capture of anti-mouse immunoglobulin G modified microparticles [72], E. coli [167] and single yeast cells [165] (shown in Figure 2-9), as well as accumulation and trapping of hepatitis A virus particles [23]. Moreover, Voldman et al [168] designed a microfabricated device with arrays of asymmetric extruded quadrupole microelectrodes to generate an electric field gradient for the trapping of single HL-60 cells [121] and polystyrene microbeads [168]. In order to improve the electrochemical stability of microfluidic platforms, carbon [169] or silicon [170] electrodes are used instead of the metal electrodes which

provides advantages such as high electric voltage applied without sample electrolysis, better biocompatibility, and excellent mechanical and chemical properties.

2.2.2 Direct current-dielectrophoresis

Direct current-dielectrophoresis (DC-DEP), the induced movement of dielectric particles in non-uniform DC electric fields, is another strategy to generate the electric gradient required for DEP effects. The non-uniform electric field is induced by applying DC electric fields via local electrically insulating obstacles or constrictions patterned inside the microchannel with external electrodes placed in the inlet and outlet reservoirs. When a DC electric field is applied, the expression for the DEP force remains the same as Equation (2-8). However, the Clausius-Mossotti (CM) factor which describes the polarizability of the particles and the suspending medium becomes solely dependent on their electrical conductivity and is expressed as [171]

$$f_{CM} = \frac{(\sigma_p - \sigma_m)}{(\sigma_p + 2\sigma_m)} \qquad (2\text{-}9)$$

In comparison with the conventional electrode-based AC-DEP systems, the insulator-based DC-DEP microfluidic systems show advantages [172] such as: (1) the fabrication process becomes simple without the metal deposition and the mass fabrication of the devices is possible due to low-cost materials; (2) since no electrodes are involved in the microchannel, the devices are mechanically robust and chemically inert and the surface fouling of the electrodes and gas evolution due to electrochemical reactions are avoided, and hence are more biologically compatible; (3) the gradient of the electric fields are constant over the whole height of the microchannel and the samples are driven by integrating the electrophoretic and electroosmotic effects instead of additional hydrodynamic flow. However, in order to generate strong electric field gradients, relatively large electrical voltages are necessary which involves the Joule heating effect.

Configurations of the insulator structures

Obstacles. In order to generate the required non-uniform electric field inside the microchannel, arrays of electrically insulating posts with a variety of different shapes, such as rectangular, triangular and circular, are exploited. For these microchips with insulating posts shown in Figure 2-10 [173,174], they are fabricated from the glass with patterned structures using wet etching and standard photolithography techniques. After thermal bonding, the microfluidic chip is fabricated. Furthermore, the orifices formed inside the microchannel with hurdles or blocks [175–177] are an alternative method. Using the same idea, an oil droplet [178] or oil meniscus [179] is used to generate spatial non-uniform electric fields. In this way, the electric field gradients become controllable by adjusting the oil droplet size as well as the radius and penetration of the oil menisci which enables a variety of application configurations.

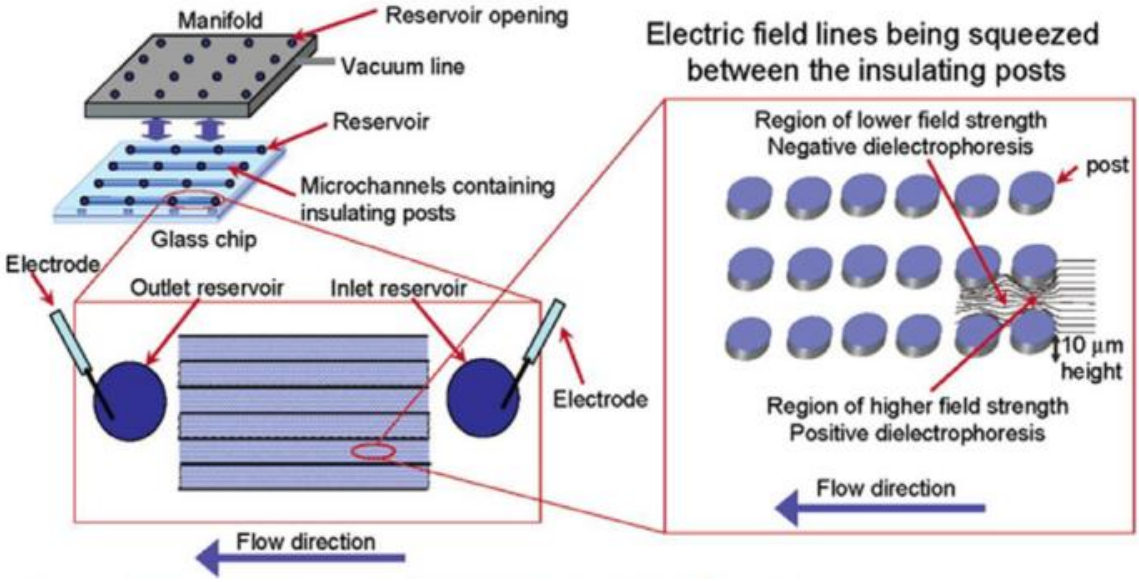

Figure 2-10 Schematic illustration of the microfluidic system and streamlines of the electric fields compressed between the insulating posts [174].

Curved microchannels. Besides patterning the insulating obstacles within the straight microchannels, 3D hurdles and barrier [180,181] are designed and manufactured for the separation and manipulation of particles. In addition, the microchannel shapes can be utilized to induce the non-uniformity of the electric fields, hence the DEP forces. Therefore, curved microchannels with various structures (i.e., serpentine [182], sawtooth [183], and circular [184–186]) are fabricated using the soft photolithography technique and employed for the continuous manipulation of particles. By using these microfluidic devices, the fabrication of in-channel micro-insulators are eliminated and a series of gradually stronger electric field gradients are induced along the microchannel.

Applications of DC-DEP

Separation. DC-DEP has been proved to be one of the highly efficient methods for the separation of microparticles by size. The local non-uniformity of the electric fields is produced by insulating obstacles such as hurdles or blocks inside the microfluidic channels. Since the DEP forces acting on the particles are proportional to their radii, particles of different sizes undergo different negative DEP forces (i.e., repulsive forces) at the corners of the hurdles, where the strongest gradient of the electric fields exists. Thus, the mixed particles of a few micrometers difference in the radius are separated and directed into distinct streams by integrating the electroosmotic flow. The size-dependent separation of particles was demonstrated by Kang et al [187,188] by patterning the insulating hurdles with rectangular structures inside the microchannel which is shown in Figure 2-11. By using similar triangular hurdles, which reduces the constricted gap region and minimizes the negative effects on the live cells, the separation of white blood cells or breast cancer

cells [176] and DNA molecules [189] of different sizes were achieved. While, for separating the target particles of a specified size, it is only required to adjust the voltage outputs of the external electrodes. In order to enhance the DEP effects and increase the controllability, an H-shaped microfluidic chip with a series of rectangular blocks was developed for the flow-through manipulation and separation of microparticles [190]. In addition, Srivastava et al [191] developed a microdevice to sort multi-particles of different size into multiple distinct outlets by adjusting the electric conductivity of the suspending medium.

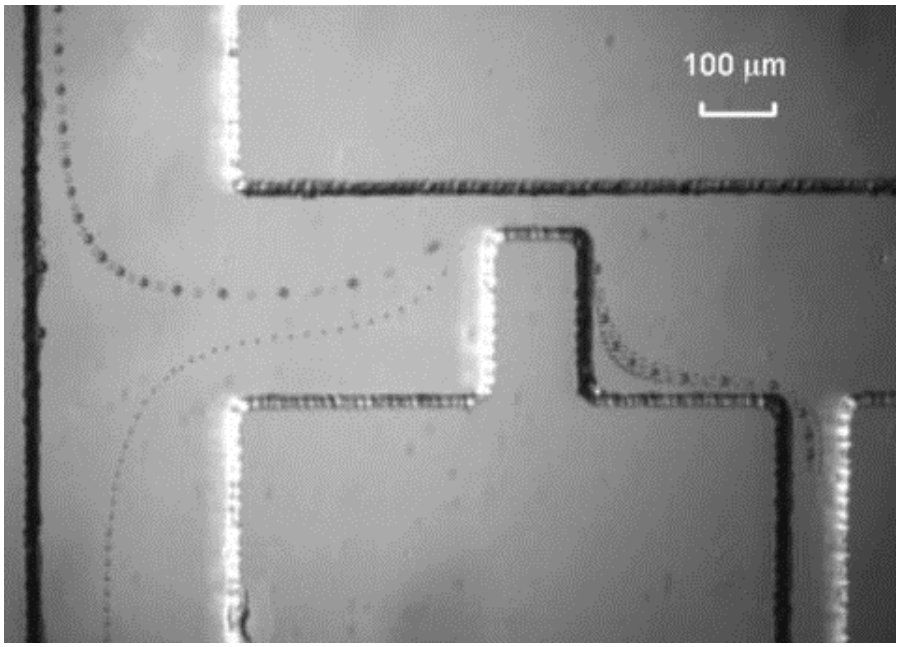

Figure 2-11 Schematic separation of 5.7 µm and 15.7 µm polystyrene particles in the microchannel with a single rectangular hurdle [187].

In microchips containing arrays of insulating posts, the effects of the post shapes and dimensions with respect to the applied electric fields on particle filtering and concentration were theoretically and experimentally investigated [173]. Using these circular post-based devices, the separation of length-dependent DNA with different conformations [192], as well as the concentration and isolation of viable and non-viable bacteria [45,174,193] or cells [194] and microalgae [195] were achieved. Additionally, a tunable orifice inside the microchannel was designed using an insulating oil droplet which is controlled by a syringe [178]. In this way, an adjustable constricted gap, hence the gradient of the electric fields and the DEP forces, is generated which enables the separation of the particles with relatively low DC electric voltages and becomes a promising method for bioanalytical applications.

A different method to generate non-uniform electric fields is to use curved microchannels. The electric fields are squeezed to induce strong gradients of the electric field at the insulating constrictions when DC electric fields are applied via external electrodes positioned at the inlet and outlet reservoirs of the

microchannel. Then different particles are separated into different streams and directed to different regions of the cross-section of the microchannel. In a circular microchannel [186], the separation of particles with different dielectric properties was predicted by numerical simulations. Following this concept, the separation of particles based on charge and size (i.e., 5/10 μm and 3/5 μm) was achieved in an asymmetric double-spiral microchannel [184,196] which provides a method to separate multiple particles by their intrinsic properties. There are various microchannels with other curved designs, the concentration and separation of particles [183] and bacterial cells [65] were theoretically and experimentally studied in a sawtooth microchannel. For this sawtooth patterned microfluidic device, a minimum gap with a width of 27 μm was formed which enables the separation of 20 nm, 200 nm as well as 1 μm polystyrene beads [197]. Furthermore, microfluidic channels with serpentine structures, where non-uniform electric fields exist at the U-turn, were developed to separate yeast cells from E. coli [198] and microparticles by size [182,199,200]. In addition, PDMS microfluidic devices with a 3D hurdle in the shape of a quarter of a circle [180] were designed to separate 2 μm and 3 μm polystyrene microspheres. By reducing the height of the microchannel down to 670 nm, the DNA and DNA/protein complexes were effectively separated [201].

Focusing and trapping. The concentration of 200 nm latex beads was demonstrated by applying DC voltages to arrays of insulating posts embedded inside the microchannel [173,202], and the efficiency of particle focusing was dependent on the shape and angle of the posts. Due to the generated non-uniformity of the electric fields, i.e., DEP effects, within the insulating constrictions, different shapes of the posts such as circular or diamond-shaped are designed for the trapping and concentration of viable and non-viable bacteria [45,174,203], protein [19], and DNA [204]. By integrating pressure-driven flow to control the particles motion and the electrical impedance measurement method for subsequent sample detection, the selective trapping of 2 μm microspheres and Bacillus subtilis spores was investigated in the insulating post-based microfluidic platform and the system shows advantages of high-throughput and no contaminations or clogging [205].

Using microfluidic chips with arrays of triangular constrictions, DNA was trapped at the tips [206,207] and the DNA hybridization kinetics, as well as the signal sensitivity through pre-concentration, were enhanced [208]. Furthermore, by employing DC-biased AC electric fields, 10 μm microparticles were focused which is shown in Figure 2-12 [209] and red blood cells were concentrated in the microchannel with a pair of symmetric rectangular hurdles [177], and the selective trapping of dead cells as well as focusing of live cells by combining the hydrodynamic flow in microfluidic chip with arrays of quadrupole-shaped insulating posts [175,210,211]. Besides inducing electric field gradients with insulators, pairs of insulating oil droplets were generated face to face to induce the electric field gradients. By adjusting the size and position of the droplets inside the microchannel, the strength of the electric fields, hence the DEP forces, becomes controllable which enables the continuous particle focusing [179].

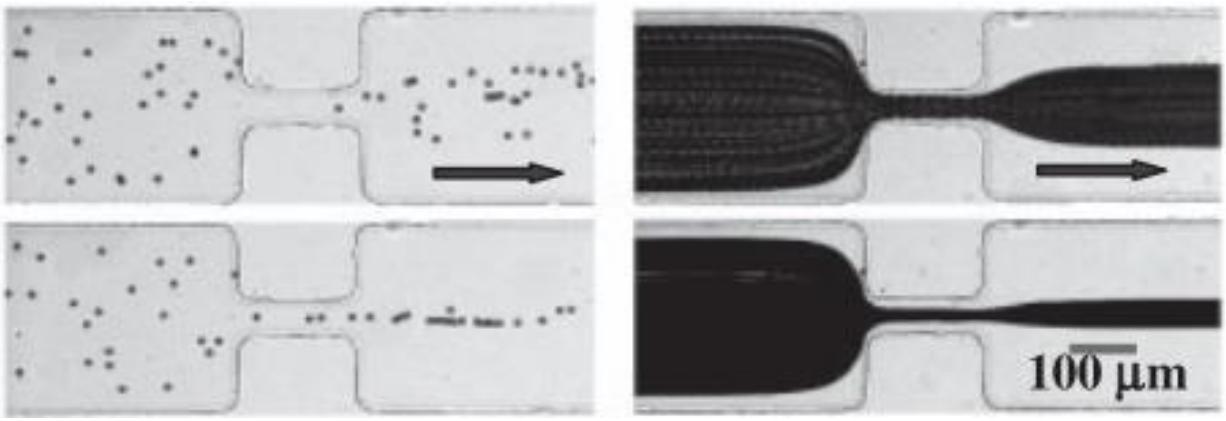

Figure 2-12 Schematic illustration of focusing of 10 µm microparticles (left: snap-shot images; right: streak images) [209].

The focusing of polystyrene microspheres [182,212] and E. coli cells [198] was demonstrated in a serpentine microchannel. The particles were focused to the center or the sidewalls of the microchannel by the U-turn induced DEP forces. Using a similar structure, a waved microchannel was presented to focus yeast cells into a continuous stream along the center of the microchannel by negative DEP forces. Moreover, an asymmetric spiral microchannel was designed to focus microspheres [184,185]. Due to the elimination of high electric field regions, the curvature induced DEP focusing method enables its applications in the manipulation of bioparticles. In addition, the concentration of 930 nm polystyrene particles into arrays of parallel microchannels was presented in a tree-shaped microfluidic device [12,213]. Inside the channel network, the electric field was efficiently squeezed and multiple trapping regions were observed inside the microchannel. In this way, the trapping efficiency is as high as 100 % which enables rapid sample concentration for the preparation of particles and detection of biomarkers.

2.2.3 Traveling wave-dielectrophoresis

Traveling wave-dielectrophoresis (twDEP) is the interaction between polarizable particles and a traveling wave electric field produced by an array of parallel electrodes patterned at the bottom surface inside the microchannel, where potentials with 90° phase variation are applied. Due to the phase lag between the dipole moment and the traveling electric field, a net force exerting on the particles is generated which leads to smooth translational particle motion. It can be inferred that the traveling wave DEP force induced in a traveling field E is presented as [214,215]

$$F_{twDEP} = -\frac{4\pi\varepsilon_m\, a^3}{\lambda}\, Im(f_{CM})E^2 \qquad (2\text{-}10)$$

where λ represents the wavelength of the traveling electric field and has the value with the repetitive distance between the electrodes of the same phase, $Im(f_{CM})$indicates the imaginary part of the Clausius-

Mossotti (CM) factor. As shown in Equation (2-10), the in-phase and out-of-phase component of the induced dipole moment and the non-uniform field magnitude or phase factor are determined by the real and imaginary particles of the CM factor, which result in the conventional DEP and twDEP, respectively [216]. When levitating above the surface of the electrodes, the twDEP force is balanced by the oppositely directed viscous drag force which leads to a constant translational velocity. The velocity u_{twDEP} of the particle in a suspending medium with viscosity, μ, is expressed as [214]

$$u_{twDEP} = -\frac{2\pi\varepsilon_m a^3}{3\lambda\mu} Im(f_{CM})E^2 \qquad (2\text{-}11)$$

As shown in Figure 2-13, electric potentials with 90° phase variation between the adjacent electrodes are applied to an array of planar microelectrodes, and co- and anti-field twDEP effects are generated which drive the particles moving towards or away from the smaller phase regions. In this way, the particles can be transported along or against the direction of the traveling wave inside the microchannels without the assistance of external driving flow. Such a configuration was proved to be able to separate particles based on size differences or different dielectric properties [217,218]. By applying high frequency traveling fields to a series of microelectrodes, the manipulation and linearly movement of pollen and cellulose particles were achieved [219–221]. Using similar structures, the twDEP was applied for particle separation by fractioning yeast cells based on size [214]. In order to enhance the separation effect, a microfluidic device with multiple layers of microelectrodes was designed which can be switched between convention and twDEP by adjusting the frequency of the traveling fields. With carefully selected electrical conductivity of the suspending medium, the live and dead yeast cells were separated. When the low frequency of the electric fields was applied, the dead yeast cells were trapped by positive DEP forces while the live cells moved to the end of the electrode arrays [222,223].

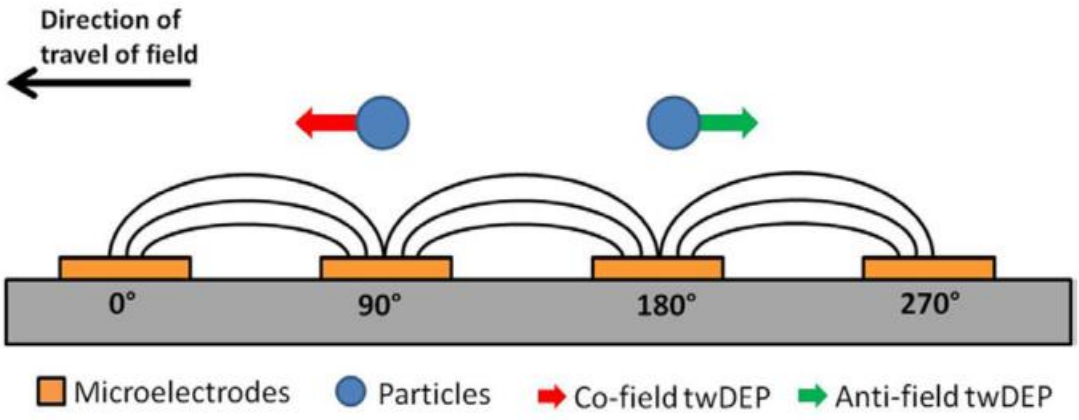

Figure 2-13 Schematic illustration of the twDEP response of the particle in a traveling wave electric field [80].

In a microfluidic device with four electrodes patterned in a circular layout and 90° phase variation between the adjacent electrodes, a circular traveling electric field is induced instead of the translational movement in twDEP. When a neutral particle is placed in the rotating field, the particle will rotate asynchronously with the electric field. The rotational torque induced in a spherical microsphere in a rotating electric field *E* is expressed as [224]

$$\Gamma = -4\pi\varepsilon_m \, a^3 \, Im(f_{CM})E^2 \qquad (2\text{-}11)$$

In a steady state, the rotational torque of the particle is balanced by the opposite torque arising from the viscous drag force, and a rotational velocity is given by [224]

$$\Omega = -\frac{\varepsilon_m}{2\mu} \, Im(f_{CM})E^2 \qquad (2\text{-}12)$$

It can be seen from Equation (2-11), the induced rotational torque in the electrorotation is proportional to the strength of electric field squared instead of the gradient of the electric field squared, and determined by the imaginary part rather than the real part of the CM factor. Then, this electrorotation method is widely used to identify the dielectric property and characterize the morphology of particles and biological cells [225–231].

2.3 Conclusion

This chapter reviews the general electrokinetic phenomena, including the classical EDL theories, EP, EOF, and DEP. Among these various methods for the manipulation of particles in the microchannel, DEP has become one of the most popular methods for the manipulation of the particles, due to its label-free property, low consumption of samples, ability to offer a selective and sensitive analysis of particles, and fast speed. In order to achieve DEP effect, a non-uniform electric field is required which can be generated by a variety of methods, such as insulator-based DC-DEP, micro-electrodes embedded AC-DEP, as well as traveling-wave DEP. In this section, various popular techniques for the dielectrophoretic manipulation of particles, droplets, and biological cells were reviewed and presented. This chapter provides a solid background for the following chapters.

CHAPTER 3 Fabrication of Nano-orifice Based Dielectrophoretic Microfluidic Chip *

3.1 Introduction

Dielectrophoresis refers to the motion of polarized particles in a dielectric suspending medium under a non-uniform electric field. To induce the spatially non-uniform electric field, the traditional DC-insulator DEP (iDEP) method uses insulator obstacles or hurdles inside the microchannel, as illustrated in Figure 3-1 [232]. The DC electric field in the microchannel is applied by the two electrodes inserting in the inlet and exit reservoirs, respectively. The flow is also induced by the applied DC electric field, i.e., electroosmotic flow (EOF). It can be seen from Equation (2-8) that the value of the DEP force is proportional to the gradient of electric field square ($\nabla|E|^2$) and the particle size (a^3). As the trajectory shift of the particles is proportional to the value of the DEP force exerting on the particles, the particles with different sizes will be separated and moved into different streams after passing over the non-uniform electric field region. However, in order to separate particles of smaller sizes and particles with small size differences, a strong DEP force is necessary, which means a high electric field gradient near the hurdle is required. To achieve high ($\nabla|E|^2$), one way is to apply a higher voltage difference along the entire channel (Figure 3-1(a)) which may cause unwanted side effects such as Joule heating as mentioned above. Another way is to make the gap between the tip of the hurdle and the channel wall very small. However, conventional microfabrication methods (e.g., soft lithography) generally cannot make the gap smaller than 10 μm. In addition, when the gap is sufficiently small, polarized particles may form clusters near the gap and block the gap, preventing the particles from passing through the gap.

To solve the above-mentioned problems in the traditional DC isolated-based DEP (iDEP) method, a novel orifice based DC-DEP method employing pressure-driven flow is proposed, as illustrated in Figure 3-1(b). The non-uniform electric field is induced by applying DC electric fields across the channel through a pair of asymmetric orifices: a larger orifice and a small orifice on the opposite sides of channel walls. As shown in Figure 3-1(b), the non-uniformity or the gradient of the electrical field is dependent on the width

* A similar version of this chapter was published as:
(a) Zhao, K.; Peng, R.; Li, D. Separation of nanoparticles by a nano-orifice based DC-dielectrophoresis method in a pressure-driven flow. Nanoscale 2016, 8 (45), 18945-18955. https://pubs.rsc.org/en/content/articlehtml/2016/nr/c6nr06952e.
(b) Zhao, K.; Li, D. Continuous separation of nanoparticles by type via localized DC-dielectrophoresis using asymmetric nano-orifice in pressure-driven flow. Sensors and Actuators B: Chemical 2017, 250, 274-284. https://www.sciencedirect.com/science/article/pii/S0925400517307943.

ratio between the large orifice and the small orifice. A strong non-uniform electrical field can be obtained if the orifices' width ratio is sufficiently large. Since the electric field is applied locally via the orifices across the microchannel, i.e., the distance between the two electrodes is very short, a small voltage difference is sufficient for generating a strong electric field; thus Joule heating is essentially avoided. Furthermore, in this design, the generation of the local electrical field gradient does not require changing the cross-section of the microchannel and hence will not impair the transport of the particles. In the traditional DC-iDEP method, the particles move with the electroosmotic flow in the microchannel, and hence the throughput of the particles is very low, typically a few particles per second. In the proposed new method, by using pressure-driven flow to transport particles, the throughput can be easily increased by ten times or more.

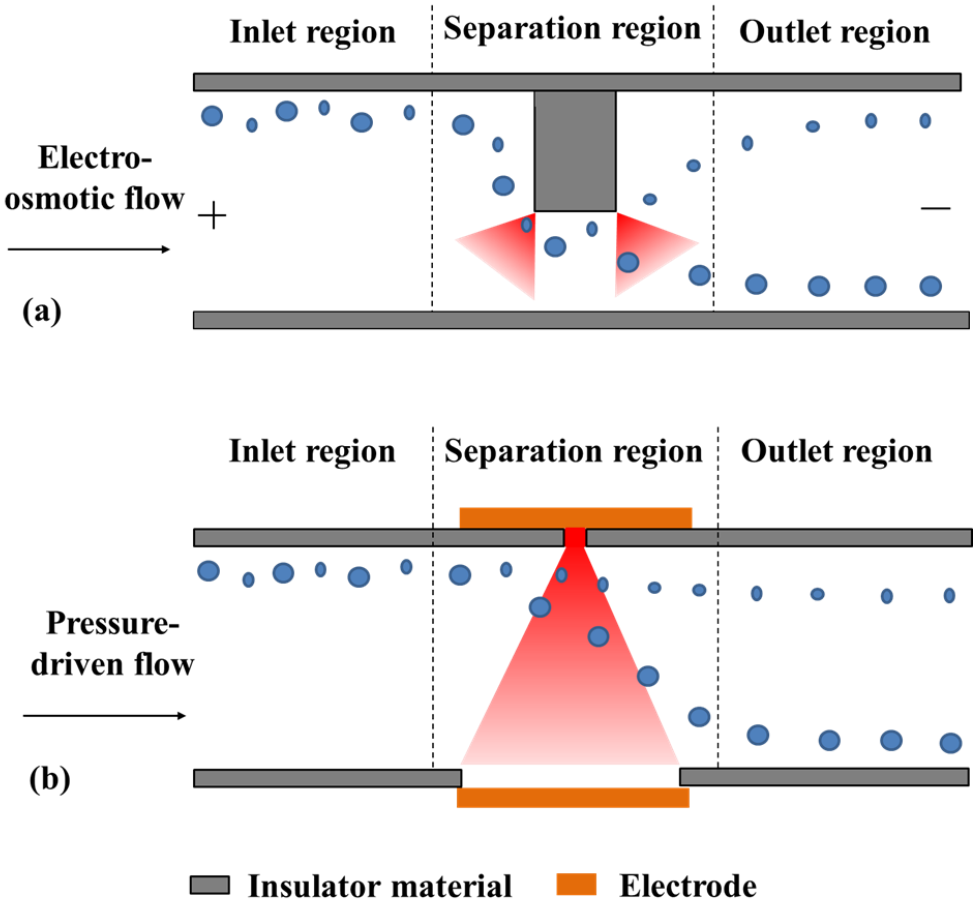

Figure 3-1 Schematic illustration of DC-DEP microfluidic channel: (a) In the traditional DC-iDEP method, the non-uniform electric field is induced by an insulator hurdle. (b) In the new orifice-based DC-DEP

method, the non-uniform electric field is created by using the asymmetric orifices on opposite channel walls (red color represents the electric field strength).

3.2 Materials and methods

3.2.1 Fabrication of nano-orifice based microfluidic chip

In order to generate strong non-uniform electric fields, a small microchannel or a nanochannel is used to form the small orifice on one side of the microchannel walls. To obtain the small microchannel or nanochannel, small micron cracks or nanocracks are created on the polystyrene surface with controllable size and spacing by two steps. Firstly, the small artificial defects are made on polystyrene surface by the micro-hardness testing system (LECO®, MHT series 200), which controls the size and the spacing between the defects. Since the cracks start to form at the defects, the locations of the nanocracks are determined. Then the nanocracks are generated on the defects by the solvent-induced method [233].

A three-step procedure is used to form the crack: a) Firstly, the liquid reagent is heated into vapor which will condense and form a thin liquid membrane on the surface of the polystyrene due to temperature difference. Consequently, the solid polystyrene will absorb the liquid and form a swollen layer. b) Then, after a long time of heating, the liquid reagent is fully vaporized. The absorbed reagent will be released from the swollen layer, as a result, the swollen layer starts shrinking, which will increase the stress of the polystyrene surface. When the surface stress is larger than the critical value, cracks initiate from the defects to release the stress. The longer the heating time, the more absorbed reagent will release from the swollen layer. As a result, the surface stress becomes larger which will, in turn, contribute to a larger crack size, in both axial and vertical directions. c) Finally, the swollen layer stops shrinking when the absorbed reagent is completely released, therefore, the cracks stop growing. Therefore, by adjusting the working parameters, i.e., the heating time and temperature as well as the volume and concentration of the reagent, the crack size becomes controllable. For example, a 3D AFM image of the polydimethylsiloxane (PDMS) nanocrack and the corresponding profile of the cross-section of the crack are shown in Figure 3-2.

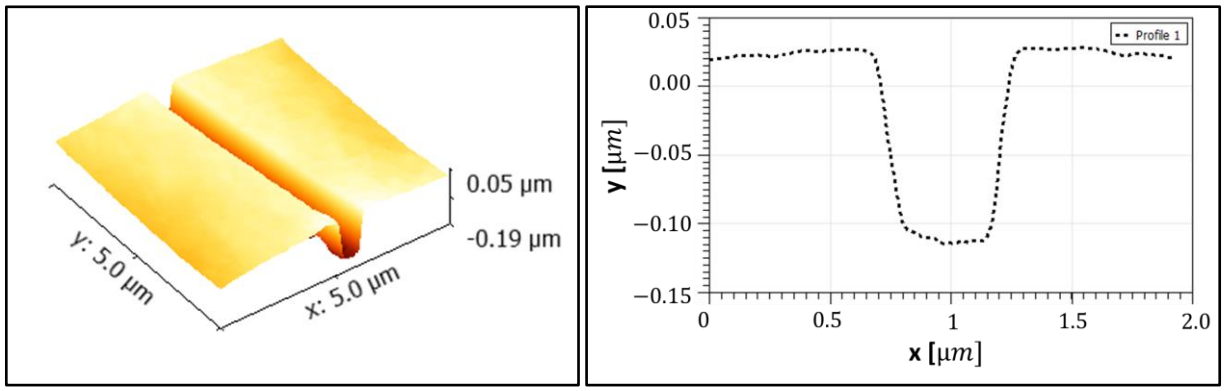

Figure 3-2 AFM image and the cross-section of a PDMS single nanocrack with the width of 626 ± 15 nm and the depth of 166 ± 21 nm created by heating 1 mL 100% ethanol solution at 90 ℃ for 12 hours.

The microfluidic chip was made by bonding a top PDMS layer having the microchannel structure (as illustrated in Figure 3-3(b)) with a bottom PDMS layer having a single small microchannel or nanochannel. The single small microchannel or nanochannel was obtained by three steps and illustrated in Figure 3-3(a). Firstly, a nano-crack with a controlled size is generated on a polystyrene surface by the solvent-induced method [233]. Thereafter, the pattern of the negative nano-crack is transferred onto a SU8 photoresist layer (MicroChem Corp.) by the soft lithography technique to work as the positive nanochannel mold. Finally, the PDMS small microchannel or nanochannel is replicated from the positive mold by casting a 30 μm layer of hard PDMS [234] with a higher Young's modulus and followed by casting a regular PDMS layer of about 2 mm in thickness to avoid the collapse of the small microchannel or nanochannel after the bonding process. The microchannel structure is designed by Auto CAD® software and fabricated by the standard soft photolithography protocol [235]. Finally, the nano-orifice based DC-DEP microfluidic chip is obtained by bonding the plasma-treated PDMS layer with the small microchannel or nanochannel and the plasma-treated PDMS layer with the microchannels together (Figure 3-3(b)) by using a custom-made alignment system under a microscope (Nikon, TE-2000) as shown in Figure 3-3(c).

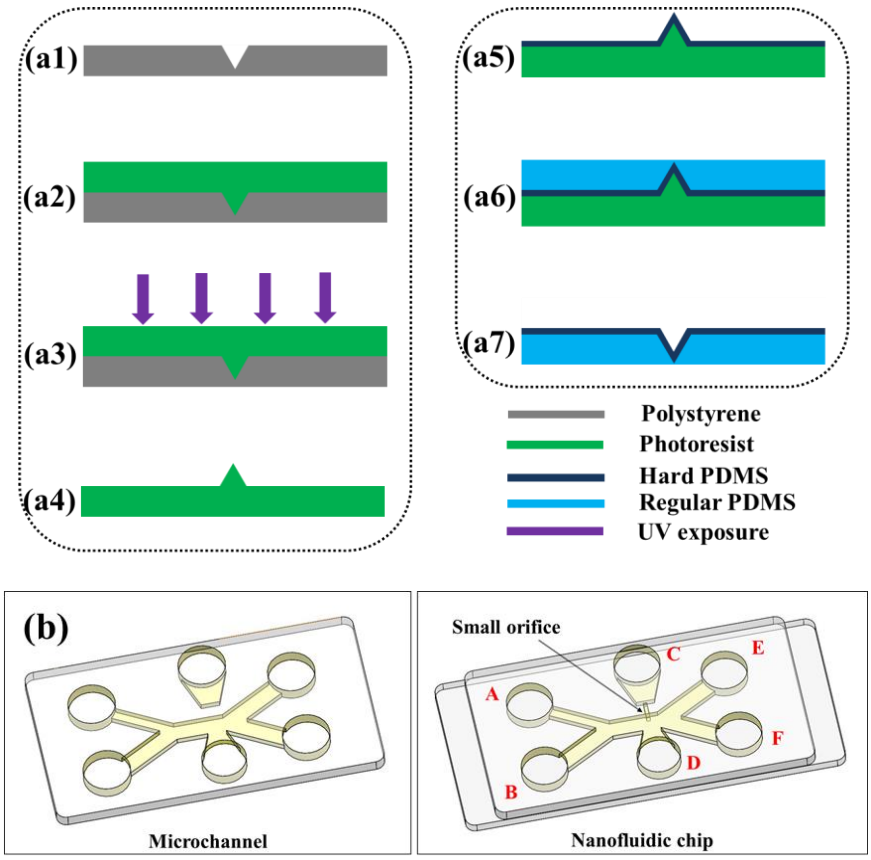

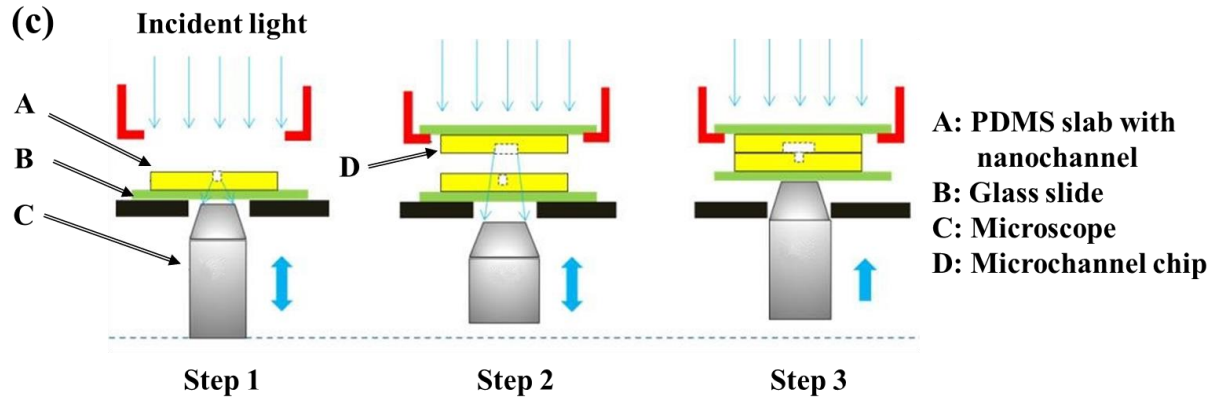

Figure 3-3 Procedures for the fabrication of the nanochannel to make a small orifice: (a1) a nano-crack crack, (a2)–(a3) spin-coating and UV exposure, (a4) positive mold of the nanochannel, (a5)–(a6) hard PDMS and regular PDMS casting, and (a7) formation of a single nanochannel. (b) The top PDMS layer with the microchannel structure and the bonded microfluidic chip. (c) The schematic of micro-nanochannel bonding by a hand-made alignment system.

3.3 Results and discussion

3.3.1 Simulation of the electric field and flow field

The schematic structure of this microfluidic chip from a top view and an example of the distribution of the electric field lines are illustrated in Figure 3-4(a). The entire chip is made of an electrical insulator material such as PDMS. The DC electric field is employed through the microchannel by two external electrodes placed in wells C and D, respectively. The non-uniform electric field is generated owing to the asymmetric size of the orifices, a small orifice on one side of the channel walls and a large orifice on the opposite side of the channel walls. The flow field in the microchannel is shown in Figure 3-4(c). Firstly, the particles' mixture comes into the main channel as one stream from the inlet channel A, and the particles are forced to move closely to the small orifice by the mainstream (focusing flow) of the suspending medium from another inlet channel B. After passing through the vicinity of the small orifice where the strongest electrical field gradient exists, the particles experience DEP force and their trajectories will change. Since the small orifices used in this study are very small, i.e., 510 nm or 1.5 μm in width, the fluid flow from channel C to the main channel is negligible. Let us consider particles all experiencing negative DEP force and they will be pushed away towards the weak electric field, i.e., from the small orifice to the large orifice. Since the value of DEP force exerting on particles is proportional to the sizes of the particles, the larger particles will be repelled away further than the smaller particles. Thus, the smaller and the larger particles can move separately into the separation outlet channels E and F, respectively.

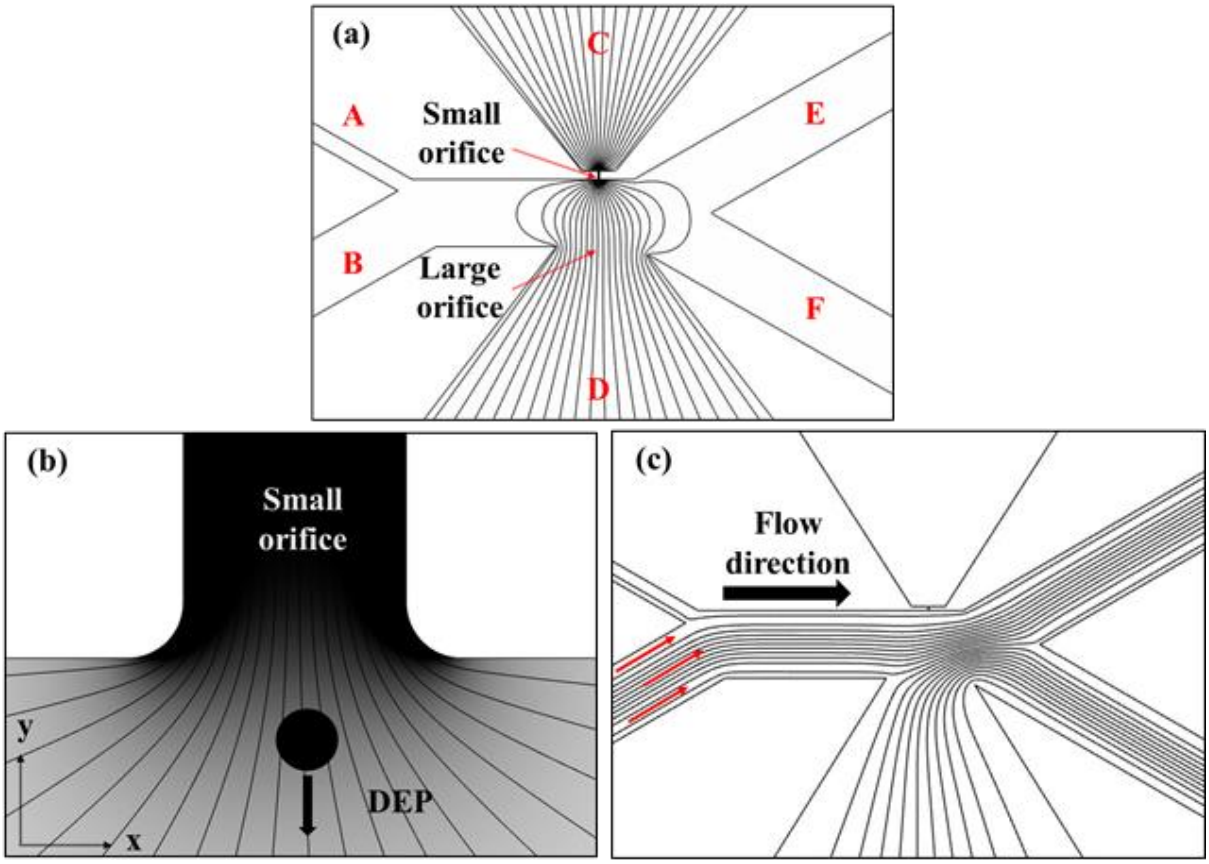

Figure 3-4 (a) The configuration of the new asymmetric orifice based DC-DEP chip and the distribution of the electric field lines (top view). The stronger electric field is indicated by the darkness. A is the particle inlet channel. B is the focusing flow inlet channel. E and F are the separation outlet channels. C and D are the wells for placing electrodes. (b) An enlarged view of the electric field lines around the small orifice region, and an example of a particle experiencing negative DEP force. (c) Streamlines of the pressure-driven flow field in the microchannel.

DEP is a highly localized force and is most likely very strong only right at the interface of the microchannel to the orifice, where strong decay in deflecting DEP force occurs as the gradient of the non-uniform electric field falls off away from the microchannel wall interface to the orifice. Hence, particles need to be focused right at the microchannel wall interface to the orifice to be able to experience deflection and this is particularly the case at higher particle flow rates since the time period for application of DEP force falls substantially with particle flow rate. Hence, a quantitative study of how well the particles should be focused at the microchannel wall interface to the orifice to experience sufficient DEP deflection force. As shown in Figure 3-4, the particles flow into the main microchannel via the sample inlet branch A by the hydrostatic pressure difference, i.e., the liquid height difference between the inlet and outlet wells. The

particles are driven to move along the sidewall with the nano-orifice by the sheath flow from the sheath flow branch B. The flow rate can be described as

$$Q = v \cdot S \qquad (3\text{-}1)$$

where $S = w \cdot h$, w and h are the width and height of the inlet branch channel, respectively. The velocity of a specific micron particle in the inlet branch is $v = L/t$, where v is the particle velocity, $L = l \cdot px$ is the distance of the particle (1 pixel =0.74 μm) and l is measured by NIS-Elements BR software in the digital camera (QImaging) system based on the recorded separation video, t is the time period. In this way, when the volumes imputed into the inlet wells A and B are same (i.e., same different liquid levels and velocity), the volume flow rate ratio between the sample inlet branch A and the sheath flow branch B is solely dependent on the width ratio of the branch A and B. determining how well the particles are focused right at the microchannel wall interface to the orifice. It can be seen from Figure 3-5 below that, when the width ratio is large, i.e., a small width of the sample inlet branch, the flow field from the sample inlet branch A is more compressed and the particles will be focused closer along the microchannel wall interface to the orifice. Therefore, normally for the manipulation of smaller particles, such as nanoparticles, a large width ratio between the sample inlet branch A and the sheath flow branch B will be utilized. While for the separation of micron particles, a small width ratio is enough.

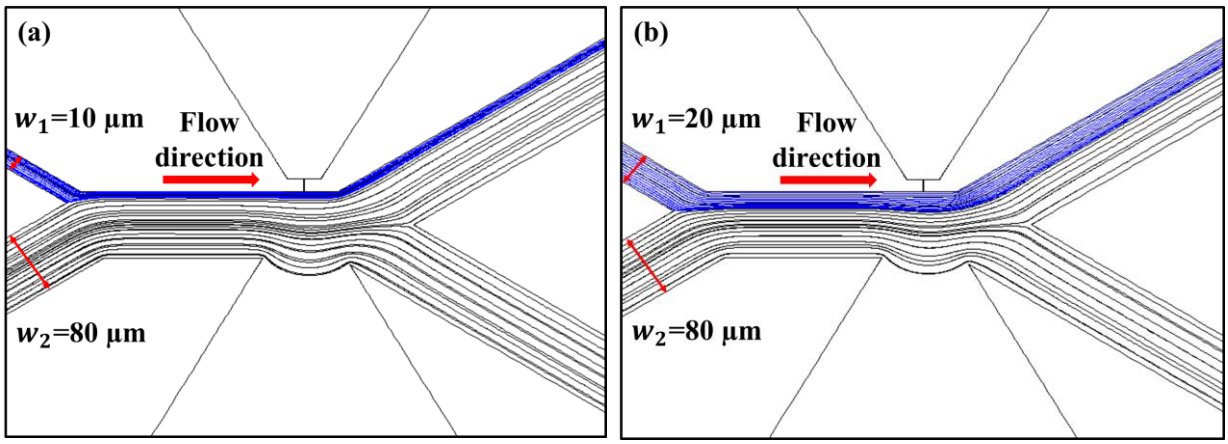

Figure 3-5 Streamlines of the pressure-driven flow field in the DC-DEP chip. (a) The width of the sample inlet branch is 10 μm. (b) The width of the sample inlet branch is 20 μm. The sheath flow branch B has a size of 80 μm in width. The nano-orifice has a size of 860 nm in width and 15 μm in length, and the large orifice is 125 μm in width.

3.3.2 Effect of applied electric field and small orifice structure

To discuss the effects of the structure of the orifices on the gradient of electric field square ($\nabla|E|^2$), extensive numerical simulations have been conducted by COMSOL 4.3b. Figure 3-6 and Table 3-1 show

some examples of the values of $\nabla|E|^2$ obtained for the orifice combinations with two different width ratios, and two different lengths of the small orifice at a given electric potential.

Table 3-1 Calculated values of ($\nabla|E|^2_{max}$) for different width ratio and different lengths of the small orifice (the width of the large orifice is fixed at 100 μm, the voltage is applied at electrode C while electrode D is grounded, and the distance between the electrodes is 0.15 cm)

Width of the small orifice (μm)	Width ratio	Length of the small orifice (μm)	Applied voltage (V)	$\nabla\|E\|^2_{max}$ (V^2/m^3)
0.5	200	5	100	5.44×10^{21}
1	100	5	100	3.73×10^{21}
1	100	15	100	1.2×10^{21}
1	100	5	150	8.38×10^{21}

As we know, a higher $\nabla|E|^2$ means a stronger DEP force. It can be inferred from Figure 3-6(a) and Figure 3-6(b), the structure with a large width ratio produces higher values of $\nabla|E|^2$ (depicted by the darker red color) in the vicinity of the small orifice, but a relatively small region of high $\nabla|E|^2$. For example, the semicircle of the darker red color has a radius of approximately 18 μm in Figure 3-6(a); while the semicircle of the darker red color has a radius of approximately 23 μm in Figure 3-6(b). This is because, when the width of the small orifice is reduced, the electric resistance of the small orifice is increased and hence the electric potential drop inside the small orifice is increased. Thus, the high $\nabla|E|^2$area outside the small orifice becomes smaller under a given applied voltage. Similarly, if the small orifice is long, the electric resistance of the small orifice is large, and hence the electric potential drop inside the small orifice is large. Consequently, the high $\nabla|E|^2$area outside the small orifice is smaller. By comparing Figure 3-6(b) and Figure 3-6(c), one can clearly see that the high $\nabla|E|^2$ area is larger in the structure with the shorter small orifice (Figure 3-6(b)). Therefore, the structure with a relatively large width ratio and a shorter small orifice can lead to large DEP force on the particles, resulting in a high separation resolution. The relationship between the maximum electric field and the size of the small orifice is derived in Appendix A. Furthermore, it can be expected that the increase of the applied voltage will increase the value of the maximum $\nabla|E|^2$ and the high $\nabla|E|^2$area significantly, as shown in Figure 3-6(d). As seen from Table 3-1, the value of the

$\nabla|E|^2_{max}$ increases about 1.5 times when the width ratio increases from 100 to 200, and the value of the $\nabla|E|^2_{max}$ increases about 3.1 times when the length of the small orifice is reduced from 15 μm to 5 μm.

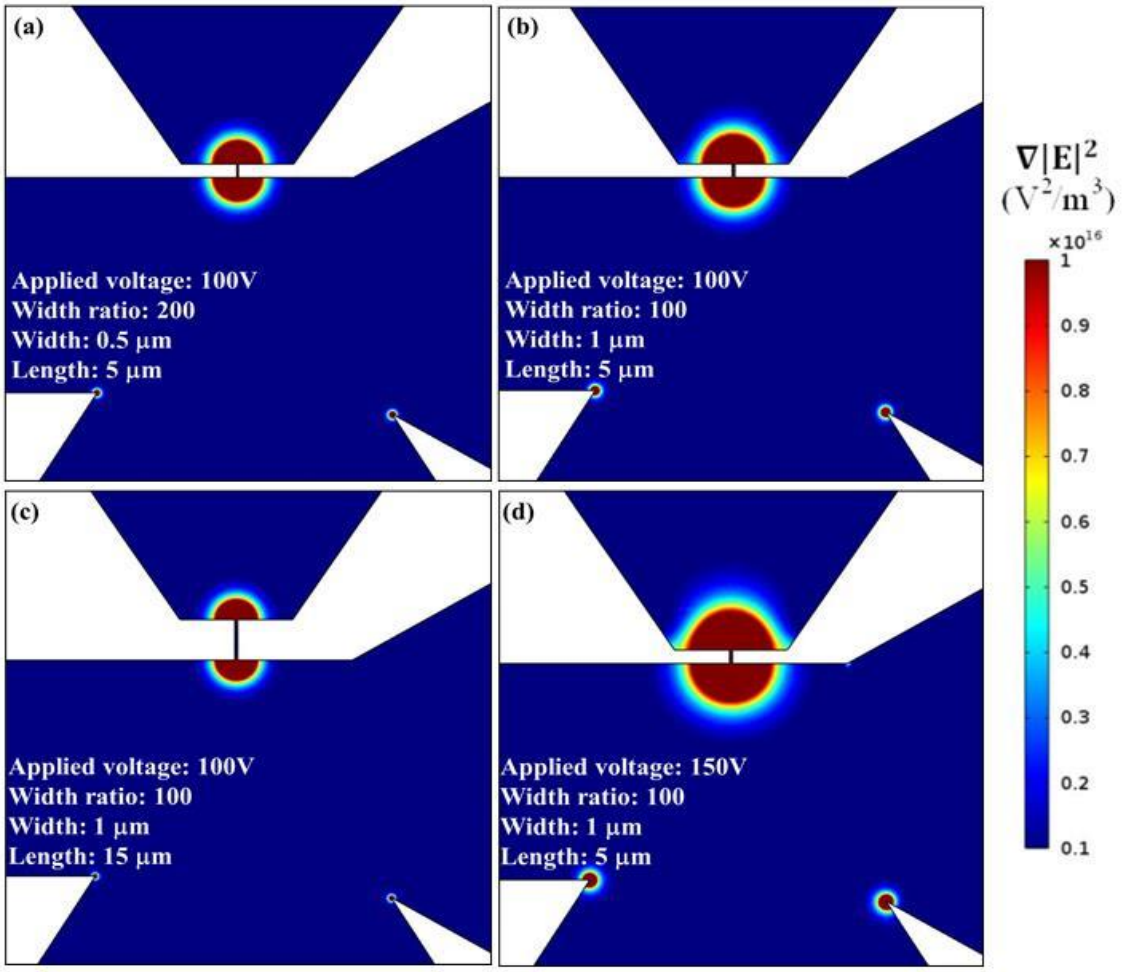

Figure 3-6 Numerical simulations of the distribution of the gradient of electric field square ($\nabla|E|^2$). (a) Width ratio of the orifices is 200, the width and the length of the small orifice are 0.5 μm and 5 μm, respectively. The applied voltage is 100 V. (b) Width ratio of the orifices is 100, the width and the length of the small orifice are 1 μm and 5 μm, respectively. The applied voltage is 100 V. (c) Width ratio of the orifices is 100, the width and the length of the small orifice are 1 μm and 15 μm, respectively. The applied voltage is 100 V, and (d) width ratio of the orifices is 100, the width and the length of the small orifice are 1 μm and 5 μm, respectively. The applied voltage is 150 V.

In addition, for the new developed asymmetric orifice based DC-DEP chip, as shown in Figure 3-6, the $\nabla|E|^2_{max}$ calculated by COMSOL is in the order of $\sim 10^{21}$ V^2/m^3 with 100 V applied across the asymmetric orifices over 0.15 cm between the external electrodes. However, in the conventional insulator-based DC-DEP devices [213,236–240], the magnitude of $\nabla|E|^2_{max}$ is in the order of $10^{11} \sim 10^{15}$ V^2/m^3 with

approximately 70~1200 V/cm applied along the length of the microchannel. Obviously, applying relatively low voltages locally *via* the asymmetric orifices across the microchannel can generate a significantly stronger non-uniform electric field, and hence much larger DEP force on the particles [41,241]. This enables the separation of smaller particles and particles with small size difference.

3.4 Conclusion

This chapter presents a new method to generate a locally spatial non-uniform electric field (i.e., DEP force) by applying electric fields via a pair of asymmetrical orifices: a small orifice and a large orifice on the opposite sides of the channel walls. The major advantages of this DC-DEP separation method include: (1) The fabrication process of the microfluidic chip is simple, and the complicated fabrication process of embedding microelectrodes, the electrode fouling, as well as electrode surface reactions, are avoided; (2) By integrating the pressure-driven flow in the microchannel to transport particles, the throughput can be easily increased by ten times or more; (3) There is no high electric field applied through the whole microchannel, and the Joule heating effect is essentially avoided; (4) The generation of the local electrical field gradient does not require the change of the cross-section of the microchannel and will not affect the transport of the particles; (5) The asymmetric orifices structure with an appropriate size ratio of the small orifice and the large orifice enables the generation of a strong electric field gradient, which allows the separation of particles with smaller size differences and separation of nanoparticles.

CHAPTER 4 Continuous Separation of Nanoparticles and Janus particles with DC-DEP †

4.1 Introduction

DC-dielectrophoresis (DC-DEP) is the induced movement of polarizable particles due to the dielectric differences between the particles and suspending medium in non-uniform DC electrical fields, which is demonstrated to be a highly effective technique for the separation and manipulation of particles. Based on the previous discussion on the fabrication of nano-orifice based DEP microfluidic chip in CHAPTER 3, the DC-DEP method could be used to manipulate the moving trajectory of the particles according to their size and electrical properties. In this CHAPTER, we develop an asymmetric orifice based microfluidic chip and propose a pressure-driven method for both DC-DEP separation of nanoparticles and manipulation of Janus particles. The DC-DEP force is generated by applying a low electric potential difference via a small micron or nano-size orifice on one sidewall of the channel and a micron size orifice on the opposite wall. The particles will experience the DEP forces when passing through the vicinity of the small orifice where the strongest non-uniform electric field exists. Experiments for DC-dielectrophoretic separation of polystyrene nanoparticles and numerical studies for the manipulation of Janus particles under DC electric field will be demonstrated respectively.

Separation of nanoparticles Microfluidic Lab-on-Chip (LOC) technologies use microfluidic platforms to achieve miniaturization, automation, and integration of complicated chemical and biological analysis in the fields of chemical, biological and medical research [80,242]. The manipulation of particles in the LOC systems is crucial in varieties of biological and clinical applications such as trapping, sorting, separation and characterization of micro and nanoparticles, cells, viruses, bacteria and DNA [9,10,12–15,22,24,26,27,174]. Compared with various techniques that have been applied in microfluidic systems for the manipulation of particles by optical, mechanical, magnetic, chemical, acoustic and electrical means [32,33,35–37], dielectrophoresis (DEP) may be one of the most popular methods due to its advantages such as label-

† A similar version of this chapter was published as:
(a) Zhao, K.; Peng, R.; Li, D. Separation of nanoparticles by a nano-orifice based DC-dielectrophoresis method in a pressure-driven flow. Nanoscale 2016, 8 (45), 18945-18955.
https://pubs.rsc.org/en/content/articlehtml/2016/nr/c6nr06952e.
(b) Zhao, K.; Li, D. Continuous separation of nanoparticles by type via localized DC-dielectrophoresis using asymmetric nano-orifice in pressure-driven flow. Sensors and Actuators B: Chemical 2017, 250, 274-284.
https://www.sciencedirect.com/science/article/pii/S0925400517307943.
(c) Zhao, K.; Li, D. Numerical studies of manipulation and separation of Janus particles in nano-orifice based DC-dielectrophoretic microfluidic chips. Journal of Micromechanics and Microengineering 2017, 27(9), 095007.
https://iopscience.iop.org/article/10.1088/1361-6439/aa7eae/meta.

free and low consumption of samples [62,63], ability to analyze particles selectively and sensitively [65,243], and capability of separating bioparticles with high efficiency and throughput [66]. Generally, DC-DEP methods have been widely employed for the separation and manipulation of particles not only by size but also by their different electrical properties.

Cummings and Singh [173] showed the trapping of 200 nm polystyrene particles by DEP force with an array of insulator rods inside the microchannel. Lapizco-Encinas et al. [45,174] investigated the manipulation and separation of live/dead E. coli, and the manipulation and selective separation of two types of live bacteria with arrays of circular insulator posts inside the microchannel in DC electric fields. Kang et al. [9,26] demonstrated the separation of polystyrene particles by size with an insulator hurdle in the microchannel in DC electric fields. Chen [12] investigated a rapid concentration of 500 nm to 1 μm nanoparticles with an insulator 'tree' structure under DC electric fields in the microchannel. A circular insulating post based microfluidic device was investigated to selectively release live and dead E. coli by applying DC electric fields [174]. Song et al. [43] showed the separation of 5 μm polystyrene particles and marine P. subcapitata algae by different DEP forces with a hurdle inside the channel. However, a sufficiently high DC electric field is required for the effective performance of these DC-DEP devices. The locally amplified electric fields around the constricted structures inside the microchannel may induce significant Joule heating, and cause large transmembrane voltages and shear stress on the biological cells [244]. Furthermore, these microfluidic devices are prone to fouling because of particle clogging [245]. In addition, due to the limitation of conventional soft lithography techniques and microfabrication methods, the smallest gap in most microchannels is approximately 10 μm, and thus the insulator-based DC-DEP devices cannot generate sufficiently strong non-uniform electrical fields and hence cannot separate smaller micron particles and nanoparticles with similar sizes. Generally, the DC-DEP separation of particles as reported in the literature cannot separate particles with a size difference smaller than a few microns and particles smaller than 500 nm [17,43–45,174].

Manipulation of Janus particles Janus particles refer to the particles with two sides possessing two distinct surface physical or chemical properties [246]. Due to their asymmetric features, Janus particles are widely applied in a great diversity of fields, such as material science, chemistry, biotechnology as well as food analysis, and show enormous potential in self-assembly [247–249], emulsion stabilizing [250], bio-detecting [251,252], micro-valve [253], and drug delivery [254,255]. Based on the anisotropic properties of Janus particles, unique phenomena are shown under temperature fields [256,257], magnetic fields [258–260], and electric fields [261–266]. Compared with the various responses of Janus particles under electric fields, such as electrorotation and electro-orientation [267,268], induced-charge electroosmosis [265] and electrophoresis [266,269], which have attracted

significant attention recently, dielectrophoresis (DEP) can be applied for the characterization of the particles and allow the controllable tuning of DEP forces exerted on the particles.

In the microchannel, Zhang et al. [247] studied the manipulation and assembly of Janus particles by DEP under a high-frequency AC electric field and found the structures of the Janus particles assembly depend on the frequency of the AC electric field, the electric conductivity of the suspending medium, and the surface chemical property of the particles. Pearl chains of the Janus particles were observed with low conductivity of the medium. The different DEP behaviors between Janus particles and homogeneous particles under an AC electric field were investigated by Zhang et al. [263], and they showed that the DEP crossover frequency, i.e. transition between negative DEP and positive DEP, was a function of the coating thickness of the Janus particles. Honegger et al. [270] presented the DEP-induced rotation of the Janus particles in a determined position and found that their rotation became controllable by adjusting the electric field gradient. The dielectrophoretic manipulation of gold-coated polystyrene particles under the AC electric field was experimentally studied by García-Sachez et al. [271], and positive DEP was observed when the frequency was higher than the characteristic frequency while negative DEP for frequencies lower than this. Gangwal et al. [264,272] demonstrated the DEP-induced assembly of the Janus particle under an AC electric field, and various structures and dynamic motion of the of Janus particle were shown with staggered chains assembled in a variety of orientations. However, there are few studies on the dielectrophoretic manipulation of Janus particles under the DC electric field. The DC-DEP approaches are important in many applications such as separation and sorting of particles as well as drug delivery. Therefore, research in the DC-DEP manipulation and separation of Janus particles in the microchannel is essential.

In this chapter, the experimental study of the direct current (DC) DEP size-dependent separation of micro and nanoparticles and the separation of similar size nanoparticles by type, and the theoretical analysis of the behaviors of the Janus particles under DC electric fields are conducted. This microfluidic chip employs a pair of asymmetric orifices on the opposite sidewalls of the microchannel to induce a strong gradient of the non-uniform electric field and sufficient DEP effect under a locally applied low voltage difference. The effects of key parameters such as electric field and the width and length of the small orifice are investigated experimentally in this study. By adjusting the applied electrical voltage and the electrical conductivity of the suspending solution, the size-dependent separation of nanoparticles and separation of nanoparticle with similar size but different type are conducted. Then in order to further understand the dielectrophoretic motion of the Janus particles under DC electric field, the DC-DEP force acting on the Janus particles was analyzed and the effects of the electric fields, as well as the coating coverage, thickness, and electric conductivity of the Janus particles, are studied. Furthermore, the separation of Janus particles

by size and the different DEP effects-based separation of Janus particles and homogeneous polystyrene particles by choosing the suspending medium with a specific electric conductivity are demonstrated.

4.2 Separation of nanoparticles

4.2.1 Particles and suspending solution

Size-dependent separation Polystyrene microspheres (Bangs Laboratory) of three different sizes, 0.5, 1, and 3 μm in diameter were used. In addition, fluorescent polystyrene spheres (Thermo SCIENTIFIC) of two different sizes, 51 nm red (Ex/Em 542/612 nm) and 140 nm green (Ex/Em 468/508 nm) in diameter, were also employed as sample particles. The particles were originally suspended in pure water and further diluted to the concentrations of 3.1×10^{9} beads/mL, 3.54×10^{8} beads/mL, 3.6×10^{7} beads/mL, 2.74×10^{13} beads/mL and 1.32×10^{11}/mL, respectively. Two suspending solutions were prepared with DI water and K_2HPO_4. A 0.4 mM K_2HPO_4 solution with a pH 7 and an electric conductivity of 1×10^{-2} S/m is used for the separation of 1 μm and 3 μm particles, and the separation of 0.5 μm and 140 nm particles. A 1.6 mM K_2HPO_4 solution with a pH 7 and an electric conductivity of 4×10^{-2} S/m is employed for the separation of 51 nm and 140 nm particles.

Separation of particles by type Two pairs of nanoparticles, i.e., 140 nm fluorescent polystyrene (PS) particles (Thermo SCIENTIFIC, green with Ex/Em 468/508 nm) and 150 nm fluorescent magnetic (Fe_3O_4 core) nanoparticles (chemicellGmbH, red with Ex/Em 578/613 nm), and 470 nm fluorescent magnetic Fe_3O_4-coated PS (Sphorotech Inc., red with Ex/Em 500/560 nm) and 490 nm PS nanoparticles (Bangs Laboratory), and two pairs of micro-particles, i.e., 5.2 μm magnetic-coated PS (Sphorotech Inc.) and 7 μm fluorescent PS particles (Bangs Laboratory, green with Ex/Em 480/520 nm), and 14 μm silver-coated hollow glass beads (Potters Industries LLC) and 15 μm PS particles (Bangs Laboratory) were used. The corresponding concentration of the particles is 0.2 mg/mL, 0.25 mg/mL, 5 mg/L, 10 mg/L, 0.25 mg/mL, 0.4 mg/mL, 0.4 mg/mL, and 0.1 mg/mL, respectively. The suspending solutions were prepared with DI water and K_2HPO_4. A solution of 1.6 mM K_2HPO_4 with a pH of 7 and an electrical conductivity of 4×10^{-2} S/m was used for the separation of 140 nm polystyrene particles and 150 nm magnetic nanoparticles. Another solution of 0.4 mM K_2HPO_4 solution with a pH 7 and an electric conductivity of 1×10^{-2} S/m was employed for the separation of rest pairs of particles.

4.2.2 Microfluidic chip design

The microfluidic chips are fabricated according to the techniques in the last CHAPTER. A picture of the DC-DEP microfluidic chip is shown in

Figure 4-1. For the size-dependent separation of nanoparticles, one nanochannel of 510 nm in width and 450 nm in depth and another small microchannel of 1.5 μm in width and 1.6 μm in depth were fabricated to make the small orifice. Correspondingly, there are two widths of the small orifices used in the experiments, 510 nm, and 1.5 μm. For all chips used in this study, the width of the large orifice is always 125 μm. Two lengths of the small orifice, 5 μm and 15 μm, were used for the studies of the effect of small orifice structure on the separation of the particles. In the chip, there are six channels connected to six different reservoirs. Channel A transports the particle mixture into the main horizontal channel where the particle stream is forced to move close to the wall of the small orifice side by the dominant stream of suspending medium entering from channel B. The main horizontal channel and the branch channels B, E, and F are all 80 μm in width. In order to drive the particles from channel A to move closely to the small orifice, the width ratio between the inlet channels A and B is selected. Two different widths for the inlet channel A were used in this study: 20 μm for the separation of micron size particles, and 10 μm for the separation of nanoparticles. All channels have a depth of 15 μm. The local electric field is induced by the platinum electrodes submerged in wells C and D. The distance between the two external electrodes is approximately 0.4 cm. The separated larger and smaller particles after passing the small orifice region move into the outlet channels E and F, respectively.

In the study of separation of nanoparticles by type, the flows through the microchannel are generated by the hydrostatic pressure difference between the inlet wells and the outlet wells, i.e., by the height difference of the liquid level between the inlet wells and the outlet wells. The mixture of the sample particles comes into the main channel as one stream through the inlet branch channel A, and is then forced to move along the sidewall of the main channel by the focusing flow from the inlet branch channel B. In the meantime, a DC electrical voltage is applied across the microchannel via the asymmetric orifices by the external electrodes inserted in wells C and D. The particles will experience different DEP forces and their trajectories will change when passing through the vicinity of the small orifice where the strongest gradient of the electric field exists. The particles whose electric conductivity is stronger than that of the suspending medium will experience positive DEP (p-DEP) force and be attracted towards the small orifice, i.e., the high electric field, and move with flow into outlet branch channel E. On the contrary, the particles those have weaker electric conductivity in comparison with the surrounding solution will experience negative DEP (n-DEP) and be pushed away from the small orifice towards the large orifice, and then move into outlet branch channel F. The width of the main channel and the branch channels B, E and F are all 80 μm. Two different widths of the branch channel A were utilized in this study, i.e., 20 μm for the separation of nano-size particles and 40 μm for the separation of micron particles, to make sure that the particles from the branch channel A flow closely to the small orifice. For the separation of nanoparticles, the depth of all channels is 15 μm, while for the separation of micron particles, all the channels have a depth of 30 μm. The

localized electric field is generated by the platinum electrodes placed in the wells C and D, and the distance between these electrodes C and D is approximately 0.4 cm. In this study, in order to obtain a strong gradient of the non-uniform electric field, a sufficiently large width ratio between the small orifice and the large orifice is employed [41,241]. To form the small orifice, one nanochannel of 860 nm in width and 290 nm in depth and another small microchannel of 1.5 μm in width and 1.6 μm in depth were fabricated. Thus, the widths of the small orifices utilized in the experiments are 860 nm for the separation of nanoparticles, and 1.5 μm for the separation of micron particles. The length of the small orifice is always 15 μm, and the width of the large orifice is always 125 μm for all the chips. In addition, by using the pressure-driven flow to transport the particles and using the asymmetric orifices to generate the non-uniform electric field in the direction perpendicular to the flow, there is no constriction in the cross-section of the main channel and hence the problems associated with the conventional insulator-based DEP methods such as difficulty of transporting particles and aggregation of the particles are avoided.

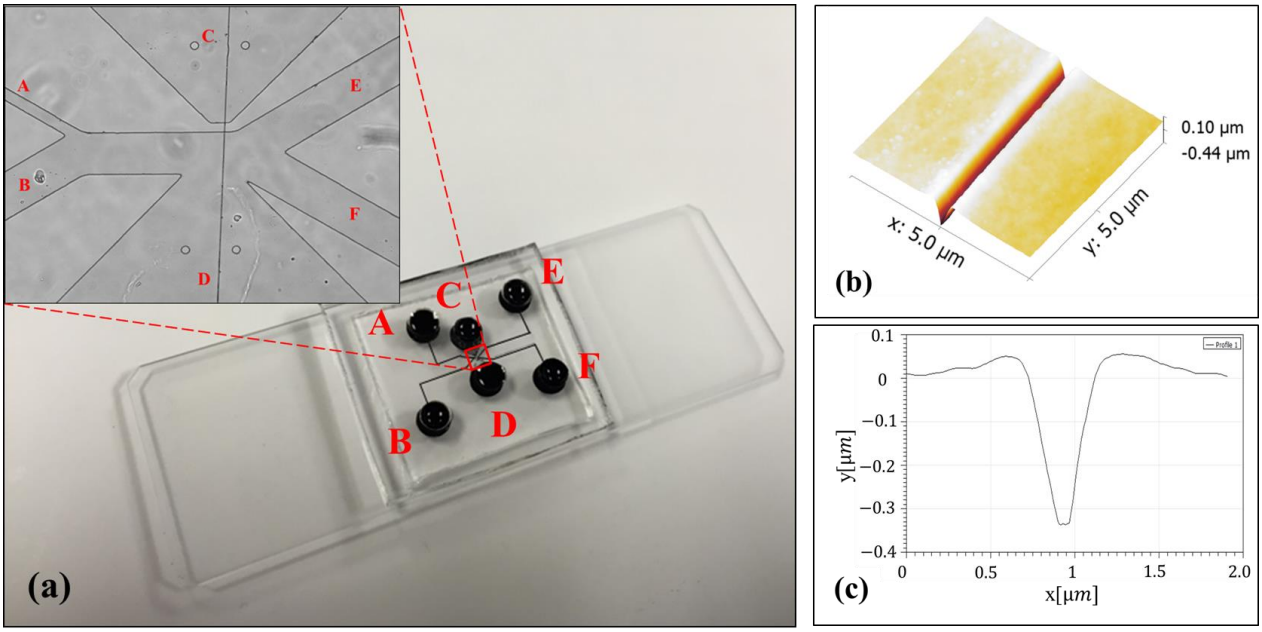

Figure 4-1 (a) The DC-DEP microfluidic chip made by PDMS. (b) AFM image of the PDMS single nanochannel. (c) Cross-section of the PDMS single nanochannel measured by AFM, the width is 510 ± 10 nm and the depth is 450 ± 20 nm.

4.2.3 Experimental procedure

The DEP particles separation experiments started by filling the microfluidic chip with the suspending medium, at a room temperature of 25±1°C. Next, 10 μL of the particle solution was introduced into the reservoir A, 10 μL of the suspending solution was introduced into the reservoir B, and 5 μL of suspending solution was loaded into the wells C and D for inserting the external electrodes. The liquid flow and the

particle transport in the microchannels were all driven by the pressure difference between the inlet and exit wells (i.e., the difference of liquid level). The particles were forced by the mainstream flow from channel B to move along the channel wall and pass the vicinity of the small orifice to experience the stronger gradient of the non-uniform electric field. Then the DC power supply (HVS448 High Voltage Sequencer, LabSmith) was utilized to apply DC electric voltages by the external platinum electrodes placed at the reservoirs C and D. The voltage output to the electrodes was adjusted by a home-made voltages controller. In the experiments, the voltage output to electrode C was carefully adjusted to ensure the best particles separation effect and the electrode D is grounded. For the separation of nanoparticles, as the DEP force exerted on nanoparticles is smaller in comparison with that on microparticles, the electrical force (i.e., interaction between the applied electric field and the electrostatic surface charge of the particle) on the particles is adjusted to be in the same direction as the negative DEP force by reversing the polarity of the applied electric field. In this way, the trajectory shifts of the nanoparticles experiencing negative DEP will be enlarged, enhancing the DEP separation. The motion of particles was visualized by an inverted optical microscope (Nikon, TE-2000) and recorded at 25 frames per second using a CCD camera (QImaging, Burnaby, British Columbia, Canada). Under each condition, 3 independent measurements were conducted.

4.2.4 Results and discussion

4.2.4.1 Size-dependent separation

DC-iDEP technique can separate particles by size, however, successful separation usually requires the particles to have a large size difference [242]. In the previously reported works of DC-DEP separation by size, the separation of particles cannot be realized for a size difference smaller than 3 μm [9,26,200,244,273,274]. However, by using the novel method developed in this work, 1 μm and 3 μm polystyrene particles (with only 2 μm size difference) were successfully separated. Moreover, by adjusting the electric conductivity of the suspending solution, 51 nm and 140 nm particles, and 140 nm and 500 nm particles were also well separated.

Effect of the applied voltage The effect of the applied voltage on the separation of 1 μm and 3 μm particles was conducted by applying different voltages at electrode C from 60 to 160 V. Electrode D is grounded. The 0.4 mM K_2HPO_4 solution with a pH 7 and an electric conductivity of 1×10^{-2} S/m is used as the suspending solution, and the particles experience negative DEP force. In these experiments, the width of the small orifice is 1.5 μm, and the length of the small orifice is 15 μm. The width of the large orifice is 125 μm. The trajectory changes of 1 μm and 3 μm particles under different applied voltages from 60 to 160 V is shown in Figure 4-2. Each picture was achieved by superimposing series of continuous pictures of the moving particles under a given condition.

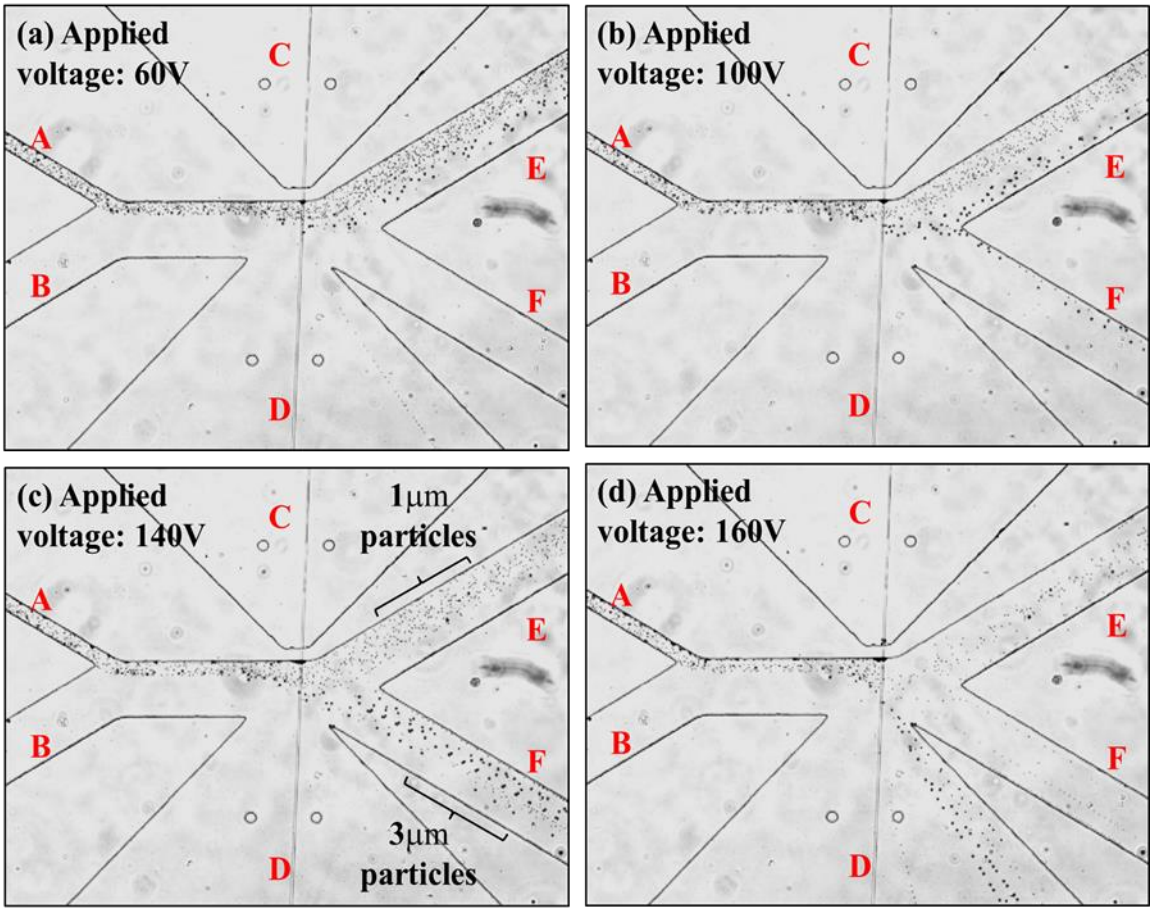

Figure 4-2 Effect of the applied electric field on the separation of 1 μm and 3 μm particles by the DC-DEP method developed in this work. The dependence of the particles' trajectories on the applied voltage at electrode C (a) 60 V, (b) 100 V, (c) 140 V, and (d) 160 V. The electrode D is grounded.

It should be realized that according to Equation (2-8), the DEP force is proportional to the gradient of electric field square ($\nabla|E|^2$). As the applied voltage increases, the DEP force will increase. Furthermore, it can be seen easily from Equation (2-8) that the value of the DEP force exerted on the 3 μm particle is 9 times larger than that on the 1 μm particle. As shown in Figure 4-2(a), under 60 volts, the DEP force is weak, thus there is no apparent trajectory difference between the small particles and the large particles after the particles passed the vicinity of the small orifice. They all moved into the outlet channel E. When the applied voltage was increased to 100 volts, as shown in Figure 4-2(b), the larger DEP force made a significant trajectory difference between the small particles and the large particles after the particles passing through the vicinity of the small orifice. However, the trajectory shift of the large particles is not large enough and a significant portion of the large particles was still moved into the outlet channel E with the small particles. As seen in Figure 4-2(c), when increasing the applied voltage to 140 volts, the strong DEP force at the small orifice region caused significant trajectory change for the large particles, so that the 1 μm

and 3 μm particles continuously moved into distinct outlet channels E and F. The separation of 1 μm particles and 3 μm particles was achieved. Further increase of the applied voltage can produce an overly strong DEP force and cannot separate the small particles and large particles into the individual outlet channels as desired. For example, under 160 volts, the 3 μm particles were pushed by the DEP force into the reservoir D and the 1 μm particles moved into reservoirs E and F, as shown in Figure 4-2(d).

Effect of pressure-driven flow To examine the effect of pressure-driven flow, four different volumes inputted into the inlet wells A and B (i.e., four different liquid levels), 10 μL, 12.5 μL, 15 μL, and 17.5 μL, were conducted for the separation of 1 μm and 3 μm particles. Correspondingly, the flow rate is 1.323×10^{-4} μL/s, 1.554×10^{-4} μL/s, 1.692×10^{-4} μL/s, and 1.886×10^{-4} μL/s. In these tests, electrode C is applied 140 V and the electrode D is grounded. The width and length of the small orifice are 1.5 μm and 15 μm, respectively, and the large orifice width is 125 μm. The trajectory shift of 1 μm and 3 μm particles with different flow rates from 1.323×10^{-4} μL/s to 1.886×10^{-4} μL/s is demonstrated in Figure 4-3.

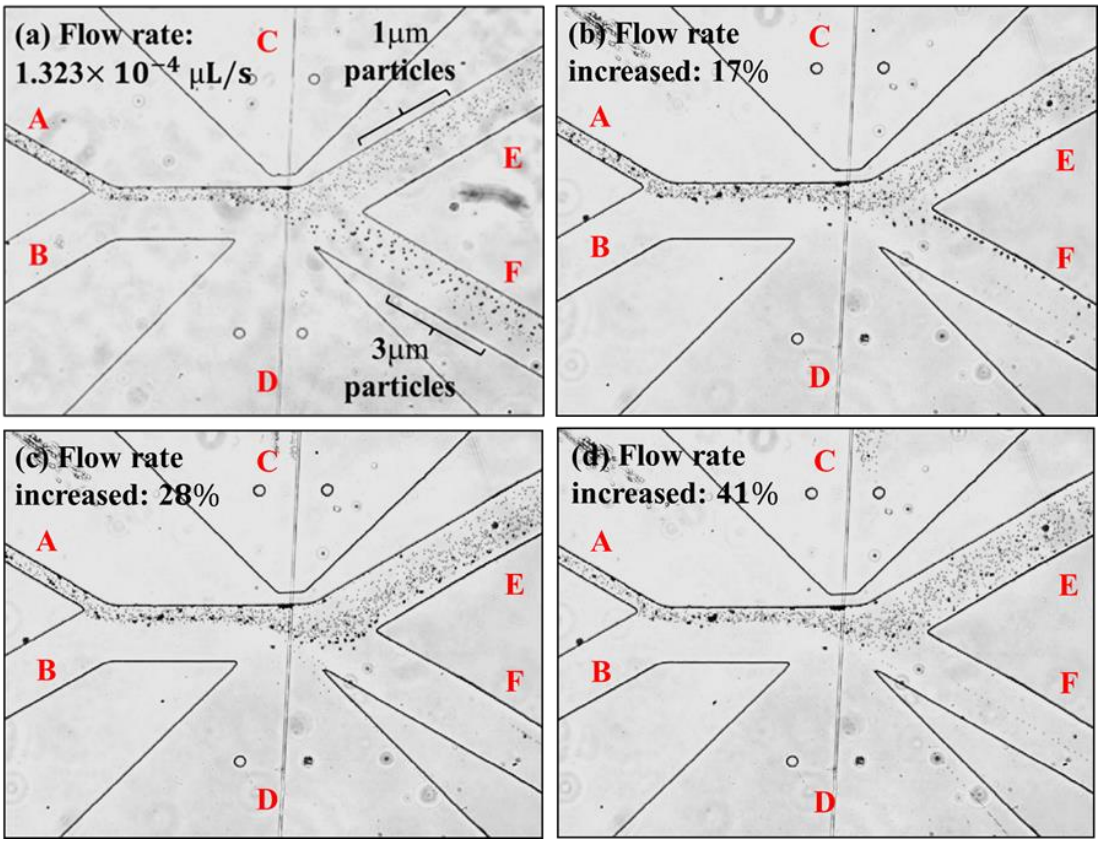

Figure 4-3 Effect of the flow rate on the separation of 1 μm and 3 μm particles by the DC-DEP method developed in this work. The dependence of the particles' trajectories on pressure-driven flow with flow rate (a)1.323×10^{-4} μL/s, (b)1.554×10^{-4} μL/s (17% increase), (c)1.692×10^{-4} μL/s (28% increase), and (d)1.866×10^{-4} μL/s (41% increase). The electrode C is applied 140 V and the electrode D is grounded. The

width and length of the small orifice are 1.5 μm and 15 μm, respectively, and the large orifice width is 125 μm.

Figure 4-3(a) illustrates that the 1 μm and 3 μm particles were separated and diverted into different outlet channels at the flow rate of 1.323×10^{-4} μL/s, under 140 volts. It is easy to understand that when the flow rate increases (i.e., the velocity of the particles), the particles move fast and pass over the vicinity of the small orifice. The time period of the particles experiencing the DEP force will decrease. As shown in Figure 4-3(b), when the flow rate increased by 17% to 1.554×10^{-4} μL/s, the time period of DEP force exerting on the particles is shortened, and the trajectory difference between the small particles and the large particles after passing the vicinity of the small orifice is reduced. Furthermore, the trajectory change of the large particles is not large enough and some of the large particles moved into the outlet channel E with the small particles. When the flow rate increased by 28% to 1.692×10^{-4} μL/s, as shown in Figure 4-3(c), there is no obvious difference of trajectory shift between the small particles and the larger particles after passing the vicinity of the small orifice. The small particles and the larger particles moved into the outlet channel E. Further increase of the flow rate will excessively shorten the action time of the DEP force exerting on the particles, and the small particles and the large particle cannot be separated into the individual outlet channels. As shown in Figure 4-3(d), when the flow rate increased by 41% to 1.866×10^{-4} μL/s, all the 1 μm and 3 μm particles were driven into the outlet channel E.

Effect of small orifice structure As discussed previously, the electric field gradient is strongly dependent on the structure of the small orifice, namely, the width and length of the small orifice. To examine the effects experimentally, three small orifices of different sizes, 0.51 μm in width and 15 μm in length, 1.5 μm in width and 15 μm in length, and 1.5 μm in width and 5 μm in length, were tested for separating 1 and 3 micron particles. In all these tests, the width of the large orifice is fixed at 125 μm.

Figure 4-4(a) shows the particle separation with a small orifice of 1.5 μm in width and 15 μm in length. In this case, the 1 μm and 3 μm particles are separated clearly under 140 volts. When the width of the small orifice is reduced from 1.5 μm to 510 nm, the width ratio between the small orifice and the large orifice is increased by 3 times, hence the electric field gradient is significantly increased. While, similar to the cases shown by Figure 3-6(a) and Figure 3-6(b) (In 3.3.2), the area of high $\nabla|E|^2$ (high DEP force area) outside the small orifice becomes smaller with the decrease of the small orifice width, weakening the DEP separation. To achieve the same separation effect, a higher electric potential has to be applied so that the area of high $\nabla|E|^2$ outside the small orifice can be larger when the width of the small orifice is smaller. Figure 4-4(b) shows particles separation with a small orifice of 0.51 μm in width and 15 μm in length. In comparison with the case of Figure 4-4(a), the width of the small orifice is smaller in this case (Figure 4-4(b)), the 1 μm and 3 μm particles are separated clearly under a higher voltage 340 volts. When the length

of the small orifice is reduced, the electric resistance of the small orifice is reduced and hence the electric potential drop inside the small orifice is reduced. Correspondingly, the area of high $\nabla|E|^2$ (high DEP force area) outside the small orifice becomes larger, under a given applied voltage, as shown in Figure 3-6(b) and Figure 3-6(c) (In 3.3.2). In other words, to achieve the same DEP separation effect, the applied voltage can be smaller when the length of the small orifice is smaller. Figure 4-4(a) and Figure 4-4(c) demonstrate that the separation of the 1 μm and 3 μm particles can be realized with a significantly reduced voltage of 30 V (from 140 V) when the length of the small orifice is reduced from 15 μm to 5 μm. In summary, greater DEP force can be generated by using a large orifice width ratio and a small orifice of short length at low voltages.

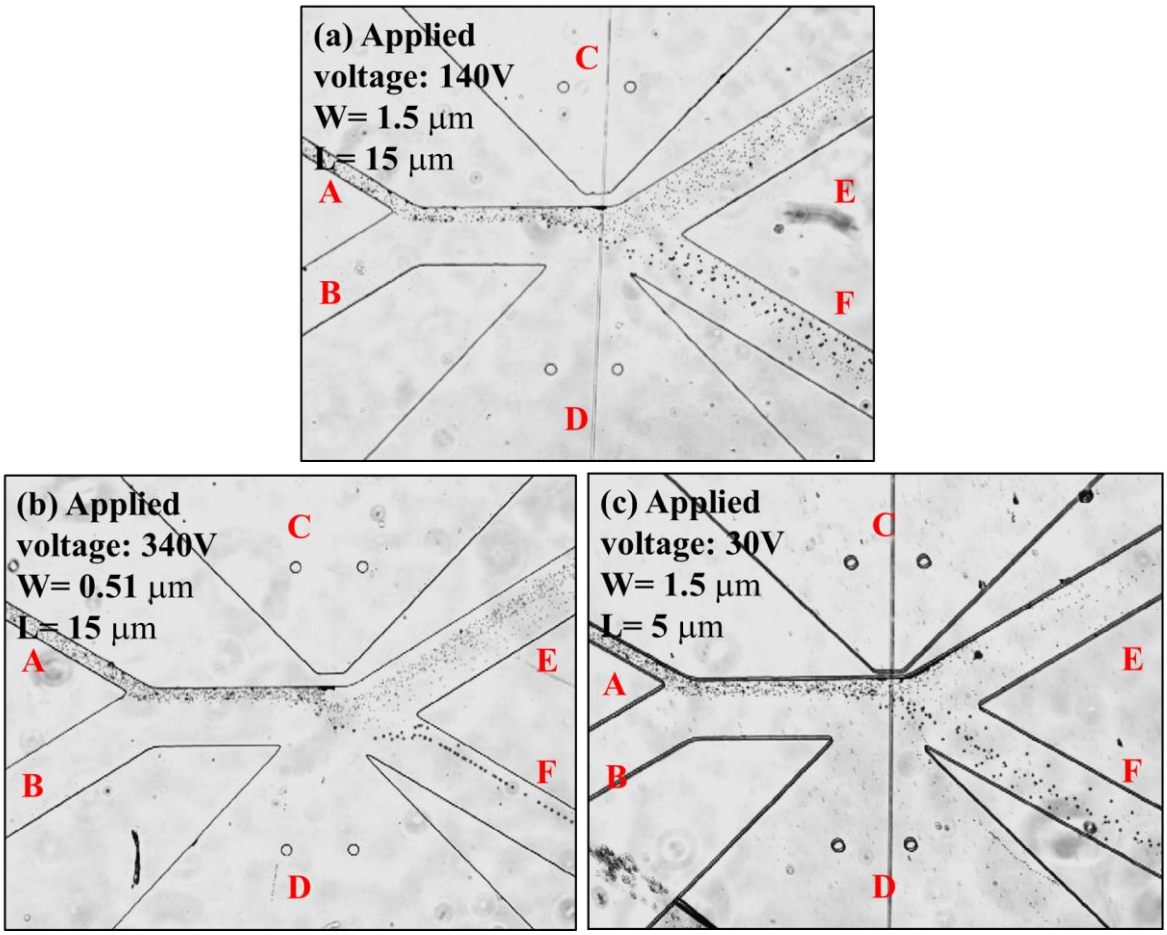

Figure 4-4 Effects of the width and length of the small orifice on DEP separation of particles in terms of the applied voltage. Differences between (a) and (b): The small orifice width is reduced from 1.5 μm to 0.51 μm, and the applied voltage is increased from 140 V to 340 V. Differences between (a) and (c): The small orifice length is reduced from 15 μm to 5 μm, and the applied voltage is reduced from 140 V to 30 V.

Separation of nanoparticles In order to examine the sensitivity of this proposed separation method, the DC-DEP separation experiments with mixtures of 140 nm particles and 500 nm particles, and mixtures

of 51 nm particles and 140 nm particles were conducted. As the particle size decreases from micron to nanometer, the DEP force exerted on the nanoparticles is dramatically reduced and hence the separation of nanoparticles by size with the same type of DEP force (i.e., negative DEP force) becomes difficult. Therefore, we propose to separate the nanoparticles by adjusting the electrical conductivity of the suspending solution, so that the nanoparticles of a given size experience positive DEP force while the nanoparticles of another size experience negative DEP. Consequently, the nanoparticles with different DEP behaviors can be continuously separated.

The conductivity of polystyrene particles can be estimated by [275,276]

$$\sigma_p = \sigma_b + \frac{2K_s}{r} \qquad (4\text{-}1)$$

where σ_b is the bulk conductivity of particle and can be considered negligible for polystyrene particles, and K_s is the surface conductance (typically $K_s = 1\ nS$ for polystyrene), and r is the radius of the particle.

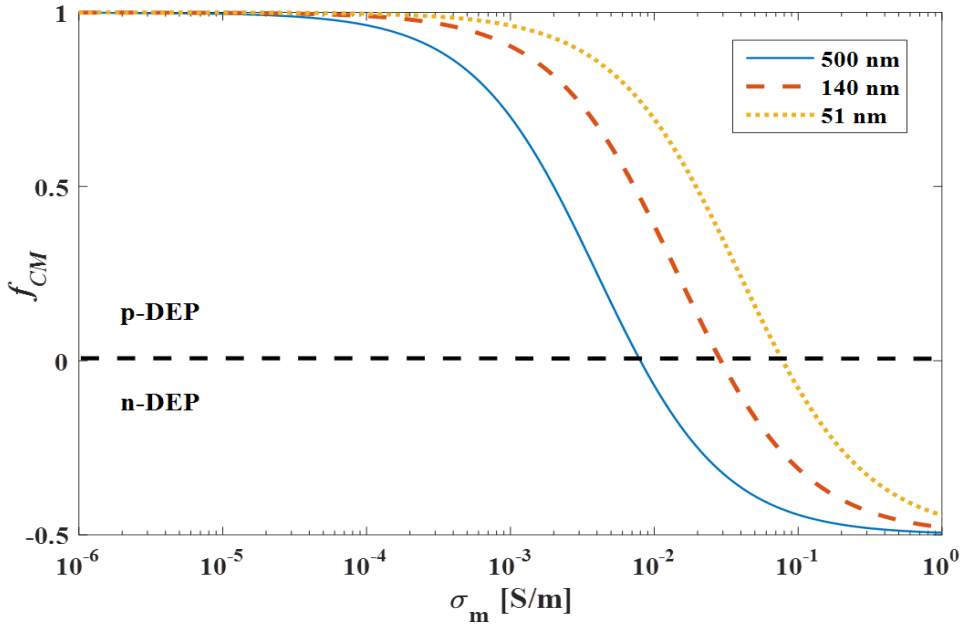

Figure 4-5 Prediction of f_{CM} for three different sizes of polystyrene particles as a function of the electric conductivity of the suspending solution σ_m.

In Figure 4-5, f_{CM} values of the nanoparticles of three different sizes, 51 nm, 140 nm, and 500 nm are plotted as a function of the electric conductivity of the suspending solution, σ_m. It can be seen that f_{CM} value ranges from −0.5 to 1, and. In a certain range of σ_m, $f_{CM} > 0$ (i.e., positive DEP force) for nanoparticles of a given size, while $f_{CM} < 0$ (i.e., negative DEP force) for nanoparticles of another size. In this study, two suspending solutions with two different conductivities were used, 0.4 mM K_2HPO_4 solution

with a pH 7 and a conductivity of 1×10^{-2} S/m was used for the separation of 140 nm and 500 nm particles, and 1.6 mM K_2HPO_4 solution with a pH 7 and a conductivity of 4×10^{-2} S/m was employed for the separation of 51 nm and 140 nm particles. The corresponding f_{CM} values are listed in Table 4-1 and Matlab codes are listed in Appendix B.

Generally, the electrical force on a spherical particle is expressed as [1]

$$\mathrm{F_e} = 4\pi\varepsilon_m \zeta_p \, r \, (1 + \kappa r) E \qquad (4\text{-}2)$$

where ζ_p is the zeta potential of particles, and $1/\kappa$ is the characteristic thickness of the electrical double layer (EDL). The particles used in this work are all negatively charged and their electrophoretic motion directs to the positive electrode. The force ratio between electrical force and DEP force is given by:

$$\frac{\mathrm{F_e}}{\mathrm{F_{DEP}}} = \frac{2\,\zeta_p\,(1+\kappa r)E}{r^2\,\mathrm{Re}(f_{\mathrm{CM}})(\nabla|E|^2)} \approx \frac{2\,\zeta_p\,k\,E}{r\,\mathrm{Re}(f_{\mathrm{CM}})\,(\nabla|E|^2)} \quad (\text{for thin EDL}) \qquad (4\text{-}3)$$

The ratio between the electrical force and DEP force on the particle is increased by 10^3 when the size of the particle decreases from the micron scale to the nanoscale. This indicates the electrophoretic motion of nanoparticles is important and can be favorable for DEP separation of nanoparticles by adjusting the position of the positive electrode (i.e., the polarity of the applied electric field). In the DC-DEP separation of nanoparticles, the electrical conductivity of the suspending medium was selected in such a way that the nanoparticles of a given size experience positive DEP force (attracting to the strong electric field at the small orifice) while the nanoparticles of another size experience negative DEP (being repelled away from the small orifice). Therefore, in these experiments, electrode D (on the opposite side to the small orifice) was selected as the positive electrode. In this way, the electrophoresis motion of the nanoparticles is in the same direction as the negative DEP, enhancing the separation of the particles undergoing negative DEP. Based on the calculated f_{CM} in Table 4-1, the numerical simulation of the trajectory of 140 nm and 500 nm particles have been conducted by COMSOL 4.3b via the particle tracing module. Figure 4-6 shows the separation of 140 nm and 500 nm particles with 60 V applied at electrode D. The width and length of the small orifice are 0.51 μm and 5 μm, respectively, and the large orifice width is 125 μm.

Table 4-1 The Clausius-Mossotti factor (f_{CM}) for the polystyrene particles of three different sizes in the suspending medium with two different electric conductivities.

Diameter of particle (nm)	f_{CM} with $\sigma_m = 1 \times 10^{-2}$ S/m 0.4 mM K_2HPO_4 solution	f_{CM} with $\sigma_m = 4 \times 10^{-2}$ S/m 1.6 mM K_2HPO_4 solution

500	−0.07	
140	0.38	−0.1
51		0.24

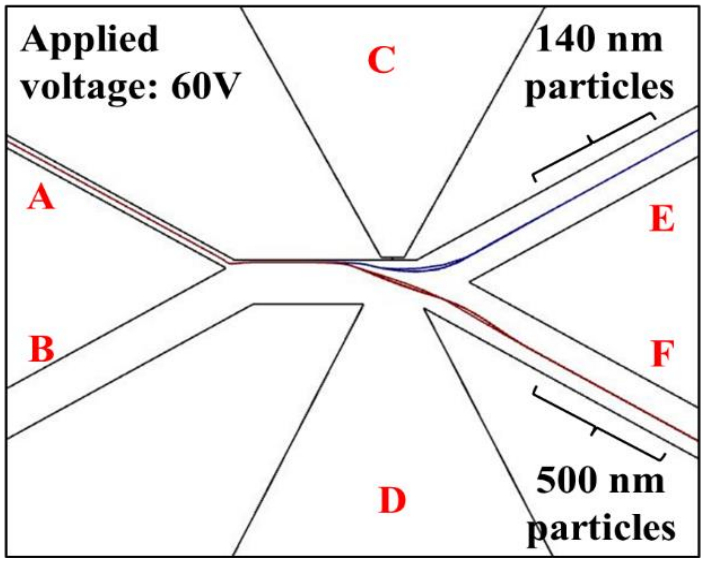

Figure 4-6 Numerical simulations of the separation of the 140 nm and 500 nm. 60 V is applied at electrode D, and zero volts is applied at electrode C. The width and length of the small orifice are 0.51 μm and 5 μm, respectively, and the large orifice width is 125 μm.

By using a selected suspending medium, the separation based on the opposite dielectrophoretic behaviors as a function of particle sizes is shown in Figure 4-7 and Figure 4-8. In these experiments, 51 nm and 140 nm fluorescent particles were used in order to show their trajectories. The 500 nm particles used in the experiments are non-fluorescent particles. Figure 4-7 shows that the mixture of 140 nm and 500 nm particles was well separated by inducing positive DEP force on 140 nm particles which were attracted to the small orifice area and moved into outlet channel E, and by inducing negative DEP force on the 500 nm particles which were repelled from the small orifice and moved to the outlet channel F. In Figure 4-8, the fluorescent images clearly show the separated trajectories of the red fluorescent 51 nm particles and green fluorescent 140 nm particles. Evidently, the mixed red fluorescent 51 nm particles and green fluorescent 140 nm particles were separated and directed into outlet channels E and F by positive-DEP and negative-DEP, respectively. This indicates that the proposed nano-orifice based DC-DEP separation method can be used for the separation of nanoparticles with smaller size differences, i.e., a 90 nm size different as demonstrated in Figure 4-8.

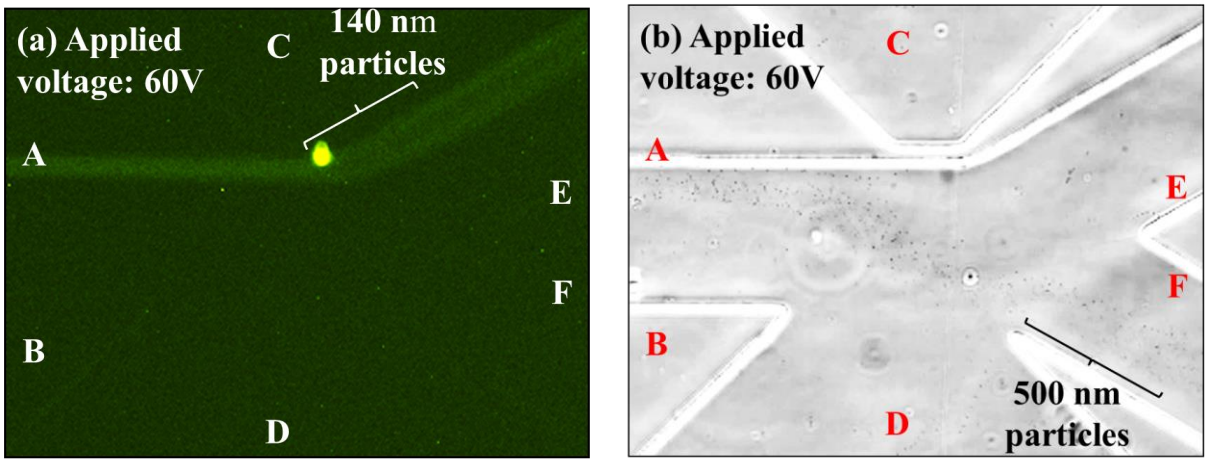

Figure 4-7 Separation of 140 nm and 500 nm particles. (a) Fluorescent image showing the trajectories of 140 nm fluorescent (green) particles. (b) Trajectories of 500 nm non-fluorescent particles. 60 V is applied at electrode D. The width and length of the small orifice are 0.51 µm and 5 µm, respectively, and the large orifice width is 125 µm.

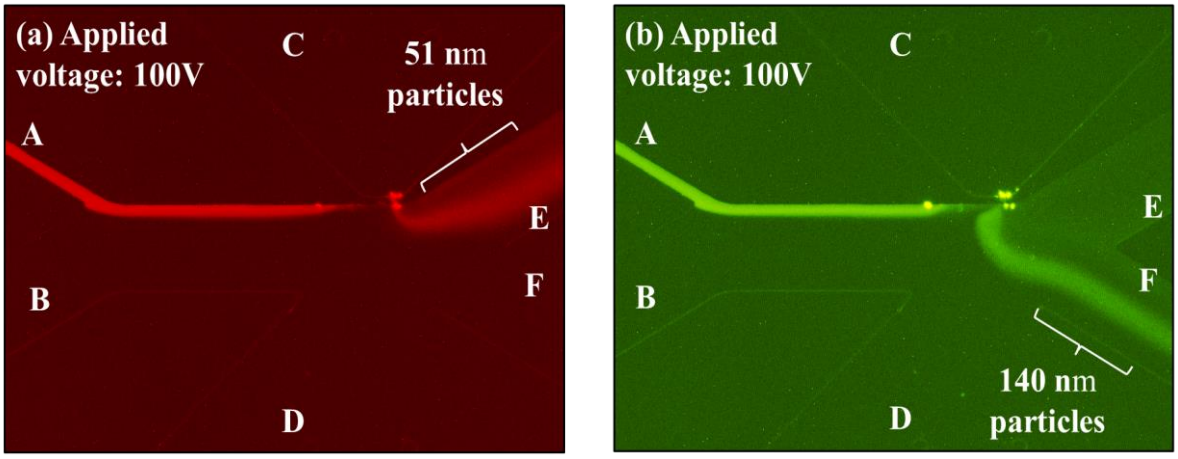

Figure 4-8 Separation of 51 nm and 140 nm particles. (a) Fluorescent image showing the trajectories of 51 nm particles. (b) Fluorescent image showing the trajectories of 140 nm particles. 100 V is applied at electrode D. The width and length of the small orifice are 0.51 µm and 5 µm, respectively, and the large orifice width is 125 µm.

4.2.4.2 Separation of nanoparticles by type

Dielectrophoresis is the induced movement of polarizable particles due to the dielectric differences between the particles and suspending medium in non-uniform electrical fields. Under DC electric fields, f_{CM} is solely determined by the electric conductivity of the particle, σ_p, and the conductivity of the suspending medium, σ_m, and expressed as [171]

$$f_{CM} = \frac{(\sigma_p - \sigma_m)}{(\sigma_p + 2\sigma_m)} \qquad (4\text{-}4)$$

It can be seen easily from Equation (4-4), the sign of the CM factor f_{CM} determines the directions of the DC-DEP effect, i.e., positive DEP or negative DEP. For two different kinds of particles with similar sizes, the particles can have opposite DEP behaviors depending on the sign of f_{CM}. If the electric conductivity of one kind of particles is larger than that of the suspending medium, i.e., $f_{\mathrm{CM}} > 0$, they will experience p-DEP force and be attracted towards high electric field region. If the other type of particles has an electric conductivity smaller than that of the suspending solution, i.e., $f_{\mathrm{CM}} < 0$, they will be pushed away by the n-DEP towards the electric field minimum. Therefore, for particles with similar sizes but different electric conductivities, they can be separated by DC-DEP and move into different outlet channels after passing through the non-uniform electric field area by selecting a suspending medium with an electric conductivity, $\sigma_{p1} < \sigma_m < \sigma_{p2}$.

Separation of microparticles by electric conductivity The separation of 5.2 μm magnetic-coated polystyrene (PS) and 7 μm fluorescent PS particles, and 14 μm silver-coated hollow glass beads and 15 μm plain PS particles were conducted by applying 150 V and 120 V, respectively, at electrode C, while electrode D is grounded. The related physicochemical data of the microparticles are listed in Table 4-2 [277]. The CM factor (f_{CM}) values of the above-mentioned four different kinds of particles are plotted as a function of the electric conductivity of the suspending solution, σ_m, and are shown in Figure 4-9. It can be seen that in a certain range of σ_m, the different kinds of particles with similar size will experience different positive and negative DEP effects, respectively. In this study, a solution of 0.4 mM K_2HPO_4 with a pH value of 7 and an electric conductivity of 1×10^{-2} S/m was utilized as the suspending medium. For the microfluidic chips used in the experiments, the width and length of the small orifice are all 1.5 μm and 15 μm, respectively, and the width of the large orifice is 125 μm. The trajectory shifts of the particles are shown in Figure 4-10, which is achieved by superimposing a series of images of the moving particles under a given condition.

Table 4-2 Physicochemical data and the Clausius-Mossotti factor (f_{CM}) for four different kinds of micro-particles in a suspending medium with electric conductivity of $\sigma_m=1\times10^{-2}$ S/m.

Material and property	Diameter (μm)	Conductivity (S/m)	f_{CM}
Fluorescent polystyrene particle	7	0.57×10^{-3}	−0.46

Magnetic Fe_3O_4 –coated Polystyrene particle	5.2	10^4~10^5	≈1
Plain polystyrene particle	15	0.26×10^{-3}	−0.48
Silver-coated hollow glass Beads	14	0.27×10^4	≈1

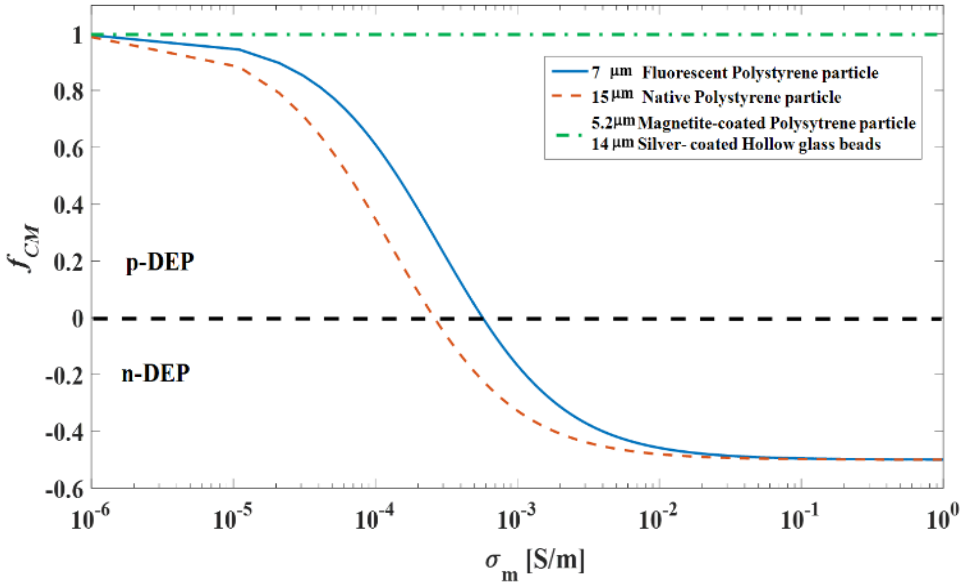

Figure 4-9 Prediction of f_{CM} for four different kinds of microparticles, i.e., 5.2 μm magnetic-coated PS and 7 μm fluorescent PS particles, and 14 μm silver-coated hollow glass beads and 15 μm plain PS particles, as a function of the electric conductivity of the suspending solution σ_m.

As shown in Figure 4-10(a), the particle mixture in the solution was introduced into the main channel from branch channel A and focused as a thin stream along the sidewall of the channel. The magnetic-coated particles (f_{CM} ≈ 1, Table 4-2) were attracted towards the small orifice by the p-DEP force and flow into branch E, while the fluorescent polystyrene particles (f_{CM} = 0.46, Table 4-2) were deflected towards the large orifice by the n-DEP force and flow into branch channel F. Furthermore, Figure 4-10(b) shows the mixture of the silver-coated hollow glass beads and the plain polystyrene particles were well separated by the positive DEP force on the silver-coated hollow glass beads (f_{CM} ≈ 1, Table 4-2) and the negative DEP force on the plain polystyrene particles (f_{CM} = 0.48, Table 4-2), and moved into branch channels E and F, respectively. It should be noted that the proper electric field required to achieve successful separation of particles depends on the dimensions of the asymmetric orifices, the electric conductivity of the suspending medium and the flow rate. Generally, the gradient of the electric field will become stronger with the increase of the applied voltage difference and the width ratio of the orifices, and with the decrease of the length of the small orifice. While a strong electric field gradient can generate a large DEP force and hence a large

trajectory change of the particles, a large volume flow rate or a high speed of the liquid carrying the particles will shorten the time period that the particles experience the DEP force in the vicinity of the small orifice. Therefore, the voltage required for the best separation effect will vary with the dimensions of the microchannel and the asymmetric orifices, as well as the flow rate of the suspending medium. Figure 4-10 shows that the mixture of the magnetic-coated polystyrene particles and the fluorescent polystyrene particles, and the mixture of the silver-coated hollow glass beads and the plain polystyrene particles were well separated by applying 150 V and 120 V, respectively, across the pair of asymmetric orifices (i.e., the small orifice with a width and length of 1.5 μm and 15 μm, respectively and the large orifice with a width of 125 μm) at a flow rate of approximate 0.468×10^{-4} μL s^{-1} and 1.315×10^{-3} μL s^{-1} respectively. Moreover, since the DEP force increases with the particle radius, the electric voltage applied in the case of Figure 4-10(b) is lower than that in the case of Figure 4-10(a). In addition, an electric current generates a magnetic field which can attract magnetic particles leading to a similar phenomenon to positive DEP. Magnetic field effects on the magnetic particles are discussed in Appendix C.

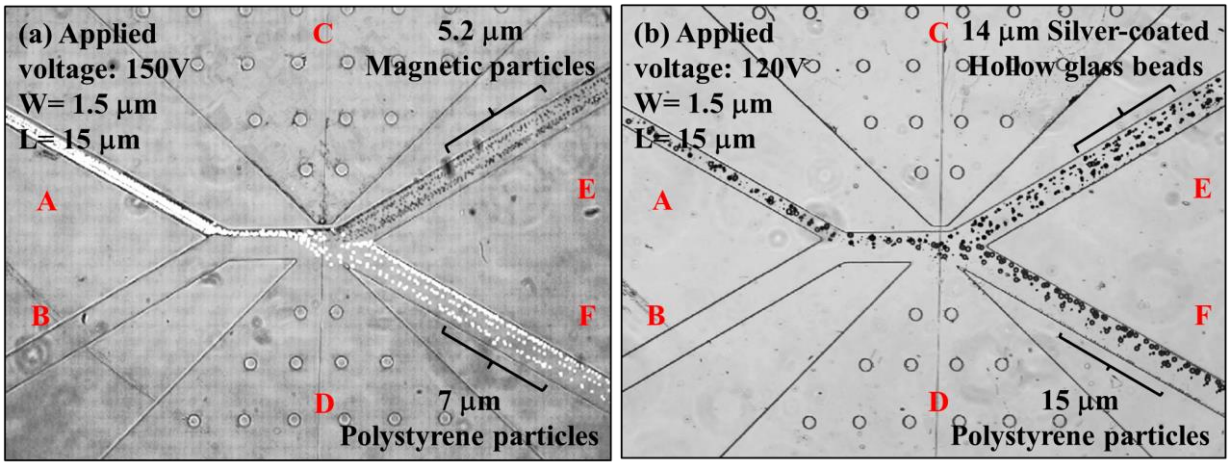

Figure 4-10 (a) Separation of 5.2 μm magnetic-coated polystyrene particles and 7 μm fluorescent polystyrene particles. 150 V is applied at electrode C. (b) Separation of 14 μm silver-coated hollow glass beads and 15 μm plain polystyrene particles. 120 V is applied at electrode C. The width and length of the small orifice is 1.5 μm and 15μm, respectively, and the width of the large orifice is 125 μm.

Separation of nanoparticles by p-DEP and n-DEP In order to examine the sensitivity of this novel DC-DEP separation method, the experiments of the separation of mixtures of 140 nm fluorescent polystyrene nanoparticles and 150 nm magnetic (Fe_3O_4 core) nanoparticles, and mixtures of 470 nm magnetic-coated particles and 490 nm plain polystyrene nanoparticles were conducted. The related physicochemical data of these nanoparticles are listed in Table 4-3. In Figure 4-11, the f_{CM} values of the nanoparticles of four different types are plotted as a function of the electric conductivity of the surrounding

medium, σ_m. In order to make sure that one kind of nanoparticles experience p-DEP force and another type of nanoparticles with similar size experiences n-DEP, two different suspending mediums were employed. A solution of 1.6 mM K_2HPO_4 with pH of 7 and a conductivity of 4×10^{-2} S/m was used for the separation of the 140 nm fluorescent polystyrene nanoparticles and 150 nm magnetic nanoparticles, and the solution of 0.4 mM K_2HPO_4 with a pH 7 and a conductivity of 1×10^{-2} S/m was used for the separation of 470 nm fluorescent magnetic-coated particles and 490 nm plain polystyrene nanoparticles.

Table 4-3 Physicochemical data and the Clausius-Mossotti factor (f_{CM}) for four different kinds of nanoparticles in the suspending medium with two different electric conductivity, i.e., $\sigma_m=4\times10^{-2}$ S/m for the mixture of 140 nm fluorescent polystyrene and 150 nm magnetic nanoparticles, and $\sigma_m=1\times10^{-2}$ S/m for the mixture of 470 nm fluorescent magnetic-coated particles and 490 nm plain polystyrene nanoparticles.

Materials and property	Diameter (nm)	Conductivity (S/m)	f_{CM}
Fluorescent polystyrene particle	140	2.6×10^{-2}	−0.1
Fluorescent magnetic (Fe_3O_4 core) nanoparticles	150	10^4~10^5	≈1
Plain polystyrene particle	490	0.8×10^{-2}	−0.07
Fluorescent magnetic–coated polystyrene particle	470	10^4~10^5	≈1

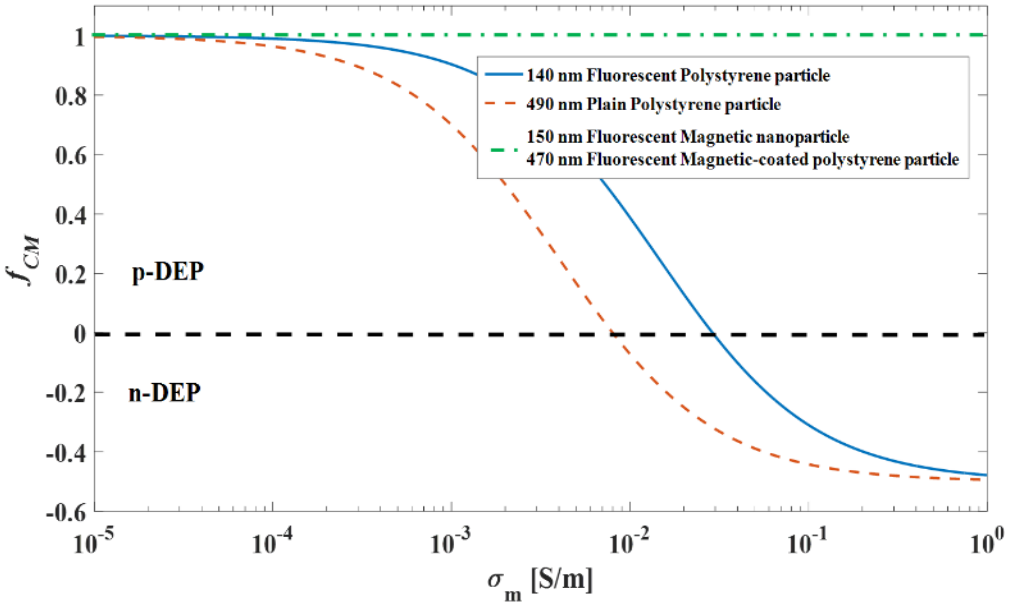

Figure 4-11 Prediction of f_{CM} for four different kinds of nanoparticles as a function of the electric conductivity of the suspending solution σ_m.

By utilizing a specific suspending medium, the separation of nanoparticles based on the opposite dielectrophoretic behaviors resulting from the difference in the particles' electric conductivity is shown in Figure 4-12 and Figure 4-13. In order to show the unique trajectories of the nanoparticles, the 140 nm polystyrene nanoparticles, 150 nm magnetic nanoparticles, and the 470 nm magnetic-coated particles used in this study are all fluorescent particles, and the 490 nm plain polystyrene nanoparticles are non-fluorescent particles. In Figure 4-12(a) and Figure 4-12(b), it clearly shows the separated trajectories of the red fluorescent 470 nm magnetic-coated particles and the 490 nm plain polystyrene nanoparticles. The mixture of the red fluorescent 470 nm magnetic-coated and 490 nm plain polystyrene nanoparticles were continuously entering the separation region from branch channel A and was separated and moved into branch channels E and F by p-DEP and n-DEP forces, respectively. In order to make sure that the 490 nm plain polystyrene nanoparticles were moved into branch channel F, Figure 4-12(c) shows the trajectories of the pure 490 nm plain polystyrene nanoparticles under the same conditions. It can be clearly seen that the plain polystyrene nanoparticles were repelled further away towards the large orifice and directed into branch channel F. Clearly, Figure 4-12(c) shows that the pure 490 plain polystyrene nanoparticles have the same trajectories as they were in the case of the mixture as shown Figure 4-12(a).

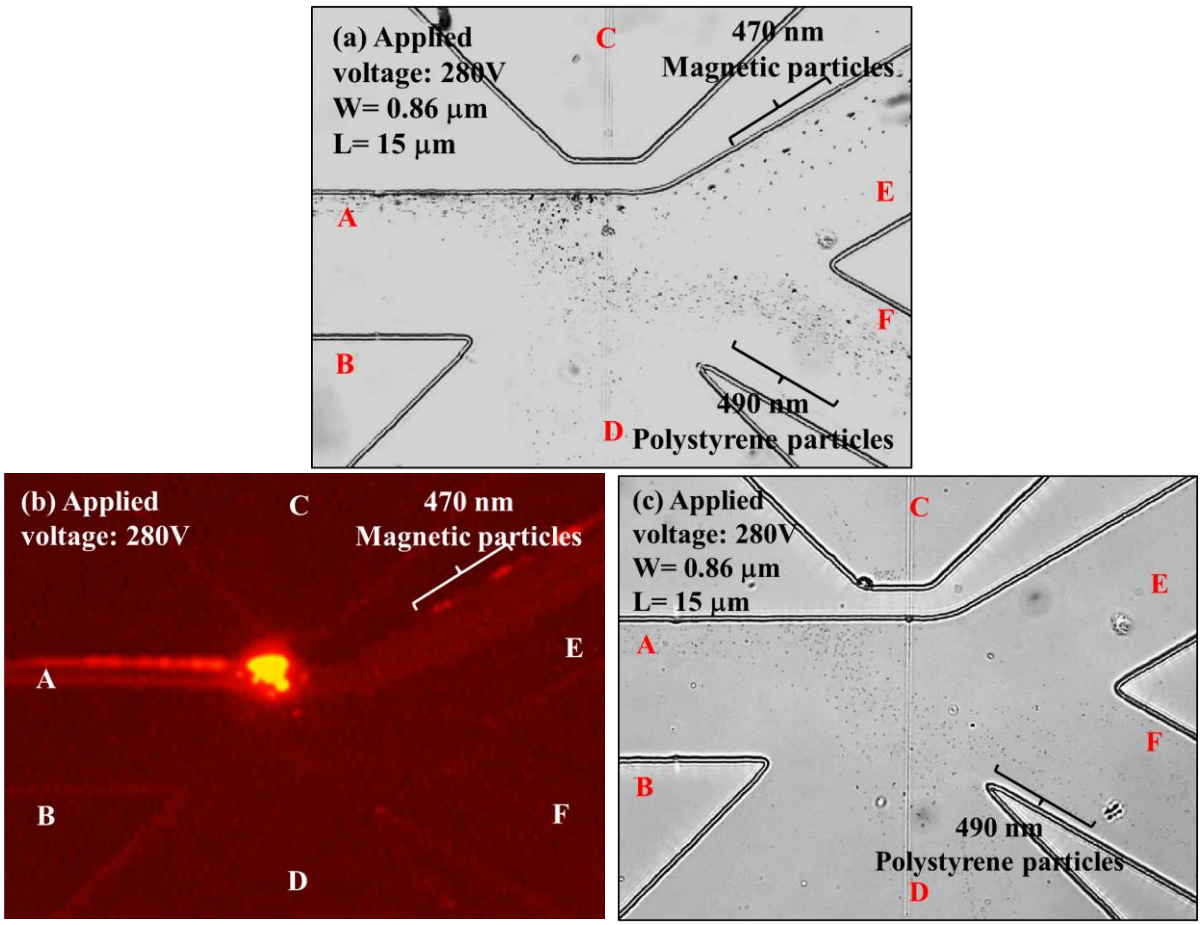

Figure 4-12 (a) Separation of 470 nm magnetic-coated particles and 490 nm plain polystyrene nanoparticles. (b) Fluorescent image shows the trajectories of the 470 nm fluorescent (red) magnetic-coated particles undergoing p-DEP. (c) Trajectories of 490 nm non-fluorescent polystyrene nanoparticles experiencing n-DEP. 280 V is applied to electrode C and electrode D is grounded. The width and length of the small orifice are 0.86 µm and 15 µm, respectively, and the width of the large orifice is 125 µm.

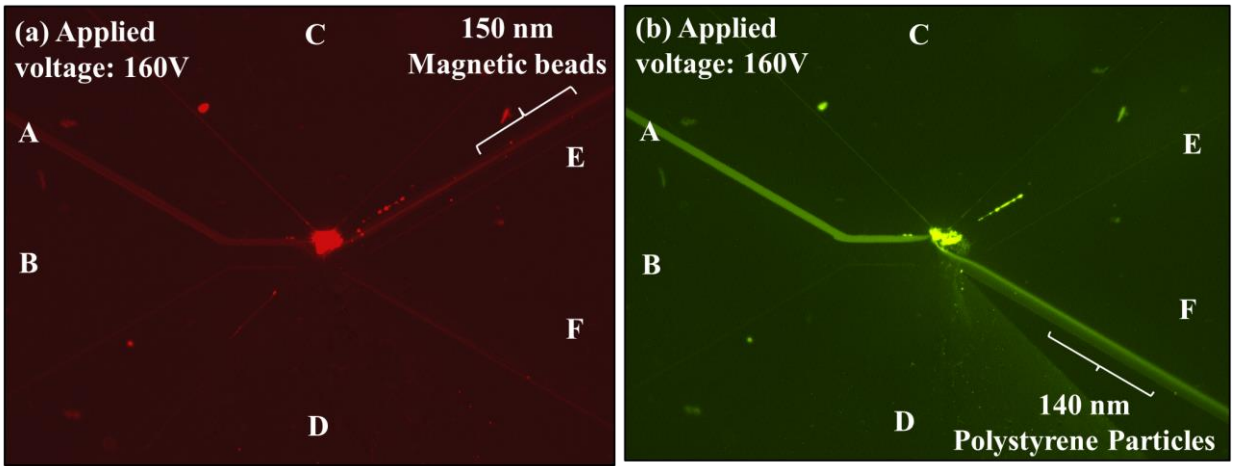

Figure 4-13 Separation of 140 nm green fluorescent polystyrene particles and 150 nm red fluorescent magnetic nanoparticles. (a) Fluorescent image shows the trajectories of the 150 nm fluorescent (red) magnetic nanoparticles experiencing p-DEP. (b) Fluorescent image shows the trajectories of the 140 nm fluorescent (green) magnetic nanoparticles experiencing n-DEP. 160 V is applied at electrode D. The width and length of the small orifice is 0.86 µm and 15 µm, respectively, and the width of the large orifice is 125 µm. (The bright dots along the boundary of the microchannel in both two figures are caused by the dust inside the channel).

As the particle size reduces to the nanometer, the DEP force exerted on the nanoparticles is significantly decreased. It should be realized that all these particles carry negative surface charges, and the ratio between the electrostatic force and the DEP force exerted on the particles can be increased by 10^3 times when the particle size reduces from micron scale to nanoscale [241]. If the electrode C is used as the positive electrode, the electrostatic attraction force (electrophoresis) on the negatively charged nanoparticles is in the opposite direction of the negative DEP force. Therefore, in order to enhance the separation effect, the polarity of the applied electric field is reversed (i.e., the electrode D is used as the positive electrode) for the separation of the smaller nanoparticles, i.e., the 140 nm polystyrene nanoparticles and the 150 nm magnetic nanoparticles. In this way, the direction of the electrophoretic motion of the nanoparticles is the same as that of the n-DEP, enhancing the separation of the nanoparticles undergoing negative DEP. As shown in Figure 4-13, the continuously flowing mixture of the 140 nm green fluorescent polystyrene particles and 150 nm red fluorescent magnetic nanoparticles were successfully separated. The polystyrene nanoparticles (green) were pushed away from the small orifice by the negative DEP force (and electrophoresis) and flowed into the branch channel F. The magnetic nanoparticles are attracted by the positive DEP force towards the vicinity of the small orifice and moved into the branch channel E. This indicated that the novel nano-orifice based DC-DEP separation method can be utilized to continuously separate small nanoparticles with similar size but different electric conductivities.

4.3 Manipulation of Janus particles

In the previous section, we have proposed a novel asymmetric orifice based method using DC-DEP for the separation of the isotropic particles in a microchannel and demonstrated that mixed nanoparticles of two different sizes or nanoparticles of similar size but different types can be continuously sorted and diverted into two individual channel branches. While in practice, we also need to manipulate the Janus particles which are anisotropic particles by using the same principle. The dielectrophoretic forces acting on Janus particles under DC electric field will be derived and the physical and mathematical models will be described in details. Then the results for the DC-dielectrophoretic manipulation of the Janus particles will be demonstrated [40].

4.3.1 DC-dielectrophoresis of Janus particles

The Janus polystyrene (PS) particle with one-half coated with a metal layer is shown in Figure 4-14.

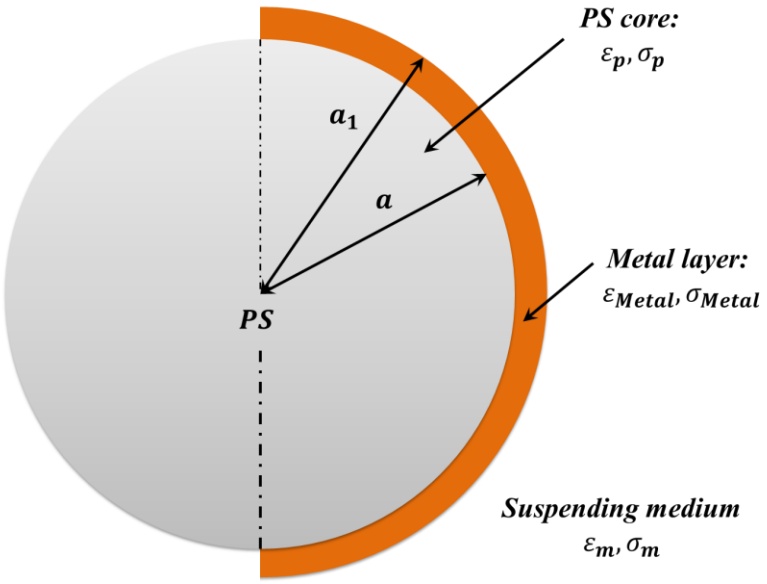

Figure 4-14 Schematic of a Janus particle with one hemisphere coated with a metal layer.

The dielectrophoretic movement of the Janus particles is the result of the combined DEP forces on the metal-coated PS (PS-Metal) hemisphere and on the untreated PS hemisphere, which is expressed as [263]

$$F_{DEP,Janus} = F_{DEP,PS} + F_{DEP,Metal} \tag{4-5}$$

Since the thickness of the metal coating can be negligible, compared with the micron-sized particle, the volume of the original polystyrene particle, with a radius of a, approximately equals to the total volume of a polystyrene sphere and a polystyrene sphere with the metal coating [263]

$$V = \frac{4}{3}\pi a^3 = V_{eff,PS} + V_{eff,Metal} = \frac{4}{3}\pi a_{eff,ps}^3 + \frac{4}{3}\pi a_{eff,Metal}^3 \tag{4-6}$$

where the $a_{eff,PS}$ and $a_{eff,PS-Metal}$ are the effective radii of the PS sphere and the PS-Metal sphere, respectively. If the volumetric percentage of the uncoated polystyrene part of the Janus particle is *K*, then *(1-K)* is the volumetric percentage of the part of the Janus particle with the metal coating.

$$V_{eff,PS} = K * V, V_{eff,PS-Metal} = (1-K) * V \tag{4-7a}$$

$$a_{eff,ps}^3 = K * a^3, a_{eff,ps-Metal}^3 = (1-K) * a^3 \tag{4-7b}$$

The surface area for the uncoated part of the Janus sphere can be written as:

$$S_{PS} = 4\pi a^2 - T * 4\pi a^2 \quad (4\text{-}8)$$

where *T* is the metal coating coverage on the Janus sphere. Moreover, the surface area for the uncoated part of the Janus sphere can also be expressed as

$$S_{PS} = 2\pi a h \quad (4\text{-}9)$$

where $h = (1 - T) \times 2a$. The corresponding volume of the uncoated part of the Janus sphere is expressed as

$$V_{PS} = \pi h^2 \left(a - \frac{h}{3}\right) = (1 - T)^2 \times 4\pi a^3 (1 - \frac{2(1 - T)}{3}) \quad (4\text{-}10)$$

Then

$$K = \frac{V_{PS}}{V} = \frac{T^2 * 4\pi a^3 (1 - \frac{2}{3}T)}{\frac{4\pi a^3}{3}} = 3(1 - T)^2 (1 - \frac{2(1 - T)}{3}) \quad (4\text{-}11)$$

In this way, when the metal coating coverage T is given, the corresponding volumetric percentage K will be known, hence the effective radii of the PS sphere and the PS-Metal sphere. The overall DEP force applied on the Janus particle can be written as:

$$\begin{aligned} F_{DEP,Janus} &= F_{DEP,PS} + F_{DEP,PS-Metal} \quad (4\text{-}12) \\ &= 2\pi\varepsilon_m \left[a_{eff,ps}^3 * Re\left(f_{CM,PS}\right) + a_{eff,ps-Metal}^3 \right. \\ &\left. * Re\left(f_{CM,PS-Metal}\right)\right](\nabla|\boldsymbol{E}|^2) \\ &= 2\pi\varepsilon_m a^3 \left[K * Re\left(f_{CM,PS}\right) + (1 - K) * Re\left(f_{CM,PS-Metal}\right)\right](\nabla|\boldsymbol{E}|^2) \end{aligned}$$

where the effective CM factor for the Janus particle can be described as

$$Re\left(f_{CM,Janus}\right) = KRe\left(f_{CM,PS}\right) + (1 - K)Re\left(f_{CM,PS-Metal}\right) \quad (4\text{-}13)$$

In Equation (4-12), the CM factor for the polystyrene sphere is calculated by

$$f_{CM,PS} = (\frac{\varepsilon_p^* - \varepsilon_m^*}{\varepsilon_p^* + 2\varepsilon_m^*}) \quad (4\text{-}14)$$

while the CM factor for the PS-Metal sphere can be expressed, based on a shell model, [60] as:

$$f_{CM,PS-Metal} = (\frac{\varepsilon_{PS-Metal}^* - \varepsilon_m^*}{\varepsilon_{PS-Metal}^* + 2\varepsilon_m^*}) \quad (4\text{-}15a)$$

$$\varepsilon^*_{PS-Metal} = \varepsilon^*_{Metal}\left[\gamma_{12}^3 + 2(\frac{\varepsilon^*_p - \varepsilon^*_{Metal}}{\varepsilon^*_p + \varepsilon^*_{Metal}})\right]\Big/\left[\gamma_{12}^3 - (\frac{\varepsilon^*_p - \varepsilon^*_{Metal}}{\varepsilon^*_p + \varepsilon^*_{Metal}})\right] \quad (4\text{-}15b)$$

where the factor $\gamma_{12} = a_1/a$, and a_1 is the radius of the PS sphere with the metal coating, and a is the radius of the polystyrene sphere. When the DC electric fields are applied, the $f_{CM,Janus}$ becomes dependent only on the conductivity of the particle and the suspending medium, and can be described as

$$f_{CM,Janus} = K\frac{\sigma_p - \sigma_m}{\sigma_p + 2\sigma_m} + (1-K)\frac{\sigma_{PS-Metal} - \sigma_m}{\sigma_{PS-Metal} + 2\sigma_m} \quad (4\text{-}16)$$

where $\sigma_{PS-Metal} = \sigma_{Metal}\left[\gamma_{12}^3 + 2(\frac{\sigma_p - \sigma_{Metal}}{\sigma_p + 2\sigma_{Metal}})\right]\Big/\left[\gamma_{12}^3 - (\frac{\sigma_p - \sigma_{Metal}}{\sigma_p + 2\sigma_{Metal}})\right]$. The electric conductivity of the particles could be calculated by the surface conductance, $\sigma_p = \sigma_b + \frac{2K_s}{a}$. The value of the bulk conductivity σ_b is negligible and the surface conductance $K_s = 1\ nS$ for polystyrene particles [278]. Therefore, based on the values of $f_{CM,Janus}$, different DEP behaviors of the Janus particle can be predicted. If $f_{CM,Janus} < 0$, the Janus par- ticles will be repelled by the negative DEP forces away from the location where the maximum electric field exists. While if $f_{CM,Janus} > 0$, positive DEP will attract the Janus particles towards the high electric filed region. Finally, the DEP force acting on the Janus particle under DC electric fields is expressed as

$$F_{DEP,Janus} = 2\pi\varepsilon_m a^3\left[K\frac{\sigma_p - \sigma_m}{\sigma_p + 2\sigma_m} + (1-K)\frac{\sigma_{PS-Metal} - \sigma_m}{\sigma_{PS-Metal} + 2\sigma_m}\right](\nabla|E|^2) \quad (4\text{-}17)$$

It can be seen from Equation (4-17) that the value of the DEP force is proportional to the particle size (a^3) and the gradient of the electric fields squared ($\nabla|E|^2$), and the DEP behaviors of the Janus particles and the direction of the particles' motion are determined by the $f_{CM,Janus}$. The Janus particles with different sizes will be separated and directed into different trajectories. Furthermore, it also can be inferred from Equation (4-11) and Equation (4-16) that the $f_{CM,Janus}$ is determined by the metal coating coverage, thickness, and electric conductivity of the Janus particles. Therefore, by choosing the suspending solution with a certain electric conductivity, the Janus particles of the same size but different $f_{CM,Janus}$, can experience negative and positive DEP, respectively, and can be separated.

4.3.2 Physical and mathematical models

Figure 4-15 shows the top view of the 2-D geometrical model of the orifice based DC-DEP microchannel. This channel consists of the main channel with a length of 300 μm and a width of 80 μm and six branch channels. The sample inlet channel (A) has a length of 300 μm and a width of 20 μm, the flow focusing inlet channel (B) has a length of 340 μm and a width of 80 μm , two channels connect the two

orifices to two wells for placing the external electrodes, the small orifice has a length of 2.5 μm and a width of 800 nm and the large orifice has a width of 100 μm, and two outlet channels (E and F) have a length of 340 μm and a width of 80 μm . The angle between the inlet channels (A and B) and the main channel is 45°, which is the same for that between the main channel and the outlet channels (E and F). Pressure-driven flows are applied to bring the mixed Janus particles and the homogeneous polystyrene particles from channel A and the focusing stream from channel B into the main channel. The particles are forced by the focusing stream to move close to the sidewall that has the small orifice. By applying a DC voltage on the external electrodes suspending in wells C and D across the microchannel, a strong non-uniform electric field gradient is generated in the vicinity of the smaller orifice. The particles passing through this region will experience the DEP forces and their trajectories will change. For the particles with $f_{CM,Janus} < 0$, they will experience the negative DEP forces and be repelled away from the smaller orifice, i.e., the electric field maximum, and flow into channel F. While for the particles with $f_{CM,Janus} > 0$, they will be attracted towards the smaller orifice and move into channel E.

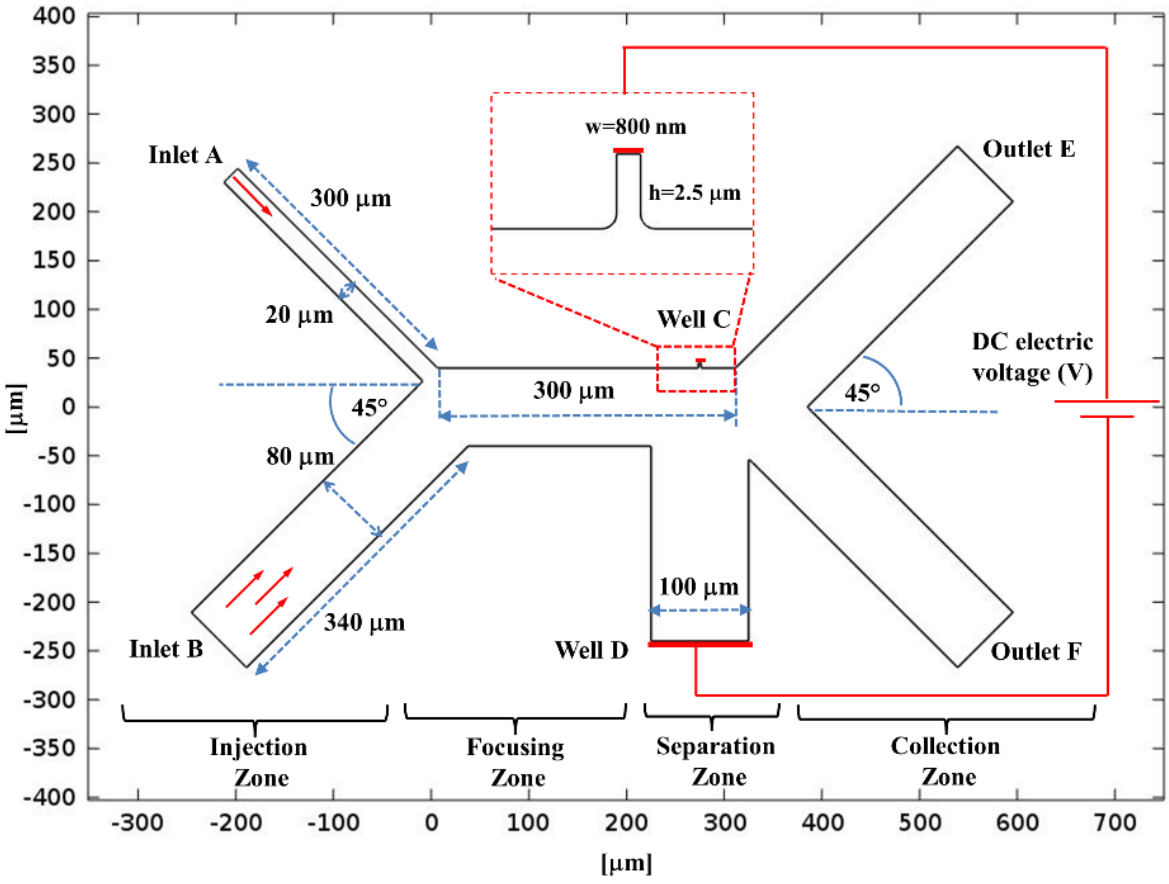

Figure 4-15 Schematic illustration of the asymmetric orifice based DC-DEP microchannel.

4.3.2.1 Electric field

As shown in Figure 4-15, the electric potential is applied across the microchannel via the smaller orifice to the large micro-orifice. The distribution of the applied electric field φ is governed by the Laplace's equation

$$\nabla^2\varphi = 0 \qquad (4\text{-}18)$$

and the non-conducting boundary conditions at the microchannel walls except the orifice areas, as well as specific electrical potentials applied at the external electrodes

$$\varphi = V_1 \text{ at the nano orifice} \qquad (4\text{-}19a)$$

$$\varphi = 0\ V \text{ at the large orifice} \qquad (4\text{-}19b)$$

$$\hat{n}(\nabla\varphi) = 0 \quad \text{at channel walls} \qquad (4\text{-}19c)$$

where $\hat{n}$ is the unit normal vector at the microchannel wall.

4.3.2.2 Flow field

As the liquid flow in the microchannel is considered as an incompressible laminar flow, the flow field is governed by the Navier-Stokes equation

$$\rho\left[\frac{\partial\vec{u}}{\partial t} + \vec{u}\cdot\nabla\vec{u}\right] = -\nabla P + \mu\nabla^2\vec{u} \qquad (4\text{-}20a)$$

and the continuity equation

$$\nabla\cdot\vec{u} = 0 \qquad (4\text{-}20b)$$

where $\vec{u}$ is the velocity vector, ρ and μ are the density and viscosity of the solution, t is the time, and ∇P is the pressure gradient. As it is a steady flow, the flow field does not change over time, then the $\frac{\partial\vec{u}}{\partial t}$ term in Equation (4-20a) is negligible. Moreover, as the velocity of the flow inside the microchannel is very low, the inertia term $\vec{u}\cdot\nabla\vec{u}$ can also be neglected. The non-slip boundary condition at the microchannel walls is described by Equation (4-19c). The inlets and outlet of the microchannels are set with specific velocity values.

$$u = u_1 \text{ at the inlets} \qquad (4\text{-}21a)$$

$$P = 0 \text{ at the outlets} \quad (4\text{-}21b)$$

$$\vec{u} = 0 \text{ at channels walls} \quad (4\text{-}21c)$$

4.3.2.3 Particle tracing

In order to trace of trajectories of the Janus particles moving in the liquid, the particle motion is considered to be coupled with the electric fields and flow fields. The particles' motion is governed by Newton's second law [66,279]

$$m_p \frac{d\vec{v}}{dt} = \vec{F}_t \quad (4\text{-}22)$$

where m_p and $\vec{v}$ are the particle mass and velocity, respectively, $\vec{F}_t$ is the net force which includes the viscous drag force and the DEP force.

Due to the fluid viscosity, the drag force is exerting on the particles when moving in the fluid flow. For laminar flow, the drag force on the particles is known as Stokes drag law and is described as

$$\vec{F}_{drag} = \frac{1}{\tau_p} m_p(\vec{u} - \vec{v}) \quad (4\text{-}23a)$$

$$\tau_p = \frac{2\rho_p r^2}{9\mu} \quad (4\text{-}23b)$$

where μ is the fluid dynamic viscosity, and ρ_p and r are the density and radius of the particle, respectively.

The dielectrophoretic force exerted on the Janus particles is given by:

$$F_{DEP,Janus} = 2\pi\varepsilon_m a^3 \left[K \frac{\sigma_p - \sigma_m}{\sigma_p + 2\sigma_m} + (1 - K) \frac{\sigma_{PS-Metal} - \sigma_m}{\sigma_{PS-Metal} + 2\sigma_m} \right] (\nabla |E|^2) \quad (4\text{-}24)$$

where $K = 3(1-T)^2(1 - \frac{2(1-T)}{3})$ and T is the coating coverage.

In this study, commercial software COMSOL 4.3b was used to solve the above-mentioned equations and boundary conditions, and to conduct the numerical simulations of the continuous separation of the Janus particles and the homogeneous particles. Firstly, the flow field and the DC electric field were computed using a stationary solver. Then, the mixed particles were intruded into the microchannel using the particle tracing module. The particle trajectories with the effects of the DEP forces were solved in the computation. In order to study the various effects, i.e., the strength of the electric fields, as well as the gold-coating coverage, thickness, and electric conductivity of the Janus particles, on the trajectories of the Janus particles, extensive numerical simulations are conducted and analyzed. The number of the meshed triangle

elements is 59178 and the boundary elements are 1958, in order to achieve the mesh independent results. The values of the parameters used in the simulation are shown in Table 4-4.

Table 4-4 Values of parameters used in the simulation.

Parameters	Values
Dielectric constant of water, ε_w	80
Permittivity of vacuum, ε_0 (F/m)	8.85×10^{-12}
Density of water, ρ_w (kg/m^3)	1000
Dynamic viscosity of water, μ_w (Pa·s)	1×10^{-3}
Density of particle, ρ_p (kg/m^3)	1050
Electric conductivity of 3 μm polystyrene particle, σ_1 (S/m) [241]	1.3×10^{-3}
Electric conductivity of 5 μm polystyrene particle, σ_2 (S/m)	0.8×10^{-3}
Electric conductivity of gold coating, σ_{Au} (S/m) [263]	4.5×10^{7}
Length of the main channel and microchannel A (μm)	300
Length of microchannel B, E, and F (μm)	340
Width of microchannel A (μm)	20
Width of the main channel and microchannel B, E and F (μm)	80
Inlet velocity of microchannel A and B, u_1 (μm)	800

4.3.3 Results and discussion

4.3.3.1 Effect of the applied voltage

The effect of the strength of the electric field on the separation of 3 μm and 5 μm Janus particles with 25% gold coverage was investigated by applying different electric voltages at electrodes C from 120 V to 290 V. The electrode D is grounded. The electric conductivity of the suspending medium is used as $\sigma_m = 5 \times 10^{-2}$ S/m, and the thickness of the gold coating is assumed as 100 nm and the conductivity of the gold coating is $\sigma_{Au} = 4.5 \times 10^7$ S/m. As shown in Figure 4, the trajectories of 3 μm and 5 μm Janus particles with 25% gold coverage varies with the applied electric field.

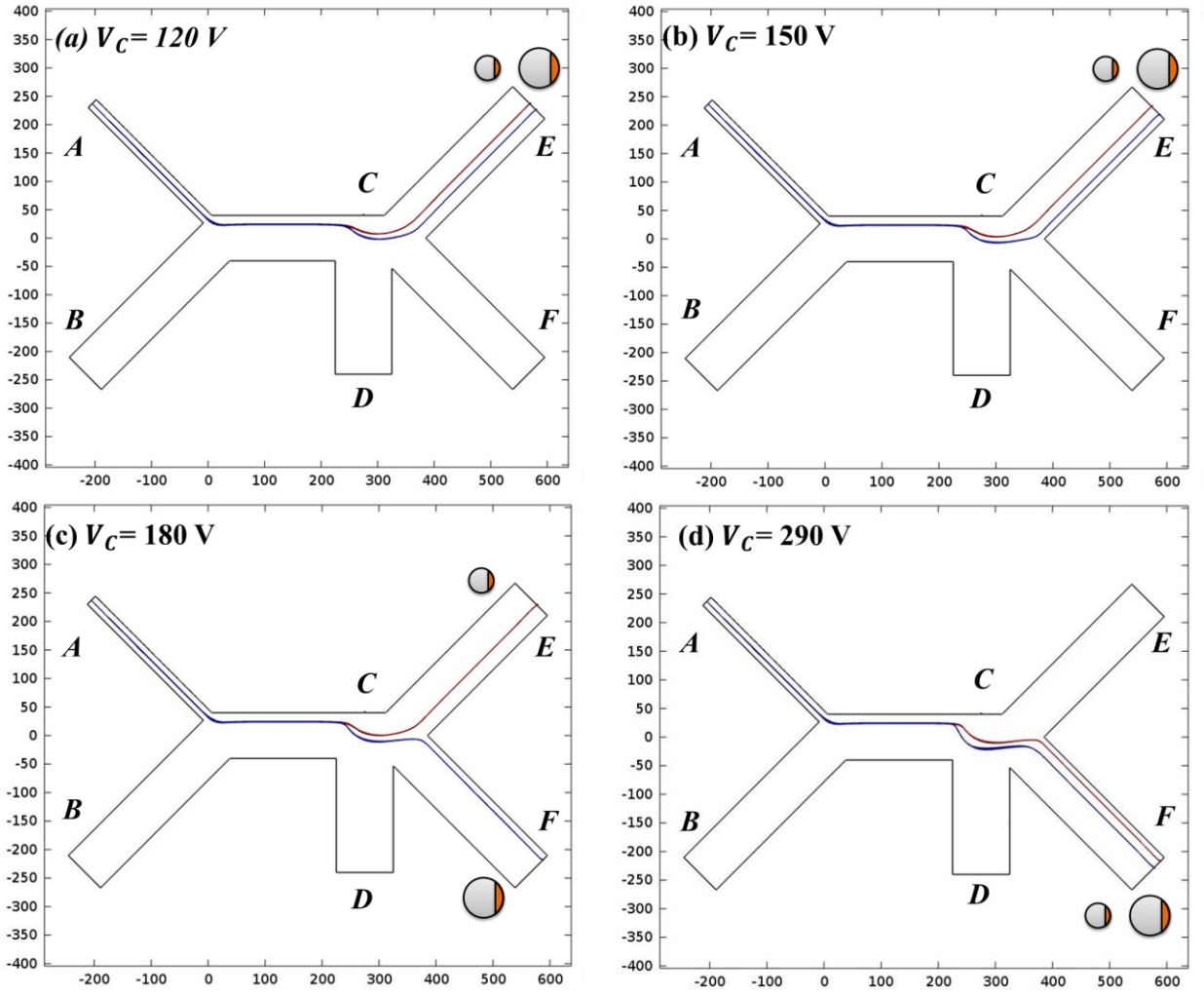

Figure 4-16 Variation of the trajectories of the 3 μm and 5 μm Janus particles with 25% gold coverage with the voltages applied at electrode C while electrode D is grounded. The electric conductivity of the suspending medium is $\sigma_m=5\times10^{-2}$ *S/m in all cases.*

As shown in Figure 4-16, the mixed 3 μm and 5 μm Janus particles with 25% gold coverage experience negative DEP forces. As indicated by Equation (4-17), the magnitude of the DEP force is proportional to the gradient of the electric field squared $\nabla|E|^2$ and the size of the particle (a^3). The DEP forces exerting on the particles will increase as the applied electric voltages increase. Moreover, the magnitude of the DEP forces acting on the 5 μm Janus particles are approximately 5 times stronger than that on the 3 μm Janus particles, leading to larger trajectory shifts. It can be seen from Figure 4-16(a), due to the weak DEP forces when 120 volts is applied, the trajectory shifts of the large Janus particles and the small Janus particles after passing through the vicinity of the nano-orifice are not large enough and the large and the small particles moved into the same outlet channel E. As shown in Figure 4-16(b), when the voltage is increased to 150 volts, a larger trajectory shift is induced by the stronger DEP forces. However, the small Janus particles and

large Janus particles still flowed into the outlet channel E. When increasing the applied voltage to 180 volts as shown in Figure 4-16(c), a significant trajectory shift is generated for the large Janus particle by the stronger DEP force at the nano-orifice region. In this way, the separation of 3 μm and 5 μm Janus particles with 25% gold coverage was achieved and they were directed into different outlet channels E and F, respectively. As shown in Figure 4-16(d), the desired separation of large Janus particles and small Janus particles into distinct outlets cannot be accomplished with the further increased applied voltage. Under 290 volts, the large Janus particles and small Janus particles both are repelled into outlet channel F by the overly stronger DEP forces.

4.3.3.2 Effect of gold coating coverage

The CM factors for 5 μm polystyrene-based Janus particles with various different gold coating coverage as a function of the electric conductivity of the suspending medium is shown in Figure 4-17. The thickness of the gold coating is assumed as 100 nm and the electric conductivity of the gold coating is σ_{Au}=4.5×10^7 S/m [263]. Moreover, the separation of the 5 μm Janus particles with 75% gold coverage from 5 μm homogeneous polystyrene particles, as well as the separation of 5 μm Janus particles with 25% and 75% gold coverage are shown in Figure 4-18. The electric conductivity of the suspending medium is utilized as σ_m=5×10^{-2} S/m.

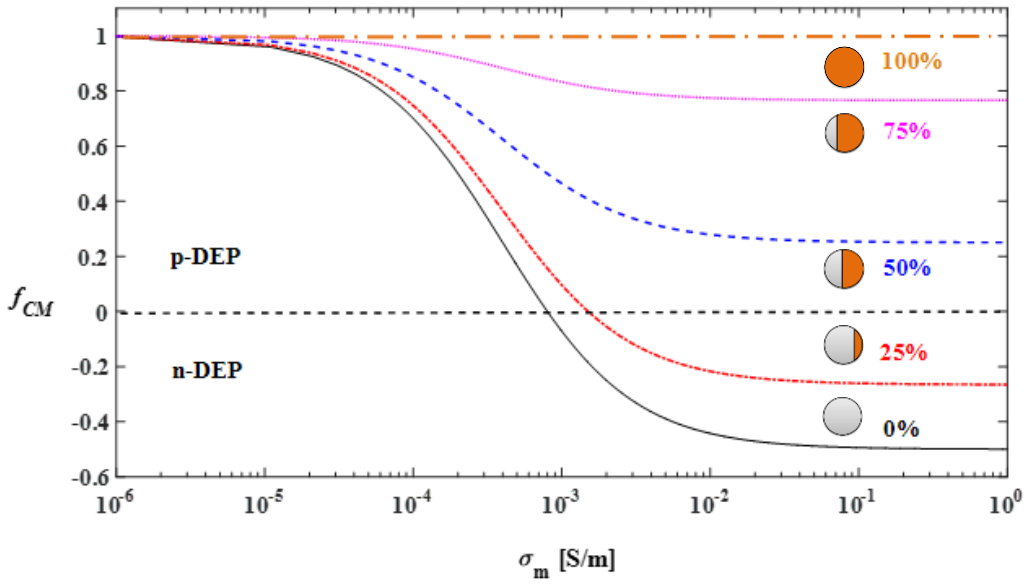

Figure 4-17 Value of $f_{CM,Janus}$ for the 5 μm polystyrene-based Janus particles with five different gold coverage: 0%, 25%, 50%, 75%, 100%, as a function of the electric conductivity of the suspending solution σ_m. The thickness of the gold coating is assumed as 100 nm.

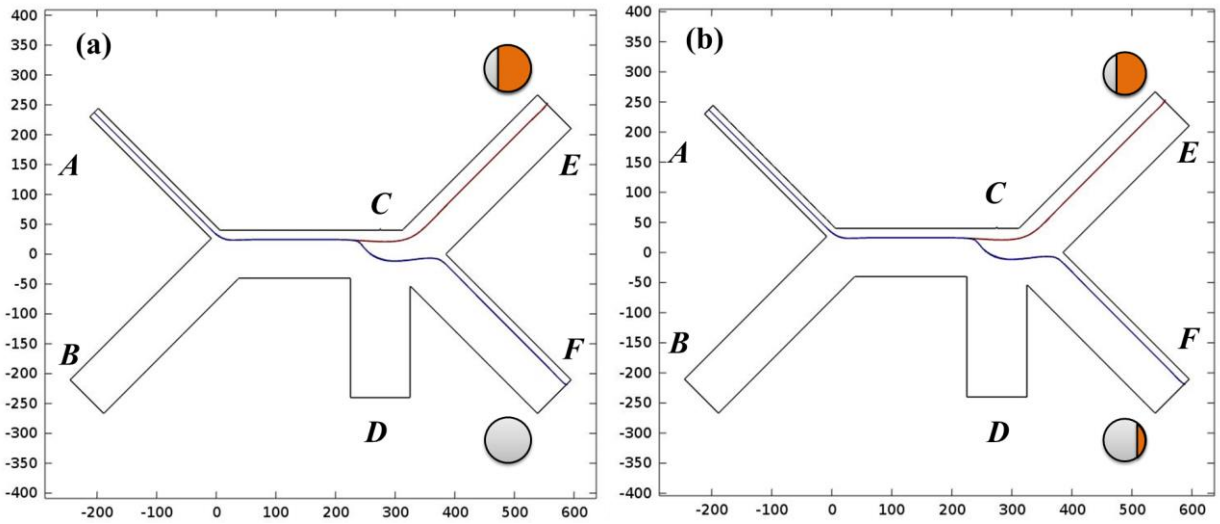

Figure 4-18 (a) Separation of 5 μm Janus particles with 75% gold coverage ($f_{CM,Janus}$=0.7675) and 5 μm homogeneous polystyrene particles ($f_{CM,Janus}$=−0.4881). (b) Separation of 5 μm Janus particles with 25% ($f_{CM,Janus}$=−0.2556) and 75% ($f_{CM,Janus}$=0.7675) gold coverage. 180 volts is applied at electrode C and electrode D is grounded. The electric conductivity of the suspending medium is σ_m=5×10^{-2} S/m, and the thickness of the gold coating is assumed as 100 nm.

It can be seen from Figure 4-17, by using a specific suspending medium, i.e., σ_m=5×10^{-2} S/m, the separation of the 5 μm Janus particles with 75% gold coverage and 5 μm homogeneous polystyrene particles, as well as the separation of 5 μm Janus particles with 25% and 75% gold coverage can be achieved based on their different dielectrophoretic behaviors, i.e., the homogeneous polystyrene particles and the Janus particles with 25% gold coverage experience negative DEP, while Janus particles with 75% gold coverage experience positive DEP. As inferred from Equation (4-17), the sign of the DEP force is determined by the value of the CM factor. The Janus particles will experience negative DEP forces if $f_{CM,Janus} < 0$, while if $f_{CM,Janus} > 0$ the Janus particles will undergo positive DEP effects. It can be seen from Figure 4-18(a), the mixture of the Janus particles with 75% gold coverage and homogeneous polystyrene particles is forced to move closely to the nano-orifice. As the values of the CM factors for the Janus particles with 75% gold coverage and the homogeneous polystyrene particles are 0.7675 and −0.4881, respectively, the Janus particles with 75% gold coverage experience positive DEP force, and are attracted towards the maximum electric field region and move into outlet branch E. While the homogeneous polystyrene particles are pushed away from the nano-orifice by the negative DEP force and flow into outlet branch F. Furthermore, as shown in Figure 4-18(b), the mixed sample of Janus particles with 25% and 75% gold coverage are well separated by the positive DEP force on the Janus particles with 75% gold coverage and by the negative DEP force on the Janus particles with 25% gold coverage and then move into outlet E and F, respectively.

4.3.3.3 Effect of gold coating thickness

The CM factors for the 5 μm polystyrene-based Janus particles with 25% gold coverage but different gold coating thicknesses as a function of the electric conductivity of the suspending medium is shown in Figure 4-19. The electric conductivity of the gold coating is σ_{Au}=4.5×10^7 S/m. As shown in Figure 4-19, the $f_{CM,Janus}$ values for the Janus particles with five different gold coating thicknesses are essentially identical. Therefore, the Janus particles with different coating thicknesses will experience the same DEP effect for a given electric conductivity of the suspending medium. The effect of the coating thickness of the Janus particles on their trajectories can be considered negligible when using DC-DEP method.

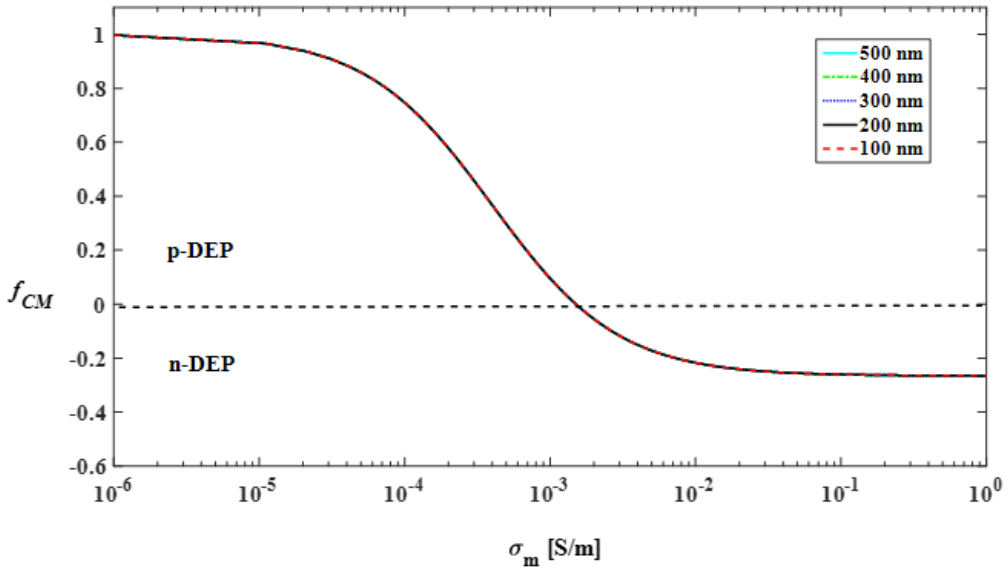

Figure 4-19 Value of $f_{CM,Janus}$ for the 5 μm Janus particles with 25% gold coverage but five different gold coating thicknesses: 100 nm, 200 nm, 300 nm, 400 nm, and 500 nm, as a function of the electric conductivity of the suspending solution σ_m. The electric conductivity of the gold coating is σ_{Au} =4.5×10^7 S/m.

4.3.3.4 Effect of electric conductivity of coating material

The CM factors for the 5 μm polystyrene-based Janus particles with 25% coating coverage but different electric conductivities of the coating material as a function of the electric conductivity of the suspending medium are shown in Figure 4-20. The coating thickness is assumed as 100 nm,

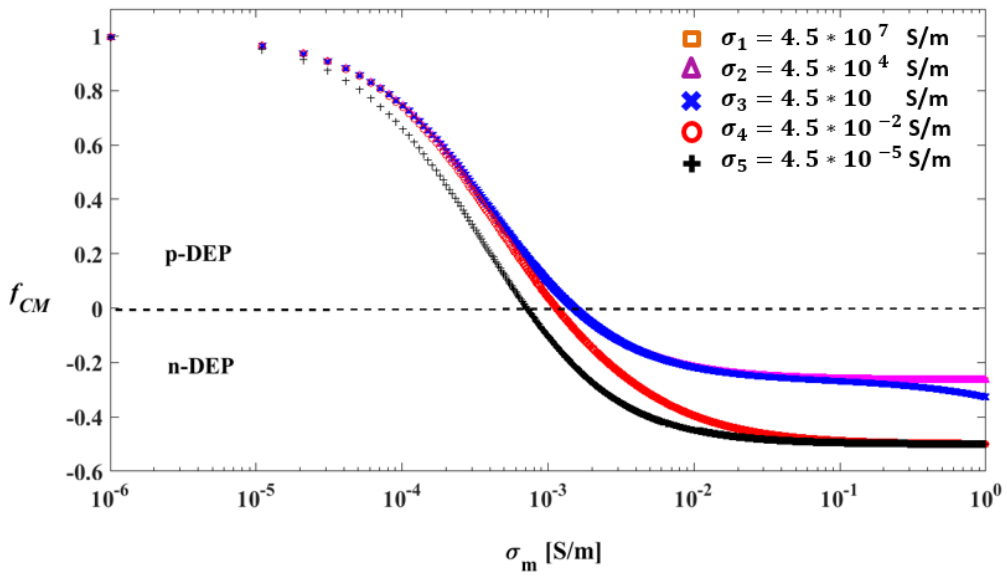

Figure 4-20 Value of $f_{CM,Janus}$ for the 5 μm polystyrene-based Janus particles with 25% coating coverage but five different coating electric conductivities: σ_1 =4.5×10^7 S/m, σ_2 =4.5×10^4 S/m, σ_3 =4.5×10 S/m, σ_4 =4.5×10^{-2} S/m, and σ_5 =4.5×10^{-5} S/m, as a function of the electric conductivity of the suspending solution σ_m. The coating thickness is 100 nm.

It can be inferred from Figure 4-20 that there are some differences in the $f_{CM,Janus}$ value for the Janus particles with different coating materials, i.e., different electric conductivities. Compared with the Janus particles with more conductive coating materials, the Janus particles with less conductive coating materials show relatively smaller $f_{CM,Janus}$ values when the electric conductivity of the suspending medium is selected. Furthermore, under a certain electric conductivity of the suspending medium, the Janus particles with different coating electric conductivities will exhibit different dielectrophoretic behaviors. For example, as shown in Figure 4-20, when the electric conductivity of the suspending medium is selected as σ_m=1×10^{-3} S/m, the Janus particles with a coating electric conductivity σ_1=4.5×10^7 S/m experience positive DEP, while the Janus particles with a coating electric conductivity σ_5=4.5×10^{-5} S/m experience negative DEP. Thus, these two types of Janus particles may be separated by the DC-DEP method described in this paper. As shown in Figure 4-21, the mixed Janus particles with two different coating electric conductivities are introduced into the main channel from inlet branch A and driven to flow along the sidewall of the channel to pass the region of the nano-orifice. The Janus particles with coating electric conductivity σ_1=4.5×10^7 S/m (i.e., $f_{CM,Janus}$=0.0960) experience positive DEP and always move to the outlet channel E. The Janus particles with coating electric conductivity σ_5=4.5×10^{-5} S/m (i.e., $f_{CM,Janus}$−0.0946) experience negative DEP and are pushed away from the nano-orifice region. When the applied electric field is sufficiently large,

i.e., V_c > 180 V in this case, the trajectory shifts of the Janus particles experiencing negative DEP are sufficiently large, these particles move into the outlet channel F and, in this way, they are separated from the particles experiencing positive DEP.

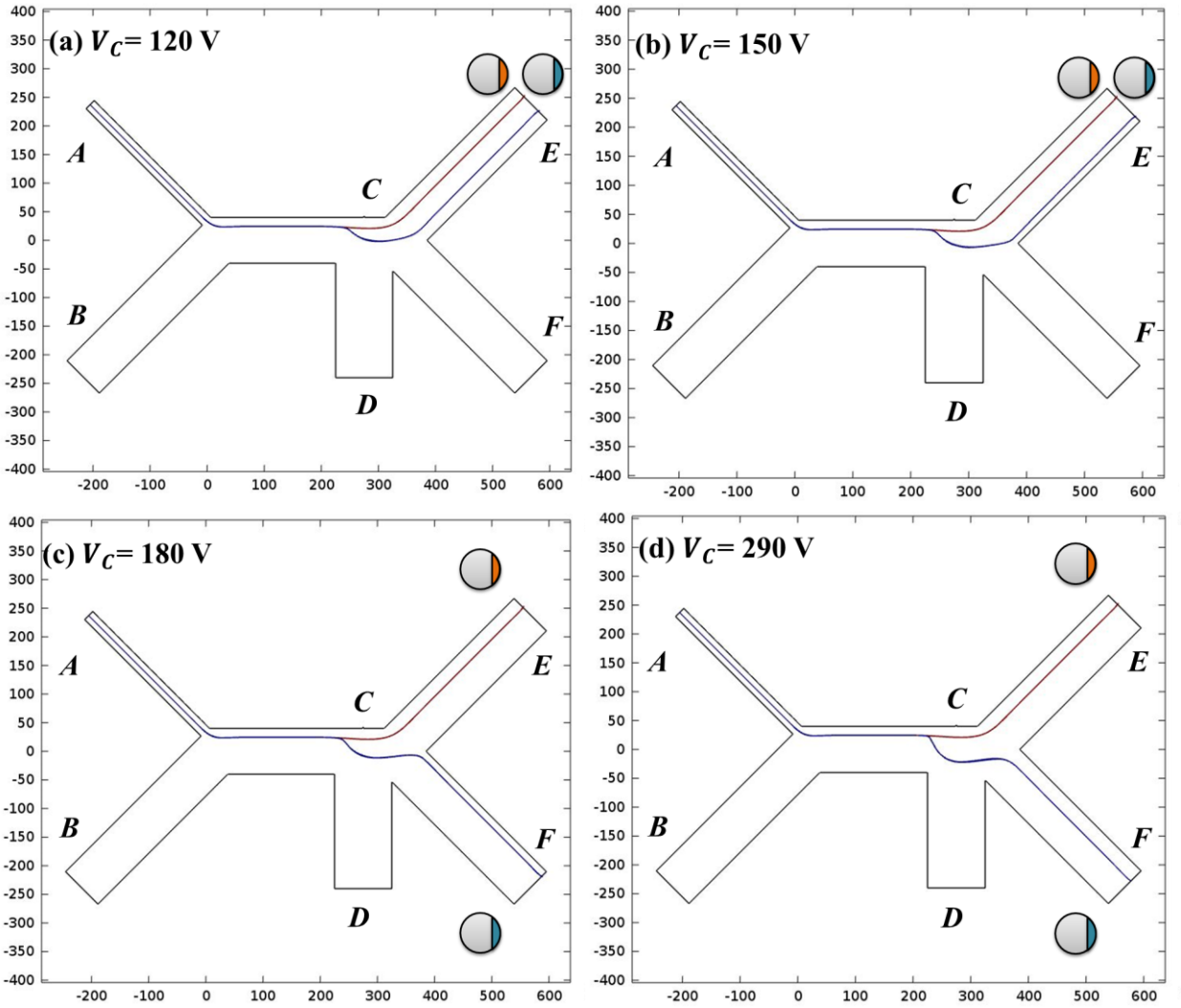

Figure 4-21 Trajectories of 5 μm Janus particles with a coating electric conductivity σ_1 =4.5×10^7 S/m ($f_{CM,Janus}$=0.0960) and 5 μm Janus particles with a coating electric conductivity σ_5 =4.5×10^{-5} S/m ($f_{CM,Janus}$=−0.0946) with different voltages applied at C while D is grounded. The electric conductivity of the suspending medium is selected as σ_m =1×10^{-3} S/m, and the coating thickness is 100 nm.

4.4 Conclusion

A new DC-DEP microfluidic device is developed for continuously separating particles with similar size but different electric conductivities. A novel nano-orifice based DC-DEP method for continuous size-dependent separation of isotropic micro and nanoparticles and the separation of similar size nanoparticles

by type, and numerical manipulation of the polystyrene-based Janus particles under DC electric fields in a pressure-driven flow is developed. The motion of particles is controlled by the pressure-driven flow, and in order to induce sufficient DEP forces, the strong non-uniform electric field is generated by applying a small DC electric voltage across the microchannel via a pair of asymmetric orifices, i.e. a nano-orifice and a micron orifice on the opposite sidewalls of the channel. The particle mixture experiences a DEP force when passing through the vicinity of the small orifice where the strongest electric field gradient exists and the mixed particles are separated into two different streams and moved into two individual outlet channels. The effects of key parameters such as electric field and the width and length of the small orifice were investigated experimentally in this study. By choosing an appropriately large width ratio of the nano-orifice and the micron orifice and a shorter small orifice, the sufficiently strong gradient of the electric field and hence sufficiently large DEP forces are generated, which enables the manipulation and separation of smaller micron and nano-sized particles and particles with the smaller size difference. By adjusting the applied electrical voltage and the electrical conductivity of the suspending solution, this new method is able to achieve the separation of nanoparticles as small as 51 nm and 140 nm in diameter, i.e. with a size difference of 90 nm, as well as the separation of smaller nanoparticles (e.g., 140 nm) with similar sizes but different electric properties. In order to further understand the dielectrophoretic motion of the Janus particles under DC electric field, the DC-DEP force acting on the Janus particles is derived and analyzed. To assess the different DEP behaviors of the Janus particles, the Clausius–Mossotti factors of the Janus particles, in terms of the electrical conductivity of the suspending solution, are studied. Furthermore, the successful size-dependent separation of 3 μm and 5 μm Janus particles and the different DEP effects-based separation of the 5 μm Janus particles and homogeneous polystyrene particles by choosing the suspending medium with a specific electric conductivity are demonstrated. By adjusting the electrical conductivity of the suspending solution, the Janus particles of the same size but different electric properties show different dielectrophoretic behaviors, i.e. one kind of the Janus particles experiencing positive DEP and another undergoing negative DEP, respectively. Thus this novel nano-orifice based DC-DEP method can be utilized for the separation of Janus particles with the same size by dielectric property. In addition, the effects of the strength of the electric fields, as well as the coating coverage, thickness and materials of the Janus particles on their dielectrophoretic behaviors and trajectories are systemically studied. Then, the effect of the coating thickness of the Janus particles on their dielectrophoretic behaviors and trajectories is negligible when using the DC-DEP method. The Janus particles with gold coating coverage over 50% will experience positive DEP effects. The asymmetric orifice based DC-DEP microfluidic device developed in this work shows advantages of simplicity of fabrication, ability to a strong gradient of the non-uniform electric field, and capability of sorting nanoparticles and manipulating Janus particles. Therefore, in the asymmetric orifice based DC-DEP microfluidic chip, the separation sensitivity and resolution depends on the applied electrical

voltage, the pressure-driven flow rate, the width and length of the small orifice, and the width ratio between the small orifice and the micron large orifice. Based on different targeted particles, all these parameters can be optimized both numerically and experimentally to achieve successful DC-DEP manipulation and sorting of particles.

CHAPTER 5 Continuous Manipulation and Sorting of Microemulsion Droplets by DC-DEP‡

5.1 Introduction

According to the previous investigation in CHAPTER 4, we found that the asymmetric-orifices based DC-DEP method could be employed to change the movement trajectory of the isotropic micron and nanoparticles based on their sizes and types, and the anisotropic Janus particles according to their different Clausius–Mossotti factors, i.e., different DEP behaviors. As an extension of the asymmetric-orifices based DC-DEP microfluidic system, we further demonstrate the practical applications of the manipulation and sorting of the oil and ionic liquid-in-water microemulsion droplets in the microchannel.

Microemulsions are the liquid droplets, which are dispersed in an immiscible liquid and have been versatile tools in chemical, biological, as well as medical fields. The emulsion droplets are applicable for the fabrication of solid particles [280–282], encapsulation, and screening of cells and DNA [283–287], as well as drug delivery and screening [288]. Generally, the microemulsion is a system of water, oil, and amphiphiles. The water-in-oil emulsions are used for the transportation of oil-soluble drugs, while the oil-in-water microemulsions are suitable for the water-soluble ones [289]. For the applications which are impossible with the conventional water-oil microemulsions, ionic liquids (ILs) have been employed. The IL droplets have led to the development of many new applications in colloid and interface science [290]. ILs are salts with melting points below 100 °C and consist of organic cation and inorganic or organic anion [291,292]. Since they are liquid at room temperature and have excellent solubility in various organic and inorganic compounds [293], the ILs can be formulated to be hydrophobic or hydrophilic and serve as the solvents for various reactions [294]. Due to the diverse structure and unique physicochemical properties [295,296], i.e., insignificant vapor pressure and excellent biochemical stability [289,297], ILs are applied in a variety of fields such as separation [293], electrochemistry [298,299], chemical engineering [300–309] and biotechnology [310–313]. Because of the favorable physical and chemical properties of the ILs, they are proved to be excellent solvents, leading to improved separation efficiency of metal ions or biomolecules from different media [314–319]. As the droplets have good compatibility with many chemical and biological reagents, the droplet-based microfluidic

‡ A similar version of this chapter was published as:
(a) Zhao, K.; Li, D. Manipulation and separation of oil droplets by using asymmetric nano-orifice induced DC dielectrophoretic method. Journal of colloid and interface science 2018, 512, 389-397. https://www.sciencedirect.com/science/article/pii/S0021979717312390.
(b) Zhao, K.; Li, D. Direct current dielectrophoretic manipulation of the ionic liquid droplets in water. Journal of Chromatography A 2018, 1558, 96-106. https://www.sciencedirect.com/science/article/pii/S0021967318305922.

technology enables the field of single-cell biology [320,321], and the droplets can function as individual microreactors and serve as carriers with a variety of kinds of biochemical reactions [322–324]. Due to the dimensional scaling benefits, the reactions of fluids in the droplet is controllable and rapid, resulting in reduced reagent consumption and high manipulation efficiencies [325]. Generally, the droplet microfluidic involves the production and manipulation of the individual droplet in the microchannels [326], and it is crucial to fabricate the droplets in a uniform structure during that process. In spite of the highly-demanded applications of the droplets, the droplet generation techniques are limited. Normally, the droplets are manufactured by stirring the mixture with large-scale instruments [327]. It is usually difficult to produce droplets with precise size and typically the droplets have wide size distributions [328]. Alternatively, microfluidics has become a prevalent technique to produce highly monodisperse emulsion droplets [329]. Depending on the channel geometry in the microfluidic device, T-junction [330–333] and flow-focusing [334–337] configurations are introduced to form droplets with controllable sizes. Recent improvements in microfluidic emulsion technology enable the generation of uniform emulsion droplets in a small volume by electrical control, such as dielectrophoretic [338–340] and electrowetting on dielectric methods [341–343]. These fabrication methods can generate large numbers of droplets with a diameter which ranges from nanometers to micrometers [344]. However, it still shows a variation of 3–10% in size of the emulsion droplets produced by these methods [345]. Moreover, the production of the daughter droplets together with the mother droplets is undesired and then the quality of the droplets becomes hard to control [346]. Thus, it is essential to develop a tool for sorting emulsion droplets by size and the droplets with well-defined size and uniform morphology can be purified for consecutive applications.

Recently, the manipulation of emulsion droplets has attracted considerable interest and the development of the related microfluidic technology provides various approaches for sorting emulsion droplets in the microchannel, which include gravity and microchannel geometry effects [347–349], mechanical valves [350–353], electrowetting-on-dielectric (EWOD) [354], and dielectrophoresis (DEP) [355–359]. As the sedimentation velocity of the smaller droplets is lower than that of the larger droplets, Huh et al. [349] designed the gravity-driven size-based separation system in the microchannel to separate the droplets with different diameter by employing the hydrodynamic sorting amplification. By using the asymmetrical widening design for the separation microchannel, the sorting effect is enhanced. However, this method has limited sensitivity for droplets of similar sizes. The droplets can also be separated mechanically by using valves which are assembled in the microfluidic devices. In the design created by Abate et al. [350], the fluid flow is manipulated by the single-layer membrane valve in the microchannel, enabling the separation of droplets into different outlets with high speed at a frequency of hundreds of hertz. However, in order to sort droplets effectively by this method, precise control over the flow field inside the microchannel is necessary. The EWOD method is also utilized for sorting droplets. Cho et al. [354] conducted the separation of droplets

and their contents in the EWOD-based microfluidic chip by adjusting the interfacial energy of the droplets and the solid surface with an array of microelectrodes, resulting in the movement of the droplets. Two different kinds of particles were first divided by electrophoresis into two areas of a master droplet and then split the droplet in half by EWOD actuation. Then the two daughter droplets with different contents can be separated. Even though the EWOD technology enables one to achieve separation inside the droplets, its throughput is very limited in comparison with the high-speed production and performance of the flow-focused based droplet systems. In addition to the above-mentioned separation methods, dielectrophoresis proves to be an effective strategy for continuously sorting particles and droplets by size and its content in microfluidic systems [40,41,241,355–357,360,361] due to its advantages of low sample consumption, label-free separation, and fast response. Due to the dielectric property differences of the droplets and the suspending solution in the electrical field gradient, the DEP force is induced and drives the droplets to move. Generally, the emulsion droplets can be manipulated in microfluidic chips by utilizing conventional DEP effects. However, the implementation of the microelectrodes in the microfluidic chips and the fabrication processes are difficult and expensive. Furthermore, the traditional dielectrophoretic methods cannot achieve the sorting of emulsion droplets with both high separation resolution and throughput. In addition, there is limited research on the dielectrophoretic behaviors of the IL-in-water emulsion droplets. It is highly desirable to study the dielectrophoretic behaviors of the IL-in-water emulsion droplets and the manipulation of the IL droplets under DC electric fields in the microchannel. These problems discussed above can be overcome by the proposed DC-DEP method using asymmetric orifices [40,41,241]. By using a pair of asymmetric orifices with large width ratio, a stronger electric field gradient and hence larger DEP force can be produced with a strong electric field strength applied through the microchannel, resulting in a high separation resolution. Furthermore, in this design, the production of the electric field gradient will not change the cross-section of the microchannel and has no influence on the particle or droplet transportation. By using the pressure-driven flow to drive the particles and droplets, the throughput can be dramatically increased in comparison with other microfluidic DEP methods.

This chapter investigates the manipulation and sorting of oil-in-water emulsion droplets inside the microchannel by asymmetric orifice based DC-DEP and the dielectrophoretic behaviors of the IL-in-water emulsion droplets under DC electric field. The DC dielectrophoretic behaviors of two different kinds of hydrophobic IL-in-water microemulsion droplets were investigated. Then, the size-dependent separation of emulsion droplets was conducted, and the prediction of the theoretical simulation was compared with the experimental results. In addition, selecting the suspending solution with a specific electrical conductivity, the microemulsion droplets with similar sizes but different contents and kinds were separated based on their opposite DEP behaviors. This work presents the size-dependent and content-dependent separation of emulsion oil droplets under a pressure-driven flow in the asymmetric orifice based microchannel by using

DC-DEP method for the first time, offering a strategy to manipulate the emulsion droplets and broadening the applications of the DC-DEP method in colloid and interface science and in industry.

5.2 Materials and Methods

5.2.1 Microfluidic chip fabrication

It can be seen from Figure 5-1 that the microfluidic chip consists of a top and a bottom polydimethylsiloxane (PDMS) layer. The chip of the top PDMS has the main microchannel with a sample inlet channel (A) and a sheath flow inlet channel (B), two outlet channels (E and F), and two reservoirs (C and D) to insert external electrodes. The gradient of the electric field and hence the DEP effects are induced by a group of asymmetric orifices located on the opposite sidewalls of the microchannel. As shown in Figure 5-1, when the mixture of the emulsion droplets comes into the horizontal main channel through the sample inlet channel A, they are forced to flow closely to the sidewall of the small orifice by the hydrodynamically dominant flow from the sheath fluid inlet channel B. Meanwhile, a DC electrical potential difference is applied through the pair of the orifices by the external electrodes, where the streamline of the electric field across the channel between the C and D is limited by the opening sizes of the asymmetric orifices. To ensure the production of a large electric field gradient near the nano-orifice, the asymmetric orifices have a large width ratio. Then, the droplets will experience the DEP effects when moving through the small orifice where the strongest gradient of the electric field exists.

As inferred from Equation (2-8) the magnitude of the dielectrophoretic forces will increase with the electric field gradient ($\nabla|E|^2$) and the radius cubic of the droplet (a^3). Since the trajectory shifts are proportional to the DEP forces acting on the droplets, the droplets with different radii can be separated and flow into individual streams, shown in Figure 5-1(a) and Figure 5-1(b). In addition, since the direction of the dielectrophoretic forces, i.e., p-DEP and n-DEP, is determined by the sign of f_{CM}, two different kinds of particles/droplets may have opposite DEP behaviors and hence can be separated. It can be inferred from Equation (2-8) that, for the droplets whose electrical conductivity is smaller than that of the suspending solution, i.e., f_{CM}, < 0, they will be repelled away by the n-DEP behaviors from the electric field maximum. While for the droplets that have a larger electrical conductivity than the medium, i.e., f_{CM}, > 0, they will be attracted by p-DEP forces towards the electric field maximum. Then, Figure 5-1(c) and Figure 5-1(d) illustrates the dielectrophoretic behaviors of the droplets experiencing positive and negative DEP forces, respectively, under DC electric field. Therefore, by using the DC-DEP device as shown in Figure 5-1, not only the separation of droplets with different sizes can be achieved, but also the separation of droplets with similar sizes but different contents (and hence different electrical conductivity) can also be accomplished by selecting a suspending solution with an electrical conductivity, $\sigma_{p1} < \sigma_m < \sigma_{p2}$.

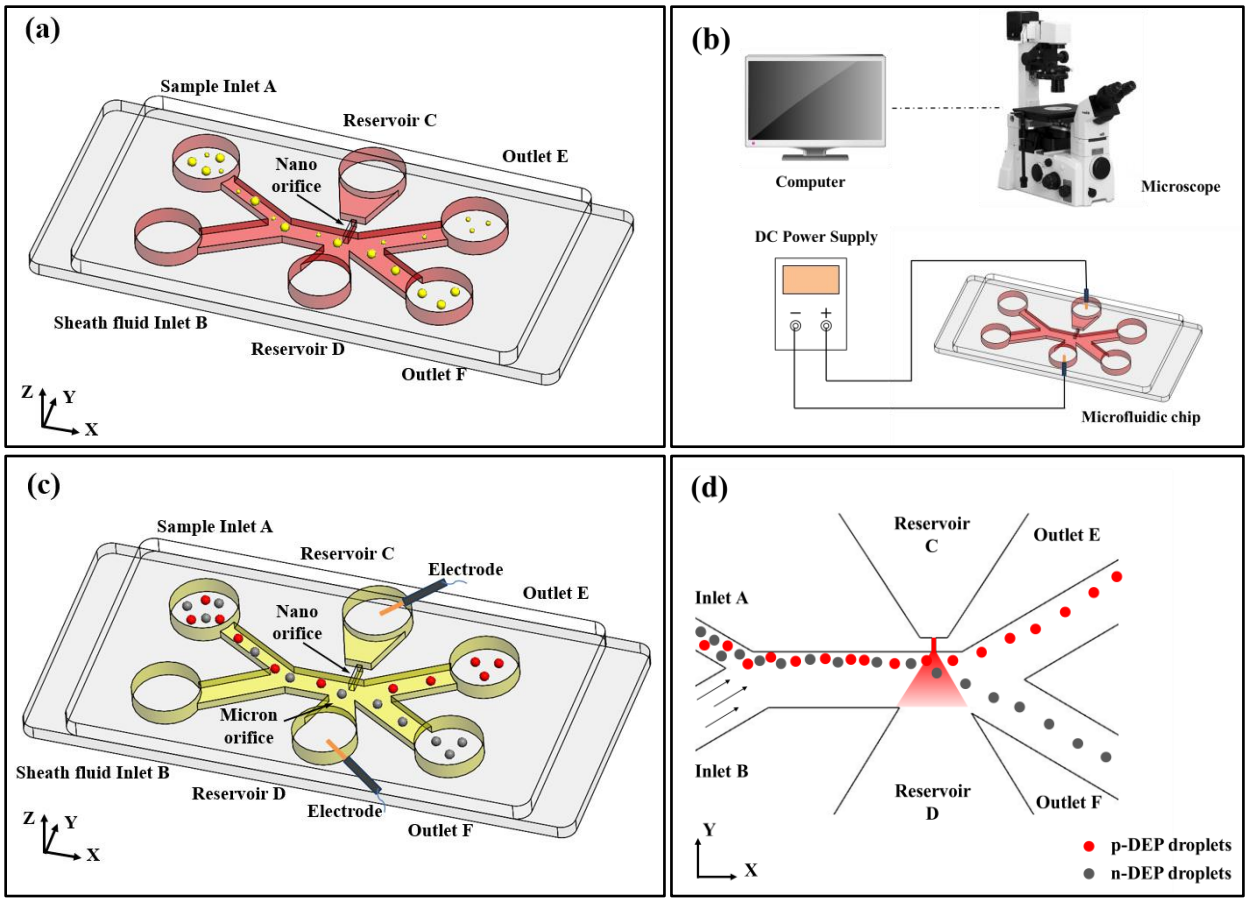

Figure 5-1 (a) Schematic diagram of the microfluidic DC-DEP chip with a pair of asymmetric orifices for droplets separation by size, (b) Illustration of the experimental system, (c) Schematic diagram of the DC-DEP microfluidic chip for the dielectrophoretic behaviors of droplets, (d) Illustration of the working principle for droplets separation by content (the gradient of the red color represents the strength of the electric field).

In this chip, the width of the branch channels B, E and F, and the main channel are 80 µm, and the width of the branch channel A is 20 µm for the silicone oil droplets and 40 µm for the IL emulsion droplets, respectively. The depth of the channels in this chip is approximately 20 µm for the silicone oil droplets and 40 µm for the IL emulsion droplets, respectively. In this study, the local electric field is produced by the platinum electrodes inserted in the reservoirs C and D where a DC electric potential is applied, and the distance between these two external electrodes is approximately 0.6 cm. In order to induce strong electric field gradient, a single nanochannel of 860 nm in width and 290 nm in depth is utilized as the nano-orifice. The length of the nano-orifice is always 15 µm and the large orifice has a width of 125 µm for all chips. As the distance between the two external electrodes is relatively small (essentially over the width of the microchannel), a low electrical potential difference applied through the orifices across the microchannel is

enough to generate a strong electric field gradient. In such a chip, by transporting the droplets under the pressure-driven flow and by inducing the non-uniform electric field with a pair of asymmetric orifices which is perpendicular to the main channel, no constriction shows in the main microchannel and these droplets are exposed to this electric field gradient only near the region of the nano-orifice. Therefore, the adverse effects associated with traditional DC-DEP techniques such as Joule heating, droplets aggregation, and transport difficulties are significantly reduced.

5.2.2 Preparation of ionic liquid/oil-in-water microemulsions

To make the ionic liquid(IL)-in-water microemulsions, one of two different kinds of hydrophobic ionic liquids, i.e., 1-Butyl-3-methylimidazolium hexafluorophosphate (BMIM-PF6) or 1-Hexyl-3-methylimidazolium hexafluorophosphate (HMIM-PF6) (IoLiTec Inc) was mixed with DI water by adding the nonionic surfactant Tween 20 (Sigma Aldrich) as the stabilizing agent, as illustrated in Figure 5-2. In order to demonstrate the different dielectrophoretic behaviors and visually differentiate different trajectories of these two different kinds of ILs, Nile Red (Sigma-Aldrich Chemical Co) was added into the BMIM-PF6 as the fluorescent dye. In this way, the BMIM-PF6 droplets become fluorescent droplets and the HMIM-PF6 droplets are non-fluorescent droplets. For the preparation of oil-in-water emulsions, silicone oil (XIAMETER PMS-200) or the silicone oil-based Carbon and Silver Conductive Grease (MG Chemicals) was used instead of the ILs. After introducing 5 mL DI water, 1 mL IL or silicone oil with 100 µL Tween 20 surfactant solution or 0.05 g conductive grease with 50 µL surfactant solution into a glass bottle (15 mL in volume), the emulsion droplets were generated by stirring the mixture with a vortex mixer (VWR Scientific) at the speed of 3200 rpm for 2 min.

In this study, two pairs of silicone oil droplets, i.e., 9 µm and 14.5 µm, and 7.5 µm and 11 µm, and three pairs of oil mixture droplets, i.e., droplets of silicone oil and carbon grease with a diameter of approximately 7.5 µm, droplets of silicone oil and carbon-plus-silver grease with a diameter of approximately 7 µm, as well as droplets of carbon grease and carbon-plus-silver grease with a diameter of approximately 7.5 µm were fabricated. A solution of 0.4 mM K2HPO4 with a pH of 7 and an electrical conductivity of 0.01 S/m was employed to separate the 7.5 µm droplets of carbon grease and carbon-plus-silver grease. Deionized water with a pH 7 and an electrical conductivity of 5.5 × 10−6 S/m S/m was used for the rest of the groups for separation. To investigate the DC-DEP behavior of the IL-in-water emulsion droplets, two different kinds of ionic liquid droplets, i.e., BMIM-PF6 droplets and HMIM-PF6 droplets, were fabricated. Deionized water with an electrical conductivity of 5.5 × 10−6 S/m, a solution of 4.8 mM K2HPO4 with an electric conductivity of 0.12 S/m, as well as a solution of 6.4 mM K2HPO4 with an electric conductivity of 0.16 S/m were employed as the suspending medium, respectively, and they all have a pH value of 7.

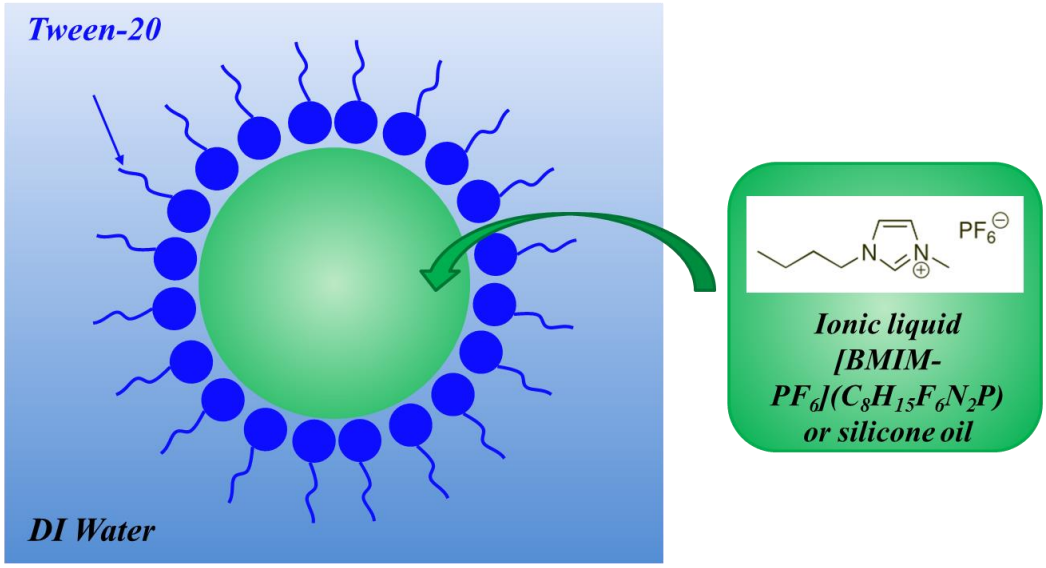

Figure 5-2 Schematic representation of the IL/oil-in-water microemulsions.

5.2.3 Experimental system setup

To start the experiments, the surrounding media was first injected into the microchannel through reservoirs A and B. Then, the microemulsion droplets were introduced into the sample inlet reservoir A and additional suspending medium was introduced into the sheath fluid reservoir B. Since the sample inlet of the channel has a limited width and depth, only the silicone oil droplets smaller than 10 μm and the IL droplets smaller than 20 μm in radius can flow into the main channel, respectively. In this work, the microemulsion droplets were driven by the pressure difference, i.e., a difference of the liquid heights between the inlets and the outlets' reservoirs, and flow from the inlet wells to the outlet wells. As pushed by the sheath liquid flow from the inlet channel B, the droplets mixture was forced to flow close to the channel wall on the side of the nano-orifice (see Figure 5-1). The electric potentials were then employed from the DC power supplier (HVS448 High Voltage Sequencer, LabSmith) and a custom-made voltage adjuster to the platinum electrodes inserted in the reservoirs C and D. The electric field gradient and hence the DEP forces were induced. In this way, the droplets experienced the DEP effects in the vicinity of the nano-orifice and their trajectories were shifted correspondingly. The movements of the emulsion droplets were visualized by inverted optical microscope (Nikon, TE-2000) and the images were recorded by a charge coupled device CCD camera (QImaging) and stored in the computer at 25 frames per second. In this study, since the K_2HPO_4 solution is a relatively weak electrolyte [362,363] and the platinum electrodes are inert and noncorrodible, the electrochemical effects are negligible and no bubbles were observed during the experiments. All experiments were conducted at the room temperature of 25 ± 1 ◦C.

5.3 Results and discussion

5.3.1 Simulation of the oil droplet trajectory

As shown in Figure 5-3, an example of the trajectories of the 7.5 μm and 11 μm silicone oil droplets is demonstrated which is calculated by using COMSOL 4.3b. In this design, the non-uniformity of the electric field is produced by applying the DC electric potential through the nano and micron orifices by the external electrodes. The greatest non-uniformity of the electric field is produced near the nano-orifice. As shown in Figure 5-3, the oil droplets are loaded into the horizontal channel and forced by the dominant sheath flow from branch channel B to move close to the upper sidewall and pass over the nano-orifice where the greatest electric field gradient exists. It can be inferred from Figure 5-3, the oil droplets are driven into individual trajectories after experiencing the dielectrophoretic effects. Since the locally applied electric potential is low and the nano-orifice has a width of 860 nm, the liquid flow from reservoir C to the main channel can be neglected. As the magnitude of the DEP force is dependent on the radius cubic of the droplet, the larger 11 μm oil droplets experience stronger n-DEP force, leading to a sufficiently large trajectory shift, and are pushed away into the outlet channel F. While, the DEP effects on the smaller 7.5 μm oil droplets are relatively weaker and they flow into outlet channel E. If the mixed emulsion droplets have similar sizes but different contents, the droplets with stronger polarizability than that of the suspending solution will be attracted by the p-DEP effects towards the nano-orifice and flow into the outlet channel E. While the droplets, whose polarizability is weaker compared with that of the medium, will undergo n-DEP and be pushed towards the large orifice where there is a weak electric field, and then move into the outlet reservoir F. Therefore, the size-dependent separation of the oil droplets and the separation of the oil droplets by its content can be achieved by using the nano-orifice based DC-DEP device.

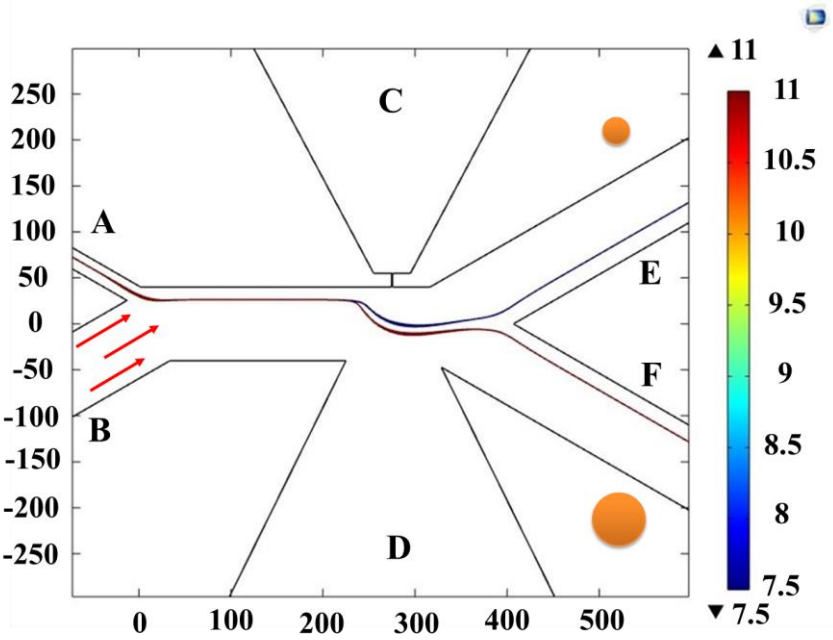

Figure 5-3 An example of the separation of the 7.5 µm and 11 µm silicone oil droplets in the channel. The width and length of the small orifice is 860 nm and 15 µm, respectively, and the width of the large orifice is 125 µm. The voltage applied is 320 V in electrode C and zero in electrode D.

5.3.2 DC-DEP behaviors of the droplets

Table 5-1 shows the electrical conductivities of three different kinds of silicone oil droplets and two different kinds of ionic liquid droplets. The f_{CM} values of the above-mentioned droplets are plotted as a function of the electric conductivity of the suspending solution, σ_m, and are shown in Figure 5-4. In this study, the deionized water with an electrical conductivity of 5.5×10^{-6} S/m, a solution of 0.4 mM K_2HPO_4 with a pH of 7 and an electrical conductivity of 0.01 S/m, a solution of 4.8 mM K_2HPO_4 with an electric conductivity of 0.12 S/m, as well as a solution of 6.4 mM K_2HPO_4 with an electric conductivity of 0.16 S/m were employed as the suspending media, and they all have a pH value of 7.

Table 5-1 Electric conductivity of five different kinds of droplets and the corresponding CM factor (f_{CM}) for the droplets in the suspending solutions with three different electric conductivities.

Property	Conductivity (S/m)	f_{CM} with σ_m = 5.5×10^{-6} S/m	f_{CM} with σ_m = 1×10^{-2} S/m
Droplet of Silicon oil (Transparent in color)	10^{-13}	≈−0.5	
Droplet of Carbon grease	0.9	≈1	≈1

(Black in color. Silicon oil based, conductive filler: carbon.)			
Droplet of Carbon-plus-Silver grease (Silver in color. Silicon oil based, conductive filler: carbon-plus-silver)	0.9×10^{-3}	≈1	≈−0.43
Property	Conductivity (S/m)	f_{CM} with σ_m = 0.12 S/m	f_{CM} with σ_m = 0.16 S/m
Droplets of BMIM-PF_6	0.137	≈−0.125	≈−0.2
Droplets of HMIM-PF_6	0.08	≈0.045	≈−0.05

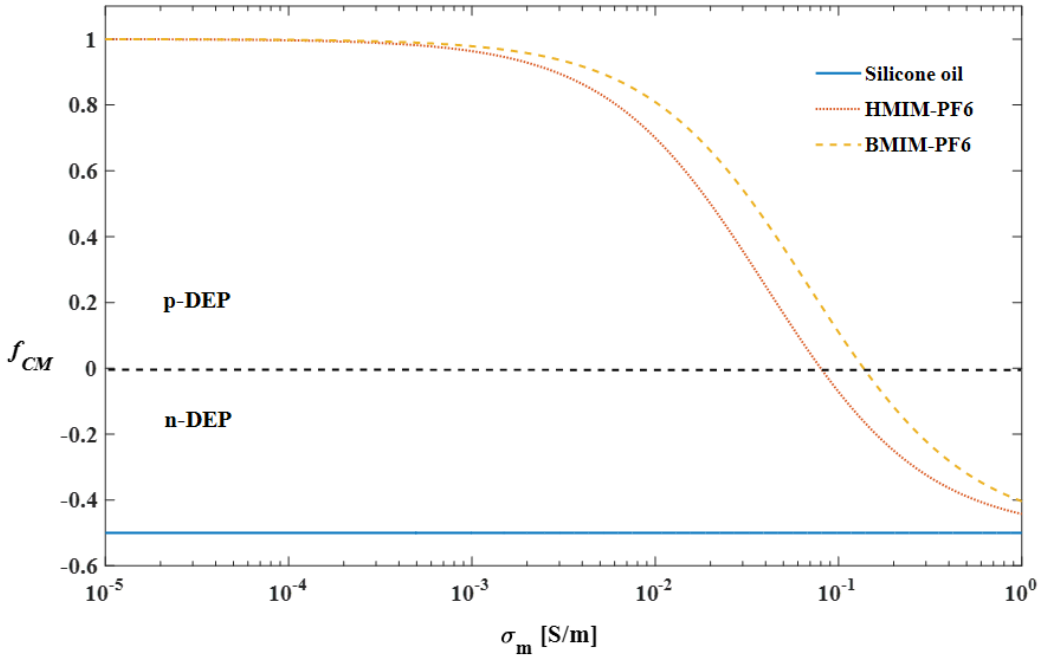

Figure 5-4 Prediction of the f_{CM} for the silicone oil droplets, HMIM-PF_6 droplets, and BMIM-PF_6 droplets, as a function of the electric conductivity of the suspending solution σ_m.

5.3.2.1 P-DEP effect

As shown in Equation (2-8), the direction of the dielectrophoretic effects, i.e., p-DEP or n-DEP is determined by the sign of f_{CM}. By using the suspending solution with a specific electrical conductivity, the dielectrophoretic behaviors of the IL-in-water emulsion droplets under DC electric field are shown in Figure 5-5. As seen in Figure 5-5(a) and Figure 5-5(b), when the solution of the deionized water with a pH 7 and

an electrical conductivity of 5.5×10^{-6} S/m was utilized as the suspending medium, the electrical conductivity of the surrounding media is lower than that of the HMIM-PF_6 droplets and BMIM-PF_6 droplets, i.e., $f_{CM} \approx 1$ (shown in Table 5-1); both types of these droplets will exhibit positive dielectrophoretic behaviors and are attracted by the positive DC-DEP effects and move into the channel E under the condition of ϕ_C=150 V and ϕ_D=0 V.

5.3.2.2 N-DEP effect

When the droplets, electrical conductivity is lower than the solution, i.e., $f_{CM} < 0$, these droplets will experience negative DEP behaviors and move away from the electric field maximum. Therefore, it can be seen from Figure 5-5(c) and Figure 5-5(d) that, when the solution of 6.4 mM K_2HPO_4 with an electric conductivity of 0.16 S/m was employed as the suspending medium, and the HMIM-PF_6 droplets (conductivity of 0.08 S/m, $f_{CM} \approx -0.2$) and BMIM-PF_6 droplets (conductivity of 0.137 S/m, $f_{CM} \approx -0.05$) were pushed away from the region of the high electric field by experiencing the n-DEP behaviors and move into channel F.

5.3.2.3 P-DEP and n-DEP

Furthermore, as inferred from Equation (2-8), when the suspending medium is selected to have a specific electrical conductivity to satisfy the condition of $\sigma_{p1} < \sigma_m < \sigma_{p2}$, the two different kinds of droplets will display opposite dielectrophoretic behaviors, i.e., one experiencing p-DEP and the other n-DEP effects, respectively. It can be seen from Figure 5-5 that, when using the solution of 4.8 mM K_2HPO_4 with an electric conductivity of 0.12 S/m as the surrounding solution, the BMIM-PF_6 droplets (conductivity of 0.137 S/m, $f_{CM} \approx 0.045$) were attracted by the p-DEP forces and move into the channel E (Figure 5-5(e)), while the HMIM-PF_6 droplets (conductivity of 0.08 S/m, $f_{CM} \approx -0.125$) experienced the n-DEP effects and were repelled away towards the channel F (Figure 5-5(f)), where ϕ_C=650 V and ϕ_D=0 V. In this way, it enables the continuous manipulation and separation of different kinds of ionic liquid droplets of similar size based on these opposite DEP behaviors in the asymmetric orifice based DC-DEP chip.

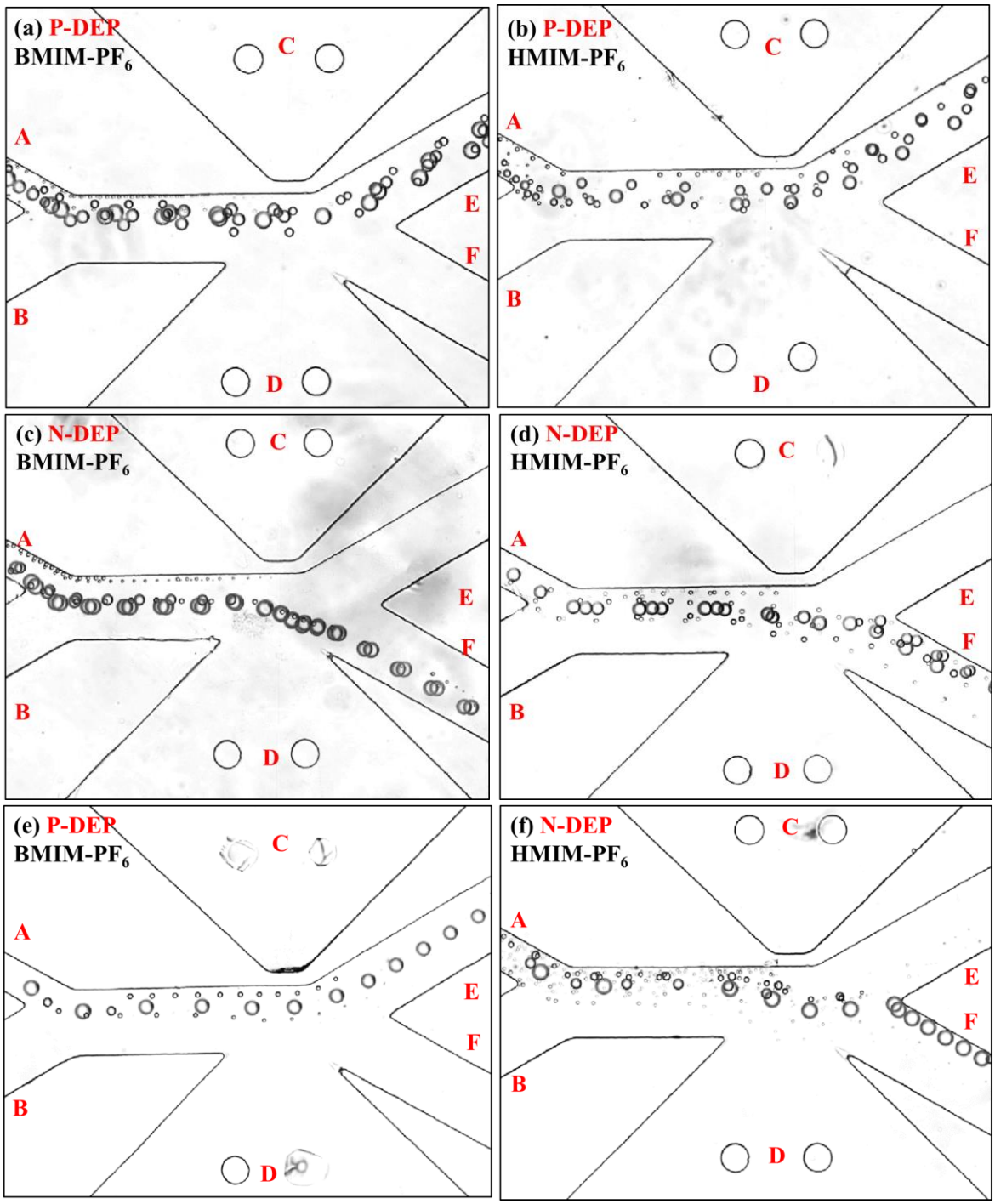

Figure 5-5 Positive DEP behaviors of the (a) BMIM-PF_6 droplets and (b) HMIM-PF_6 droplets, under the condition: ϕ_C=150 V, ϕ_D=0 V, and the electrical conductivity of the surrounding media is lower than that of the HMIM-PF_6 droplets and BMIM-PF_6 droplets. The negative DEP behaviors of the (c) BMIM-PF_6 droplets and (d) HMIM-PF_6 droplets, under the condition: ϕ_C=300 V, ϕ_D=0 V, and the electrical conductivity of the surrounding media is higher than that of the HMIM-PF_6 droplets and BMIM-PF_6

droplets. The trajectories of the (e) BMIM-PF_6 droplets by p-DEP forces and (f) HMIM-PF_6 droplets under n-DEP effects, where ϕ_C=650 V and ϕ_D=0 V, and $\sigma_{HMIM\text{-}PF6} < \sigma_m < \sigma_{BMIM\text{-}PF6}$. The nano-orifice has a size of 860 nm in width and 15 μm in length, and the large orifice is 125 μm in width.

5.3.3 Separation of emulsion droplets by size

In this DC-DEP chip, the DC-DEP separation of the HMIM-PF_6 droplets with a diameter of 11.5 μm or 19.5 μm was conducted by applying 650 V to the electrode C and 0 V to the electrode D. 4.8 mM K_2HPO_4 with an electric conductivity of 0.12 S/m was utilized as the suspending medium, and then the droplets will undergo the n-DEP. The trajectories of the droplets as shown in Figure 5-6 and Figure 5-7 are achieved by superimposing the sequential images of the motion of the droplets under the given condition. For the separation of 7.5 μm and 11 μm silicone oil droplets, and 9 μm and 14.5 μm silicone oil droplets, the DC-DEP effects were induced by applying an electric potential to electrode C of 320 V and 240 V, respectively, and the electrode D is grounded. The DI water with a pH value of 7 and an electric conductivity of 5.5×10^{-6} S/m was utilized as the suspending medium, and hence the silicone oil droplets will experience the n-DEP forces. In the experiments, the nano-orifice has a width of 860 nm and a length of 15 μm, and the large orifice has a width of 125 μm in all chips.

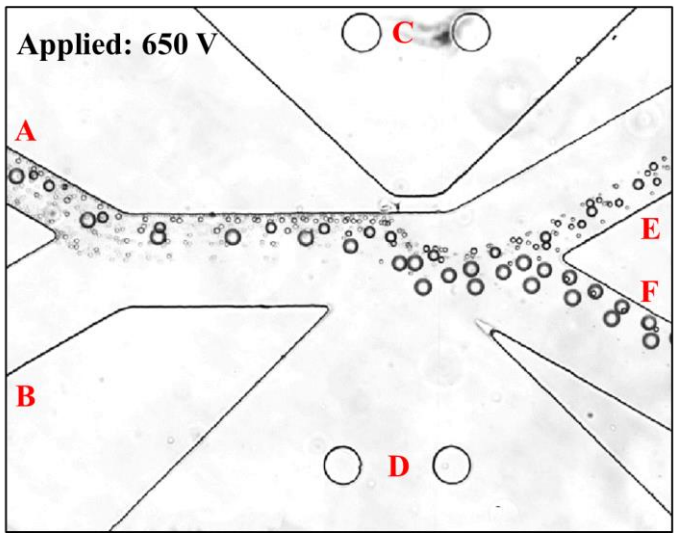

Figure 5-6 Separation of HMIM-PF_6 droplets with average diameters of 11.5 μm and 19.5 μm, under ϕ_C=650 V and ϕ_D=0 V. ϕ_C and ϕ_D indicate the voltages applied to the reservoirs C and D. In this chip, the nano-orifice has a size of 860 nm in width and 15 μm in length, and the large orifice is 125 μm in width.

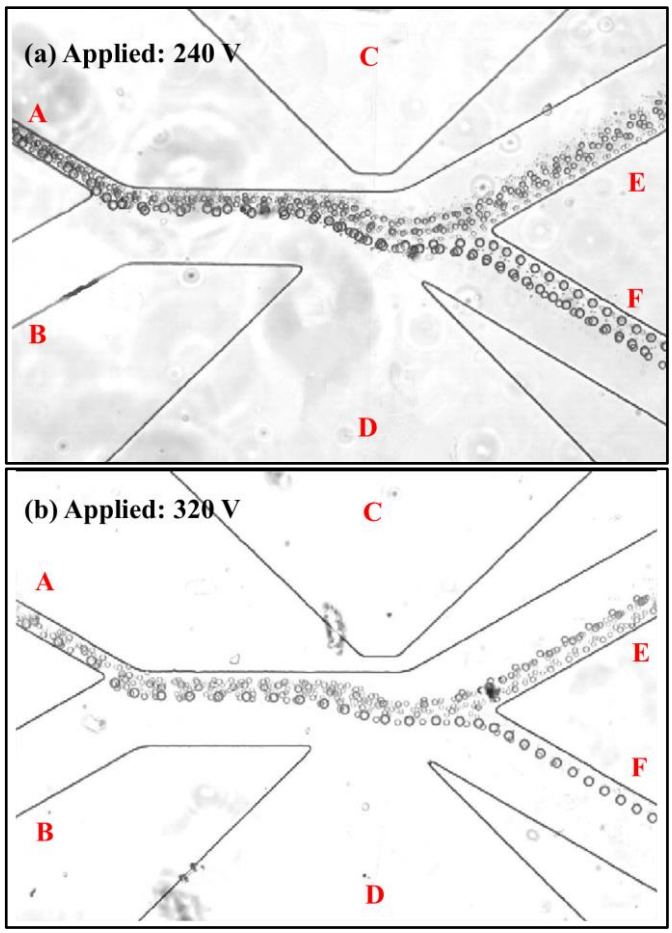

Figure 5-7 Separation of the silicone oil droplets by size. (a) Separation of 9 µm and 14.5 µm diameter silicone oil droplets ϕ_C=240 V, ϕ_D=0 V. (b) separation of 7.5 µm and 11 µm diameter silicone oil droplets, ϕ_C=320 V, ϕ_D=0 V. ϕ_C and ϕ_D indicate the voltages applied to the reservoirs C and D. In this chip, the width and length of the small orifice is 860 nm and 15µm, respectively, and the width of the large orifice is 125 µm.

As discussed in Equation (2-8), the dielectrophoretic forces and hence the lateral shifts of the oil droplets are dependent upon the electric field gradient and the diameter of droplets. Thus, as shown in Figure 5-1(a), the oil droplets of different radii are sorted into the individual trajectory and separated when moving closely to the small orifice in the main channel. An example of the size-dependent separation of the emulsion droplets is illustrated in Figure 5-7. The mixture of oil droplets flows into channel A and they are pushed by the sheath fluid from branch channel B to move along the upper channel wall. When the silicone oil droplets move through the region of the electric field gradient, the n-DEP forces take effects, leading to the lateral shifts of their trajectories, and they are thus moved into different streams. By controlling the custom-made voltage adjuster, the smaller and larger oil droplets flow into the outlet channel E and outlet channel F, respectively. Under ϕ_C=240 V, the larger oil droplets with d=14.5 µm experience

stronger DEP forces and flow into the outlet F, while the oil droplets with a smaller diameter of d=9 μm experience weaker DEP effects and flow into the outlet E (Figure 5-7(a)). Furthermore, based on Equation (2-8), as the magnitude of the DEP force will increase with the droplet size, a higher electric voltage should be applied for the separation of oil droplets with smaller diameters such as 7.5 μm and 11 μm. Figure 5-7(b) shows that the mixture of the oil droplets with two different sizes, 7.5 μm and 11 μm, were successfully separated under ϕ_C=320 V. The experimental result (Figure 5-7(b)) shows good agreement with the simulation trajectories of the 9 μm and 14.5 μm diameter silicone oil droplets (Figure 5-3). It should be noted that this nano-orifice based DC-DEP separation system can be employed for continuously sorting smaller oil droplets of 7.5 μm and 11 μm with a high separation resolution of 3.5 μm (difference in diameter) as illustrated in Figure 5-7(b). In addition, by controlling the applied voltages to electrodes C, the separation of oil droplets of different sizes can be achieved. Thus, the applied voltages can be optimized for the specific size of the targeted droplets by theoretical predictions and experimental calibrations.

5.3.4 Separation of emulsion droplets by content

In order to examine the sensitivity of this nano-orifice based DC-DEP separation system, the separation of the oil droplets of similar sizes but different contents, i.e., the droplets of silicone oil and carbon grease with a diameter of 7.5 μm, the droplets of silicone oil and carbon-plus-silver grease with a diameter of 7 μm, as well as the droplets of carbon grease and carbon-plus-silver grease with a diameter of 7.5 μm were conducted under ϕ_C=320 V, ϕ_C=360 V, and ϕ_C=360 V, respectively, and the BMIM-PF_6 droplets and HMIM-PF_6 droplets with a diameter of approximately 21 μm, and the droplets of silicone oil and BMIM-PF_6 droplets with a diameter of approximately 22 μm were conducted under the condition of ϕ_C = 650 V and ϕ_D = 0 V. Examples are shown in Figure 5-9, Figure 5-10 and Figure 5-11. As shown in Figure 5-8, the f_{CM} values of the silicone oil droplets with three different contents are plotted varying with the conductivity of the surrounding solution, σ_m. In order to make sure that the oil droplets with different contents experience p-DEP and n-DEP forces, respectively, suspending solutions with two different electrical conductivities were used. Deionized water with an electrical conductivity of 5.5×10^{-6} S/m was utilized for the separation of the droplets of silicone oil and BMIM-PF_6 droplets, a solution of 4.8 mM K_2HPO_4 with an electric conductivity of 0.12 S/m was employed for the sorting of the BMIM-PF_6 droplets and HMIM-PF_6 droplets, a solution of 0.4 mM K_2HPO_4 with an electric conductivity of 1×10^{-2} S/m was used for the sorting of the droplets of carbon grease and carbon-plus-silver grease, and the deionized water with an electric conductivity of 5.5×10^{-6} S/m for the rest of the groups of silicone oil droplets separation.

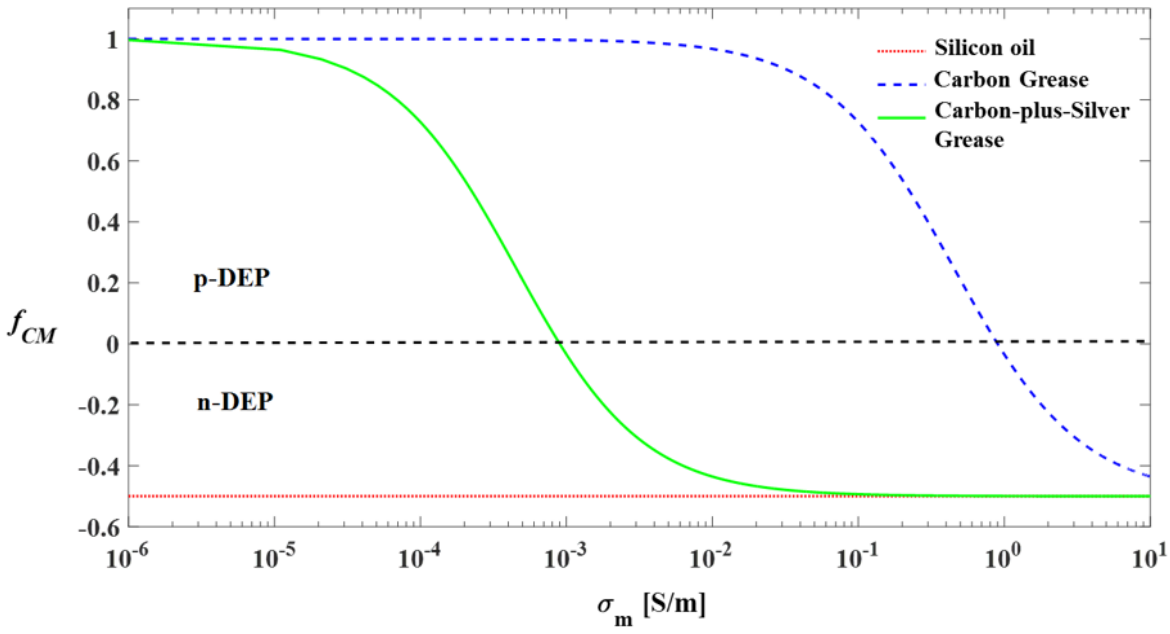

Figure 5-8 Clausius-Mossotti factor f_{CM} for the silicone oil droplets with three different contents as a function of the electric conductivity of the suspending solution σ_m.

In Figure 5-9, as the electrical conductivity of the droplets of carbon grease is higher than that of the surrounding solution, i.e., $f_{CM} \approx 1$ (Table 5-1), these droplets were attracted by the p-DEP forces towards the electric field maximum area and flowed into the outlet branch E. On the contrary, the droplets of silicone oil have an electrical conductivity smaller than that of the medium, i.e., $f_{CM} \approx -0.5$ (Table 5-1), the droplets experienced n-DEP effects and were repelled from electric field maximum region and flowed into the outlet branch F. It clearly shows the mixtures of the droplets of carbon-plus-silver grease ($f_{CM} \approx 1$) and silicon oil ($f_{CM} \approx -0.5$) with a diameter of 7 μm in Figure 5-9(b), and the droplets of carbon grease ($f_{CM} \approx 1$) and carbon-plus-silver grease ($f_{CM} \approx -0.43$) with a diameter of 7.5 μm and in Figure 5-9(c) were successfully separated by experiencing p-DEP and n-DEP forces, respectively.

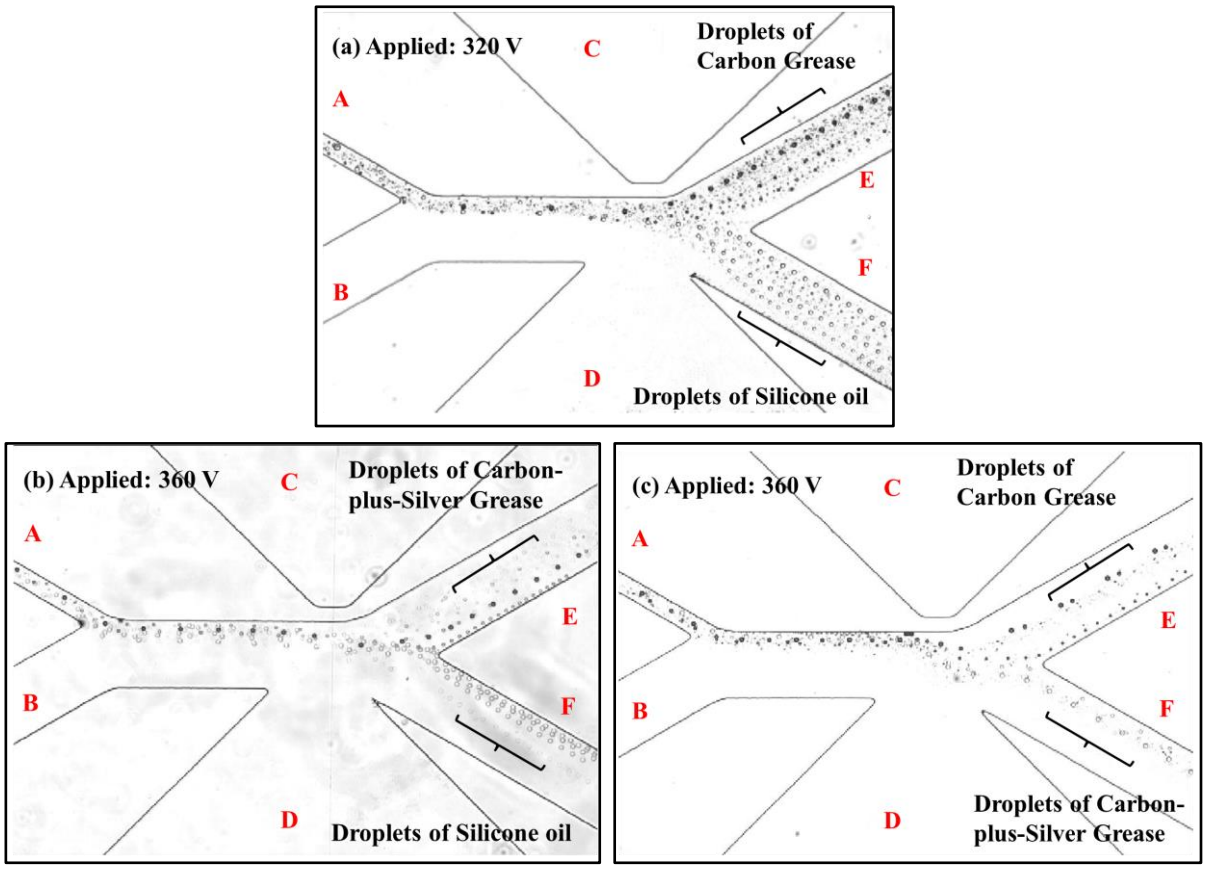

Figure 5-9 Separation of silicone oil droplets of similar sizes by content. (a) Separation of the silicon oil droplets and carbon grease droplets with a diameter of 7.5 μm, ϕ_C =320 V, ϕ_D=0 V. (b) Separation of silicon oil droplets and carbon-plus-silver grease droplets with a diameter of 7 μm, ϕ_C =360 V, ϕ_D=0 V. (c) Separation of carbon grease droplets and carbon-plus-silver grease droplets with a diameter of 7.5 μm, ϕ_C =360 V, ϕ_D=0 V. The width and length of the small orifice is 860 nm and 15 μm, respectively, and the width of the large orifice is 125 μm. The small dots are the impurities of grease.

Figure 5-10 shows the separation of two kinds of IL-in-water microemulsion droplets, i.e., BMIM-PF_6 and HMIM-PF_6 droplets, based on their opposite DEP behaviors, by choosing the suspending solution with a specific electrical conductivity. In order to demonstrate the different trajectories of the two different types of droplets, the BMIM-PF_6 droplets are fluorescent droplets. Since the BMIM-PF_6 droplets have a higher electrical conductivity than that of the suspending solution, $f_{CM} \approx 0.045$ (Table 5-1), the droplets experienced p-DEP forces and were attracted towards the nano-orifice area, flowing into the outlet channel E. This is clearly demonstrated by the trajectories of the BMIM-PF_6 droplets in the fluorescent image, Figure 5-10(b). While the electrical conductivity of the HMIM-PF_6 droplets is smaller than that of the suspending medium, correspondingly, $f_{CM} \approx -0.125$ (Table 5-1), these droplets were pushed away from the electric field maximum by undergoing the negative dielectrophoretic forces and moved into the outlet

channel F. Moreover, the separation of silicone oil droplets and BMIM-PF_6 droplets was conducted. Figure 5-11(a) and Figure 5-11(b) clearly show the different trajectory shifts of the fluorescent BMIM-PF_6 droplets and the non-fluorescent droplets of the silicone oil. The mixed emulsion droplets of the BMIM-PF_6 droplets (f_{CM} ≈1) and silicone oil droplets (f_{CM} ≈−0.5) were continuously sorted and flowed into branch E and branch F by positive and negative dielectrophoretic effects, respectively. To verify that the silicone oil droplets moved into outlet channel F, the experiments were repeated by using only the silicone oil droplets under the same condition. The trajectories of the silicone oil droplets under the same condition are shown in Figure 5-11(c). It clearly shows that the silicone oil droplets were pushed by the n-DEP forces into the outlet branch F, and the silicone oil droplets had similar trajectories as in the case of the mixed droplets as shown in Figure 5-11(a). This indicates that the continuous microemulsion droplets sorting by size and the manipulation of different types of emulsion droplets with similar sizes but different contents based on these opposite DEP behaviors can be achieved in the newly developed asymmetric orifice based DC-DEP chip. Furthermore, it should be noticed that the separation of the oil droplets of similar sizes with other different contents can be achieved by simply controlling the applied voltages and selecting the suspending solution with a specific electrical conductivity. The relationships among the voltages, electrical conductivity, and the content of the oil droplets can be easily obtained through numerical simulation and experiments.

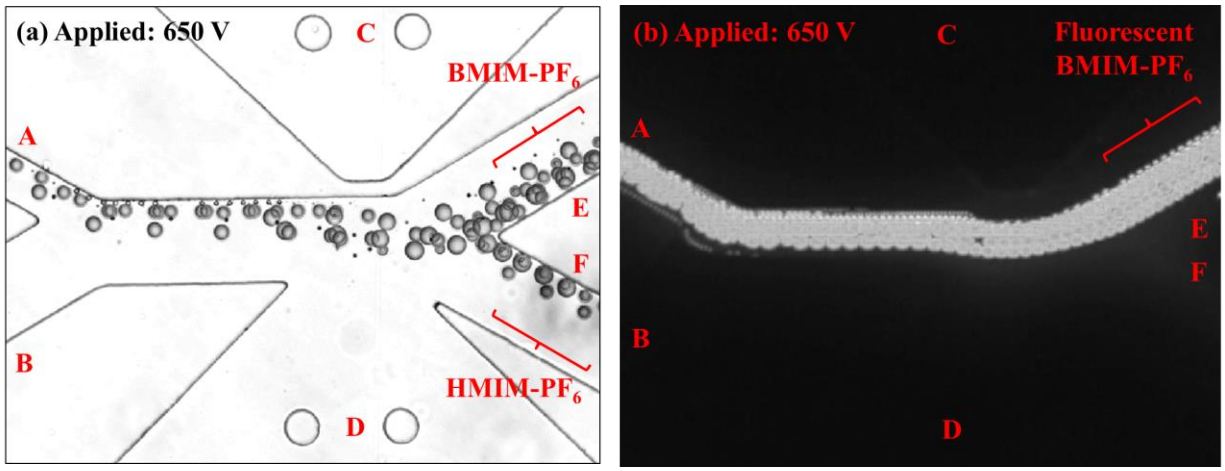

Figure 5-10 (a) Separation of BMIM-PF_6 and HMIM-PF_6 droplets with similar size 21 μm (average). (b) Fluorescent photograph shows the trajectories of the fluorescent BMIM-PF_6 droplets experiencing p-DEP. The employed voltages are ϕ_C=650 V and ϕ_D=0 V. The nano-orifice has a size of 860 nm in width and 15 μm in length, and the large orifice is 125 μm in width.

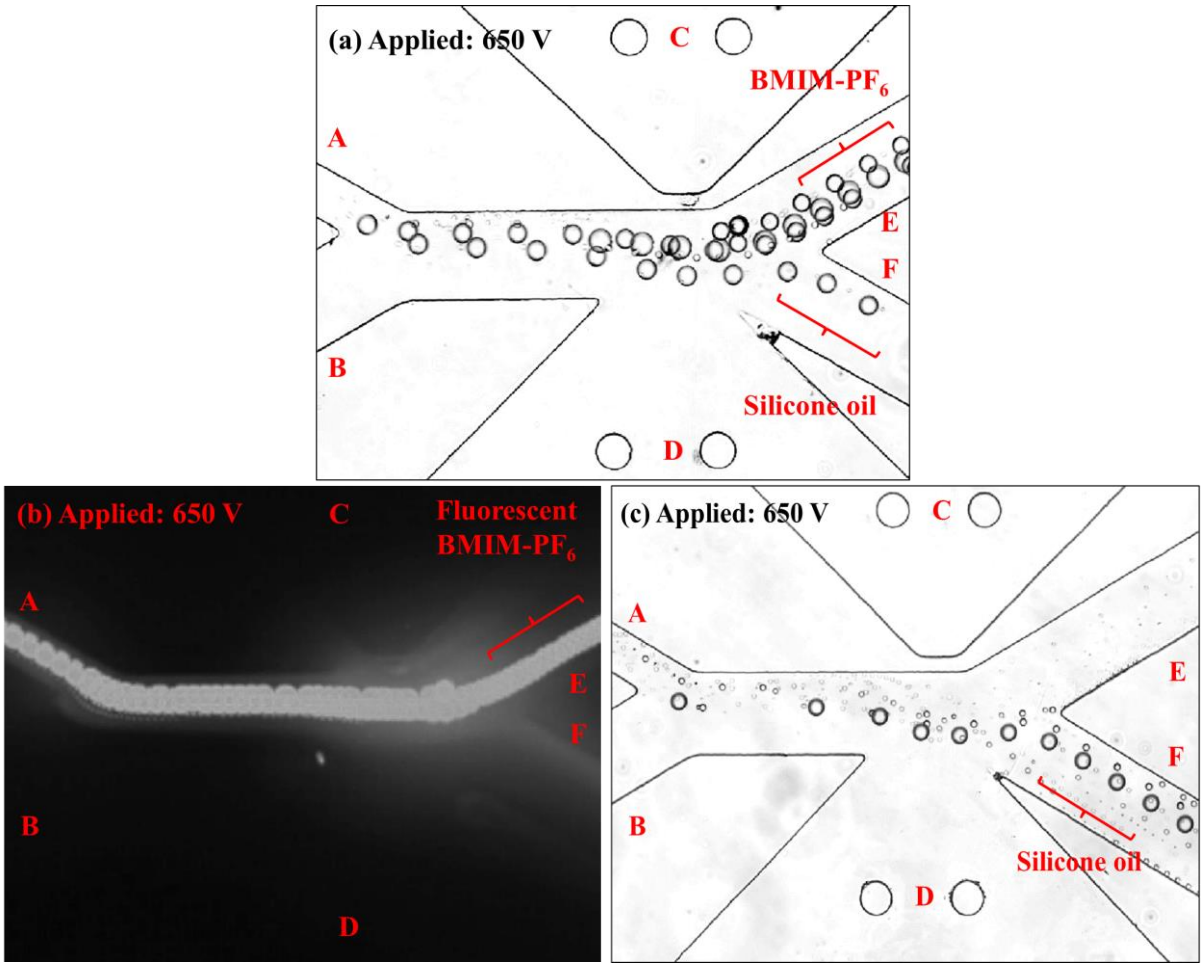

Figure 5-11 (a) Separation of silicone oil droplets and BMIM-PF_6 droplets with a similar size 22 μm (average). (b) Fluorescent photograph shows the trajectories of the fluorescent BMIM-PF_6 droplets undergoing p-DEP. (c) Trajectories of silicone oil droplets experiencing n-DEP. The employed voltages are ϕ_C=650 V and ϕ_D=0 V. The nano-orifice has a size of 860 nm in width and 15 μm in length, and the large orifice is 125 μm in width.

5.4 Conclusion

This chapter presents the dielectrophoretic manipulation and sorting of the ionic liquid/oil-in-water microemulsion droplets under DC electric field. The DC-DEP chip employs a pair of the asymmetric orifices located on opposite sidewalls in the channel to generate the strong gradient of the non-uniform electric field and hence sufficiently large DEP forces. By using pressure-driven flow and a stream of sheath flow, the mixed emulsion droplets move closely to the vicinity of the nano-orifice and experience the stronger DEP effects. Because the magnitude of DEP forces exerting on the droplets is determined by the size of the droplet, the separation of the HMIM- PF_6 droplets with two different diameters of 11.5 μm and

19.5 μm and separation of smaller silicone oil droplets with a small size difference of only 3.5 μm were demonstrated. When the electrical conductivity of the surrounding media is lower than that of the HMIM-PF_6 droplets and BMIM-PF_6 droplets, both IL droplets undergo positive DEP. When the electrical conductivity of the surrounding media is higher than that of the HMIM-PF_6 droplets and BMIM-PF_6 droplets, both IL droplets experience negative DEP. When the electrical conductivity of the suspending medium is lower than that of BMIM-PF_6 droplets but higher than that of HMIM-PF_6 droplets, the BMIM-PF_6 droplets will undergo positive DEP while the HMIM-PF_6 droplets undergo negative DEP. Based on this, the continuous separation of different types of ionic liquid droplets with similar sizes was achieved by choosing the suspending medium with an appropriate electrical conductivity. Therefore, by simply adjusting the applied voltage and the electrical conductivity of the surrounding solution, the separation of target oil droplets with specific size and content can be achieved, presenting a simple and effective method using DC-DEP to manipulate and sort the microemulsion droplets by size and by content for wide applications in industry and research.

CHAPTER 6 Tunable Characterization and Identification of Droplets and Biological Cells by AC-DEP [§]

6.1 Introduction

Integrated biological analysis devices are used in numerous areas of environmental assessment [364], food hygiene and water quality [365,366], point-of-care diagnostics [367], and biomedical and chemical research [320,321,323,368]. In these applications, the separation of particles and cells is crucial. Various methods, such as filtration [369], flow cytometry [370] are exploited for cell manipulation and separation. Inspired by microelectromechanical technologies, microfluidic platforms are widely utilized for miniaturizing and automating the separation and characterization systems because of the advantages of portability, simplicity, low cost, and quick response. Within a variety of approaches utilized in microfluidic chips, dielectrophoresis is one of the most effective techniques and provides the label-free, controllable, and accurate manipulation of targeted biological samples by inducing negative and positive effects on the samples [242,371]. Furthermore, since the magnitude and the direction of the dielectrophoretic forces rely on the dielectric property [41,241,372–374], which represents the corresponding structure, morphology, and chemical feature [375] of the sample, the dielectrophoresis (DEP) enables the analysis of the bioparticles selectively and sensitively [376].

DEP means the induced movement of a polarizable particle in the non-uniform electric fields. For the particles whose polarizabilities are higher than that of the suspending solution, they experience the positive DEP (p-DEP) force and move toward the area of the strongest electric fields. Otherwise, the particles undergoing negative DEP (n-DEP) are pushed away and move toward the weak electric field region if they have lower polarizability than that of the surrounding medium. Both the p-DEP and n-DEP effects have been widely employed for the manipulation and sorting of the particles and biological cells. Generally, different kinds of droplets and biological cells have different but unique dielectric signatures. Such a distinct dielectric characteristic is widely used to sort and characterize the targets by means of AC-DEP. To induce the inhomogeneous electric field, that is, the DEP effects, the microelectrodes of various structures and dimensions, as well as the ionic liquid electrodes [47] and the liquid metal electrodes [48,49] with different configurations and shapes in the desired pattern, are usually integrated into the microfluidic systems [50]. In

[§] A similar version of this chapter was submitted or published as:
(a) Zhao, K.; Li, D. Tunable droplet manipulation and characterization by AC-DEP. ACS applied materials & interfaces 2018, 10(42), 36572-36581. https://pubs.acs.org/doi/abs/10.1021/acsami.8b14430.
(b) Zhao, K.; Li, D. Continuous Cell Characterization and Separation by Microfluidic AC Dielectrophoresis. Analytical chemistry 2019, 91(9), 6304-6314. https://pubs.acs.org/doi/abs/10.1021/acs.analchem.9b01104.

the microdevices with interdigitated microelectrodes, Li et al. [377] investigated the separation of live Listeria innocua cells and heat-treated dead cells by p-DEP and n-DEP, respectively. Kim et al. [378] demonstrated the multi-target cells sorting with high purity using a microfluidic device that has a couple of electrodes placed at two different glancing angles to the flow direction. In comparison with the two-dimensional micro-electrode structures, which suffer from the adhesion of the particles on the microelectrodes or channel walls and a confined DEP effective area over the electrode surface [242], hence a low efficiency, the three-dimensional electrode-based micro-systems offer an increased DEP effective region, leading to an efficiency increase of the microfluidic devices and avoiding the particle adhesion. Because of the adjustable widths of the microelectrodes, the electric field strength changes through the transverse direction of the microchannel, which results in an increased separation sensitivity and achieves the separation of red blood cells and mouse P19 cells. Furthermore, by manufacturing arrays of microelectrodes with a defined geometry by silicone, the required gradient of the electric fields for DEP effects and the gradient of the liquid velocity were generated, which lead to the successful separation of living and dead yeast cells [142]. The manipulation and sorting of microbeads and cells [379,380] were demonstrated by patterning pairs of vertical interdigitated microelectrodes on the microchannel sidewalls to generate non-uniformity of the electric fields in a microfluidic device. As the height of the microchannels can be adjusted without reducing the strength of the electric fields, this dual-frequency DEP device achieves high sorting throughput. Generally, the embedded electrode-based DEP systems suffer from the complicated fabrication of the microelectrodes, electrolytic reactions at the electrodes, as well as bubble generation. The insulating structure-based DEP platforms eliminate these problems by placing the electrode outside of the working fluidic channel. For such an approach, the gradient of the non-uniform electric field is produced by employing insulating structures between the electrodes in the microchannels. By fabricating arrays of insulating posts within a microchannel, the concentration and separation of particles and cells become achievable [40,381]. By using the insulating circular cylinders in the microchannel to generate DEP effects, the concentration and sorting of live and dead bacteria [382], the selective isolation of viable and nonviable human leukemia cells [383], and the manipulation of pET28b plasmids [384] were demonstrated. However, all these current AC-DEP methods involve issues of complicated fabrication of microelectrodes in microchannels with patterned structures and electrochemical reactions on the surface of electrodes. Furthermore, because of the challenge of producing a high gradient of the non-uniform electric field, these methods always involve high electrical potentials, which require the expensive amplifier instruments [52,385].

In the AC-DEP methods, by modifying the frequency of the applied ac electric fields, various soft droplets or biological cells will show different DEP behaviors. The key parameter of the transition between p-DEP and n-DEP effects is named as the crossover frequency, where the DEP forces are zero. This important AC-DEP characteristic is reflected by the Clausius−Mossotti (CM) curve for each kind of targets.

As the crossover frequency depends on the electrical properties of the particles and surrounding solution, this unique information can be utilized to optimize the characterization and separation schemes [53–55]. Nevertheless, very little information can be found in the literature about experimentally determined CM factor curves and the critical frequency for the cells, and it is difficult to calculate the CM factor of particles, cells, or biomolecules and to find the corresponding crossover frequency, owing to the heterogeneous structures in the biological cells, complex compositions, and charging distributions [372].

This chapter presents a newly designed AC-DEP microfluidic chip for tunable manipulation and characterization of droplets/particles and cells [386,387]. The microfluidic chip employs a pair of asymmetric orifices on opposite sidewalls of the main channel with inserted electrodes to generate a non-uniform electric field by using the ac electric field. By utilizing pressure-driven flow, the droplets and cells experience DEP behaviors only when passing through the vicinity of the small orifice, where the strongest gradient of the non-uniform electric field exists. The AC-DEP behaviors of polystyrene particles and oil/IL-in-water droplets and the effects of the medium electric conductivity on the CM factors of the viable and nonviable yeast cells are investigated. For the first time, the lateral migrations of the polystyrene particles, BMIM-PF_6 droplets, and yeast cells as a function of the AC frequency are measured. The trends of the lateral migrations of the cells are similar to the corresponding curves of CM factors. By adjusting the medium conductivity, the desired DEP response of the bioparticles for the various applications can be achieved. Measuring the lateral migration of cells throughout the frequency spectrum provides a strategy to evaluate the crossover frequency of the biological particles and characterize the cells. By simply controlling the frequency of the AC electric field, the sorting of the live and dead yeast cells with similar size but different dielectric properties and the separation of different types of emulsions droplets in the same diameter are demonstrated. The developed microfluidic chip provides a powerful tool to recognize the crossover frequency of the biological particles and characterize the cells.

6.2 Materials and methods

6.2.1 Dielectrophoresis of droplets and yeast cells

Dielectrophoresis describes the motion of polarizable particles in a non-uniform electric field, E. The DEP force creates such a movement and is defined as [46,60]

$$\mathrm{F_{DEP}} = 2\pi\varepsilon_m r^3 \mathrm{Re}(f_{\mathrm{CM}})(\nabla|E|^2) \qquad (6\text{-}1)$$

in which r represents the radius of the particle, ε_m is the dielectric constant of the medium, $\nabla|E|^2$ is the electrical field gradient squared and Re represents the real part of the complex function known as the Clausius-Mossotti (CM) factor, f_{CM}. The CM factor, f_{CM}, describes the relative polarization of a particle

with respect to the surrounding medium, and is a geometry- and frequency-dependent function. For yeast cells, the CM factor using the double-shell structures model [60,228,388] is given by:

$$f_{\mathrm{CM}} = \frac{\varepsilon^*_{cell} - \varepsilon^*_m}{\varepsilon^*_{cell} + 2\varepsilon^*_m} \tag{6-2}$$

$$\varepsilon^*_{cell} = \varepsilon^*_{wall} \frac{\left[\frac{r_{wall}}{r_{membrane}}\right]^3 + 2\left[\frac{\varepsilon^*_{interior+membrane} - \varepsilon^*_{wall}}{\varepsilon^*_{interior+membrane} + 2\varepsilon^*_{wall}}\right]}{\left[\frac{r_{wall}}{r_{membrane}}\right]^3 - \left[\frac{\varepsilon^*_{interior+membrane} - \varepsilon^*_{wall}}{\varepsilon^*_{interior+membrane} + 2\varepsilon^*_{wall}}\right]}$$

$$\varepsilon^*_{interior+membrane} = \varepsilon^*_{membrane} \frac{\left[\frac{r_{membrane}}{r_{internal}}\right]^3 + 2\left[\frac{\varepsilon^*_{internal} - \varepsilon^*_{membrane}}{\varepsilon^*_{internal} + 2\varepsilon^*_{membrane}}\right]}{\left[\frac{r_{membrane}}{r_{internal}}\right]^3 - \left[\frac{\varepsilon^*_{internal} - \varepsilon^*_{membrane}}{\varepsilon^*_{internal} + 2\varepsilon^*_{membrane}}\right]} \tag{6-3}$$

where the subscript *cell* denotes the yeast cell, and ε^* represents the complex permittivity of the particles and the solution which is expressed as:

$$\varepsilon^* = \varepsilon - (j\sigma/\omega) \tag{6-4}$$

where ε expresses the permittivity of the targets or the surrounding medium and σ indicates the corresponding electrical conductivity, and $j = \sqrt{-1}$; $\omega = 2\pi f$ is the angular frequency of the electric field, and f is the ordinary frequency (in Hz).

For a single cell in suspension, there are two intrinsic relaxation frequencies for the system [389,390]. Under low frequency, the first relaxation, i.e., the first crossover frequency, occurs due to the Maxwell-Wagner polarization of the cell membrane-surrounding solution interface and the cells experience negative DEP forces. In this condition, the f_{CM} is solely dependent on the electrical conductivity of the cell and the suspending media. After the first critical frequency, the cell membrane capacitance is short-circuited due to the polarization between the cell interior and the suspension, where the second relaxation happens at a higher frequency and leads to the positive DEP effects. Beyond the second critical frequency, the relatively smaller dielectric permittivity of the cell interior than the suspending medium result in the negative DEP behaviors again.

It can be seen from Equation (6-1) that the DEP force increases with the volume of the yeast cells (r^3) and the gradient of the electric fields squared ($\nabla|E|^2$), while the sign of f_{CM}, ranging from −0.5 to 1, determines the direction of the cells' DEP motion. A positive value of the CM factor means that the particle will move towards the stronger electric field, this is referred to as positive dielectrophoresis (p-DEP). A negative value of the CM factor means that the particle will move towards the weaker electric field, this is referred to as the negative dielectrophoresis (n-DEP). As illustrated by Equation (6-2), the CM factor

embodies the influential parameters of the dielectric characteristics of the cells and the surrounding solution in terms of their conductivity and permittivity. In addition, the f_{CM} for the yeast cells is also a function of its interior multi-layer structures, as well as the applied frequency. By adjusting the frequency of the AC electric field, the value of f_{CM} can be switched from negative to positive and vice versa. The changeover between the positive and negative dielectrophoretic behaviors is characterized by the crossover frequency which corresponds to $f_{CM} = 0$. Such a critical or crossover frequency reflects the intrinsic properties for various biological particles under AC-DEP, leading to the characterization of different kinds of cells as well as the manipulation and separation of the target cells.

6.2.2 Fabrication of the microfluidic chip

The design of a microfluidic chip to measure the AC-DEP lateral migration of droplets and yeast cells is shown in Figure 6-1(a) and Figure 6-1(b). In the chip, there is a microchannel, as shown in Figure 1(A), which is composed of three inlet branches and the main channel connecting to four different reservoirs. The main channel is 200 μm in width and has a length of 500 μm. The sheath flow inlets B and C, and the sample inlet A are 100 μm and 200 μm in width, respectively. All channels have a uniform height of 27 μm. Because of the height restriction of the sample inlet channel, only the droplets smaller than 27 μm in diameter are allowed to enter into the sample inlet branch and move through the microchannel. The dimensions of the patterned copper electrode pads re 25 μm in thickness and 500 μm in width, shown in the Appendix D. Two asymmetric orifices, a 10 μm wide small orifice and a 500 μm wide large orifice are situated in the horizontal main channel, as shown in Figure 6-1(b). The droplets/particles and yeast cell samples are loaded in the inlet A and introduced into the main channel by pressure-driven flow (i.e., the differences between the liquid heights in the inlet and outlet reservoirs). Focusing by the sheath liquid flowing from inlets B and C, the droplets and yeast cells move along the center streamline of the main channel and enter the DEP affecting regions between the two orifices where the corresponding lateral migrations are measured.

To achieve the AC-DEP manipulation and isolation of the droplets/particles, as well as the live and dead yeast cells, a different microfluidic chip was designed, as shown in Figure 6-1(c-f). This microfluidic chip includes four branches which are connected to four different wells. Reservoirs A and B are used to load the mixture of the droplets/particles or the yeast cells and the sheath liquid, respectively. After moving through the vicinity of the asymmetric orifices, these isolated droplets/particles or yeast cells are isolated by experiencing the p-DEP and n-DEP effects and collected in the wells C and D, respectively. For the main channel, it is 200 μm in width and the height of the entire channel is 27 μm. The width of the sample channel and the width of the sheath flow channel are 100 μm and 200 μm, respectively, while the outlet

branch connecting reservoir C and the outlet channel D has a width of 100 µm and 200 µm, respectively. The microfluidic chip was bonded on a glass substrate by using the soft lithography method.

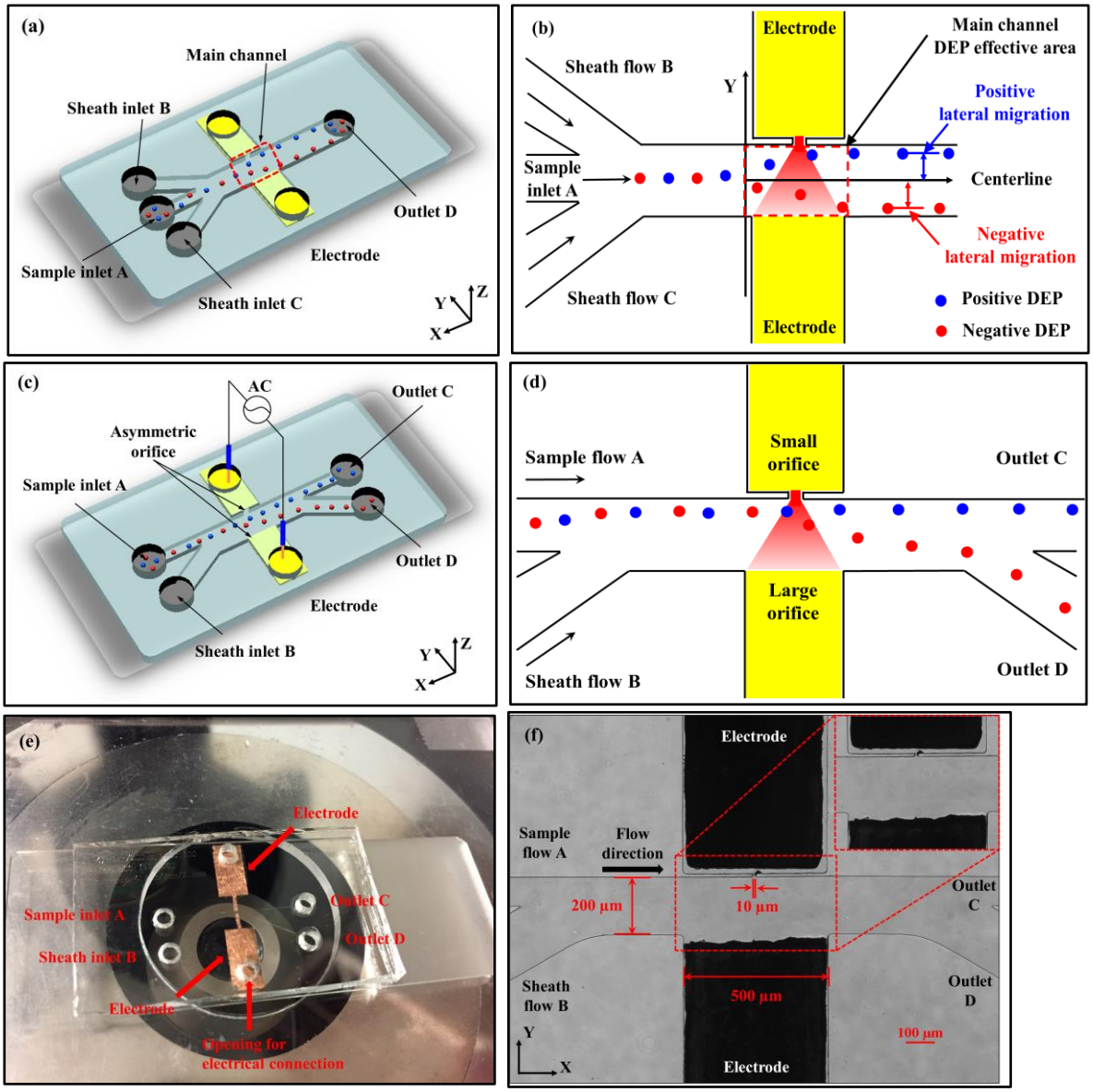

Figure 6-1 (a) Schematic illustration of the microchannel for the measurement of the lateral migration of the yeast cells (red color indicates the electric field strength). (b) Top view illustrates the working principle for measuring the lateral migration of the cells. (c) Schematic diagram of the microchannel for droplet/cell separation. (d) Top diagram of the working principle for continuously separating the samples. (e) Schematic diagram of the microfluidic device with embedded electrodes by AC-DEP. (f) Microscopic image of the AC-DEP microchannel and a zoom-in photograph of the asymmetric orifice area.

6.2.3 Sample preparation and experimental procedure

Polystyrene (PS) microparticles of two different diameters, 5 μm and 10 μm (Bangs Laboratory), the mixture of the 1-Butyl-3-methylimidazolium hexafluorophosphate (BMIM-PF_6) droplets and 1-Hexyl-3-methylimidazolium hexafluorophosphate (HMIM-PF_6) (IoLiTec Inc) droplets, as well as the mixture of the BMIM-PF_6 droplets and silicone oil (XIAMETER PMS-200) droplets are used to examine their DEP behaviours. The physical-chemical properties of these particles and droplets are shown in Table 6-1. The values of the CM factor (f_{CM}) for the above-mentioned particles and droplets are plotted as a function of the frequency of the AC electric field, f, and is shown in Figure 6-2. In this work, the DI is employed as the suspending media. It can be seen from Figure 6-2 that, the 5 μm and 10 μm PS particles and the droplets of silicone oil always experience negative dielectrophoretic forces throughout the frequency spectrum of the AC electric field. While the BMIM-PF_6 droplets experience positive DEP effects before the critical frequency, i.e., 2.3×10^7 Hz in DI water and then undergo negative DEP when the frequency of the AC electric field is higher than the critical frequency. Likewise, the crossover frequency of the HMIM-PF_6 droplets is 1.3×10^7 Hz in DI water. In the experiments, all the particles and droplets are suspended in the DI water with a pH value of 7, a dielectric constant of 80, and an electric conductivity of 5.5×10^{-6} S/m. The ionic liquid(IL)-in-water microemulsion and the oil-in-water microemulsion are generated by mixing the DI water and the silicone oil or the hydrophobic ionic liquids with the non-ionic surfactant Tween 20 (Sigma-Aldrich) as the stabilizer. In order to visually observe the different DEP behaviors, i.e., different trajectories, of these emulsion droplets, the fluorescent dye of Nile Red (Sigma-Aldrich) is injected inside the BMIM-PF_6 droplets. To fabricate the IL/oil-in-water emulsion, 1 mL IL or silicone oil, 5 mL DI water, and 100 μL Tween 20 are added in the glass bottle and the mixture was stirred vigorously by a vortex mixer (VWR Scientific) at a speed of 3200 rpm for 1.5 min.

Table 6-1 Physical-chemical properties and critical frequency of the 5 μm and 10 μm PS particles, the silicone oil droplets, the droplets of BMIM-PF_6 and HMIM-PF_6 in DI water with a pH value of 7, a dielectric constant of 80, and an electric conductivity of 5.5×10^{-6} S/m.

Property	Conductivity (S/m)	Dielectric Constant	Critical frequency (Hz)
5 μm PS particles	10^{-13}	$\approx 2\varepsilon_0$	n/a
10 μm PS particles	10^{-13}	$\approx 2\varepsilon_0$	n/a
Silicone oil droplets	10^{-13}	$\approx 2\varepsilon_0$	n/a
Droplets of BMIM-PF_6	0.137	$\approx 11\varepsilon_0$ [391]	$\approx 2.3\times10^7$

Droplets of HMIM-PF$_6$	0.008	≈14ε_0 [391]	≈1.3×10^7

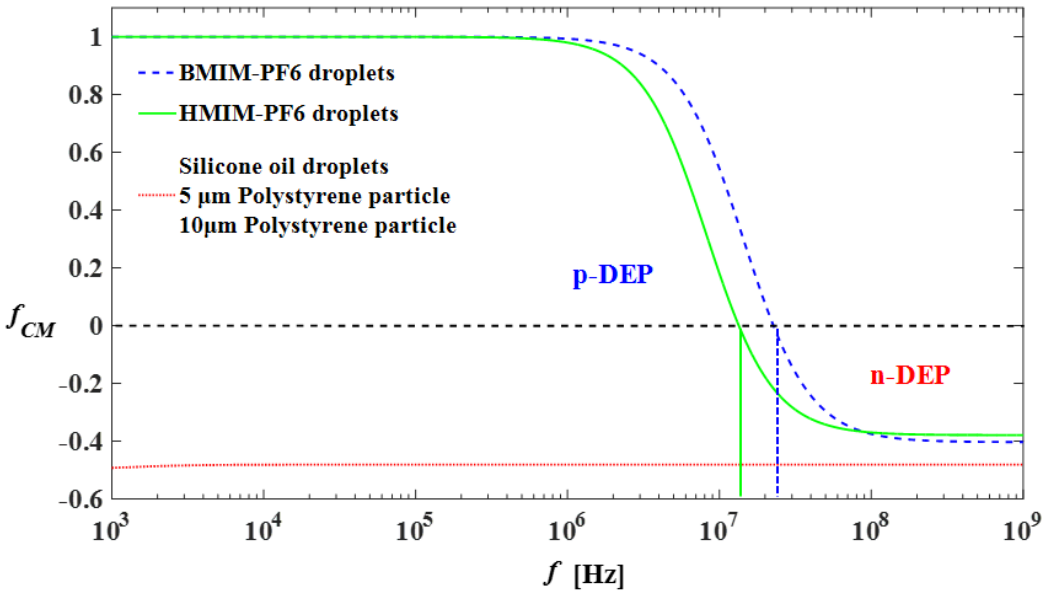

Figure 6-2 Prediction of f_{CM} for the 5 μm and 10 μm PS particle, the droplets of silicone oil, BMIM-PF$_6$, and HMIM-PF$_6$ as a function of the frequency of the applied AC electric field f.

For the yeast cells (standard lab yeast strain, Saccharomyces cerevisiae S288c), they are initially grown in liquid YPD media (1% yeast extract, 2% peptone, and 2% glucose) at 30°C with shaking. After 2 days, the cells are divided into two sets: one was kept in YPD media and the other one in DI water to induce nutrient deprivation. All of the samples are suspended in three liquids: (1) DI water with σ_m =0.0002 S/m, a dielectric constant of 80, and a pH value of 7; (2) the 0.4mM K_2HPO_4 solution with σ_m =0.01 S/m, a dielectric constant of 80, and a pH value of 7; and (3) the 4.8mM K_2HPO_4 solution with σ_m =0.12 S/m, a dielectric constant of 80, and a pH value of 7, respectively. To stain the dead cells, Methylene blue (Sigma-Aldrich) is added to the suspension and kept stirring for 2 min [392,393]. Methylene blue is a dye that is used to differentiate viable and non-viable yeast cells [394]. It enters all the yeast cells, however, only the viable cells will remain colorless due to their enzymatic ability to reduce the dye. The dead cells will be stained dark blue [395], shown in the Appendix G. During the experiments, the samples are introduced into the inlets channel and transported through the outlets by the pressure-driven flow, i.e., the liquid heights difference between the inlet reservoir and the outlet reservoir. In this study, the flow rate is approximately 3.75×10^{-3} μLs^{-1}. By controlling the liquid volumes deposited into the inlet reservoirs (i.e., different liquid levels), the flow rate is adjustable. The microchannel is observed with an inverted optical microscope (Nikon TE 2000) to examine the responses of the viable and non-viable yeast cell samples. An alternating square wave of the

AC electric field was applied to the embedded electrodes using the function generator (model 8550, Tabor Electronics Ltd.).

In the investigation of the lateral migration of the droplets and yeast cells, the triple-inlet shaped microfluidic chip is utilized, as shown in Figure 6-1(a). The non-uniformity of the electric field was produced by a pair of asymmetric orifices between the inserted electrode pads. The samples are loaded into the sample inlet reservoir A after injecting the suspending solution into the whole channel. As the sample solution and sheath flow solution are added into the corresponding wells with the same volume, the trajectory of the cells moving along the main microchannel becomes solely determined by the ratio between the widths of the sample inlet branch and the focusing inlet branch. In this system, the width of the sheath flow inlet channel is 2 times larger than that of the sample inlet channel, which is 200 μm and 100 μm, respectively; hence the samples are focused to flow along the centerline of the main channel by the sheath fluids from inlet branches B and C. When moving through the area of the asymmetric orifices, the cells undergo the DEP forces. For the droplets or yeast cells experiencing the p-DEP, they are attracted toward the small orifice and move away from the centerline of the main channel. On the contrary, the droplets or yeast cells subjected to the n-DEP effects migrate away from the centerline of the main microchannel toward the large orifice. Then, the lateral migrations of the viable and non-viable yeast cells in the suspending solutions with different electrical conductivity can be measured.

In order to sort the live and dead yeast cells, a mixture of 50-50% viable and non-viable samples in DI water is prepared. For the separation of droplets/particles, the microchannel with a pair of asymmetric orifices in between the embedded electrodes was utilized. In the experiments, 10 μL of the relevant suspending medium was introduced into the inlet reservoir to wet the whole microchannel. Then, 10 μL of the droplets/particles or mixed cells are injected into the sample inlet branch and are transported to the outlet well by the pressure-driven flow. The samples from the inlet branch A moved into the main channel and were focused by the flow from branch B to move closely to the small orifice. Limited to the height of the microchannel, only the droplets smaller than 27 μm are allowed to enter the main channel. After submerging the platinum wires into the opening of the microelectrode chambers, the electric field was applied via the asymmetric orifice to the microchannel with the ac power supply (model 8550, Tabor Electronics Ltd.). These droplets/particles or cells experienced DEP forces and hence the trajectories shift correspondingly when moving through the area of the asymmetric orifices. As the magnitude of the DEP force is proportional to the diameter of the particles and droplets, the separation by size can be achieved straightforwardly. In this way, the particles with a smaller size will flow into the outlet branch C and the ones with a larger size will move into the outlet branch D. By using this chip, the separation of the mixed droplets of BMIM-PF_6 and HMIM-PF_6, mixed droplets of silicone oil and BMIM-PF_6, as well as the live

and dead yeast cells with a similar size, is achieved. By tuning the applied electrical frequency, the droplets or cells whose CM factor are positive will experience the p-DEP forces and be attracted toward the small orifice, leading to the movement into the outlet branch C. For the droplets or cells having a negative value of CM factor, they are repelled away from the small orifice by the n-DEP effects and move into the output branch D. The characterization and separation of the droplets/particles and yeast cells are visualized under the microscope and a CCD camera (QImaging) is applied to record the images at 25 frames. In this work, all the experiments are carried out at room temperature approximately 25 ± 1 °C.

6.3 Results and discussion

6.3.1 Simulation of the electric field and droplet trajectory

Figure 6-3 shows the distribution of the electric field near the asymmetric orifices and an example of the trajectories of the 15 μm droplets of silicone oil and BMIM-PF_6 and are demonstrated, which are calculated by using COMSOL 4.3b. In this chip, the gradient of the electric fields is induced by applying the AC electric field via the asymmetric orifices across the microchannel through the embedded electrodes. The strongest non-uniform electric field is generated near the small orifice, as shown in Figure 6-3(a). As the magnitude of the DEP forces increase with the particle radius, the DEP forces on the larger particles are stronger, resulting in larger trajectory shifts. As an example, the trajectory changes of 5 and 10 μm polystyrene particles are shown in Figure 6-3(b). The smaller ones experience relatively weaker negative dielectrophoretic effects and flow into the upper outlet channel C. While the larger particles are repelled away from the small orifice area into the outlet channel D. However, it can be inferred from Figure 6-3(c), the 15 μm silicone oil droplets and 15 μm BMIM-PF_6 droplets are injected into the main microchannel from inlet branch A and forced by the sheath flow from channel B to flow along the side walls with the small orifice, where the maximum gradient of the electric fields exits. The BMIM-PF_6 droplets experiencing p-DEP forces, i.e., positive lateral migration from the centerline of the main channel, are attracted towards the small orifice and move into the output reservoir C. The silicone oil droplets are repelled away from the small orifice by the negative dielectrophoretic effects, i.e., negative lateral migration from the centerline of the main channel, and then flow into the outlet reservoir D. Polystyrene particles always experience negative DEP. Therefore, the asymmetric orifice based AC-DEP microfluidic chip can realize the size-dependent separation of particles/droplets and the sorting of different kinds of particles/droplets by experiencing the opposite DEP behaviors.

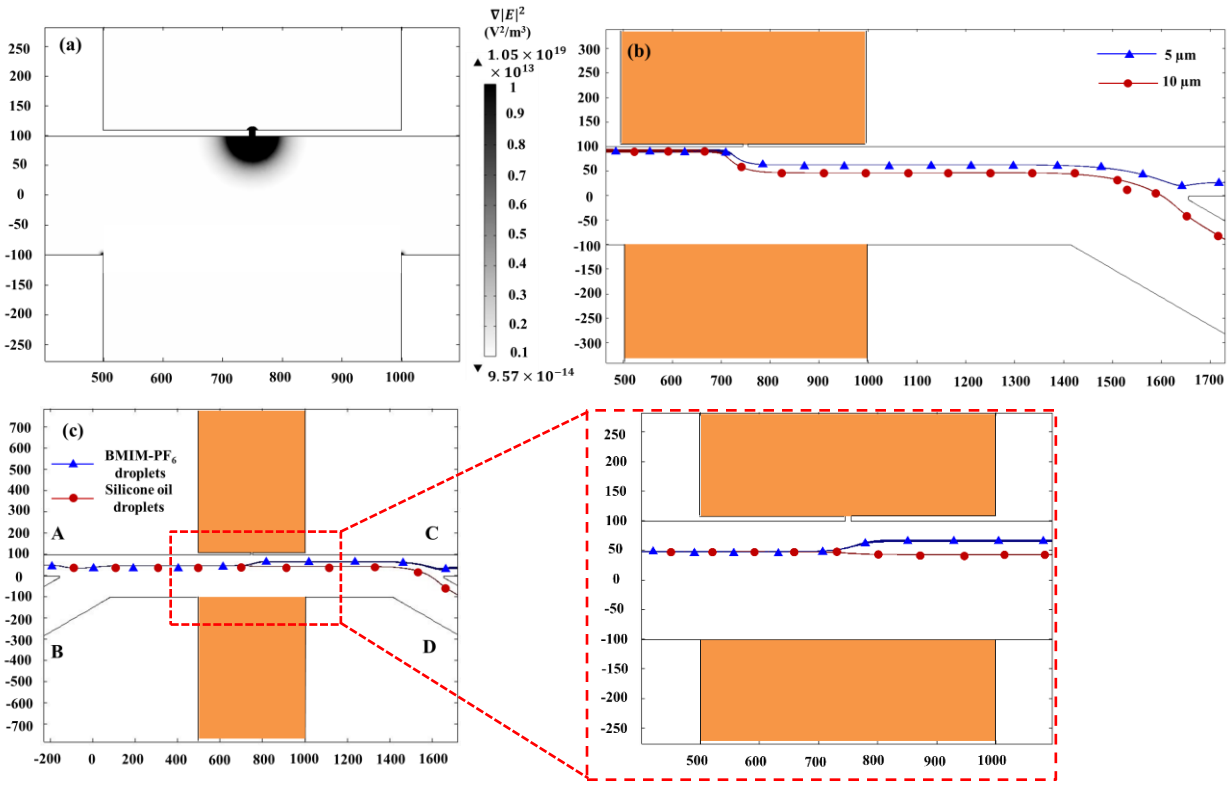

Figure 6-3 Distribution of the electric field in the microchannel and trajectory of the PS particles, and the droplets of silicone oil droplets and BMIM-PF_6. (a) Distribution of the gradient of the electrical field squared ($\nabla|E|^2$). (b) An example of the separation of the 5 and 10 µm polystyrene particles under the electric voltage of 10 Vp-p and the frequency of 100 kHz. (c) An example of the separation of the 15 µm the BMIM-PF_6 droplets (blue) and the silicone oil droplets (red) in the channel. The small orifice has a width and length of 10 µm, and the large orifice is 500 µm in width. The applied frequency of the AC electric field is 100 kHz and the electric voltage is 5 Vp-p.

6.3.2 Effect of the frequency and $V_{peak\text{-}peak}$ of AC electric field

6.3.2.1 Effect of the applied voltage $V_{peak\text{-}peak}$

The effect of the applied voltage on the trajectory of 10 µm polystyrene particles was conducted by applying the Vpeak-peak from 0 to 8 V (alternating square waves of 100 kHz). The DI water with a pH value of 7, a dielectric constant of 80, and an electric conductivity of 5.5×10^{-6} S/m was employed as the suspending solution. The applied frequency of the AC electric field is 100 kHz and the polystyrene particles always experience negative DEP forces, as inferred from the Figure 6-2. In these experiments, the width of the small and large orifice is 10 µm and 500 µm, respectively.

It should be realized that according to Equation (6-1), the DEP forces increase with the gradient of the electric field square ($\nabla|E|^2$). As the applied voltage increases, the DEP force will increase. As shown in

Figure 6-4(a) under 0 volts, the DEP force is zero, thus there is no trajectory change of the particles after passing the small orifice. They all flowed into the outlet reservoir C. When 2 Vp-p was applied, as shown in Figure 6-2(b), the DEP force made an apparent trajectory shift from the small orifice. However, the trajectory shift of the particles is not large enough and a portion of them still flowed into the outlet reservoir C. It can be found from Figure 6-2(c), when the applied potential was increased to 8 Vp-p, the strong DEP force at the small orifice region caused significant trajectory change for the particles, so that the particles continuously moved into outlet channel D.

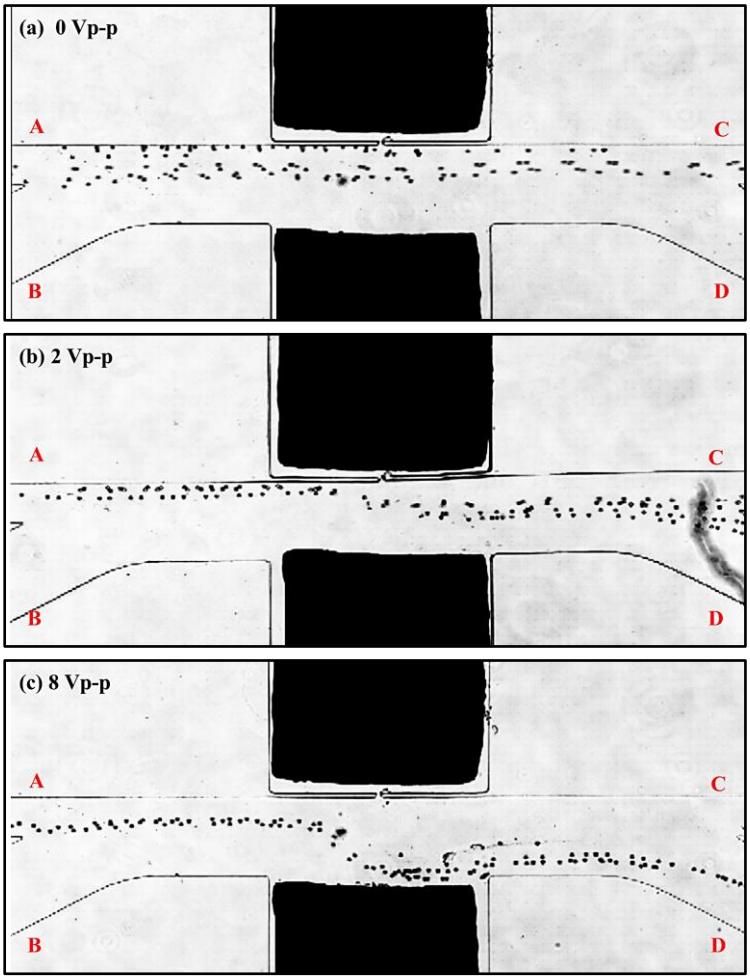

Figure 6-4 (a) Effects of the applied voltage on the trajectory of 10 µm particles by n-DEP forces in the AC-DEP chip developed in this work. The dependence of the particles' trajectories on the applied Vp-p (A) 0 V, (B) 2 V, (C) 8 V. The applied frequency of the AC electric field is 100 kHz.

6.3.2.2 Effect of frequency

Polystyrene particles

To examine the effects of the frequency of the AC electric field on the trajectory of 10 μm PS particles, two different frequencies, 100 kHz, and 10 MHz, were conducted. As demonstrated in Figure 6-2, the value of the f_{CM} for the 10 μm PS particles is always around −0.5. This indicates that they will undergo negative DEP effects throughout the frequency spectrum of the AC electric field. It is clearly seen from Figure 6-5 that the 10 μm PS particles indeed undergo n-DEP effects and are repelled away from the small orifice in the wide frequency range. In addition, it can be seen that the trajectory shift of PS particles under 10 MHz (Figure 6-5(b)) is slightly smaller than that under 100 kHz (Figure 6-5(a)). This can be understood as follows. Because the dielectrophoretic forces are proportional to the magnitude of CM factor; by using Equation (6-1), the magnitude of the f_{CM} is 0.48 under the frequency of 10 MHz, while $f_{CM} = 0.5$ at the frequency of 100 KHz. Therefore, the trajectory shift of the PS particles under a higher frequency (10 MHz) in Figure 6-5(b) is smaller than the trajectory shift under the frequency of 100 kHz demonstrated in Figure 6-5(a).

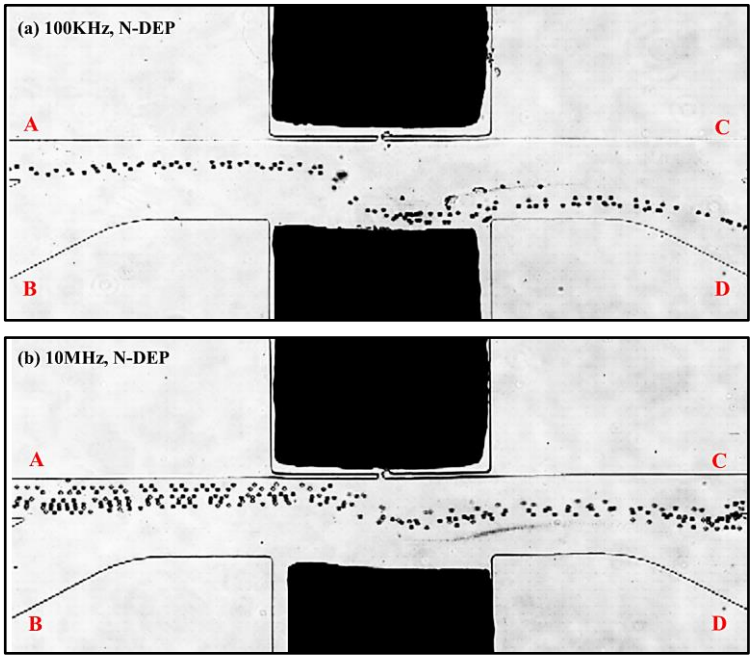

Figure 6-5 Effects of the frequency of the AC electric field on the trajectory of 10 μm PS particles. The dependence of the particles' trajectories on the applied frequency f (A) 100 KHz, (B) 10 MHz, and the applied electric voltage is 8Vp-p.

BMIM-PF_6 droplets

It can be seen from Figure 6-2 that, the ionic liquid droplets of BMIM-PF_6 experience positive DEP effects below the critical frequency, i.e., 2.3×10^7 Hz in DI water and undergo negative DEP forces when the applied frequency is higher than the crossover frequency. To examine the effect of the frequency of the AC electric field on the trajectory of BMIM-PF_6 droplets, two different frequencies, i.e., 100 kHz (below the crossover frequency) and 35 MHz, (above the crossover frequency) were applied separately. In this way, the BMIM-PF_6 droplets should undergo from the positive DEP to the negative DEP. It can be figured out from Figure 6-6 that when the critical frequency of the BMIM-PF_6 droplets is higher than the frequency of the AC electric field, $f_{CM} > 0$, the droplets are attracted towards the maximum electric field gradient by the positive DEP forces and flow in outlet channel C. When the frequency of the AC electric field is higher than the critical frequency, $f_{CM} < 0$, the droplets will be repelled away from the high electric fields region by the n-DEP effects and move into the outlet reservoir D. The experimentally observed frequency dependence of DEP behaviors of the BMIM-PF_6 droplets matches well with the prediction of DEP theory.

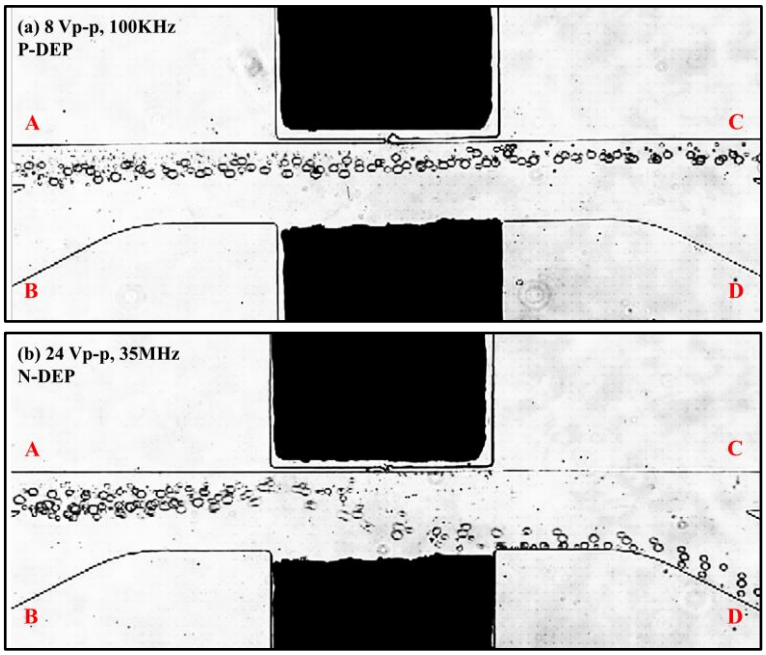

Figure 6-6 Effects of the frequency of the AC electric field on the trajectory of the 15 μm BMIM-PF_6 droplets, whose critical frequency is 2.3×10^7 Hz in DI water. The dependence of the particles' trajectories on the applied frequency f (A) 100 KHz, (B) 35 MHz.

6.3.3 Prediction of the CM factor spectra of yeast cells

The DEP manipulation of the cells has been conducted in a wide range of the electrical conductivity of the suspending solutions [7]. In the surrounding medium with low electric conductivity, the cells

experience the p-DEP forces. In a solution of low electric conductivity, the Joule heating and the bubble generation become negligible. Whereas, due to the diffusion pressure disrupting the plasma membrane, the ions from the cells may leak into the solution. Alternatively, when increasing the electrical conductivity of the media, various DEP applications such as lateral sorting and electrothermal-assisted DEP can be achieved, which mainly rely on the n-DEP behaviors of the cells. To examine the effects of the medium conductivity, the CM factors of the viable and non-viable yeast cells in the suspending media with different concentrations, i.e., different electrical conductivities, are drawn varying with the AC electric field frequency, f. The results are plotted in Figure 6-7 and Matlab codes are listed in Appendix B. The physical-chemical properties of the live and dead yeast cells are shown in Table 6-2.

Table 6-2 The physical-chemical properties of the viable and non-viable yeast cells [228].

Property	Viable	Non-viable
Interiors Conductivity (S/m)	0.2	7×10^{-3}
Membrane Conductivity (S/m)	2.5×10^{-7}	1.6×10^{-4}
Wall Conductivity (S/m)	1.4×10^{-2}	1.5×10^{-3}
Interiors Dielectric Constant	50	50
Membrane Dielectric Constant	6	6
Wall Dielectric Constant	60	60
Interiors Radius (μm)	3.772	3.242
Membrane Radius (μm)	3.78	3.25
Wall Radius (μm)	4	3.5

As shown in Figure 6-7, the live and dead yeast cells in solutions of different ionic concentrations have different CM factor curves varying with AC electric field frequency. For the viable cells, as shown in Figure 6-7(a), when the medium conductivity is low, most of them demonstrate positive DEP behaviors. When the conductivity of the solution increases to $\sigma_{\mathrm{medium3}}$=0.01 S/m, the cells first experience the negative DEP and then positive DEP after passing through the first critical frequency. Finally, the cell transit to the n-DEP effects again when the critical frequency is smaller than the applied frequency. However, the live yeast cells undergo negative DEP in most parts of the frequency spectrum when the solution's conductivity is as high as $\sigma_{\mathrm{medium4}}$=0.12 S/m. For the dead yeast cells, when the AC frequency

increases, they experience positive DEP and then transfer to negative DEP when the solution's conductivity is lower than 0.001 S/m. However, when the solution's conductivity is raised to higher than 0.01 S/m, they always exhibit negative DEP behaviors throughout the frequency spectrum. Therefore, the electrical conductivity of the suspending solution can be utilized to achieve the desired DEP response of the cells for the specific applications.

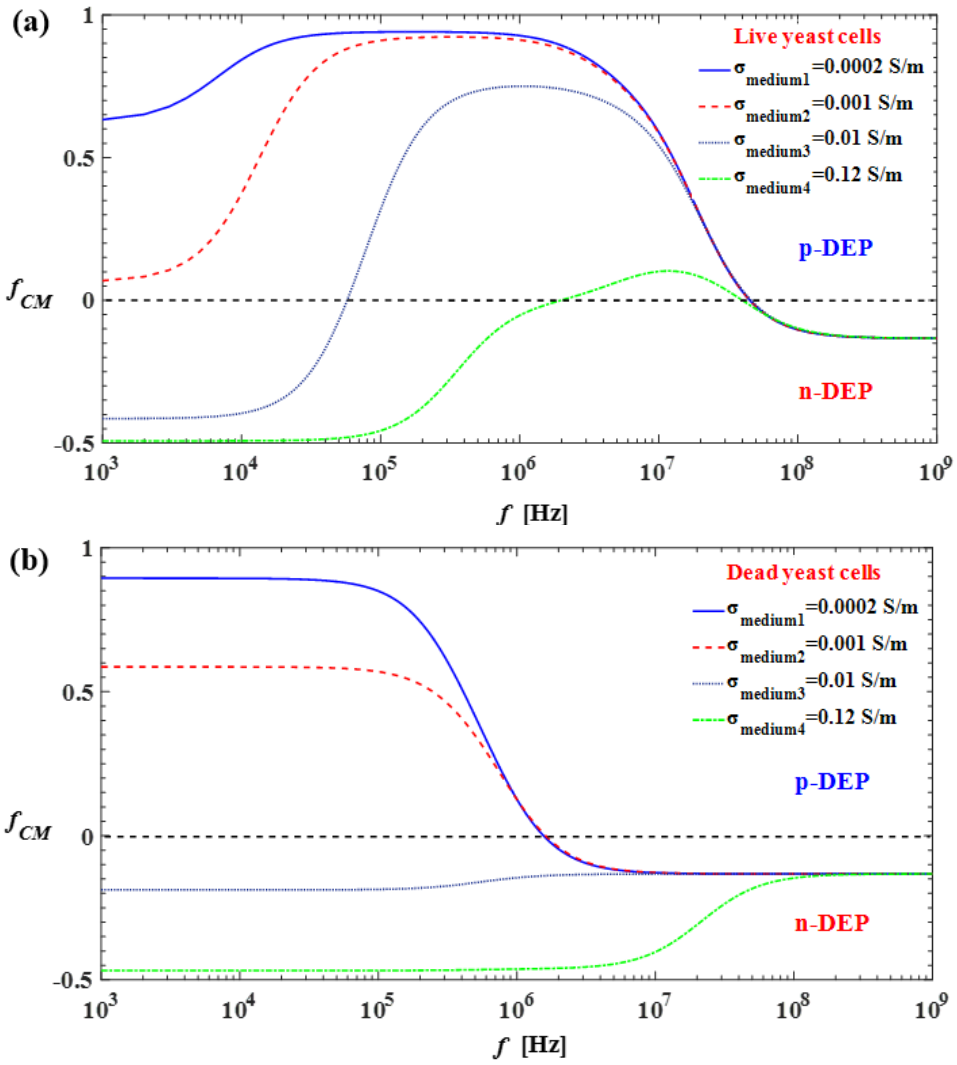

Figure 6-7 Prediction of the f_{CM} for the (a) *viable and* (b) *non-viable yeast cells in the suspending medium with different concentration, i.e., different electrical conductivities, varying with AC electric field frequency.*

6.3.4 Measurement of the lateral migration

Yeast cells

In the AC-DEP, the DEP behaviors become dependent on the frequency of the applied AC electric fields and the medium conductivity. Because of the unique dielectric properties of the bioparticles, for

example, the live yeast cells in DI water, as shown in Figure 6-7(a), exhibit positive DEP behaviors when the frequency is low and negative DEP behaviors when the frequency is high, and display p-DEP behaviors in most parts of the frequency spectrum when they are suspended in the high conductivity medium of 0.12 S/m. Whereas the dead yeast cells suspending in DI water undergo positive DEP when the frequency is low and transfer to n-DEP behaviors in the range of high-frequency. The dead yeast cells undergo only n-DEP when the suspending solution with high conductivity is employed. However, as these distinct DEP characteristics are theoretical predictions, it is becoming essential to verify the dependence of these DEP behaviors on the frequency and the solution conductivity experimentally. Therefore, in this work, the lateral migrations of viable and non-viable yeast cells under the AC electric field were measured in three liquids: (1) the DI water having a pH value of 7 and σ_m =0.0002 S/m, (2) a 0.4mM K_2HPO_4 solution with a pH value of 7 and σ_m =0.01 S/m, and (3) a 4.8mM K_2HPO_4 solution with a pH value of 7 and σ_m =0.12 S/m, respectively, by using the AC-DEP system as illustrated in Figure 6-1(a). These yeast cells, whose sizes are approximately 7.5 μm in diameter were utilized and 6 volts of peak-to-peak electric voltage was applied throughout the AC frequency range. Then, the lateral migrations of the cells suspended in different solutions throughout the 1 kHz ~ 10^3 MHz frequency range were obtained by measuring the distance between the cells center and the centerline of the main channel. The experimental measurement of the migrations at each frequency in Figure 6-8, Figure 6-9, and Figure 6-10 were performed three times in three different chips, and the corresponding numerical measurement of the lateral migrations are conducted with the particle tracing mold by using COMSOL 4.3b.

The f_{CM} curves for the live and dead cells in DI water are plotted varying with AC electric field frequency, f, in Figure 6-7. It can be figured out from Figure 6-7(a) that the viable yeast cells undergo positive DEP forces when the frequency is lower than the crossover frequency, i.e., 4.3×10^7 Hz and thereafter undergo the n-DEP effects. Figure 6-7(b) also shows that the crossover frequency of the non-viable yeast cells is 1.7×10^6 Hz. As a comparison, Figure 6-8(a) presents the experimentally measured lateral migrations of both the live and dead yeast cells. It can be seen that the lateral migrations of both types of yeast cells transit from positive to negative as the applied frequency is increased from low to high. Apparently, the CM factor curves of the yeast cells have a trend similar to that of the corresponding lateral migrations. Furthermore, the crossover frequency of the live yeast cells can be estimated by the measured lateral migration curve from Figure 6-8(a) as 3.6×10^7 Hz, while the theoretical crossover frequency of the CM factor in Figure 6-7(a) is 4.3×10^7 Hz. Moreover, as shown in Figure 6-8(a) and Figure 6-8(b), the experimentally measured lateral migrations of both the live and dead yeast cells have a trend similar to that of the corresponding numerical simulated lateral migrations. The experimental results show a good agreement with the theoretical predictions. This demonstrates that the DEP critical frequency of the bio-particles can be evaluated by measuring the lateral migrations varying with AC electric field frequency.

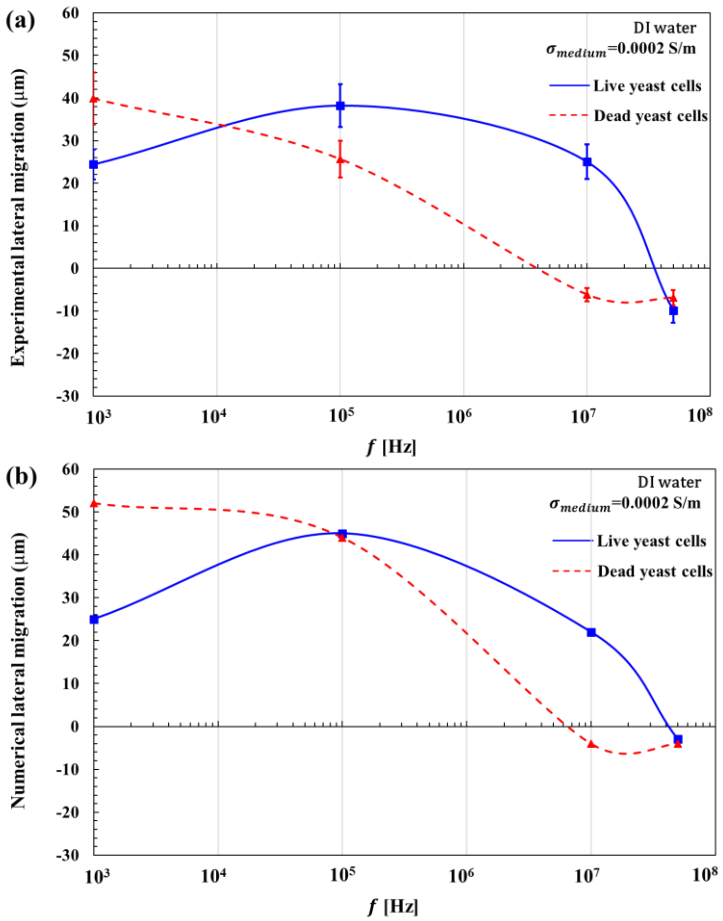

Figure 6-8 (a) The experimentally measured lateral migrations of the live (blue solid line) and dead (red dash line) yeast cells in DI water varying with the AC electric field frequency f at 6 $V_{p\text{-}p}$, and (b) the corresponding numerical simulation.

For higher values of the medium electric conductivity, the 0.4mM K_2HPO_4 solution with a pH value of 7 and σ_m =0.01 S/m (shown in Figure 6-9), and the 4.8mM K_2HPO_4 solution with a pH value of 7 and σ_m =0.12 S/m (shown in Figure 6-10) were used as the suspending solutions. It can be inferred from the CM factor plotted in Figure 6-7, when suspending in the 0.4mM K_2HPO_4 solution, only the live cells undergo positive DEP behaviors in the frequency range of 6×10^4 to 4.1×10^7 Hz, whereas the live cells experience n-DEP under the other frequency range. The dead yeast cells experience the n-DEP in the whole range of the frequency. Similarly, in Figure 6-7, for the live cells in the 4.8mM K_2HPO_4 solution, they exhibit p-DEP behaviors in a narrow frequency range from 1.8×10^6 to 4×10^7 Hz. Other than that frequency range, they undergo n-DEP effects, while the dead cells always demonstrate n-DEP behaviors throughout the frequency spectrum. For comparison, the measured lateral migrations of the live and dead yeast cells in these two solutions are plotted in Figure 6-9 and Figure 6-10. Clearly, the overall trends of the measured

lateral migration curves are similar to the corresponding CM factor curves. In the 0.4mM K_2HPO_4 solution, the crossover frequency of the live yeast cells can be estimated from Figure 6-9(a) as 3.7×10^7 Hz, while the theoretical crossover frequency of the CM factor in Figure 6-7(a) is 4.1×10^7 Hz. In the 4.8mM K_2HPO_4 solution, the crossover frequency of the live yeast cells can be estimated from Figure 6-10(a) as 1.5×10^6, while the theoretical crossover frequency of the CM factor in Figure 6-7(a) is 1.8×10^6. Similarly, as shown in Figure 6-9 and Figure 6-10, the experimentally measured lateral migrations of both the live and dead yeast cells have trends similar to those of the corresponding numerical measured lateral migrations. The experimental results show good agreements with the theoretical predictions. Therefore, by controlling the applied AC frequency and the medium conductivity, the desired DEP response of the bioparticles for the various applications can be achieved. The critical DEP frequency of cells can be estimated by measuring the corresponding lateral migration throughout the frequency spectrum.

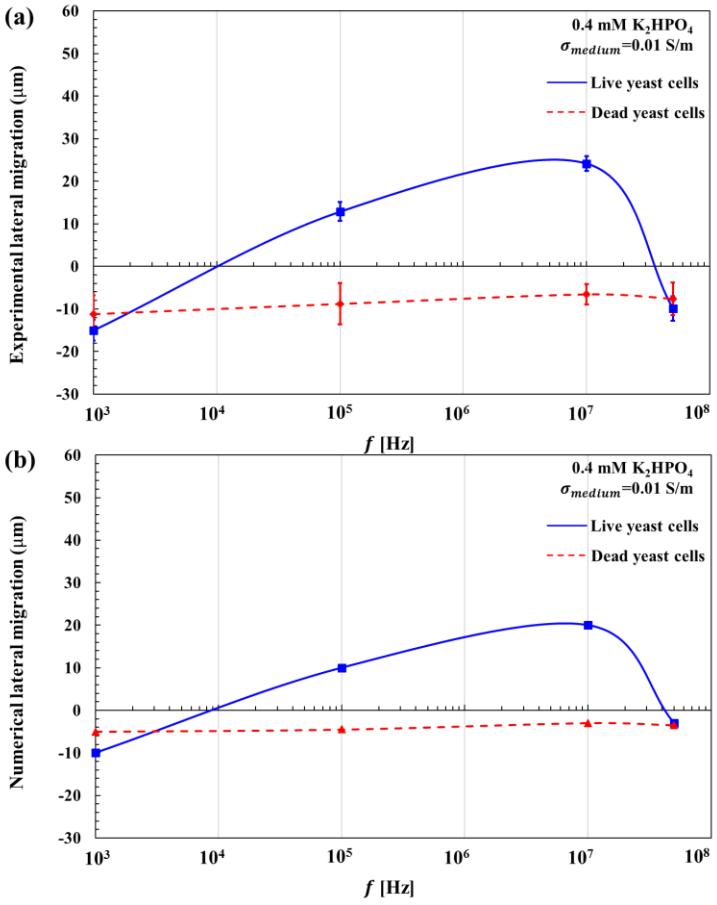

Figure 6-9 (a) The experimentally measured lateral migrations of the live (blue solid line) and dead (red dash line) yeast cells in 0.4 mM K_2HPO_4 solution varying with the AC electric field frequency f at 6 $V_{p\text{-}p}$, and (b) the corresponding numerical simulation.

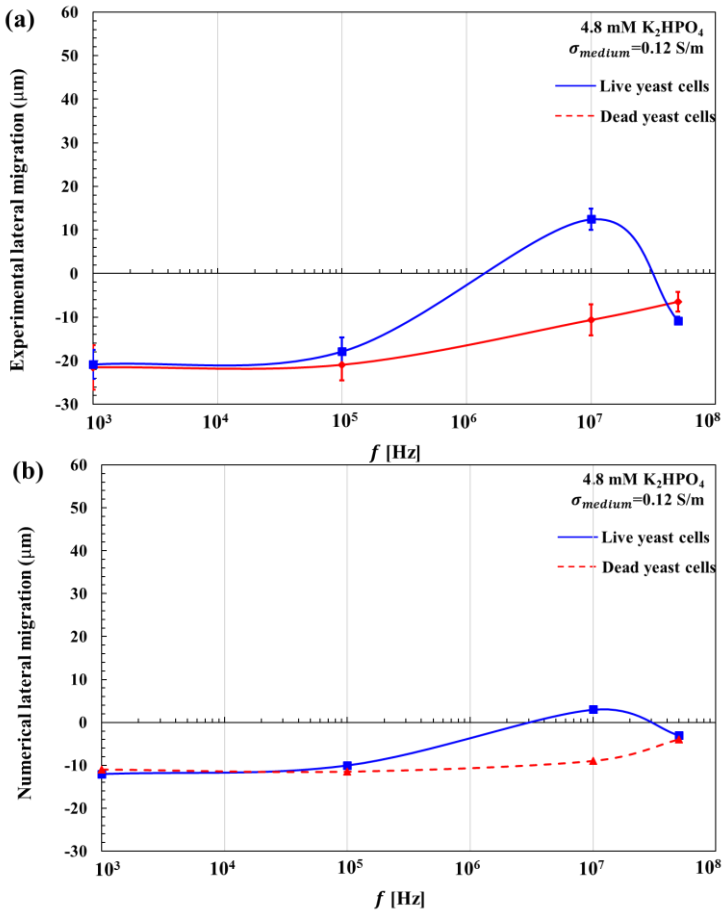

Figure 6-10 (a) The experimentally measured lateral migrations of the live (blue solid line) and dead (red dash line) yeast cells in 4.8 mM K_2HPO_4 solution varying with the AC electric field frequency f at 6 $V_{p\text{-}p}$, and (b) the corresponding numerical simulation.

Polystyrene particles and droplets

The CM factor (f_{CM}) values for the polystyrene particles and BMIM-PF_6 droplets are plotted as a function of the frequency of the applied AC electric field, f, and are shown in Figure 6-11(a). As discussed in the Equation (6-1), the direction of the dielectrophoretic behaviors is determined by the sign of f_{CM} and the trajectory shifts of the particles/droplets increase with the value of the f_{CM}. For the PS particles, $f_{CM} \approx -0.5$ throughout the frequency spectrum of the AC electric field, they always experience the negative DEP forces, resulting in negative lateral migrations. This is clearly confirmed by the experimentally measured results of the frequency dependence of the lateral migration of PS particles as shown in Figure 6-11(b). As seen in Figure 6-11(a), for the BMIM-PF_6 droplets, the f_{CM} is positive, i.e., p-DEP, when the frequency is lower than its crossover frequency 2.3×10^7 Hz. The magnitude of the f_{CM} decreases quickly to zero as the frequency increases to its crossover frequency. Then, the CM factor becomes negative, i.e. $f_{CM} < 0$, BMIM-

PF_6 droplets will undergo n-DEP, after the frequency is larger than the critical frequency. It can be seen from Figure 6-11(b) that the lateral migration of BMIM-PF_6 droplets indeed changes from positive to negative (see Figure 6-1(b)) when the AC frequency increases from low to high. The curve of the lateral migration varying with the frequency in Figure 6-11(b) is similar to the corresponding CM factor curve in Figure 6-11(a). The curve of the experimentally measured lateral migration vs frequency in Figure 6-11(b) has a crossover frequency of approximately 2.5×10^7 Hz, which is in a good agreement with the theoretically calculated crossover frequency 2.3×10^7 Hz (CM factor curve). This demonstrates that the crossover frequency of each kind of particle, droplet or biological cell can be determined by measuring the lateral migration as a function of the frequency of the applied AC electric field.

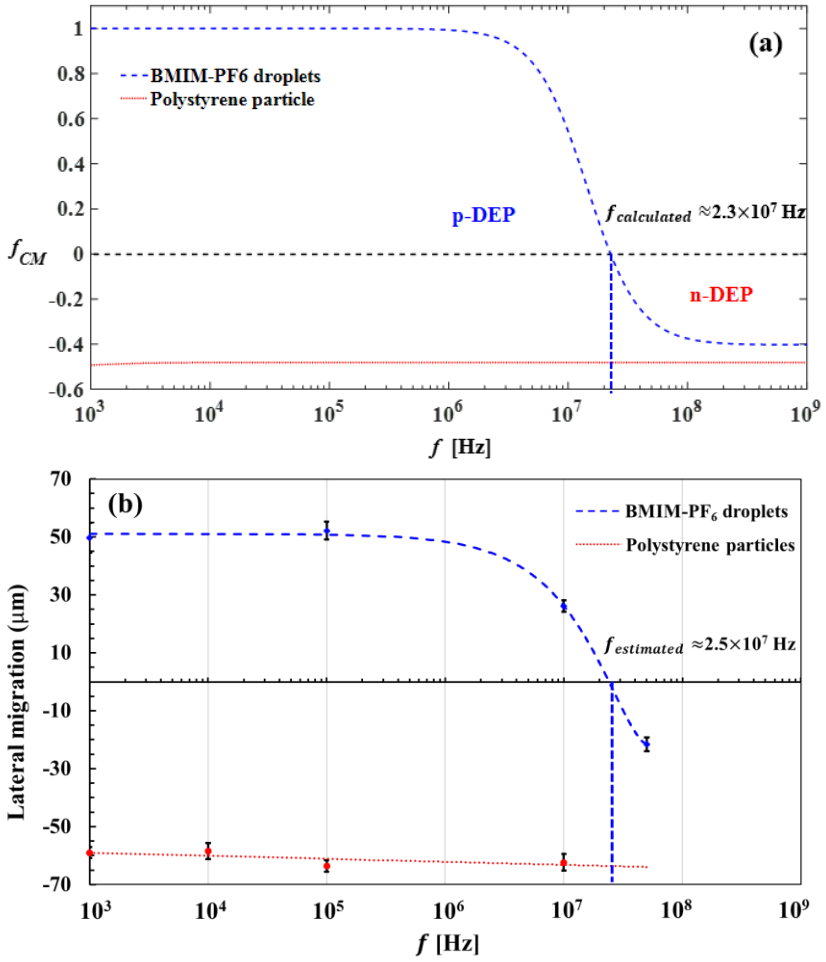

Figure 6-11 (a) Theoretical prediction of f_{CM} for the PS particles and BMIM-PF_6, and (b) lateral migrations of 19 μm (average) BMIM-PF_6 droplets (blue line) where 12Vp-p is applied, and 10 μm PS particles (red line) where 6Vp-p is applied, as a function of the frequency of the applied AC electric field f.

6.3.5 Separation of droplets by n-DEP and p-DEP response

As discussed previously, different types of droplets with different electrical properties, and hence different critical frequencies, may exhibit different DEP behaviors, i.e., positive and negative dielectrophoresis, respectively. In this work, the separation of different types of droplets with similar diameter, i.e., the droplets of BMIM-PF_6 and HMIM-PF_6 of approximately 15 µm, and the silicone oil droplets and BMIM-PF_6 droplets of approximately 15 µm were conducted. It can be seen from Figure 6-2 that, the critical frequency of BMIM-PF_6 droplets is 2.3×10^7 Hz in DI water, the droplets experience positive DEP effects when the crossover frequency is higher than the applied frequency and will experience negative DEP forces when the critical frequency is lower than the applied frequency. However, the critical frequency of HMIM-PF_6 droplets is 1.3×10^7 Hz in DI water. This means that the BMIM-PF_6 droplets and the HMIM-PF_6 droplets will show opposite DEP behaviors, i.e., positive and negative dielectrophoretic effects, respectively when the frequency of the applied AC electric field is in the range of 1.3×10^7 Hz to 2.3×10^7 Hz. The silicone oil droplets always experience negative DEP effects throughout the frequency spectrum.

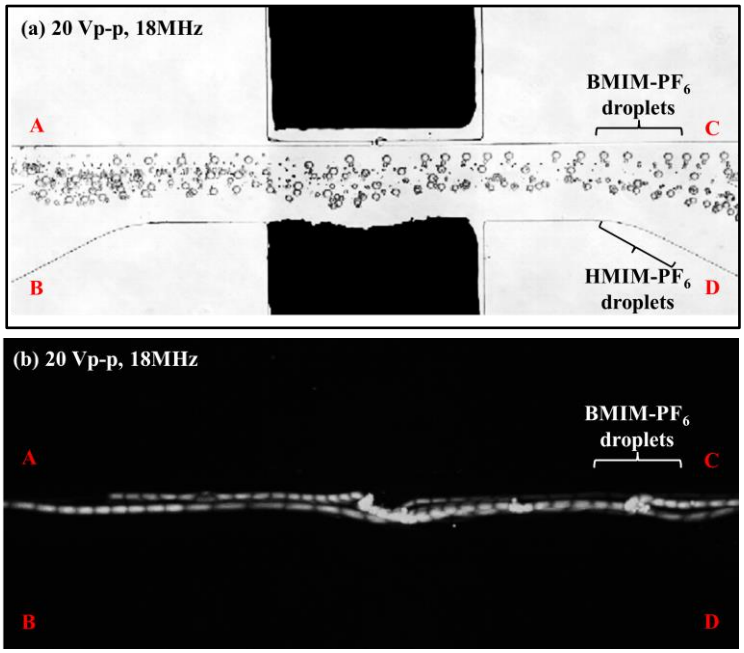

Figure 6-12 (a) The separation of the droplets of BMIM-PF_6 and HMIM-PF_6 in the diameter of 15 µm (average). (b) The fluorescent diagram of the trajectory of the fluorescent BMIM-PF_6 droplets with a size of 15 µm undergoing positive DEP, where 20Vp-p and 18 MHz are applied.

In the experiments, DI water was used as the suspending solution. Error! Reference source not found. shows the separation of two types of the IL-in-water emulsions, i.e., the droplets of BMIM-PF_6 and HMIM-PF_6, owing to their opposite dielectrophoretic behaviors, under a specific applied electric frequency, i.e.,

1.8×10^7 Hz. In order to illustrate the individual trajectory of two different kinds of droplets, the fluorescent dye Nile Red was added into BMIM-PF_6 so that the droplets of BMIM-PF_6 become fluorescent. As the droplets of BMIM-PF_6 have f_{CM} ≈0.2 (Figure 6-2), they experienced positive dielectrophoretic effects and were attracted towards the high electric field region, moving into the outlet reservoir C. This is clearly shown by the fluorescent trajectories of the BMIM-PF_6 droplets in **Error! Reference source not found.**(b). While the HMIM-PF_6 droplets have f_{CM} ≈−0.2 (Figure 6-2), experiencing negative DEP, were pushed away from the electric field maximum and moved into the outlet channel D.

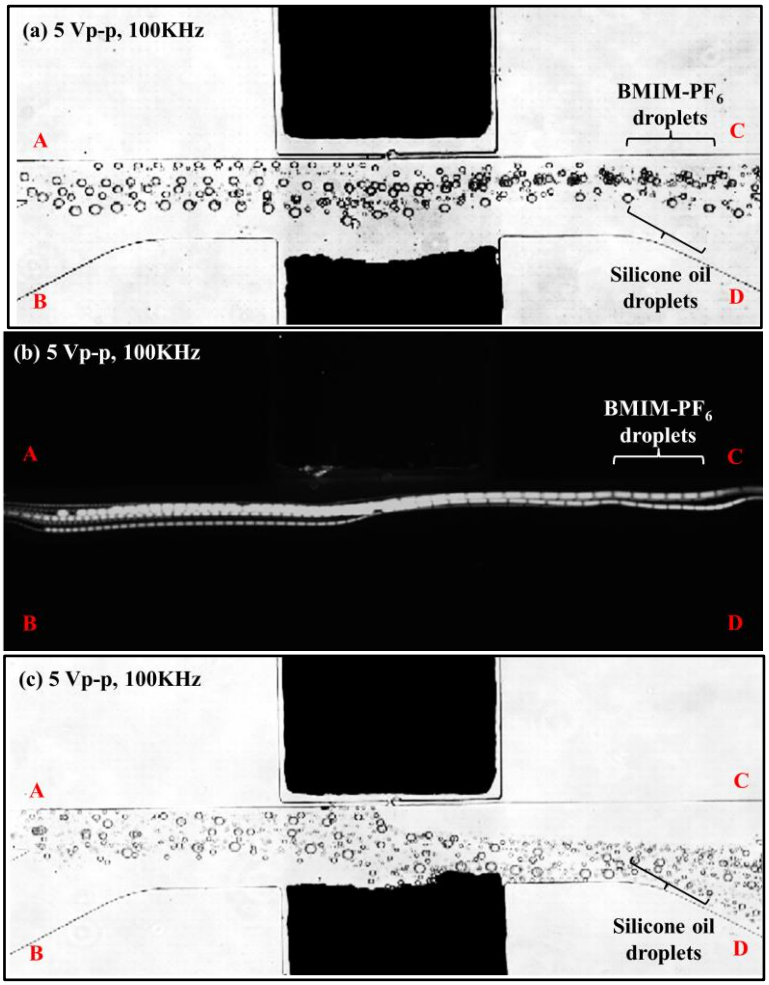

Figure 6-13 (a) *Separation of 15 μm BMIM-PF_6 droplets and the silicone oil droplets* (b) *The fluorescent diagram of the trajectory of the fluorescent BMIM-PF_6 droplets with a size of 15 μm experiencing positive DEP.* (c) *The trajectory shifts of the pure silicone oil droplets undergoing negative DEP, where 5Vp-p and 100 kHz are applied.*

Furthermore, the separation of the droplets of silicone oil and BMIM-PF_6 was carried out. The different trajectories of the fluorescent droplets of BMIM-PF_6 and the non-fluorescent silicone oil droplets

are shown in Figure 6-13(a) and Figure 6-13(b). The mixture of the droplets of BMIM-PF_6 ($f_{CM} \approx 1$) and silicone oil ($f_{CM} \approx -0.5$) was separated and moved into outlet reservoir C and D by the p-DEP and n-DEP, respectively. In order to examine the droplets of silicone oil flowed into the output reservoir D, the experiments were repeated by manipulating the pure droplets of silicone oil under the same condition, which are demonstrated in Figure 6-13(c). It clearly illustrates that the droplets of silicone oil were repelled and moved into the output reservoir D by the negative dielectrophoretic effects, and the pure droplets of silicone oil had the similar trajectory shifts as they had in the case of the mixture as demonstrated in Figure 6-13(a). The experimental results match well with the numerical simulation as shown in Figure 6-3(c). It indicates again that the continuous sorting of different kinds of emulsions with the same diameter according to their opposite dielectrophoretic behaviors can be realized by simply adjusting the applied frequency of the AC electric field in the newly developed asymmetric orifice based AC-DEP chip.

6.3.6 Manipulation and separation of live and dead yeast cells

As discussed previously, the biological cells with different dielectric properties, i.e., different crossover frequencies, may demonstrate the opposite DEP behaviors under a given AC frequency, and thus can be separated by the negative and positive DEP effects, respectively. In this study, the manipulation and sorting of live and dead yeast cells in the DI water with an electric conductivity of 5.5×10^{-6} S/m, and a dielectric constant of 80 were conducted by applying two different frequencies, i.e., 1 kHz and 10 MHz with 6 Vp-p, respectively. Figure 6-14 shows the trajectories of the live and dead yeast cells under these two AC frequencies. As inferred from Figure 6-7(a), the crossover frequency of live yeast cells is 4.3×10^7 Hz in DI water. When the applied frequency is lower than that, the live yeast cells undergo positive DEP behaviors. Then, they will experience negative DEP effects as the applied frequency increasing over the crossover frequency. While, for the dead cells in DI water, the crossover frequency becomes 1.7×10^6 Hz. Therefore, if the applied frequency is higher than 1.7×10^6 Hz and lower than 4.3×10^7 Hz, the live and dead cells show the opposite DEP behaviors, i.e., positive and negative dielectrophoretic effects, respectively. This distinction enables the sorting of cells based on their properties and enables the separation of live and dead cells.

As shown in Figure 6-14(a), when the applied frequency of the AC electric field, i.e., 1KHz, $f_{CM} > 0$, all the live and dead yeast cells experienced positive DEP and were attracted towards the maximum electric field gradient (i.e., near the small orifice), then flowing into outlet channel C. Figure 6-14(b) shows the successful separation of the live (light dots) and dead (black dots) yeast cells, due to their opposite dielectrophoretic behaviours by applying a specific electric frequency, i.e., 1×10^7 Hz. Under this condition, the live yeast cells have $f_{CM} \approx 0.7$ (Figure 6-7(a)) they experienced positive dielectrophoretic behaviors and were pull towards the small orifice, then flowed into the outlet branch C. While the dead yeast cells have

$f_{CM} \approx -0.15$, experiencing negative DEP, were repelled towards the large orifice and flowed into the outlet branch D. Clearly, this demonstrates that the separation of the biological cells of similar size with different dielectric properties can be achieved by simply adjusting the frequency of the AC electric field in the microfluidic system developed in this work.

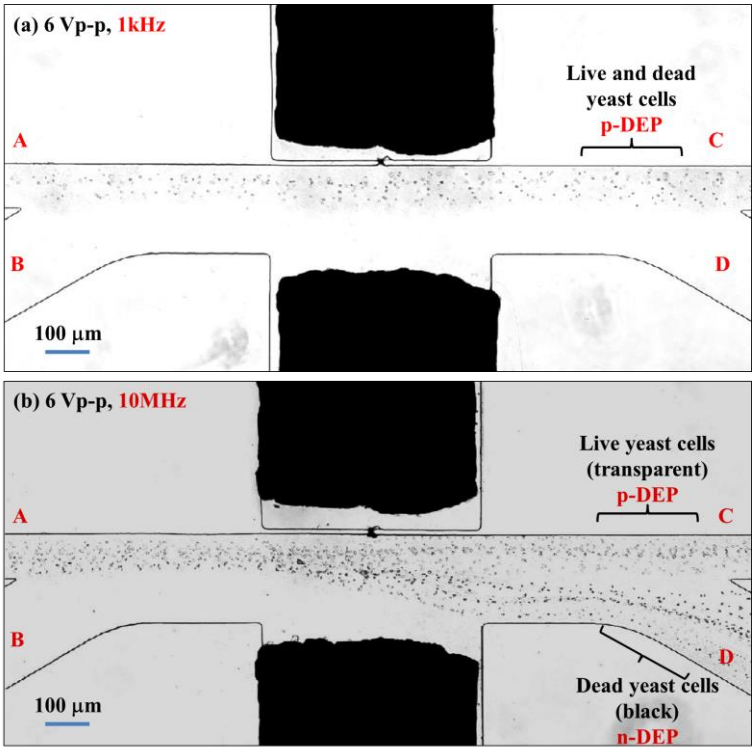

Figure 6-14 AC DEP separation of the live and dead yeast cells in DI water by adjusting the applied AC frequency.

6.4 Conclusion

In conclusion, in this chapter, we developed AC-DEP microfluidic chips for continuous droplet/particle and cell characterization and separation. The microfluidic chip induces the non-uniform electric field by applying the AC electric fields via a set of asymmetric orifices located on the opposite sidewalls in the main channel. In the vicinity of the orifices, the droplets/particles and cells experiencing the positive DEP forces are attracted toward the small orifice where the strongest non-uniformity of the electric field exists and moved away from the central line of the channel, while the negative DEP cells are repelled away from the central line of the channel and flowed toward the large orifice, i.e., the weak electric field. The effects of the applied frequency and voltage on the AC-DEP behaviors of droplets and particles, and the effects of the medium ionic concentrations, i.e., different electrical conductivities, on the CM factors of the yeast cells over a large range of the AC electric field frequency are investigated. Then, the lateral

migrations of the droplets/particles and cells as a function of the AC frequency are measured, which have trends similar to the corresponding curves of CM factors and match well with the numerical simulation results, providing a strategy to evaluate the critical frequency of the biological particles and characterize the cells. By simply adjusting the frequency and strength of the AC electric field, desired DEP behaviors of the droplets/particles and cells for the various applications can be achieved which enable the separation of different types of emulsions in the same diameter and sorting of viable and non-viable yeast cells as well as the yeast cells with targeted diameter and dielectric property. This developed AC-DEP system provides a method to characterize the critical frequency of the specific cells and manipulate the targeted cells.

CHAPTER 7 Conclusions and Future Work

This chapter presents an overall summary of this thesis. Contributions of this thesis are also listed below. Based on these conclusions, future directions in the asymmetric orifice based dielectrophoretic microfluidic system and potential applications in the biological and clinical analysis are recommended.

7.1 Conclusions and contributions

This thesis starts with the fabrication of the asymmetric-orifices based dielectrophoretic microfluidic chip. Two fundamental research projects and an extension of the practical application using the DC-DEP method and one systemically research project using the AC-DEP method are conducted on the asymmetric-orifices based microfluidic devices. In the nano-orifice based dielectrophoretic microchannel fabrication part, the non-uniform electric field is generated by applying the electric field via a pair of asymmetric orifices, a small orifice on one side of the channel walls and a large orifice on the opposite side of the channel walls. In order to obtain a strong gradient of the non-uniform electric fields, i.e., a large width ratio between the small orifice and the large orifice, a small microchannel or a nanochannel fabricated by the solvent-induced cracking method is used to form the small orifice. The asymmetric orifices structure allows the dielectrophoretic manipulation and separation of particles with smaller size differences and separation of nanoparticles for the first time. The fundamental research projects and an extension of the practical application project investigate the DC dielectrophoretic sorting of the nanoparticles, microemulsion droplets, and Janus particles in microchannels numerically and experimentally, providing a platform to manipulate different kinds of targets not only by size but also by type. Lastly, by using the AC-DEP microfluidic chips, the tunable characterization and identification of droplets and biological cells are investigated. To generate DEP forces, two electrode-pads are embedded in a set of asymmetric orifices on the opposite sidewalls to produce the non-uniform electric fields. In the vicinity of a small orifice, the cells experience the strongest non-uniform gradient. The effects of the strength and frequency of the applied AC electric field, as well as the ionic concentrations, i.e., different electrical conductivities on their DEP behaviors, are investigated, respectively. To evaluate the critical frequency of the specific droplets and cells and manipulate the targeted cells, a microfluidic system is developed to measure the lateral distance between the cells center and the centerline of the main channel as a function of the AC frequency. The trends of measured lateral migrations of yeast cells are similar to the corresponding Clausius−Mossotti (CM) factors. This system provides a method to characterize the crossover frequency of the specific cells and manipulate the targeted cells. Overall, based on the studies presented in the previous chapters, the major contributions of this research are briefly summarized as follows:

1) We developed a novel asymmetric-orifices based method to dielectrophoretic manipulate and characterize nanoparticles, microemulsion droplets, and biological cells.

2) Regarding the generation of the non-uniform electric field, i.e., dielectrophoretic forces, the electric field is employed via a pair of asymmetric orifices, a small orifice on one side of the channel walls and a large orifice on the opposite side of the channel walls.

3) In order to obtain a strong gradient of the non-uniform electric fields, a large width ratio between the small orifice and the large orifice and a short small orifice is necessary. We fabricated a small microchannel or a nanochannel by the solvent-induced cracking method to form the small orifice.

4) We developed a home-made alignment system by using an inverted optical microscope, and the resolution of the alignment system is high enough for general microfluidic applications.

5) The asymmetry-orifices based dielectrophoretic microchannels used in our experiments are simple to fabricate and the throughput can be easily increased by ten times or more by integrating the pressure-driven flow in the microchannel for transportation. There is no high electric field applied through the whole microchannel, and the Joule heating effect is essentially avoided. The generation of the local electrical field gradient does not require a change of the cross-section of the microchannel and will not affect the transport of the particles.

6) The asymmetric orifices structure enables the separation of particles with smaller size differences and separation of nanoparticles. We believe that asymmetry-orifices based dielectrophoretic devices will benefit the microfluidic fields in the future.

7) The smaller nanoparticles separated by size in our experiments are as small as 51 nm and 140 nm, i.e., with a size difference of 90 nm which was the highest separation resolution in the microchannel by DC-DEP method to the best of our knowledge. The experimental results expand our understanding of the DC-DEP techniques and applications in a microchannel.

8) We demonstrated the effects of the applied electric field, the flow rate as well as the width and length of the small orifice on the DC-DEP separation resolution and sensitivity. The experimental results of the particle trajectory show good agreements with the numerical simulation results.

9) The performance of the asymmetry-orifices based DC-DEP system on the separation of the nanoparticles by type, including separation resolution (10 nm), sensitivity (separation of 140 nm polystyrene and 150 nm magnetic nanoparticles) and capability of sorting different kinds of nanoparticles is investigated systematically for the first time.

10) Very limited studies have been done on the dielectrophoretic manipulation of Janus particles under DC electric field. We derived the DC-DEP forces acting on the Janus particles and developed a numerical model for Janus particles movement in the microchannel for the first time.

11) We studied the effects of the strength of the electric fields, as well as the coating coverage, thickness, and electrical conductivity of the Janus particles on their DEP behaviors and trajectories under DC electric field systematically. The effect of the coating thickness of the Janus particles on their dielectrophoretic behaviors is negligible when using the DC-DEP method and the Janus particles with gold coating coverage over 50% will experience positive DEP effects.

12) We demonstrated the extension of the asymmetry-orifices based DC-DEP system on manipulation and separation of the oil and ionic liquid-in-water microemulsion droplets, resulting in the separation of smaller silicone oil droplets with a small size difference of only 3.5 μm. By selecting the surrounding solution with a specific electrical conductivity, the separation of the emulsion droplets of similar size but different contents is achieved by opposite DEP effects, i.e., p-DEP and n-DEP, respectively, providing a platform to manipulate different kinds of emulsion droplets carrying different biomolecules or bioparticles.

13) We developed a novel AC-DEP microfluidic system for the tunable characterization and identification of droplets and biological cells based on two electrode-pads embedded in a set of asymmetric orifices on the opposite sidewalls to produce the non-uniform electric fields.

14) The non-uniformity of the electric field in the AC-DEP becomes solely dependent on the width ratio of the insulated small and large orifices as well as the length of the small orifice, the fabrication of the microelectrodes is simplified and the electrolytic reactions at the electrodes are avoided.

15) We demonstrated a novel AC-DEP method in measuring the lateral migrations of the particles/droplets and yeast cells from the centerline of the main channel to the center of the targets in the recorded images for the first time. The trends of measured lateral migrations are similar to the corresponding Clausius-Mossotti factors.

16) We demonstrated the effects of the applied frequency and voltage on the AC-DEP behaviors of droplets/particles, and the effects of the medium ionic concentrations, i.e., different electrical conductivities, on the AC-DEP lateral migrations and Clausius-Mossotti factors of the yeast cells over a large range of the AC electric field frequency.

17) The asymmetry-orifices based AC-DEP system is capable of separating different types of emulsions in the same diameter and sorting of viable and non-viable yeast cells as well as the yeast cells with the targeted diameter and dielectric property.

18) We developed an AC-DEP method to identify the critical frequency of specific biological cells and manipulate the targeted cells, as well as a fingerprint to characterize the cells.

7.2 Recommendations and future research

Possible directions and extensions of the present work are as followings.

7.2.1 Microfluidic device fabrication

The asymmetric-orifice based microfluidic chip presented in this thesis is easy to fabricate; however, improvements are still needed for practical applications, including:

a. To induce strong non-uniform electric fields in the asymmetric-orifices based microchannel, a small microchannel or a nanochannel is used to form the small orifice on one side of the microchannel walls. To obtain the small microchannel or nanochannel, small micron cracks or nanocracks are created on polystyrene surface, which is generally larger than 100 nm in width and difficult to be produced smaller than 100 nm. This problem may be solved by using a polymer with different molecular structures such as PMMA and smaller crackers in nanoscale may be created by their nature.

b. The pattern of the small micron cracks or nanocracks is transferred onto a SU8 photoresist layer by the soft lithography technique to work as the positive small micron channel or nanochannel mold and the crack on the polystyrene surface is not stable during the replication because of the solvent in the duplication. It becomes necessary to find a suitable material for the positive channel mold replication from these cracks.

c. For the asymmetric-orifices based DEP system, the small micron orifice or nano orifice was fabricated by PDMS which is relatively soft when the size of the structure is smaller than 50 nm and results in channel collapse. The hard PDMS may solve this problem in most cases, which is generally complexed and time-consuming. It is urgent to find a ready-to-use material with high Young's modulus and nanomaterials such as CNT, nanowires, or nanoribbons may be utilized to replace the PDMS nano orifice and perform as the small orifice.

d. The microfluidic chips presented in this thesis were made by bonding a top PDMS layer having the microchannel structure with a bottom PDMS layer having a single small microchannel or nanochannel by using a custom-made alignment system under a microscope. The fabrication of the repeatable microfluidic device would be simplified and an alignment system would no longer be required by integrating the top microchannel and the bottom small microchannel or nanochannel onto one channel mold.

e. For the AC-DEP characterization of biological cells, micro copper electrodes were utilized to generate the non-uniform electric field, which are not compatible with the bioparticles. Electrodes with good biocompatibility and that are inert and noncorrodible such as platinum electrode pads may solve this problem, and the electrochemical effects would be negligible and no bubbles would be observed during the experiments.

7.2.2 Continuous DC-DEP manipulation of nanoparticles and droplets

In this thesis, we only demonstrated the separation of nanoparticles as small as 51 nm and 140 nm, as well as 140 nm polystyrene and 150 nm magnetic nanoparticles, and conducted the numerical studies of dielectrophoretic behaviors of Janus particles under DC electric field. The separation resolutions we studied are very limited and the systematically experimental studies on the DC-DEP manipulation of Janus particles are necessary. More experiments are needed to explore these behaviors:

f. The DC-DEP method enables the size-dependent separation of the nanoparticles of 51 nm and 140 nm, i.e., with a size difference of 90 nm in diameter, and the separation of 140 nm polystyrene and 150 nm magnetic nanoparticles by type, however, a higher separation resolution and sensitivity should be carried out and achieved, such as the manipulation of smaller DNA or protein.

g. The effects of the electrophoretic forces acting on the particles, especially nanoparticles, may disturb the particle trajectories near the orifices, and efforts should be made to improve this problem.

h. Magnetic particles are used in cases of type-dependent separation, and an electric current generates a magnetic field which can attract magnetic particles leading to a similar phenomenon to positive DEP. To be noted, an explanation has been demonstrated in Appendix C.

i. Due to the small dimensions of the small nano-orifice and low electrical conductivity of the suspending solution, EDL overlap may occur and result in concentration-polarization effect across the nano-orifice. Efforts should be made to improve this problem.

j. Experimental studies of Janus particles with various coating coverage, coating thickness, and coating materials under DC electric field should be carried out to verify the simulation and fully understand their DC-DEP behaviors.

k. For the asymmetric orifice based DC-DEP technique, the devices developed for the manipulation and separation of targeted individual droplets with specific size and content can be integrated into conventional microfluidic droplet generation systems and provides a simple and effective method for wide droplet-based applications in industry and research.

7.2.3 Applications of AC-DEP microfluidic systems

In this thesis we only studied the most common cases: lateral migrations measurement of viable and non-viable yeast cells, and ionic liquid-in-water emulsion droplets in three different suspending solutions, and the critical frequencies we studied were very limited. More experiments are needed to explore these fingerprints:

l. When the frequency of the AC electric field is varied, there appears to be a significant difference in the particles trajectories (between f_{CM}=−0.48 and f_{CM}=−0.5) and the marginal difference may not be sufficient to explain this trajectory change. To be noted, an explanation has been demonstrated in Appendix F.

m. For the asymmetric orifices based AC-DEP system, the working principle and procedures developed in measuring the lateral migrations and locating the critical frequency of the viable and non-viable yeast cells can also be applied to various biological particles, such as DNA, viruses, and bacteria in various suspending solutions. The developed strategy provides a method to identify the distinct property, i.e., crossover frequency of the bioparticles and the fingerprints to characterize the bioparticles.

n. To induce the non-uniform electric field in the developed AC-DEP microfluidic system, one pair of asymmetric orifices was utilized. It may be beneficial to show the operation of the system with multiple sets of asymmetric orifices. In this way, the sorting efficiency of the system may be improved and the flow rate may become operational.

PUBLICATIONS AND LETTER OF COPYRIGHT PERMISSION

Kai Zhao, Larasati, Bernard P. Duncker and Dongqing Li*, "Continuous Cell Characterization and Separation by Microfluidic AC Dielectrophoresis," ***Analytical Chemistry,*** 91, 6304-6314 (2019)

Kai Zhao, and Dongqing Li*, "Tunable droplets manipulation and characterization by AC-DEP", ***ACS Applied Materials & Interfaces***, 10, 42: 36572-36581 (2018).

Kai Zhao, and Dongqing Li, "Manipulation and separation of oil droplets by using asymmetric nano-orifice induced DC dielectrophoretic method", ***Journal of colloid and interface science***, 512, 389-397 (2018).

Kai Zhao, and Dongqing Li, "Direct current dielectrophoretic manipulation of the ionic liquid droplets in water", ***Journal of Chromatography A***, 1558, 96-108 (2018).

Kai Zhao, and Dongqing Li, "Continuous separation of nanoparticles by type via localized DC-Dielectrophoresis using asymmetric nano-orifice in pressure-driven flow", ***Sensors and Actuators B: Chemical***, 250, 274-284 (2017).

Kai Zhao, and Dongqing Li, "Numerical studies of manipulation and separation of Janus particles in nano-orifice based DC-Dielectrophoretic microfluidic chips", ***Journal of Micromechanics and Microengineering***, 27, 095007 (2017).

Kai Zhao, Ran Peng, and Dongqing Li, "Separation of Nanoparticles by a Nano-orifice based DC-Dielectrophoresis Method in Pressure-Driven Flow", ***Nanoscale***, 8, 18945-18955 (2016).

REFERENCES

(1) Dongqing Li. *Elsevier* **2004**, 635.

(2) Lim, Y. C.; Kouzani, A. Z.; Duan, W. *Microsyst. Technol.* **2010**, *16*, 1995–2015.

(3) Arora, A.; Simone, G.; Salieb-Beugelaar, G. B.; Kim, J. T.; Manz, A. *Anal. Chem.* **2010**, *82*, 4830–4847.

(4) Haeberle, S.; Mark, D.; Von Stetten, F.; Zengerle, R. *Microsystems Nanotechnol.* **2012**, No. 9, 853–895.

(5) Andersson, H.; Van den Berg, A. *Sensors Actuators, B Chem.* **2003**, *92*, 315–325.

(6) Hölzel, R.; Bier, F. F. *IEE Proc. - Nanobiotechnology* **2003**, *150*, 47.

(7) Khoshmanesh, K.; Nahavandi, S.; Baratchi, S.; Mitchell, A.; Kalantar-zadeh, K. *Biosens. Bioelectron.* **2011**, *26*, 1800–1814.

(8) Hughes, M. P. *Electrophoresis* **2002**, *23*, 2569–2582.

(9) Kang, K. H.; Kang, Y.; Xuan, X.; Li, D. *Electrophoresis* **2006**, *27*, 694–702.

(10) Barbulovic-Nad, I.; Xuan, X.; Lee, J. S. H.; Li, D. *Lab Chip* **2006**, *6*, 274–279.

(11) Zhang, C.; Khoshmanesh, K.; Mitchell, A.; Kalantar-Zadeh, K. *Anal. Bioanal. Chem.* **2010**, *396*, 401–420.

(12) Chen, D.; Du, H.; Tay, C. Y. *Nanoscale Res. Lett.* **2010**, *5*, 55–60.

(13) Krishnan, R.; Sullivan, B. D.; Mifflin, R. L.; Esener, S. C.; Heller, M. J. *Electrophoresis* **2008**, *29*, 1765–1774.

(14) Shin, D. H.; Kim, J. E.; Shim, H. C.; Song, J. W.; Yoon, J. H.; Kim, J.; Jeong, S.; Kang, J.; Baik, S.; Han, C. S. *Nano Lett.* **2008**, *8*, 4380–4385.

(15) Zhang, C.; Khoshmanesh, K.; Tovar-Lopez, F. J.; Mitchell, A.; Wlodarski, W.; Klantar-Zadeh, K. *Microfluid. Nanofluidics* **2009**, *7*, 633–645.

(16) Lapizco-Encinas, B. H.; Simmons, B. A.; Cummings, E. B.; Fintschenko, Y. *Anal. Chem.* **2004**, *76*, 1571–1579.

(17) Lapizco-Encinas, B. H.; Davalos, R. V.; Simmons, B. A.; Cummings, E. B.; Fintschenko, Y. *J.*

Microbiol. Methods **2005**, *62*, 317–326.

(18) Huang, Y.; Yang, J. M.; Hopkins, P. J.; Kassegne, S.; Tirado, M.; Forster, A. H.; Reese, H. *Biomed. Microdevices* **2003**, *5*, 217–225.

(19) Lapizco-Encinas, B. H.; Ozuna-Chacón, S.; Rito-Palomares, M. *J. Chromatogr. A* **2008**, *1206*, 45–51.

(20) Washizu, M. *J. Electrostat.* **2005**, *63*, 795–802.

(21) Zheng, L.; Brody, J. P.; Burke, P. J. *Biosens. Bioelectron.* **2004**, *20*, 606–619.

(22) Lao, A. I. K.; Hsing, I. M. *Lab Chip* **2005**, *5*, 687–690.

(23) Grom, F.; Kentsch, J.; Müller, T.; Schnelle, T.; Stelzle, M. *Electrophoresis* **2006**, *27*, 1386–1393.

(24) Oita, I.; Halewyck, H.; Thys, B.; Rombaut, B.; Vander Heyden, Y.; Mangelings, D. *Anal. Bioanal. Chem.* **2010**, *398*, 239–264.

(25) Ermolina, I.; Morgan, H.; Green, N. G.; Milner, J. J.; Feldman, Y. *Biochim. Biophys. Acta - Gen. Subj.* **2003**, *1622*, 57–63.

(26) Kang, Y.; Li, D.; Kalams, S. A.; Eid, J. E. *Biomed. Microdevices* **2008**, *10*, 243–249.

(27) Voldman, J. *Annu. Rev. Biomed. Eng.* **2006**, *8*, 425–454.

(28) Gagnon, Z. R. *Electrophoresis* **2011**, *32*, 2466–2487.

(29) Kang, Y.; Li, D. *Microfluid. Nanofluidics* **2009**, *6*, 431–460.

(30) Gossett, D. R.; Weaver, W. M.; MacH, A. J.; Hur, S. C.; Tse, H. T. K.; Lee, W.; Amini, H.; Di Carlo, D. *Anal. Bioanal. Chem.* **2010**, *397*, 3249–3267.

(31) Carlson, R. H.; Gabel, C. V.; Chan, S. S.; Austin, R. H.; Brody, J. P.; Winkelman, J. W. *Phys. Rev. Lett.* **1997**, *79*, 2149–2152.

(32) Grier, D. G. *Nature* **2003**, *424*, 810–816.

(33) Mccloskey, K. E.; Chalmers, J. J.; Zborowski, M. *Anal. Chem.* **2003**, *75*, 6868–6874.

(34) Ramos, A.; Morgan, H.; Green, N. G.; Castellanos, A. *J. Electrostat.* **1999**, *47*, 71–81.

(35) Juncker, D.; Schmid, H.; Delamarche, E. *Nat. Mater.* **2005**, *4*, 622–627.

(36) Nilsson, A.; Petersson, F.; Jönsson, H.; Laurell, T. *Lab Chip* **2004**, *4*, 131–135.

(37) Petersson, F.; Nilsson, A.; Holm, C.; Jönsson, H.; Laurell, T. *Lab Chip* **2005**, *5*, 20–22.

(38) Costa, R. C. de A.; Mogensen, K. B.; Kutter, J. P. *Lab Chip* **2005**, *5*, 1310–1314.

(39) Kang, Y.; Cetin, B.; Wu, Z.; Li, D. *Electrochim. Acta* **2009**, *54*, 1715–1720.

(40) Zhao, K.; Li, D. *J. Micromechanics Microengineering* **2017**, *27*.

(41) Zhao, K.; Li, D. *Sensors Actuators, B Chem.* **2017**, *250*, 274–284.

(42) Cetin, B.; Li, D. *Electrophoresis* **2008**, *29*, 994–1005.

(43) Song, Y.; Yang, J.; Shi, X.; Jiang, H.; Wu, Y.; Peng, R.; Wang, Q.; Gong, N.; Pan, X.; Sun, Y.; Li, D. *Sci. China Chem.* **2012**, *55*, 524–530.

(44) Gallo-Villanueva, R. C.; Rodríguez-López, C. E.; Díaz-de-la-Garza, R. I.; Reyes-Betanzo, C.; Lapizco-Encinas, B. H. *Electrophoresis* **2009**, *30*, 4195–4205.

(45) Lapizco-Encinas, B. H.; Simmons, B. A.; Cummings, E. B.; Fintschenko, Y. *Electrophoresis* **2004**, *25*, 1695–1704.

(46) Jones, T. B. *Cambridge Univ. Press* **1995**.

(47) Sun, M.; Agarwal, P.; Zhao, S.; Zhao, Y.; Lu, X.; He, X. *Anal. Chem.* **2016**, *88*, 8264–8271.

(48) So, J. H.; Dickey, M. D. *Lab Chip* **2011**, *11*, 905–911.

(49) Tang, S. Y.; Zhu, J.; Sivan, V.; Gol, B.; Soffe, R.; Zhang, W.; Mitchell, A.; Khoshmanesh, K. *Adv. Funct. Mater.* **2015**, *25*, 4445–4452.

(50) Wu, C.; Chen, R.; Liu, Y.; Yu, Z.; Jiang, Y.; Cheng, X. *Lab Chip* **2017**, *17*, 4008–4014.

(51) Modarres, P.; Tabrizian, M. *Sensors Actuators, B Chem.* **2017**, *252*, 391–408.

(52) Jia, Y.; Ren, Y.; Jiang, H. *Electrophoresis* **2015**, *36*, 1744–1753.

(53) Adekanmbi, E. O.; Srivastava, S. K. *Lab Chip* **2016**, *16*, 2148–2167.

(54) Viefhues, M.; Eichhorn, R. *Electrophoresis* **2017**, *38*, 1483–1506.

(55) Dash, S.; Mohanty, S. *Electrophoresis* **2014**, *35*, 2656–2672.

(56) Pysher, M. D.; Hayes, M. A. *Anal. Chem.* **2007**, *79*, 4552–4557.

(57) Qian, S.; Ai, Y. *CRC Press* **2012**, *153*, 382.

(58) Ronald F. Probstein. *Wiley-Interscience* **1994**.

(59) Lyklema, J. *Acad. Press* **1995**.

(60) Hywel Morgan_ Nicolas G Green. *Encycl. Microfluid. Nanofluidics* **2003**, 8–8.

(61) Çetin, B.; Li, D. *Electrophoresis* **2011**, *32*, 2410–2427.

(62) Khoshmanesh, K.; Nahavandi, S.; Baratchi, S.; Mitchell, A.; Kalantar-zadeh, K. *Biosens. Bioelectron.* **2011**, *26*, 1800–1814.

(63) Zhang, C.; Khoshmanesh, K.; Mitchell, A.; Kalantar-Zadeh, K. *Anal. Bioanal. Chem.* **2010**, *396*, 401–420.

(64) Gascoyne, P. R. C.; Vykoukal, J. V. *Proc. IEEE* **2004**, *92*, 22–42.

(65) Pysher, M. D.; Hayes, M. A. *Anal. Chem.* **2007**, *79*, 4552–4557.

(66) Nahavandi, M. *Ind. Eng. Chem. Res.* **2016**, *55*, 5484–5499.

(67) Wang, M. W. *Jpn. J. Appl. Phys.* **2008**, *47*, 2270–2274.

(68) Wang, L.; Flanagan, L. A.; Jeon, N. L.; Monuki, E.; Lee, A. P. *Lab Chip* **2007**, *7*, 1114–1120.

(69) Çetin, B.; Kang, Y.; Wu, Z.; Li, D. *Electrophoresis* **2009**, *30*, 766–772.

(70) Kang, Y.; Cetin, B.; Wu, Z.; Li, D. *Electrochim. Acta* **2009**, *54*, 1715–1720.

(71) Choi, W.; Kim, J. S.; Lee, D. H.; Lee, K. K.; Koo, D. B.; Park, J. K. *Biomed. Microdevices* **2008**, *10*, 337–345.

(72) Yasukawa, T.; Suzuki, M.; Sekiya, T.; Shiku, H.; Matsue, T. *Biosens. Bioelectron.* **2007**, *22*, 2730–2736.

(73) Çetin, B.; Li, D. *Electrophoresis* **2010**, *31*, 3035–3043.

(74) Zhao, K.; Peng, R.; Li, D. *Nanoscale* **2016**, *8*, 18945–18955.

(75) Lin, J. T. Y.; Yeow, J. T. W. *Biomed. Microdevices* **2007**, *9*, 823–831.

(76) Chen, D.; Du, H. *Microfluid. Nanofluidics* **2007**, *3*, 603–610.

(77) Jia, Y.; Ren, Y.; Jiang, H. *Electrophoresis* **2015**, *36*, 1744–1753.

(78) Jaramillo, M. D. C.; Torrents, E.; Martínez-Duarte, R.; Madou, M. J.; Juárez, A. *Electrophoresis* **2010**, *31*, 2921–2928.

(79) Martinez-Duarte, R.; Gorkin, R. A.; Abi-Samra, K.; Madou, M. J. *Lab Chip* **2010**, *10*, 1030–1043.

(80) Li, M.; Li, W. H.; Zhang, J.; Alici, G.; Wen, W. *J. Phys. D. Appl. Phys.* **2014**, *47*, 063001.

(81) Yang, L.; Banada, P. P.; Chatni, M. R.; Seop Lim, K.; Bhunia, A. K.; Ladisch, M.; Bashir, R. *Lab Chip* **2006**, *6*, 896–905.

(82) Giraud, G.; Pethig, R.; Schulze, H.; Henihan, G.; Terry, J. G.; Menachery, A.; Ciani, I.; Corrigan, D.; Campbell, C. J.; Mount, A. R.; Ghazal, P.; Walton, A. J.; Crain, J.; Bachmann, T. T. *Biomicrofluidics* **2011**, *5*.

(83) Suehiro, J.; Shutou, M.; Hatano, T.; Hara, M. *Sensors Actuators, B Chem.* **2003**, *96*, 144–151.

(84) Gadish, N.; Voldman, J. *Anal. Chem.* **2006**, *78*, 7870–7876.

(85) Lagally, E. T.; Lee, S. H.; Soh, H. T. *Lab Chip* **2005**, *5*, 1053–1058.

(86) Suehiro, J.; Yatsunami, R.; Hamada, R.; Hara, M. *J. Phys. D. Appl. Phys.* **1999**, *32*, 2814–2820.

(87) Asbury, C. L.; Diercks, A. H.; Van Den Engh, G. *Electrophoresis* **2002**, *23*, 2658–2666.

(88) Narayanan Unni, H.; Hartono, D.; Yue Lanry Yung, L.; Mah-Lee Ng, M.; Pueh Lee, H.; Cheong Khoo, B.; Lim, K. M. *Biomicrofluidics* **2012**, *6*.

(89) Li, Y.; Dalton, C.; Crabtree, H. J.; Nilsson, G.; Kaler, K. V. I. S. *Lab Chip* **2007**, *7*, 239–248.

(90) Wu, L.; Lanry Yung, L. Y.; Lim, K. M. *Biomicrofluidics* **2012**, *6*.

(91) Li, H.; Bashir, R. *Sensors Actuators, B Chem.* **2002**, *86*, 215–221.

(92) Auerswald, J.; Knapp, H. F. *Microelectron. Eng.* **2003**, *67–68*, 879–886.

(93) Morgan, H.; Hughes, M. P.; Green, N. G. *Biophys. J.* **1999**, *77*, 516–525.

(94) Chung, C. C.; Cheng, I. F.; Yang, W. H.; Chang, H. C. *Biomicrofluidics* **2011**, *5*.

(95) Du, J. R.; Juang, Y. J.; Wu, J. T.; Wei, H. H. *Biomicrofluidics* **2008**, *2*.

(96) Hughes, M. P.; Morgan, H.; Rixon, F. J.; Burt, J. P. H.; Pethig, R. *Biochim. Biophys. Acta - Gen. Subj.* **1998**, *1425*, 119–126.

(97) Asokan, S. B.; Jawerth, L.; Carroll, R. L.; Cheney, R. E.; Washburn, S.; Superfine, R. *Nano Lett.* **2003**, *3*, 431–437.

(98) Beck, J. D.; Shang, L.; Li, B.; Marcus, M. S.; Hemers, R. J. *Anal. Chem.* **2008**, *80*, 3757–3761.

(99) Hölzel, R.; Calander, N.; Chiragwandi, Z.; Willander, M.; Bier, F. F. *Phys. Rev. Lett.* **2005**, *95*, 128102.

(100) Yang, F.; Yang, X.; Jiang, H.; Bulkhaults, P.; Wood, P.; Hrushesky, W.; Wang, G. *Biomicrofluidics* **2010**, *4*.

(101) Alshareef, M.; Metrakos, N.; Juarez Perez, E.; Azer, F.; Yang, F.; Yang, X.; Wang, G. *Biomicrofluidics* **2013**, *7*.

(102) Agarwal, S.; Sebastian, A.; Forrester, L. M.; Markx, G. H. *Biomicrofluidics* **2012**, *6*.

(103) Germishuizen, W. A.; Wälti, C.; Wirtz, R.; Johnston, M. B.; Pepper, M.; Davies, A. G.; Middelberg, A. P. J. *Nanotechnology* **2003**, *14*, 896–902.

(104) Zhu, K.; Kaprelyants, A. S.; Salina, E. G.; Markx, G. H. *Biomicrofluidics* **2010**, *4*.

(105) Suehiro, J.; Nakagawa, N.; Hidaka, S. I.; Ueda, M.; Imasaka, K.; Higashihata, M.; Okada, T.; Hara, M. *Nanotechnology* **2006**, *17*, 2567–2573.

(106) Suehiro, J. *Biomicrofluidics* **2010**, *4*.

(107) Kuczenski, R. S.; Chang, H. C.; Revzin, A. *Biomicrofluidics* **2011**, *5*.

(108) Kralj, J. G.; Lis, M. T. W.; Schmidt, M. A.; Jensen, K. F. *Anal. Chem.* **2006**, *78*, 5019–5025.

(109) Vahey, M. D.; Voldman, J. *Anal. Chem.* **2008**, *80*, 3135–3143.

(110) Han, K. H.; Frazier, A. B. *Lab Chip* **2008**, *8*, 1079–1086.

(111) Han, S. I.; Joo, Y. D.; Han, K. H. *Trans. Korean Soc. Mech. Eng. B* **2012**, *36*, 241–249.

(112) Thomas, R. S. W.; Mitchell, P. D.; Oreffo, R. O. C.; Morgan, H. *Biomicrofluidics* **2010**, *4*.

(113) Thomas, R. S.; Morgan, H.; Green, N. G. *Lab Chip* **2009**, *9*, 1534–1540.

(114) Chen, D. F.; Du, H.; Li, W. H. *J. Micromechanics Microengineering* **2006**, *16*, 1162–1169.

(115) Cheng, I. F.; Chang, H. C.; Hou, D.; Chang, H. C. *Biomicrofluidics* **2007**, *1*.

(116) Dürr, M.; Kentsch, J.; Müller, T.; Schnelle, T.; Stelzle, M. *Electrophoresis* **2003**, *24*, 722–731.

(117) Kentsch, J.; Dürr, M.; Schnelle, T.; Gradl, G.; Müller, T.; Jager, M.; Normann, A.; Stelzle, M. *IEE Proc. - Nanobiotechnology* **2003**, *150*, 82.

(118) Voldman, J.; Toner, M.; Gray, M. L.; Schmidt, M. A. *Transducers '01 Eurosensors XV* **2013**, No. C, 322–325.

(119) Martinez-Duarte, R.; Renaud, P.; Madou, M. J. *Electrophoresis* **2011**, *32*, 2385–2392.

(120) Iliescu, C.; Xu, G. L.; Samper, V.; Tay, F. E. H. *J. Micromechanics Microengineering* **2005**, *15*, 494–500.

(121) Voldman, J.; Gray, M. L.; Toner, M.; Schmidt, M. A. *Anal. Chem.* **2002**, *74*, 3984–3990.

(122) Wang, L.; Flanagan, L.; Lee, A. P. *J. Microelectromechanical Syst.* **2007**, *16*, 454–461.

(123) Li, S.; Li, M.; Hui, Y. S.; Cao, W.; Li, W.; Wen, W. *Microfluid. Nanofluidics* **2013**, *14*, 499–508.

(124) Demierre, N.; Braschler, T.; Linderholm, P.; Seger, U.; Van Lintel, H.; Renaud, P. *Lab Chip* **2007**, *7*, 355–365.

(125) Luo, J.; Nelson, E.; Li, G. P.; Bachman, M. *Proc. - Electron. Components Technol. Conf.* **2013**, 1905–1911.

(126) Lewpiriyawong, N.; Yang, C.; Lam, Y. C. *Electrophoresis* **2010**, *31*, 2622–2631.

(127) Zhang, C.; Khoshmanesh, K.; Tovar-Lopez, F. J.; Mitchell, A.; Wlodarski, W.; Klantar-Zadeh, K. *Microfluid. Nanofluidics* **2009**, *7*, 633–645.

(128) Becker, F. F.; Wang, X. B.; Huang, Y.; Pethig, R.; Vykoukal, J.; Gascoyne, P. R. *Proc. Natl. Acad. Sci.* **1995**, *92*, 860–864.

(129) Pethig, R.; Huang, Y.; Wang, X. B.; Burt, J. P. H. *J. Phys. D. Appl. Phys.* **1992**, *25*, 881–888.

(130) Green, N. G.; Morgan, H. *J. Phys. D. Appl. Phys.* **1998**, *31*, L25–L30.

(131) Tai, C. H.; Hsiung, S. K.; Chen, C. Y.; Tsai, M. L.; Lee, G. Bin. *Biomed. Microdevices* **2007**, *9*, 533–543.

(132) Shim, S.; Stemke-Hale, K.; Tsimberidou, A. M.; Noshari, J.; Anderson, T. E.; Gascoyne, P. R. C. *Biomicrofluidics* **2013**, *7*.

(133) Shim, S.; Stemke-Hale, K.; Noshari, J.; Becker, F. F.; Gascoyne, P. R. C. *Biomicrofluidics* **2013**, *7*.

(134) Khoshmanesh, K.; Zhang, C.; Nahavandi, S.; Tovar-Lopez, F. J.; Baratchi, S.; Mitchell, A.; Kalantar-Zadeh, K. *J. Appl. Phys.* **2010**, *108*, 034904.

(135) Khoshmanesh, K.; Zhang, C.; Tovar-Lopez, F. J.; Nahavandi, S.; Baratchi, S.; Kalantar-Zadeh, K.; Mitchell, A. *Electrophoresis* **2009**, *30*, 3707–3717.

(136) Kim, U.; Qian, J.; Kenrick, S. A.; Daugherty, P. S.; Soh, H. T. *Anal. Chem.* **2008**, *80*, 8656–8661.

(137) Krishnan, R.; Heller, M. J. *J. Biophotonics* **2009**, *2*, 253–261.

(138) Sonnenberg, A.; Marciniak, J. Y.; Krishnan, R.; Heller, M. J. *Electrophoresis* **2012**, *33*, 2482–2490.

(139) Sonnenberg, A.; Marciniak, J. Y.; Mccanna, J.; Krishnan, R.; Rassenti, L.; Kipps, T. J.; Heller, M. J. *Electrophoresis* **2013**, *34*, 1076–1084.

(140) Park, J.; Kim, B.; Choi, S. K.; Hong, S.; Lee, S. H.; Lee, K. Il. *Lab Chip* **2005**, *5*, 1264–1270.

(141) Iliescu, C.; Yu, L.; Tay, F. E. H.; Pang, A. J. *TRANSDUCERS EUROSENSORS '07 - 4th Int. Conf.*

Solid-State Sensors, Actuators Microsystems **2007**, *129*, 1837–1840.

(142) Liming Yu; Iliescu, C.; Guolin Xu; Tay, F. E. H. *J. Microelectromechanical Syst.* **2007**, *16*, 1120–1129.

(143) Wang, L.; Lu, J.; Marchenko, S. A.; Monuki, E. S.; Flanagan, L. A.; Lee, A. P. *Electrophoresis* **2009**, *30*, 782–791.

(144) Tornay, R.; Braschler, T.; Demierre, N.; Steitz, B.; Finka, A.; Hofmann, H.; Hubbell, J. A.; Renaud, P. *Lab Chip* **2008**, *8*, 267–273.

(145) Piacentini, N.; Mernier, G.; Tornay, R.; Renaud, P. *Biomicrofluidics* **2011**, *5*.

(146) Braschler, T.; Demierre, N.; Nascimento, E.; Silva, T.; Oliva, A. G.; Renaud, P. *Lab Chip* **2008**, *8*, 280–286.

(147) Valero, A.; Braschler, T.; Demierre, N.; Renaud, P. *Biomicrofluidics* **2010**, *4*.

(148) Nascimento, E. M.; Nogueira, N.; Silva, T.; Braschler, T.; Demierre, N.; Renaud, P.; Oliva, A. G. *Bioelectrochemistry* **2008**, *73*, 123–128.

(149) Lewpiriyawong, N.; Yang, C. *Biomicrofluidics* **2012**, *6*.

(150) Lewpiriyawong, N.; Kandaswamy, K.; Yang, C.; Ivanov, V.; Stocker, R. *Anal. Chem.* **2011**, *83*, 9579–9585.

(151) Huh, D.; Gu, W.; Kamotani, Y.; Grotberg, J. B.; Takayama, S. *Physiol. Meas.* **2005**, *26*, R73–R98.

(152) Morgan, H.; Holmes, D.; Green, N. G. *Curr. Appl. Phys.* **2006**, *6*, 367–370.

(153) Holmes, D.; Morgan, H.; Green, N. G. *Biosens. Bioelectron.* **2006**, *21*, 1621–1630.

(154) Yu, C.; Vykoukal, J.; Vykoukal, D. M.; Schwartz, J. A.; Shi, L.; Gascoyne, P. R. C. *J. Microelectromechanical Syst.* **2005**, *14*, 480–487.

(155) Demierre, N.; Braschler, T.; Muller, R.; Renaud, P. *TRANSDUCERS EUROSENSORS '07 - 4th Int. Conf. Solid-State Sensors, Actuators Microsystems* **2007**, *132*, 1777–1780.

(156) Ramadan, Q.; Samper, V.; Poenar, D.; Liang, Z.; Yu, C.; Lim, T. M. *Sensors Actuators, B Chem.* **2006**, *113*, 944–955.

(157) Fuhr, G.; Müller, T.; Baukloh, V.; Lucas, K. *Hum. Reprod.* **1998**, *13*, 136–141.

(158) Jang, L. S.; Huang, P. H.; Lan, K. C. *Biosens. Bioelectron.* **2009**, *24*, 3637–3644.

(159) Rosenthal, A.; Voldman, J. *Biophys. J.* **2005**, *88*, 2193–2205.

(160) Voldman, J.; Braff, R. A.; Toner, M.; Gray, M. L.; Schmidt, M. A. *Biophys. J.* **2001**, *80*, 531–542.

(161) Manaresi, N.; Romani, A.; Medoro, G.; Altomare, L.; Leonardi, A.; Tartagni, M.; Guerrieri, R. *IEEE J. Solid-State Circuits* **2003**, *38*, 2297–2305.

(162) Hunt, T. P.; Issadore, D.; Westervelt, R. M. *Lab Chip* **2007**, *8*, 81–87.

(163) Gascoyne, P. R. C.; Vykoukal, J. V.; Schwartz, J. A.; Anderson, T. J.; Vykoukal, D. M.; Current, K. W.; McConaghy, C.; Becker, F. F.; Andrews, C. *Lab Chip* **2004**, *4*, 299–309.

(164) Hsiung, L. C.; Yang, C. H.; Chiu, C. L.; Chen, C. L.; Wang, Y.; Lee, H.; Cheng, J. Y.; Ho, M. C.; Wo, A. M. *Biosens. Bioelectron.* **2008**, *24*, 869–875.

(165) Jaeger, M. S.; Uhlig, K.; Schnelle, T.; Mueller, T. *J. Phys. D. Appl. Phys.* **2008**, *41*, 175502.

(166) Li, M.; Li, S.; Cao, W.; Li, W.; Wen, W.; Alici, G. *Microfluid. Nanofluidics* **2013**, *14*, 527–539.

(167) Li, S.; Li, M.; Bougot-Robin, K.; Cao, W.; Yeung Yeung Chau, I.; Li, W.; Wen, W. *Biomicrofluidics* **2013**, *7*.

(168) Voldman, J.; Toner, M.; Gray, M. L.; Schmidt, M. A. *J. Electrostat.* **2003**, *57*, 69–90.

(169) Park, B. Y.; Madou, M. J. *Electrophoresis* **2005**, *26*, 3745–3757.

(170) Tay, F. E. H.; Yu, L.; Pang, A. J.; Iliescu, C. *Electrochim. Acta* **2007**, *52*, 2862–2868.

(171) Markx, G. H.; Dyda, P. A.; Pethig, R. *J. Biotechnol.* **1996**, *51*, 175–180.

(172) Regtmeier, J.; Eichhorn, R.; Viefhues, M.; Bogunovic, L.; Anselmetti, D. *Electrophoresis* **2011**, *32*, 2253–2273.

(173) Cummings, E. B.; Singh, A. K. *Anal. Chem.* **2003**, *75*, 4724–4731.

(174) Lapizco-Encinas, B. H.; Simmons, B. A.; Cummings, E. B.; Fintschenko, Y. *Anal. Chem.* **2004**, *76*, 1571–1579.

(175) Jen, C. P.; Huang, C. Te; Weng, C. H. *Microelectron. Eng.* **2010**, *87*, 773–777.

(176) Kang, Y.; Li, D.; Kalams, S. A.; Eid, J. E. *Biomed. Microdevices* **2008**, *10*, 243–249.

(177) Church, C.; Zhu, J.; Huang, G.; Tzeng, T. R.; Xuan, X. *Biomicrofluidics* **2010**, *4*.

(178) Barbulovic-Nad, I.; Xuan, X.; Lee, J. S. H.; Li, D. *Lab Chip* **2006**, *6*, 274–279.

(179) Thwar, P. K.; Linderman, J. J.; Burns, M. A. *Electrophoresis* **2007**, *28*, 4572–4581.

(180) Hawkins, B. G.; Smith, A. E.; Syed, Y. A.; Kirby, B. J. *Anal. Chem.* **2007**, *79*, 7291–7300.

(181) Barrett, L. M.; Skulan, A. J.; Singh, A. K.; Cummings, E. B.; Fiechtner, G. J. *Anal. Chem.* **2005**, *77*, 6798–6804.

(182) Church, C.; Zhu, J.; Nieto, J.; Keten, G.; Ibarra, E.; Xuan, X. *J. Micromechanics Microengineering* **2010**, *20*, 065011.

(183) Chen, K. P.; Pacheco, J. R.; Hayes, M. A.; Staton, S. J. R. *Electrophoresis* **2009**, *30*, 1441–1448.

(184) Zhu, J.; Tzeng, T. R. J.; Xuan, X. *Electrophoresis* **2010**, *31*, 1382–1388.

(185) Zhu, J.; Xuan, X. *J. Colloid Interface Sci.* **2009**, *340*, 285–290.

(186) Zhang, L.; Tatar, F.; Turmezei, P.; Bastemeijer, J.; Mollinger, J. R.; Piciu, O.; Bossche, A. *J. Phys. Conf. Ser.* **2006**, *34*, 527–532.

(187) Kang, K. H.; Kang, Y.; Xuan, X.; Li, D. *Electrophoresis* **2006**, *27*, 694–702.

(188) Hyoung Kang, K.; Xuan, X.; Kang, Y.; Li, D. *J. Appl. Phys.* **2006**, *99*.

(189) Parikesit, G. O. F.; Markesteijn, A. P.; Piciu, O. M.; Bossche, A.; Westerweel, J.; Young, I. T.; Garini, Y. *Biomicrofluidics* **2008**, *2*.

(190) Lewpiriyawong, N.; Yang, C.; Lam Cheong, Y. *Biomicrofluidics* **2008**, *2*.

(191) Srivastava, S. K.; Baylon-Cardiel, J. L.; Lapizco-Encinas, B. H.; Minerick, A. R. *J. Chromatogr. A* **2011**, *1218*, 1780–1789.

(192) Regtmeier, J.; Thanh, T. D.; Eichhorn, R.; Anselmetti, D.; Ros, A. *Anal. Chem.* **2007**, *79*, 3925–3932.

(193) Moncada-Hernandez, H.; Baylon-Cardiel, J. L.; Pérez-González, V. H.; Lapizco-Encinas, B. H. *Electrophoresis* **2011**, *32*, 2502–2511.

(194) Shafiee, H.; Sano, M. B.; Henslee, E. A.; Caldwell, J. L.; Davalos, R. V. *Lab Chip* **2010**, *10*, 438–445.

(195) Gallo-Villanueva, R. C.; Jesús-Pérez, N. M.; Martínez-López, J. I.; Pacheco, A.; Lapizco-Encinas, B. H. *Microfluid. Nanofluidics* **2011**, *10*, 1305–1315.

(196) Zhu, J.; Xuan, X. *Biomicrofluidics* **2011**, *5*.

(197) Staton, S. J. R.; Chen, K. P.; Taylor, T. J.; Pacheco, J. R.; Hayes, M. A. *Electrophoresis* **2010**, *31*, 3634–3641.

(198) Church, C.; Zhu, J.; Wang, G.; Tzeng, T. R. J.; Xuan, X. *Biomicrofluidics* **2009**, *3*.

(199) Zhu, J.; Canter, R. C.; Keten, G.; Vedantam, P.; Tzeng, T. R. J.; Xuan, X. *Microfluid. Nanofluidics* **2011**, *11*, 743–752.

(200) Church, C.; Zhu, J.; Xuan, X. *Electrophoresis* **2011**, *32*, 527–531.

(201) Everwand, M.; Anselmetti, D.; Regtmeier, J. *14th Int. Conf. Miniaturized Syst. Chem. Life Sci.* **2010**, No. October, 19–21.

(202) Cummings, E. B.; Singh, A. K. *Microfluid. Devices Syst. III* **2006**, *4177*, 151–160.

(203) Lapizco-Encinas, B. H.; Davalos, R. V.; Simmons, B. A.; Cummings, E. B.; Fintschenko, Y. *J. Microbiol. Methods* **2005**, *62*, 317–326.

(204) Gallo-Villanueva, R. C.; Rodríguez-López, C. E.; Díaz-de-la-Garza, R. I.; Reyes-Betanzo, C.; Lapizco-Encinas, B. H. *Electrophoresis* **2009**, *30*, 4195–4205.

(205) Sabounchi, P.; Morales, A. M.; Ponce, P.; Lee, L. P.; Simmons, B. A.; Davalos, R. V. *Biomed. Microdevices* **2008**, *10*, 661–670.

(206) Chou, C. F.; Tegenfeldt, J. O.; Bakajin, O.; Chan, S. S.; Cox, E. C.; Darnton, N.; Duke, T.; Austin, R. H. *Biophys. J.* **2002**, *83*, 2170–2179.

(207) Chou, C. F.; Zenhausern, F. *IEEE Eng. Med. Biol. Mag.* **2003**, *22*, 62–67.

(208) Swami, N.; Chou, C. F.; Ramamurthy, V.; Chaurey, V. *Lab Chip* **2009**, *9*, 3212–3220.

(209) Zhu, J.; Xuan, X. *Electrophoresis* **2009**, *30*, 2668–2675.

(210) Jen, C. P.; Weng, C. H.; Huang, C. Te. *Electrophoresis* **2011**, *32*, 2428–2435.

(211) Jen, C. P.; Huang, C. Te; Shih, H. Y. *Microsyst. Technol.* **2010**, *16*, 1097–1104.

(212) Zhu, J.; Tzeng, T. R. J.; Hu, G.; Xuan, X. *Microfluid. Nanofluidics* **2009**, *7*, 751–756.

(213) Chen, D.; Du, H. *Microfluid. Nanofluidics* **2010**, *9*, 281–291.

(214) Huang, Y.; Wang, X.-B.; Tame, J. A.; Pethig, R. *J. Phys. D, Appl. Phys.* **1993**, *26*, 1528–1535.

(215) Wang, X. B.; Huang, Y.; Holzel, R.; Burt, J. P. H.; Pethig, R. *J. Phys. D. Appl. Phys.* **1993**, *26*, 312–322.

(216) Wang, X. B.; Huang, Y.; Becker, F. F.; Gascoyne, P. R. C. *J. Phys. D-Applied Phys.* **1994**, *27*, 1571–1574.

(217) Masuda, S.; Washizu, M.; Iwadare, M. *IEEE Trans. Ind. Appl.* **1987**, *IA-23*, 474–480.

(218) Kawabata, I. *IEEE Trans. Ind. Appl.* **1988**, *24*, 217–222.

(219) Fuhr, G.; Hagedorn, R. *Ieee Mems* **1991**, *30*, 259–264.

(220) Hagedorn, R.; Fuhr, G.; Müller, T.; Gimsa, J. *Electrophoresis* **1992**, *13*, 49–54.

(221) Fuhr, G.; Schnelle, T.; Wagner, B. *J. Micromechanics Microengineering* **1994**, *4*, 217–226.

(222) Talary, M. S.; Burt, J. P. H.; Tame, J. A.; Pethig, R. *J. Phys. D. Appl. Phys.* **1996**, *29*, 2198–2203.

(223) Hughes, M. P.; Pethig, R.; Wang, X. B. *J. Phys. D. Appl. Phys.* **1996**, *29*, 474–482.

(224) Arnold, W. M.; Zimmermann, U. *J. Electrostat.* **1988**, *21*, 151–191.

(225) Yang, J.; Huang, Y.; Wang, X.; Wang, X. B.; Becker, F. F.; Gascoyne, P. R. C. *Biophys. J.* **1999**, *76*, 3307–3314.

(226) Gimsa, J.; Marszalek, P.; Loewe, U.; Tsong, T. Y. *Biophys. J.* **1991**, *60*, 749–760.

(227) Huang, J. P.; Yu, K. W.; Gu, G. Q. *Phys. Rev. E - Stat. Physics, Plasmas, Fluids, Relat. Interdiscip. Top.* **2002**, *65*.

(228) Huang, Y.; Holzel, R.; Pethig, R.; Xiao-B.Wang. *Phys. Med. Biol.* **1992**, *37*, 1499–1517.

(229) Huang, Y.; Wang, X. B.; Holzel, R.; Becker, F. F.; Gascoyne, P. R. C. *Phys. Med. Biol.* **1995**, *40*, 1789–1806.

(230) Hölzel, R. *Biophys. J.* **1997**, *73*, 1103–1109.

(231) Gimsa, J.; Wachner, D. *Biophys. J.* **1998**, *75*, 1107–1116.

(232) Çetin, B.; Li, D. *Electrophoresis* **2011**, *32*, 2410–2427.

(233) Peng, R.; Li, D. *Biomicrofluidics* **2015**, *9*.

(234) Choi, K. M.; Rogers, J. A. *J. Am. Chem. Soc.* **2003**, *125*, 4060–4061.

(235) Duffy, D. C.; McDonald, J. C.; Schueller, O. J. A.; Whitesides, G. M. *Anal. Chem.* **1998**, *70*, 4974–4984.

(236) Lalonde, A.; Romero-Creel, M. F.; Lapizco-Encinas, B. H. *Electrophoresis* **2015**, *36*, 1479–1484.

(237) Saucedo-Espinosa, M. A.; Lalonde, A.; Gencoglu, A.; Romero-Creel, M. F.; Dolas, J. R.; Lapizco-Encinas, B. H. *Electrophoresis* **2016**, *37*, 282–290.

(238) Srivastava, S. K.; Artemiou, A.; Minerick, A. R. *Electrophoresis* **2011**, *32*, 2530–2540.

(239) Gallo-Villanueva, R. C.; Pérez-González, V. H.; Davalos, R. V.; Lapizco-Encinas, B. H. *Electrophoresis* **2011**, *32*, 2456–2465.

(240) Zellner, P.; Agah, M. *Electrophoresis* **2012**, *33*, 2498–2507.

(241) Zhao, K.; Peng, R.; Li, D. *Nanoscale* **2016**, *8*, 18945–18955.

(242) Çetin, B.; Li, D. *Electrophoresis* **2011**, *32*, 2410–2427.

(243) Gascoyne, P. R. C.; Vykoukal, J. V. *Proc. IEEE* **2004**, *92*, 22–42.

(244) Li, M.; Li, S.; Li, W.; Wen, W.; Alici, G. *Electrophoresis* **2013**, *34*, 952–960.

(245) Xuan, X.; Zhu, J.; Church, C. *Microfluid. Nanofluidics* **2010**, *9*, 1–16.

(246) Walther, A.; Müller, A. H. E. *Soft Matter* **2008**, *4*, 663–668.

(247) Zhang, L.; Zhu, Y. *Langmuir* **2012**, *28*, 13201–13207.

(248) Hong, L.; Jiang, S.; Granick, S. *Langmuir* **2006**, *22*, 9495–9499.

(249) Liang, H.; Cacciuto, A.; Luijter, E.; Granick, S. *Nano Lett.* **2006**, *6*, 2510–2514.

(250) Zhao, Y.; Gu, H.; Xie, Z.; Shum, H. C.; Wang, B.; Gu, Z. *J. Am. Chem. Soc.* **2013**, *135*, 54–57.

(251) Yang, Y. T.; Wei, J.; Li, X.; Wu, L. J.; Chang, Z. Q.; Serra, C. A. *Adv. Powder Technol.* **2015**, *26*, 156–162.

(252) Lan, J.; Chen, J.; Li, N.; Ji, X.; Yu, M.; He, Z. *Talanta* **2016**, *151*, 126–131.

(253) Daghighi, Y.; Li, D. *Lab Chip* **2011**, *11*, 2929–2940.

(254) Laugel, C.; Baillet, A.; Youenang Piemi, M. P.; Marty, J. P.; Ferrier, D. *Int. J. Pharm.* **1998**, *160*, 109–117.

(255) Zhao, C. X. *Adv. Drug Deliv. Rev.* **2013**, *65*, 1420–1446.

(256) Bickel, T.; Majee, A.; Würger, A. *Phys. Rev. E - Stat. Nonlinear, Soft Matter Phys.* **2013**, *88*, 012301.

(257) Jiang, H. R.; Yoshinaga, N.; Sano, M. *Phys. Rev. Lett.* **2010**, *105*, 268302.

(258) Ren, B.; Ruditskiy, A.; Song, J. H.; Kretzschmar, I. *Langmuir* **2012**, *28*, 1149–1156.

(259) Ruditskiy, A.; Ren, B.; Kretzschmar, I. *Soft Matter* **2013**, *9*, 9174–9181.

(260) Smoukov, S. K.; Gangwal, S.; Marquez, M.; Velev, O. D. *Soft Matter* **2009**, *5*, 1285–1292.

(261) Chen, J.; Zhang, H.; Zheng, X.; Cui, H. *AIP Adv.* **2014**, *4*, 031325.

(262) Boymelgreen, A.; Yossifon, G.; Park, S.; Miloh, T. *Phys. Rev. E - Stat. Nonlinear, Soft Matter Phys.* **2014**, *89*, 011003.

(263) Zhang, L.; Zhu, Y. *Appl. Phys. Lett.* **2010**, *96*, 141902.

(264) Gangwal, S.; Cayre, O. J.; Velev, O. D. *Langmuir* **2008**, *24*, 13312–13320.

(265) Peng, C.; Lazo, I.; Shiyanovskii, S. V.; Lavrentovich, O. D. *Phys. Rev. E - Stat. Nonlinear, Soft Matter Phys.* **2014**, *90*, 051002.

(266) Gangwal, S.; Cayre, O. J.; Bazant, M. Z.; Velev, O. D. *Phys. Rev. Lett.* **2008**, *100*, 058302.

(267) Ren, Y. K.; Morganti, D.; Jiang, H. Y.; Ramos, A.; Morgan, H. *Langmuir* **2011**, *27*, 2128–2131.

(268) Chen, Y. L.; Jiang, H. R. *Appl. Phys. Lett.* **2016**, *109*, 191605.

(269) Daghighi, Y.; Li, D. *Microfluid. Nanofluidics* **2010**, *9*, 593–611.

(270) Honegger, T.; Lecarme, O.; Berton, K.; Peyrade, D. *Microelectron. Eng.* **2010**, *87*, 756–759.

(271) García-Sánchez, P.; Ren, Y.; Arcenegui, J. J.; Morgan, H.; Ramos, A. *Langmuir* **2012**, *28*, 13861–13870.

(272) Gangwal, S.; Pawar, A.; Kretzschmar, I.; Velev, O. D. *Soft Matter* **2010**, *6*, 1413–1418.

(273) Zhu, J.; Canter, R. C.; Keten, G.; Vedantam, P.; Tzeng, T. R. J.; Xuan, X. *Microfluid. Nanofluidics* **2011**, *11*, 743–752.

(274) Sun, J.; Gao, Y.; Isaacs, R. J.; Boelte, K. C.; Charles Lin, P.; Boczko, E. M.; Li, D. *Anal. Chem.* **2012**, *84*, 2017–2024.

(275) Ermolina, I.; Morgan, H. *J. Colloid Interface Sci.* **2005**, *285*, 419–428.

(276) O'Konski, C. T. *J. Phys. Chem.* **1960**, *64*, 605–619.

(277) Blaney, L. *Lehigh Rev.* **2007**, *15*.

(278) Ermolina, I.; Morgan, H. *J. Colloid Interface Sci.* **2005**, *285*, 419–428.

(279) Das, D.; Biswas, K.; Das, S. *Med. Eng. Phys.* **2014**, *36*, 726–731.

(280) Millman, J. R.; Bhatt, K. H.; Prevo, B. G.; Velev, O. D. *Nat. Mater.* **2005**, *4*, 98–102.

(281) De Geest, B. G.; Urbanski, J. P.; Thorsen, T.; Demeester, J.; De Smedt, S. C. *Langmuir* **2005**, *21*, 10275–10279.

(282) Yang, W. W.; Lu, Y. C.; Xiang, Z. Y.; Luo, G. S. *React. Funct. Polym.* **2007**, *67*, 81–86.

(283) Sakai, S.; Hashimoto, I.; Kawakami, K. *Biochem. Eng. J.* **2006**, *30*, 218–221.

(284) Kato, A.; Shindo, E.; Sakaue, T.; Tsuji, A.; Yoshikawa, K. *Biophys. J.* **2009**, *97*, 1678–1686.

(285) Clausell-Tormos, J.; Lieber, D.; Baret, J. C.; El-Harrak, A.; Miller, O. J.; Frenz, L.; Blouwolff, J.; Humphry, K. J.; Köster, S.; Duan, H.; Holtze, C.; Weitz, D. A.; Griffiths, A. D.; Merten, C. A. *Chem. Biol.* **2008**, *15*, 427–437.

(286) Akbari, S.; Pirbodaghi, T. *Lab Chip* **2014**, *14*, 3275–3280.

(287) Chen, W. W.; Balaj, L.; Liau, L. M.; Samuels, M. L.; Kotsopoulos, S. K.; Maguire, C. A.; LoGuidice, L.; Soto, H.; Garrett, M.; Zhu, L. D.; Sivaraman, S.; Chen, C.; Wong, E. T.; Carter, B. S.; Hochberg, F. H.; Breakefield, X. O.; Skog, J. *Mol. Ther. - Nucleic Acids* **2013**, *2*, e109.

(288) Du, G. S.; Pan, J. Z.; Zhao, S. P.; Zhu, Y.; Den Toonder, J. M. J.; Fang, Q. *Anal. Chem.* **2013**, *85*, 6740–6747.

(289) Moniruzzaman, M.; Kamiya, N.; Goto, M. *J. Colloid Interface Sci.* **2010**, *352*, 136–142.

(290) Porada, J. H.; Mansueto, M.; Laschat, S.; Stubenrauch, C. *J. Mol. Liq.* **2017**, *227*, 202–209.

(291) Somers, A.; Howlett, P.; MacFarlane, D.; Forsyth, M. *Lubricants* **2013**, *1*, 3–21.

(292) Chen, S.; Zhang, S.; Liu, X.; Wang, J.; Wang, J.; Dong, K.; Sun, J.; Xu, B. *Phys. Chem. Chem. Phys.* **2014**, *16*, 5893–5906.

(293) Han, X.; Armstrong, D. W. *Acc. Chem. Res.* **2007**, *40*, 1079–1086.

(294) Siódmiak, T.; Marsza, M. P.; Proszowska, A. *Mini. Rev. Org. Chem.* **2012**, *9*, 0–0.

(295) Laali, K. K. *Synthesis (Stuttg).* **2003**, *2003*, 1752–1752.

(296) Plechkova, N. V.; Seddon, K. R. *Chem. Soc. Rev.* **2008**, *37*, 123–150.

(297) Kosmulski, M.; Gustafsson, J.; Rosenholm, J. B. *Thermochim. Acta* **2004**, *412*, 47–53.

(298) Harada, M.; Kimura, Y.; Saijo, K.; Ogawa, T.; Isoda, S. *J. Colloid Interface Sci.* **2009**, *339*, 373–381.

(299) Welton, T. *Chem. Rev.* **1999**, *99*, 2071–2084.

(300) Endres, F.; Zein El Abedin, S. *Phys. Chem. Chem. Phys.* **2006**, *8*, 2101–2116.

(301) Binnemans, K. *Chem. Rev.* **2005**, *105*, 4148–4204.

(302) Anderson, J. L.; Armstrong, D. W.; Wei, G.-T. *Anal. Chem.* **2006**, *78*, 2892–2902.

(303) Capello, C.; Fischer, U.; Hungerbühler, K. *Green Chem.* **2007**, *9*, 927–934.

(304) Hallett, J. P.; Welton, T. *Chem. Rev.* **2011**, *111*, 3508–3576.

(305) Sun, P.; Armstrong, D. W. *Anal. Chim. Acta* **2010**, *661*, 1–16.

(306) Zhou, F.; Liang, Y.; Liu, W. *Chem. Soc. Rev.* **2009**, *38*, 2590–2599.

(307) Forsyth, M.; Neil, W. C.; Howlett, P. C.; MacFarlane, D. R.; Hinton, B. R. W.; Rocher, N.; Kemp, T. F.; Smith, M. E. *ACS Appl. Mater. Interfaces* **2009**, *1*, 1045–1052.

(308) Visser, A. E.; Swatloski, R. P.; Griffin, S. T.; Hartman, D. H.; Rogers, R. D. *Sep. Sci. Technol.* **2001**, *36*, 785–804.

(309) Anderson, J. L.; Armstrong, D. W. *Anal. Chem.* **2005**, *77*, 6453–6462.

(310) Yang, Z.; Pan, W. *Enzyme Microb. Technol.* **2005**, *37*, 19–28.

(311) Sheldon, R. A.; Lau, R. M.; Sorgedrager, M. J.; van Rantwijk, F.; Seddon, K. R. *Green Chem.* **2002**, *4*, 147–151.

(312) Moniruzzaman, M.; Nakashima, K.; Kamiya, N.; Goto, M. *Biochem. Eng. J.* **2010**, *48*, 295–314.

(313) Moniruzzaman, M.; Kamiya, N.; Goto, M. *Org. Biomol. Chem.* **2010**, *8*, 2887–2899.

(314) Visser, A. E.; Swatloski, R. P.; Reichert, W. M.; Mayton, R.; Sheff, S.; Wierzbicki, A.; Davis, J.; Rogers, R. D. *Chem. Commun.* **2001**, No. 1, 135–136.

(315) Patel, R.; Kumari, M.; Khan, A. B. *Appl. Biochem. Biotechnol.* **2014**, *172*, 3701–3720.

(316) Taha, M.; Almeida, M. R.; Silva, F. A. E.; Domingues, P.; Ventura, S. P. M.; Coutinho, J. A. P.; Freire, M. G. *Chem. - A Eur. J.* **2015**, *21*, 4781–4788.

(317) Holbrey, J. D.; Visser, A. E.; Spear, S. K.; Reichert, W. M.; Swatloski, R. P.; Broker, G. A.; Rogers, R. D. *Green Chem.* **2003**, *5*, 129–135.

(318) Heller, W. T.; O'Neill, H. M.; Zhang, Q.; Baker, G. A. *J. Phys. Chem. B* **2010**, *114*, 13866–13871.

(319) Sivapragasam, M.; Moniruzzaman, M.; Goto, M. *Biotechnol. J.* **2016**, *11*, 1000–1013.

(320) Joensson, H. N.; Andersson Svahn, H. *Angew. Chemie - Int. Ed.* **2012**, *51*, 12176–12192.

(321) Guo, M. T.; Rotem, A.; Heyman, J. A.; Weitz, D. A. *Lab Chip* **2012**, *12*, 2146–2155.

(322) Song, H.; Ismagilov, R. F. *J. Am. Chem. Soc.* **2003**, *125*, 14613–14619.

(323) Henkel, T.; Bermig, T.; Kielpinski, M.; Grodrian, A.; Metze, J.; Köhler, J. M. *Chem. Eng. J.* **2004**, *101*, 439–445.

(324) Ju, J.; Zeng, C.; Zhang, L.; Xu, N. *Chem. Eng. J.* **2006**, *116*, 115–121.

(325) Zilionis, R.; Nainys, J.; Veres, A.; Savova, V.; Zemmour, D.; Klein, A. M.; Mazutis, L. *Nat. Protoc.* **2017**, *12*, 44–73.

(326) Teh, S. Y.; Lin, R.; Hung, L. H.; Lee, A. P. *Lab Chip* **2008**, *8*, 198–220.

(327) Schramm, L. L. *Emuls. Foam. Suspens. Fundam. Appl.* **2006**, 1–448.

(328) Ganguli, D.; Ganguli, M. *Inorganic Particle Synthesis via Macro and Microemulsions: A Micrometer to Nanometer Landscape*; Springer Science & Business Media, 2003.

(329) Nisisako, T.; Torii, T.; Takahashi, T.; Takizawa, Y. *Adv. Mater.* **2006**, *18*, 1152–1156.

(330) Xu, J. H.; Li, S. W.; Tan, J.; Wang, Y. J.; Luo, G. S. *AIChE J.* **2006**, *52*, 3005–3010.

(331) Nisisako, T.; Torii, T.; Higuchi, T. *Lab Chip* **2002**, *2*, 24–26.

(332) Priest, C.; Herminghaus, S.; Seemann, R. *Appl. Phys. Lett.* **2006**, *88*, 1–3.

(333) Thorsen, T.; Roberts, R. W.; Arnold, F. H.; Quake, S. R. *Phys. Rev. Lett.* **2001**, *86*, 4163–4166.

(334) Takeuchi, S.; Garstecki, P.; Weibel, D. B.; Whitesides, G. M. *Adv. Mater.* **2005**, *17*, 1067–1072.

(335) Woodward, A.; Cosgrove, T.; Espidel, J.; Jenkins, P.; Shaw, N. *Soft Matter* **2007**, *3*, 627–633.

(336) Yobas, L.; Martens, S.; Ong, W. L.; Ranganathan, N. *Lab Chip* **2006**, *6*, 1073–1079.

(337) Anna, S. L.; Bontoux, N.; Stone, H. A. *Appl. Phys. Lett.* **2003**, *82*, 364–366.

(338) Ahmed, R.; Jones, T. B. *J. Electrostat.* **2006**, *64*, 543–549.

(339) Jones, T. B.; Gunji, M.; Washizu, M.; Feldman, M. J. *J. Appl. Phys.* **2001**, *89*, 1441–1448.

(340) Jones, T. B. *J. Electrostat.* **2001**, *51–52*, 290–299.

(341) Cho, S. K.; Moon, H.; Kim, C. J. *J. Microelectromechanical Syst.* **2003**, *12*, 70–80.

(342) Roux, J. M.; Fouillet, Y.; Achard, J. L. *Sensors Actuators, A Phys.* **2007**, *134*, 486–493.

(343) Berthier, J.; Clementz, P.; Raccurt, O.; Jary, D.; Claustre, P.; Peponnet, C.; Fouillet, Y. *Sensors Actuators, A Phys.* **2006**, *127*, 283–294.

(344) Christopher, G. F.; Anna, S. L. *J. Phys. D. Appl. Phys.* **2007**, *40*, R319–R336.

(345) Chen, C. T.; Lee, G. B. *J. Microelectromechanical Syst.* **2006**, *15*, 1492–1498.

(346) Tan, Y. C.; Lee, A. P. *Lab Chip* **2005**, *5*, 1178–1183.

(347) Tan, Y. C.; Fisher, J. S.; Lee, A. I.; Cristini, V.; Lee, A. P. *Lab Chip* **2004**, *4*, 292–298.

(348) Tan, Y. C.; Ho, Y. L.; Lee, A. P. *Microfluid. Nanofluidics* **2007**, *3*, 495–499.

(349) Huh, D.; Bahng, J. H.; Ling, Y.; Wei, H. H.; Kripfgans, O. D.; Fowlkes, J. B.; Grotberg, J. B.; Takayama, S. *Anal. Chem.* **2007**, *79*, 1369–1376.

(350) Abate, A. R.; Agresti, J. J.; Weitz, D. A. *Appl. Phys. Lett.* **2010**, *96*.

(351) Cao, Z.; Chen, F.; Bao, N.; He, H.; Xu, P.; Jana, S.; Jung, S.; Lian, H.; Lu, C. *Lab Chip* **2013**, *13*, 171–178.

(352) Lai, C. W.; Lin, Y. H.; Lee, G. Bin. *Biomed. Microdevices* **2008**, *10*, 749–756.

(353) Krüger, J.; Singh, K.; O'Neill, A.; Jackson, C.; Morrison, A.; O'Brein, P. *J. Micromechanics Microengineering* **2002**, *12*, 486–494.

(354) Cho, S. K.; Zhao, Y.; Kim, C. J. *Lab Chip* **2007**, *7*, 490–498.

(355) Ahn, K.; Kerbage, C.; Hunt, T. P.; Westervelt, R. M.; Link, D. R.; Weitz, D. A. *Appl. Phys. Lett.* **2006**, *88*, 1–3.

(356) Hung, S. H.; Lin, Y. H.; Lee, G. Bin. *J. Micromechanics Microengineering* **2010**, *20*, 045026.

(357) Baret, J. C.; Miller, O. J.; Taly, V.; Ryckelynck, M.; El-Harrak, A.; Frenz, L.; Rick, C.; Samuels, M. L.; Hutchison, J. B.; Agresti, J. J.; Link, D. R.; Weitz, D. A.; Griffiths, A. D. *Lab Chip* **2009**, *9*, 1850–1858.

(358) Hunt, T. P.; Issadore, D.; Westervelt, R. M. *Lab Chip* **2007**, *8*, 81–87.

(359) Guo, F.; Ji, X. H.; Liu, K.; He, R. X.; Zhao, L. B.; Guo, Z. X.; Liu, W.; Guo, S. S.; Zhao, X. Z. *Appl. Phys. Lett.* **2010**, *96*, 193701.

(360) Fidalgo, L. M.; Whyte, G.; Bratton, D.; Kaminski, C. F.; Abell, C.; Huck, W. T. S. *Angew. Chemie - Int. Ed.* **2008**, *47*, 2042–2045.

(361) Han, S. I.; Soo Kim, H.; Han, A. *Biosens. Bioelectron.* **2017**, *97*, 41–45.

(362) Da Silva, S.; Basséguy, R.; Bergel, A. *Electrochim. Acta* **2004**, *49*, 4553–4561.

(363) De Silva Muñoz, L.; Bergel, A.; Féron, D.; Basséguy, R. *Int. J. Hydrogen Energy* **2010**, *35*, 8561–8568.

(364) Dockery, D. W.; Schwartz, J.; Spengler, J. D. *Environ. Res.* **1992**, *59*, 362–373.

(365) Andersson, H.; Van den Berg, A. *Sensors Actuators, B Chem.* **2003**, *92*, 315–325.

(366) Joslyn, M. *Methods in food analysis: Applied to plant products*; 2012.

(367) Yang, J. *Anal. Chem.* **1999**, *71*, 911–918.

(368) Sackmann, E. K.; Fulton, A. L.; Beebe, D. J. *Nature* **2014**, *507*, 181–189.

(369) Yoon, Y.; Park, H.; Cros, F.; Allen, M. G. *Sixt. Annu. Int. Conf. Micro Electro Mech. Syst. 2003*

2003, 227–230.

(370) Shapiro, H. M. *John Wiley Sons* **2005**.

(371) Voldman, J. *Annu. Rev. Biomed. Eng.* **2006**, *8*, 425–454.

(372) Pysher, M. D.; Hayes, M. A. *Anal. Chem.* **2007**, *79*, 4552–4557.

(373) Zhao, K.; Li, D. *J. Chromatogr. A* **2018**, *1558*, 96–106.

(374) Zhao, K.; Li, D. *J. Colloid Interface Sci.* **2018**, *512*, 389–397.

(375) Hughes, M. P. *Electrophoresis*. 2002, pp 2569–2582.

(376) Gascoyne, P. R. C.; Vykoukal, J. V.; Schwartz, J. A.; Anderson, T. J.; Vykoukal, D. M.; Current, K. W.; McConaghy, C.; Becker, F. F.; Andrews, C. *Lab Chip* **2004**, *4*, 299–309.

(377) Li, H.; Bashir, R. *Sensors Actuators, B Chem.* **2002**, *86*, 215–221.

(378) Kim, U.; Qian, J.; Kenrick, S. A.; Daugherty, P. S.; Soh, H. T. *Anal. Chem.* **2008**, *80*, 8656–8661.

(379) Wang, L.; Flanagan, L. A.; Jeon, N. L.; Monuki, E.; Lee, A. P. *Lab Chip* **2007**, *7*, 1114–1120.

(380) Wang, L.; Lu, J.; Marchenko, S. A.; Monuki, E. S.; Flanagan, L. A.; Lee, A. P. *Electrophoresis* **2009**, *30*, 782–791.

(381) Cummings, E. B.; Singh, A. K. *Anal. Chem.* **2003**, *75*, 4724–4731.

(382) Lapizco-Encinas, B. H.; Simmons, B. A.; Cummings, E. B.; Fintschenko, Y. *Anal. Chem.* **2004**, *76*, 1571–1579.

(383) Shafiee, H.; Sano, M. B.; Henslee, E. A.; Caldwell, J. L.; Davalos, R. V. *Lab Chip* **2010**, *10*, 438–445.

(384) Gallo-Villanueva, R. C.; Rodríguez-López, C. E.; Díaz-de-la-Garza, R. I.; Reyes-Betanzo, C.; Lapizco-Encinas, B. H. *Electrophoresis* **2009**, *30*, 4195–4205.

(385) Vaidyanathan, R.; Dey, S.; Carrascosa, L. G.; Shiddiky, M. J. A.; Trau, M. *Biomicrofluidics* **2015**, *9*.

(386) Zhao, K.; Li, D. *ACS Appl. Mater. Interfaces* **2018**, *10*, 36572–36581.

(387) Zhao, K.; Larasati, L.; Duncker, B. P.; Li, D. *Anal. Chem.* **2019**, *18*, acs.analchem.9b01104.

(388) Lin, R. Z.; Ho, C. T.; Liu, C. H.; Chang, H. Y. *Biotechnol. J.* **2006**, *1*, 949–957.

(389) Ramos, A. *Springer Sci. Bus. Media* **2011**, *530*.

(390) Sun, T.; Morgan, H. *Microfluid. Nanofluidics* **2010**, *8*, 423–443.

(391) Singh, T.; Kumar, A. *J. Phys. Chem. B* **2008**, *112*, 12968–12972.

(392) Urdaneta, M.; Smela, E. *Lab Chip* **2008**, *8*, 550–556.

(393) Urdaneta, M.; Smela, E. *Electrophoresis* **2007**, *28*, 3145–3155.

(394) Vairo, M. L. R. *Stain Technol.* **1961**, *36*, 329–330.

(395) Painting, K.; Kirsop, B. *World J. Microbiol. Biotechnol.* **1990**, *6*, 346–347.

Appendix A

Effect of small orifice size on the maximum electric field

As discussed in CHAPTER 3, the asymmetric orifices structure with a relatively large width ratio and a shorter small orifice can induce a stronger electric field gradient and hence larger DEP force, leading to a high separation resolution. The equation relating the $\nabla|E|^2{}_{\max}$ to the size of the small orifice may be obtained by numerical simulation. Numerical simulations have been conducted using COMSOL 4.3b. Table A-1, Table A-2, and Figure A-1 show the example values of $\nabla|E|^2{}_{\max}$ obtained for different orifice combinations, as a function of the width and length of the small orifice at a given electric potential.

Table A-1 Calculated values of $\nabla|E|^2{}_{max}$ for different width ratios (the width of the large orifice is fixed at 500 μm and the length of the small orifice is fixed at 10 μm).

Width of the small orifice (μm)	Width ratio	Length of the small orifice (μm)	Applied voltage (V)	$\nabla\|E\|^2{}_{max}$ (V^2/m^3)
5	100	10	10	7.95×10^{18}
2.5	200	10	10	1.03×10^{19}
1.25	400	10	10	1.15×10^{19}
1	500	10	10	1.28×10^{19}
0.5	1000	10	10	1.98×10^{19}

Table A-2 Calculated values of $\nabla|E|^2{}_{max}$ for different lengths of the small orifice (the width ratio is fixed at 100).

Length of the small orifice (μm)	Width of the small orifice (μm)	Width ratio	Applied voltage (V)	$\nabla\|E\|^2{}_{max}$ (V^2/m^3)
10	5	100	10	7.95×10^{18}
20	5	100	10	6.01×10^{18}

30	5	100	10	3.04×10^{18}
40	5	100	10	2.61×10^{18}
50	5	100	10	2.04×10^{18}

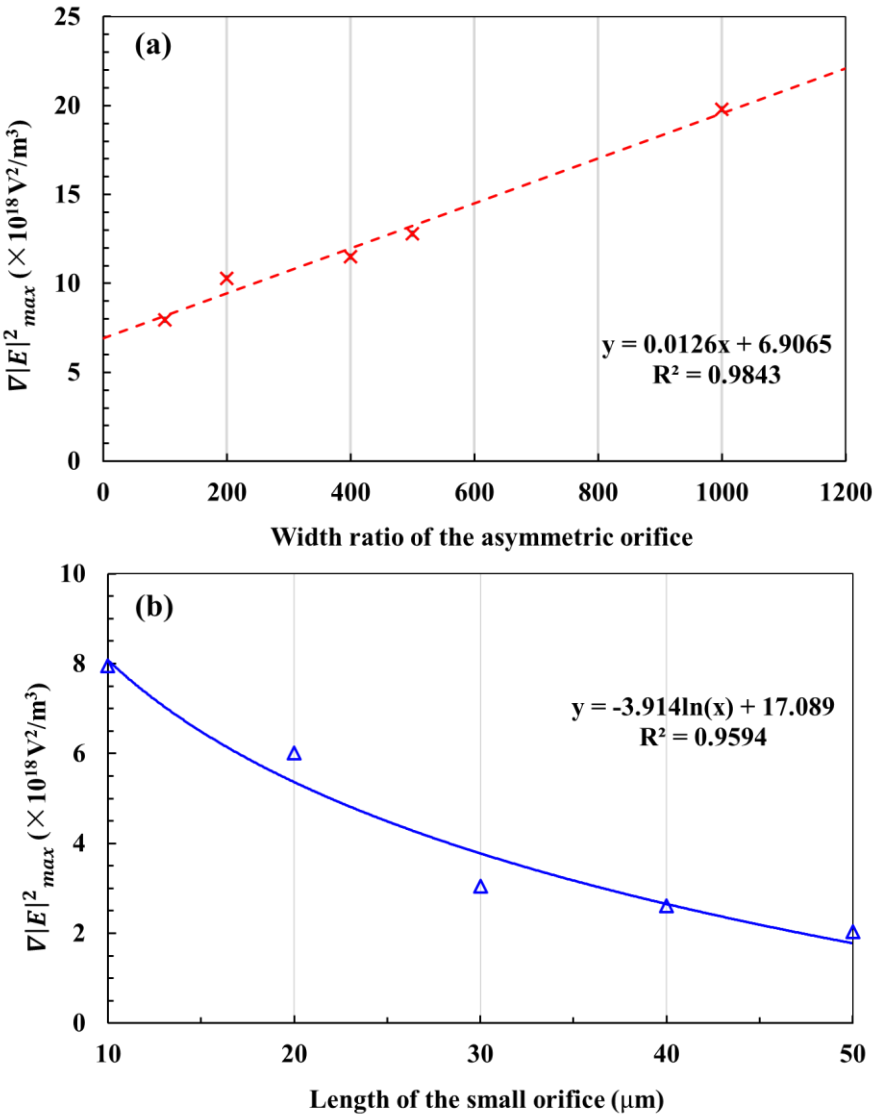

Figure A-1 Numerical simulations of $\nabla|E|^2_{max}$ for: (a) different width ratios (the width of the large orifice is fixed at 500 μm and the length of the small orifice is fixed at 10 μm), (b) different lengths of the small orifice (the width ratio is fixed at 100).

It can be inferred from Figure A-1 that the relation between the $\nabla|E|^2_{max}$ and the width ratio of the asymmetric orifices is expressed as

$$\nabla|E|^2{}_{max} = 0.0126w + 6.9065$$

where w represents the width ratio of the asymmetric orifices.

While the relation between the $\nabla|E|^2{}_{max}$ and the length of the small orifice is expressed as

$$\nabla|E|^2{}_{max} = -3.914 \ln L + 17.089$$

where L represents the length of the small orifice.

Therefore, by choosing an appropriately large width ratio of the nano-orifice and the micron orifice and a shorter small orifice, the sufficiently strong gradient of the electric field and hence sufficiently large DEP forces are generated, which enables the manipulation and separation of smaller micron and nano-sized particles and particles with the smaller size difference.

Appendix B

An example of Matlab code for calculating Clausius-Mossotti factor (f_{CM})

The Clausius-Mossotti factor (f_{CM}) varying with the electrical conductivity of the suspending solution under DC electric field

```
clc
Sigma_m=1e-6:1e-5:1e0; %% electrical conductivity of the suspending solution
Sigma_p=[7.8*1e-2 2.9*1e-2 0.8*1e-2]; %% electrical conductivity of 51nm, 140nm,
and 500nm polystyrene particle
f_cm=zeros(length(Sigma_m),length(Sigma_p)); %% Clausiu-Massotti factor (fCM)
varying with the electrical conductivity of the suspending solution under DC
electric field
for i=1:length(Sigma_p)
     f_cm(:,i)=((Sigma_p(i)-Sigma_m)./(Sigma_p(i)+2*Sigma_m));
end
figure
semilogx(Sigma_m,real(f_cm)); %% real part of fCM
```

The Clausius-Mossotti factor (f_{CM}) varying with the frequency of AC electric field

```
clc
epsilon_0=8.854*1e-12; %% permittivity of vacuum
f=1e3:1e3:1e9; %% frequency of the AC electric field
w=2*pi*f; %% angular frequency of the AC electric field
Sigma_m=2*1e-4; %% electric conductivity of DI water%
epsilon_m=78*epsilon_0; %% dielectric constant
Sigma_interior=0.2; %% interior conductivity of viable yeast cells
Sigma_membrane=2.5*1e-7; %% membrane conductivity of viable yeast cells
Sigma_wall=1.4*1e-2; %% wall conductivity of viable yeast cells
epsilon_interior=50*epsilon_0; %% interior dielectric constant of viable yeast
cells
epsilon_membrane=6*epsilon_0; %% membrane dielectric constant of viable yeast
cells
epsilon_wall=60*epsilon_0; %% wall dielectric constant of viable yeast cells
radius_interior=3.772; %% interior radius of viable yeast cells
radius_membrane=3.78; %% membrane radius of viable yeast cells
radius_wall=4; %% wall radius of viable yeast cells
r1=radius_membrane/radius_interior;
b1=epsilon_membrane-(i./w)*Sigma_membrane;
c1=epsilon_interior-(i./w)*Sigma_interior;
d1=r1^2+2*(c1-b1)./(c1+2*b1);
e1=r1^2-(c1-b1)./(c1+2*b1);
a1=b1.*d1./e1; %% complex permittivity of interior and membrane of viable yeast
cells
r2=radius_wall/radius_membrane;
b2=epsilon_wall-(i./w)*Sigma_wall;
d2=r2^2+2*(a1-b2)./(a1+2*b2);
e2=r2^2-(a1-b2)./(a1+2*b2);
a2=b2.*d2./e2; %% complex permittivity of viable yeast cells
c2=epsilon_m-(i./w)*Sigma_m; %% complex permittivity of suspending solution
m2=a2-c2;
n2=a2+2*c2;
```

```
f_cm2=m2./n2; %% Clausius-Mossotti factor (fCM) varying with the frequency of AC
electric field
semilogx(f,real(f_cm2));
hold on
Sigma_interior=7*1e-3; %% interior conductivity of non-viable yeast cells
Sigma_membrane=1.6*1e-4; %% membrane conductivity of non-viable yeast cells
Sigma_wall=1.5*1e-3; %% wall conductivity of non-viable yeast cells
epsilon_interior=50*epsilon_0; %% interior dielectric constant of non-viable
yeast cells
epsilon_membrane=6*epsilon_0; %% membrane dielectric constant of non-viable
yeast cells
epsilon_wall=60*epsilon_0; %% wall dielectric constant of non-viable yeast
cells
radius_interior=3.242; %% interior radius of non-viable yeast cells
radius_membrane=3.25; %% membrane radius of non-viable yeast cells
radius_wall=3.5; %% wall radius of non-viable yeast cells
r1=radius_membrane/radius_interior;
b1=epsilon_membrane-(i./w)*Sigma_membrane;
c1=epsilon_interior-(i./w)*Sigma_interior;
d1=r1^2+2*(c1-b1)./(c1+2*b1);
e1=r1^2-(c1-b1)./(c1+2*b1);
a1=b1.*d1./e1; %% complex permittivity of interior and membrane of non-viable
yeast cells
r2=radius_wall/radius_membrane;
b2=epsilon_wall-(i./w)*Sigma_wall;
d2=r2^2+2*(a1-b2)./(a1+2*b2);
e2=r2^2-(a1-b2)./(a1+2*b2);
a2=b2.*d2./e2; %% complex permittivity of non-viable yeast cells
c2=epsilon_m-(i./w)*Sigma_m; %% complex permittivity of suspending solution
m2=a2-c2;
n2=a2+2*c2;
f_cm2=m2./n2; %% Clausius-Mossotti factor (fCM) varying with the frequency of AC
electric field
semilogx(f,real(f_cm2));
hold on
```

Appendix C

Effects of the magnetic field in the microchannel

The electric current generates a magnetic field which can attract magnetic particles and leads to a similar phenomenon to positive DEP the magnetic field effects on the magnetic particles. However, the magnetic particles used in CHAPTER 4 are the magnetic coated polystyrene beads and the Fe_3O_4 coating thickness is approximately 40 ~ 200 nm which can be neglected in comparison with the micron-sized particles. Furthermore, the *Lorentz force* on a charged particle moving in a magnetic field is given by

$$\boldsymbol{F} = q\boldsymbol{v} \times \boldsymbol{B}$$

$$\boldsymbol{B} = \frac{\mu_0 \boldsymbol{I}}{\boldsymbol{2}\pi r}$$

where q is the electric charge of the particle, $\boldsymbol{v}$ is the instantaneous velocity of the particle, $\boldsymbol{B}$ is the magnetic field, $\boldsymbol{I}$ is the electric current, μ_0 is the magnetic constant, and r is the radius.

Because the electric current involved in this study is very small, for example, the current is about 0.9×10^{-6} A in the case of separation of 5.2 μm magnetic-coated polystyrene particles and 7 μm fluorescent polystyrene particles, there is no significant magnetic field and hence no significant magnetic field force $\boldsymbol{F}$ generated on the magnetic particles. Therefore, the magnetic field effect is negligible.

Appendix D

Fabrication procedure of the micro copper electrodes

For the fabrication of the copper electrode pads, the procedure is illustrated in Figure A-2. The thick photoresist layer was firstly spin-coated on the electrode pad (Sigma-Aldrich) at the speed of 3000 rpm in the steps (a) and (b) as shown in Figure A-2. Afterward, by submerging in the photoresist developer (MicroChem), the exposure parts of the photoresist were dissolved after UV treatment (steps (c) and (d)). Following the step (e), the uncovered pads were etched from the copper sheet with the exposed photoresist in the copper electrode etchant (1CE-100, Transene Inc.) at 65 °C. Then, the photoresist was removed from the electrode-photoresist sandwich in the NaOH (30%) bath at 130 ◦C for 40 min and the copper electrode pads with patterned structures were obtained in step (f). After manually inserting the electrodes into the microfluidic chambers under the microscope, the chip was produced by bonding it with a plasma-treated glass substrate. The microelectrodes (25 μm in thickness) lying in the deformable PDMS chamber (27 μm in depth) were firmly compressed. Then, the microchannel was filled in with the surrounding solution which automatically sealed the tiny gaps adjacent to the electrode pads. By tuning the liquid level in the wells of the copper chambers, the medium leaking through the gaps was negligible。

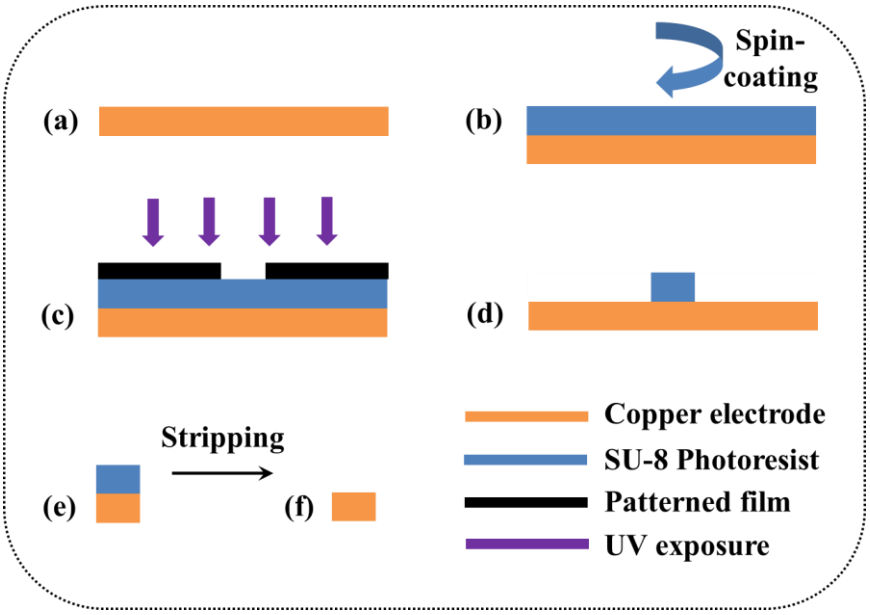

Figure A-2 Fabrication of the copper electrode pads with a patterned structure by using extended soft-lithography.

Appendix E

AC-DEP separation of 5 μm and 10 μm PS particles

As discussed in CHAPTER 6, the separation of 5 μm and 10 μm PS particles by size was conducted by applying the 5Vp-p and 100 kHz. The DI water with a pH value of 7, a dielectric constant of 80, and an electric conductivity of 5.5 $\times$ 10^{-6} S/m was used as the surrounding media. In the experiment, the width of the small and large orifice is 10 μm and 500 μm, respectively. It should be realized that according to Equation (6-1), the magnitude of the DEP force increases with the particle volume (a^3). The particles with different sizes will be driven into individual trajectories after passing through the dielectrophoretic force area. As discussed in Equation (6-1), the magnitude of the DEP force exerted on the 10 μm particles is 8 times larger than that on the 5 μm particles. Therefore, the 5 μm particles experienced relatively weaker n-DEP effects and moved into the outlet channel C. The 10 μm particles experienced stronger DEP force, resulting in sufficiently large trajectory shifts, and moved into the outlet channel D, as shown in Figure A-3. The size-dependent separation of 5 μm particles and 10 μm particles was achieved. Therefore, by using this AC-DEP method, the manipulation and separation of the targeted particles/droplets can be successfully achieved by optimizing the applied electric potential, the width and length of the small orifice, as well as the asymmetric orifices' width ratio. In addition, by selecting the asymmetric orifices with a large width ratio, low electric potentials are enough to produce sufficiently strong electric field gradient, which enables the separation with high sensitivity without using the voltage amplifier instruments.

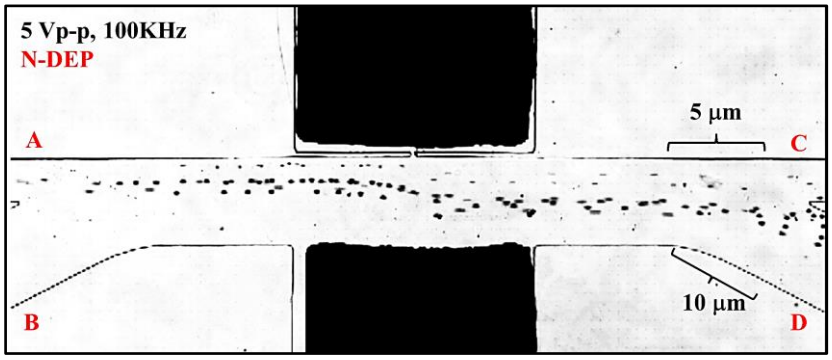

Figure A-3 Size-dependent separation of 5 μm and 10 μm PS particles with 5Vp-p and 100 kHz applied.

Appendix F

Effect of f_{CM} on particle trajectory change

As discussed in CHAPTER 6, there appears to be a significant difference in the particle trajectories in Figure 6-5 when the AC field frequency is varied. The marginal difference between the estimated CM factor (f_{CM}) (-0.48 vs. -0.5) leads to the trajectory changes. Besides the AC-DEP effects, other possible factors may include Brownian motion and gravity. As shown in Figure A-4 [60], the changing effects of the magnitudes of three dominant forces, i.e., Brownian motion, gravity, and dielectrophoresis, on particle behaviors in an AC field are illustrated. Here the displacement of a particle has been calculated over a time interval of 1 second, plotted as a function of particle size. For large particles, the Brownian motion is minuscule, resulting in a displacement of the order of nanometers, so that to all extents and purposes it can be ignored even for particles up to 1 μm in radius. Compare this with the influence of the gravitational force, this scales linearly with volume so that the bigger the particles the further they move. Contrast these effects with dielectrophoretic forces, for particles larger than 1 μm, Figure A-4 shows that the DEP force dominates over both the gravitational force and Brownian motion, i.e., DEP is the solely deterministic force over this period of time.

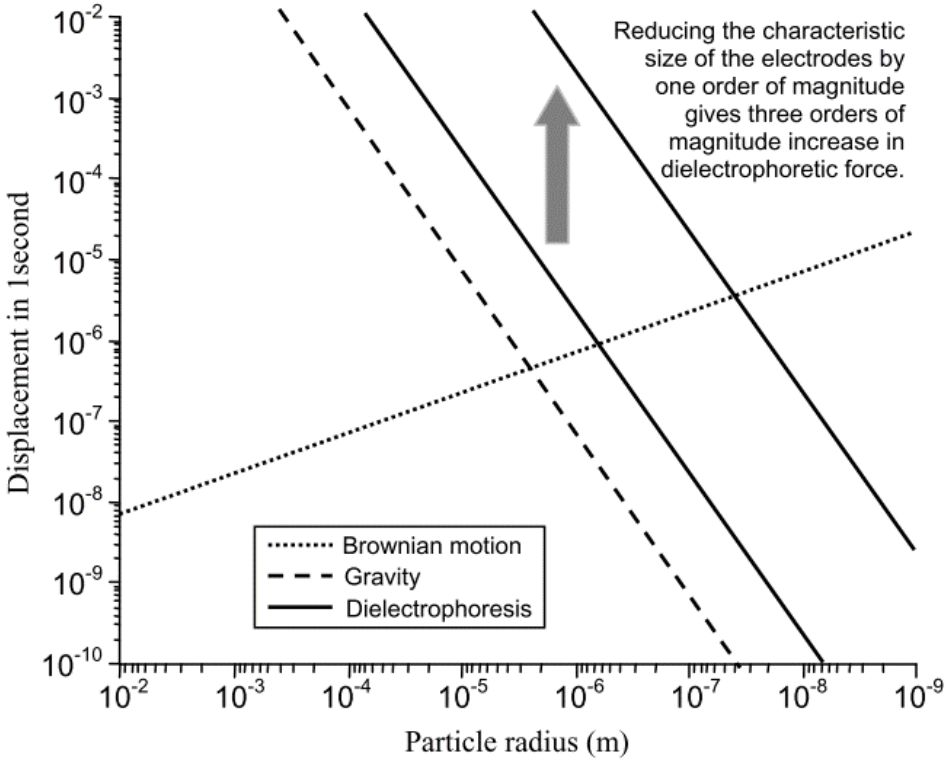

Figure A-4 Diagram of the relative magnitudes of displacement in one second due to three physical mechanisms: Brownian motion, gravity, and dielectrophoresis as a function of particle radius from 1 cm down to 1 nm [60].

Therefore, in this study, the DEP forces acting on the 10 μm PS particles are the dominant forces. As we know, the magnitude of the dielectrophoretic force is proportional to the magnitude of f_{CM}, while the direction of the dielectrophoretic behaviors is depending on the sign of f_{CM}. Due to the magnitude difference between the CM factors at different frequencies of the AC electric field, the trajectory shifts of the PS particles under 10 MHz (the magnitude of the f_{CM} is 0.48) are slightly smaller than that at the frequency of 100 kHz ($f_{CM} = 0.5$).

Appendix G

Methylene blue stain of yeast samples

For the yeast cells (standard lab yeast strain, Saccharomyces cerevisiae S288c) used in CHAPTER 6, they are initially grown in liquid YPD media (1% yeast extract, 2% peptone, and 2% glucose) at 30°C with shaking. After 2 days, the cells are divided into two sets: one was kept in YPD media and the other one in DI water to induce nutrient deprivation. All of the samples are suspended in three liquids: (1) DI water with σ_m =0.0002 S/m, a dielectric constant of 80, and a pH value of 7; (2) the 0.4mM K_2HPO_4 solution with σ_m =0.01 S/m, a dielectric constant of 80, and a pH value of 7; and (3) the 4.8mM K_2HPO_4 solution with σ_m =0.12 S/m, a dielectric constant of 80, and a pH value of 7, respectively. To stain the dead cells, the Methylene blue (Sigma-Aldrich) is added to the suspension and kept stirring for 2 min. Methylene blue is a dye that is used to differentiate viable and non-viable yeast cells. It enters all the yeast cells, however, only the viable cells will remain colorless due to their enzymatic ability to reduce the dye. The dead cells will be stained dark blue, as shown in Figure A-5.

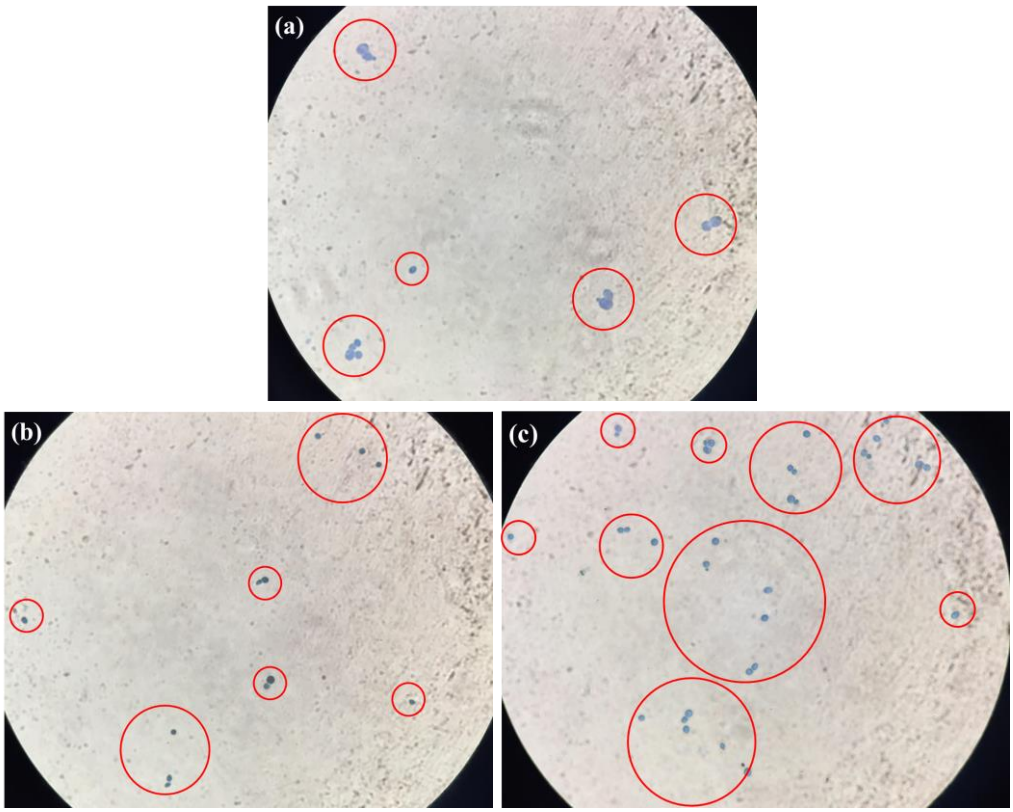

Figure A-5 Methylene blue stain of non-viable yeast samples in the (a) DI water, (b) 0.4mM K_2HPO_4 solution, and (c) 4.8mM K_2HPO_4 solution.